The Pennsylvania State University

The Graduate School

Department of Chemical Engineering

DEVELOPMENT OF MULTI-SCALE COMPUTATIONAL METHODS FOR MODELING PHASE FORMATION IN Pd-BASED CATALYSTS

A Dissertation in

Chemical Engineering

by

Thomas Patrick Senftle

Submitted in Partial Fulfillment
of the Requirements
for the Degree of

Doctor of Philosophy

August 2015

The dissertation of Thomas Patrick Senftle was reviewed and approved* by the following:

Michael J. Janik
Associate Professor of Chemical Engineering
John J. and Jean M. Brennan Clean Energy Early Career Professor
Dissertation Co-advisor
Co-Chair of Committee

Adri C.T. van Duin
Associate Professor of Mechanical Engineering
Kenneth Kuan-Yuo Kuo Early Career Professor
Dissertation Co-advisor
Co-Chair of Committee

Robert M. Rioux
Friedrich G. Helfferich Associate Professor of Chemical Engineering

Scott T. Milner
Joyce Chair and Professor of Chemical Engineering

Phillip E. Savage
Walter L. Robb Chair and Professor of Chemical Engineering
Head of the Department

*Signatures are on file in the Graduate School

ABSTRACT

In Pd/ceria catalysts, mixed Pd-Ce oxide formations at the cluster-support interface offer unique activity toward hydrocarbon activation. Both experimental and computational investigations in the literature suggest that unique Pd-O-Ce surface formations yield highly reactive sites on the catalyst surface. However, structural details and the corresponding reaction mechanisms governing the behavior of such sites are not well understood. As such, this dissertation employs Density Functional Theory (DFT) in tandem with classical ReaxFF modeling to determine the stability and activity of methane activation sites at the Pd/ceria interface.

The ReaxFF interaction potential is used to investigate cluster-support interactions at length and time scales inaccessible to quantum methods. In particular, this dissertation develops a hybrid grand canonical Monte Carlo/molecular dynamics (GC-MC/MD) approach that is suited to assess oxide formation in regions where the Pd cluster contacts the underlying ceria support. When coupled with DFT, this multi-scale approach demonstrates that Pd atoms incorporated in the fluorite lattice structure of ceria alternate between Pd^{4+} and Pd^{2+} oxidation states during operation. In general, Pd^{4+} states are effective hydrocarbon activation sites, as the dissociative adsorption of the hydrocarbon reduces Pd^{4+} to its thermodynamically preferred Pd^{2+} state. Therefore, maximizing the number of transient Pd^{4+} states under operating conditions is essential for achieving optimal catalytic performance. The multi-scale simulation methodology developed and applied in this dissertation can evaluate the trade-off between stability and activity exhibited by Pd/CeO_2, and can be readily extended to other catalytic systems.

TABLE OF CONTENTS

LIST OF FIGURES

LIST OF TABLES

ACKNOWLEDGEMENTS

I would first like to express my gratitude for my dissertation advisors, Mike Janik and Adri van Duin. One would be considered fortunate to have a dedicated, talented, and encouraging mentor throughout the tribulations of graduate school. I must be doubly fortunate because I had two. Thank you for teaching me to be excited about my research.

I am also grateful for the support of my family, who have always taken a sincere interest in my work. And for always being 'understanding' when I was 'too deep in thought' to do the dishes. Thanks Mom, Dad, Melissa (and Ted), Shannan (and Mike and Georgie), Anita, Tess, and Luke. I am thankful for my Grandparents' support as well, especially from both of my Grandfathers. Discussing science with you taught me that knowledge gained through research should be its own reward.

Finally I would like to thank my friends and colleagues at Penn State – I can't imagine a place I'd rather be. Thanks to everyone in the Janik and van Duin labs, especially Matt and Siddarth who arrived at the same time as me. Good luck Ian, Sneha, Joel, Gaurav, and Jiyun – I wish you the best in your research endeavors. Thanks Maggie, Charlie, Kelsey, and Tony for the game nights (and informative presentations). And thanks Joe, Chris, Sergio, and Chelsea for always being up for a round of Mario Kart. I would also like to thank Lily for her constructive criticisms.

Domine Ut Videam
Mark 10:51

Chapter 1
Introduction

1.1. Overview

Enhancing the design of oxide-supported metal catalysts, featuring highly-dispersed metal atoms supported on an oxide surface, is essential for optimizing the performance of numerous industrial chemical processes. Processes reliant on such catalysts include: catalytic combustion,[1-13] hydrocarbon steam-reforming,[14-25] CO removal from syngas *via* the water-gas-shift (WGS) reaction,[26-35] CO and NO oxidation,[36-42] automotive three-way catalysis,[43-47] solid oxide fuel cell (SOFC) electrodes,[48-54] selective hydrogenation,[55-60] and numerous others. In particular, Palladium supported on ceria is an effective catalyst for hydrocarbon oxidation and is a promising candidate for application in solid-oxide fuel cell (SOFC) anodes[49-51], automotive three-way catalysis,[44, 47] catalytic combustion,[3, 12, 13] and water-gas-shift catalysis.[32, 61, 62] The activity of Pd/CeO_2 catalysts can be uniquely controlled by altering the structure of the metal-support interface to induce Pd mixing in the ceria lattice. To connect performance to active site structure in Pd/CeO_2 catalysts, and in similar metal/metal-oxide catalysts, one must first obtain an atomistic-scale understanding of the catalytic conversion mechanisms dependent on cluster-support interactions influencing catalytic activity, selectivity, and stability.

Identifying stable surface morphologies, active surface sites, and reaction mechanisms is a difficult task due to the complexity of competing factors affecting catalytic properties.[63] Catalyst activity and stability are directly linked to: the size and distribution

of metal clusters on the oxide surface,[64-66] the oxidation state of the metal,[67-69] the charge transfer between the cluster and the support,[70-73] the electronic structure of atoms at the metal-oxide interface,[72, 74-78] the concentration of oxygen vacancies on the oxide surface,[79-81] the formation of mixed-metal-oxide surface phases,[82-85] the incorporation of metal atoms in oxide lattice positions,[4, 13, 71, 80, 86-90] and the coverage effects of adsorbates.[91-94] Furthermore, these effects are dependent on variable reaction conditions; namely, gas phase partial pressures and temperature. A fundamental understanding of how these phenomena are linked to catalytic behavior is essential for making informed design decisions that will yield stable and active catalysts. Toward this objective, multi-scale computational methods can complement experimental efforts seeking to build an atomic level understanding of supported metal-oxide catalysts.

The research objectives of this dissertation include the development, validation, and application of multi-scale simulation methods to investigate the structure and reactivity of oxide-supported Pd catalyst, with a particular emphasis on CeO_2-based supports. Density Functional Theory (DFT) serves as the foundation of this simulation methodology, providing accurate relative energies and reaction barriers for a range of structures relevant at the Pd/CeO_2 interface. To circumvent the computational intensity of DFT, a parameter set for the empirical ReaxFF interaction potential will be developed to reproduce training sets populated with DFT data, allowing simulation methods to access greater length and time scales. As a reactive interaction potential, ReaxFF will enable simulations that can fully include dynamical effects involving diffusion and surface rearrangements occurring during phase formation. The ReaxFF force-field will be used to provide additional configurations for DFT studies, thus providing both an error evaluation on ReaxFF

predictions as well as a low-CPU-cost tool to sample the vast configuration space of the metal/oxide system *via* molecular dynamics (MD) and Monte Carlo (MC) methods.

The sections in this introductory chapter are organized as follows. A review of recent literature and previous studies investigating Pd/CeO_2 catalysts is provided in Section 1.2. Section 1.3 outlines specific research questions, hypothesis, and objectives for this dissertation. Background information regarding computational theories and methods employed throughout this dissertation is provided in Section 1.4. Finally, Section 1.5 contains an overview of the dissertation's organization and chapter layout.

1.2. Background: Pd/ceria Catalysis

(Note: adapted from a book chapter written by T.P.S. appearing in *Computational Catalysis*[95])

Under varying reaction conditions, multiple Pd/ceria surface morphologies are possible, each with unique catalytic activity. Examples of such morphologies include metallic Pd clusters adsorbed on the ceria support, oxidized palladium in PdO surface phases, and palladium incorporated in cerium lattice vacancies as solid-solution $Pd_xCe_{1-x}O_\delta$ phases. Each surface morphology can contribute unique activation sites, making Pd/CeO_2 a versatile catalytic material. There is, however, little consensus in the literature regarding the chemical and structural properties of the active sites and reaction mechanisms in Pd/ceria catalysts. This is a particular issue regarding investigations of active sites involving the metal-cluster/oxide-support interface.

Experimental evidence suggests that strong electronic interactions between Pd and ceria stabilize oxidized Pd species, which in turn are capable of activating C-H bonds in

hydrocarbons. This is evident in the work of Colussi *et al.*,[13] who used high-resolution transmission electron microscopy (HRTEM) and DFT to show that Pd/ceria catalysts prepared by solution combustion synthesis (SCS) contain a Pd^{2+}/CeO_{δ} solid solution that is absent in Pd/ceria catalysts prepared by traditional incipient wetness impregnation (IWI). The Pd^{2+}/CeO_{δ} surface phase is composed of Pd atoms substituted in the ceria lattice at Ce vacancy positions, thus forming a square planar geometry characteristic of Pd^{2+} in bulk PdO (Figure 1-1). Pd/ceria samples prepared by SCS achieved considerably higher methane combustion rates compared to the analogous catalysts prepared by IWI, as summarized in Figure 1-1. Similar results for the combustion of propane and dimethyl ether over Pd/ceria catalysts prepared by SCS further emphasize the importance of incorporated $Pd^{\delta+}$ surface states.[4]

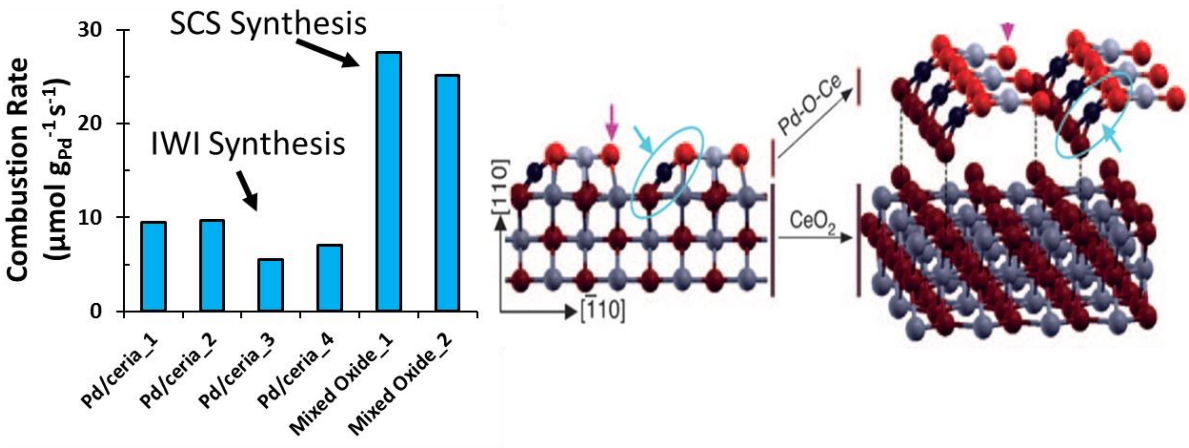

Figure 1-1. (Left) Methane combustion rate at 553 K over Pd/ceria catalysts prepared by IWI and SCS. (Right) DFT optimized structure of SCS synthesized Pd/ceria showing Pd incorporated in a Pd^{2+} square planar geometry. (Data and surface figure adapted from Colussi *et al.*, Ref. 7)

Analogously, Gorte and co-workers[12] synthesized Pd-core/ceria-shell catalysts ($Pd@CeO_2$) that achieve high methane conversion rates by maximizing the concentration of active Pd/ceria interfacial sites. The authors demonstrate that $Pd@CeO_2$ catalysts display a similar apparent activation barrier compared to traditional Pd/ceria catalysts with metallic clusters adsorbed on the ceria surface, suggesting that the same activation site is present on in both catalysts. This points to a synergistic interaction between Pd and CeO_2 at the active site. Compared to traditional Pd/ceria catalysts, the core-shell construction maximizes the number of sites exposed to reactants, as nearly the entire exposed Pd cluster surface is in contact with the ceria lattice. In traditional IWI catalysts, such sites are only exposed on the contact line at the metal-cluster/oxide-support boundary. In a separate study, Gorte and co-workers also demonstrated that CO oxidation rates over Pd/ceria catalysts are directly proportionate to the number of sites at the Pd/ceria interfacial boundary.[96] Other literature examples that highlight synergistic Pd/ceria interactions include the work of Xiao *et al.*,[3] in which XPS results link Pd-O-Ce interactions to methane combustion activity, and of Priolkar *et al.*,[97] in which XRD, XPS, and EXAFS results show high CO oxidation activity in Pd/ceria prepared by SCS. Together, these results demonstrate the complex nature of Pd/ceria catalysis, in which strong metal-support interactions lead to the coexistence of multiple surface morphologies with unique catalytic properties.

Each of the possible catalyst morphologies described above may contribute differently to the catalytic activity of the system, and it is essential to identify surface morphologies that are both *stable* and *active* under the reaction conditions of interest. DFT electronic structure calculations and *ab initio* thermodynamics are applied in this

dissertation to determine Pd/ceria surface morphologies that are stable under typical operating conditions and that provide a low energy path for hydrocarbon oxidation. Previous DFT studies completed in our lab examined the nature of oxygen vacancy formation and methane activation over Pd-substituted CeO_2(111), (110), and (100) surfaces.[71, 80, 90] The results demonstrated that methane activation and oxygen vacancy formation are surface reduction processes, and that the substitution of a Pd atom in the ceria lattice greatly affects the energetics of these processes. The removal of a surface oxygen when forming a vacancy in the ceria lattice results in a single-spin gap state above the valence band, which is attributed to the single occupation of *4f* states on two cerium atoms, as seen in the density of sates (DOS) plot in Figure 1-2. This is confirmed by orbital imaging of this state, demonstrating that oxygen vacancy formation results in electron localization on two cerium atoms adjacent to the oxygen vacancy. Similar Ce^{4+} to Ce^{3+} reductions occur on adjacent to CH_3 and H adsorption sites upon methane activation, thus demonstrating that oxygen vacancy formation and methane adsorption are analogs of the same surface reduction processes.[98]

Conversely, the formation of an oxygen vacancy in Pd-substituted CeO_2(111) results in a spin-paired gap state. Orbital imaging of this state demonstrates charge accumulation on a single Pd atom neighboring the vacancy, confirming that the spin-paired state is the result of a Pd^{4+} reduction to Pd^{2+}. A comparison of Pd-substituted surface structures before and after reduction shows that Pd assumes a square planar coordination geometry similar to that of Pd^{2+} in bulk PdO. Hence, the reduction of Pd-substituted surfaces results in one Pd^{4+} to Pd^{2+} reduction, as opposed to two Ce^{4+} to Ce^{3+} reductions in stoichiometric ceria. The dissociative adsorption of methane yields similar electronic

rearrangements, thus leading to a correlation between oxygen vacancy formation energy and methane adsorption energy.[98] Generally, a substituted Pd atom serves as a reduction center, and the resultant gap state is lower in energy than the resulting gap state over clean CeO_2. This yields lower vacancy formation energies and lower methane dissociation barriers over Pd-substituted surfaces. The DOS of oxygen vacancy formation in clean CeO_2 and $Pd_xCe_{1-x}O_2$ is summarized in Figure 1-2.

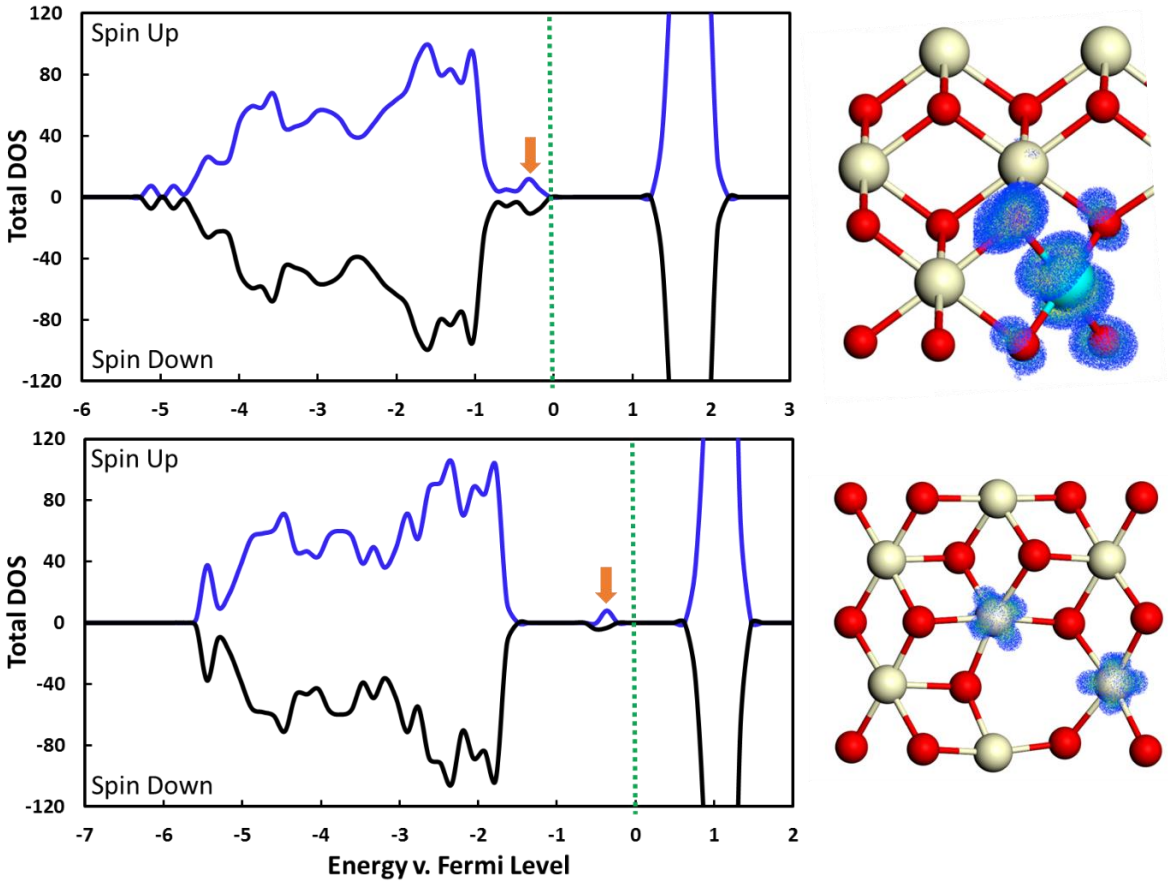

Figure 1-2. DOS of oxygen vacant (a) CeO_2 and (b) $Pd_xO_{1-x}O_\delta$ surfaces. The Fermi level is indicated by the vertical green line. Orange arrows indicate the state imaged on the right.

The employed DFT method is only valid at zero temperature and pressure and, correspondingly, cannot evaluate the thermodynamic stability of Pd incorporated surfaces. *Ab initio* thermodynamics must be utilized to determine the stability of possible Pd/ceria surface morphologies at operating temperatures and pressures. Our lab employed such an approach to investigate the stability of single Pd atom states on CeO_2(111), (110), and (100) surfaces.[80] Figure 1-3 contains the resulting phase diagrams, which show the temperature and oxygen chemical potential ranges where Pd atoms are stable either as (1) adsorbed Pd* atoms, (2) adsorbed PdO* or PdO_2* clusters, or (3) incorporated in Ce lattice positions on either a fully oxidized surface (as Pd^{4+}) or oxygen deficient surfaces (as Pd^{2+} or Pd^0). On the CeO_2(111) facet, Pd^{4+} ions are thermodynamically stable when incorporated into the fully oxidized surface under high oxygen pressures or low temperatures. The DFT optimized structure of this surface, shown in Figure 1-3(b), demonstrates that Pd-incorporation is stabilized by a surface reconstruction of the fluorite ceria lattice providing a favorable octahedral oxygen coordination environment for the d^6 metal center. Both oxygen vacancy formation and methane dissociation cause a restructuring of the surface, providing a square-planar oxygen coordination that stabilizes the d^8 metal center of Pd^{2+}.

These studies suggest that the incorporated Pd atoms in the CeO_2 surface lattice may be both stable and active for methane dissociation. However, the high reducibility of the Pd-incorporated surface could alter the free energy landscape of the reaction mechanism so that re-oxidation of the surface becomes rate limiting. To consider this possibility *ab initio* thermodynamics approaches were used to derive a free energy diagram accounting for the impact of varying redox conditions (differing CH_4, O_2, and H_2O chemical potentials) on the reaction energy diagram. Figure 1-4 shows the reaction free

energy diagram for methane combustion over $CeO_2(111)$ and $Pd_xCe_{1-x}O_2(111)$ surfaces. Pd incorporation reduces the reaction energy for each C-H bond activation step, and therefore leads to a faster overall combustion rate. These results suggest that Pd incorporated sites are present under combustion conditions, and that such sites lower the activation barrier of the rate determining CH_4 activation step.

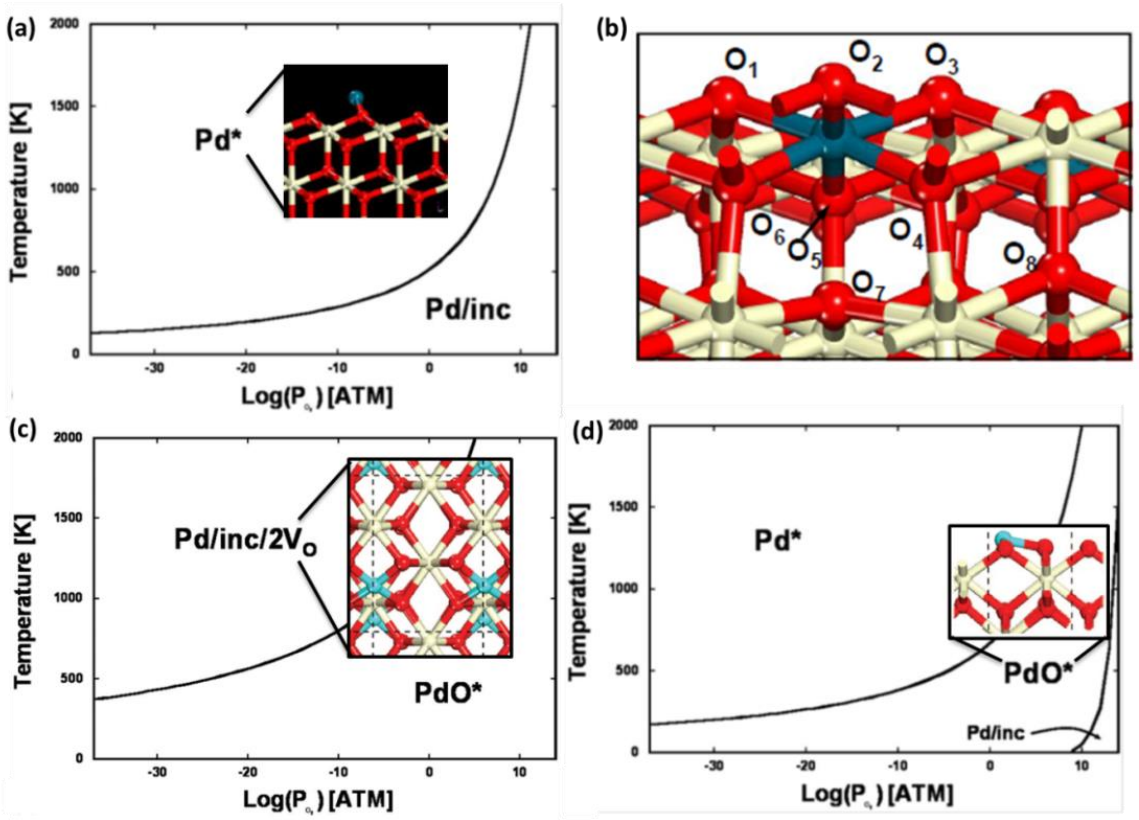

Figure 1-3. (a), (c), (d) *Ab initio* thermodynamic phase diagrams and insets depicting DFT optimized surface structures for Pd/ceria surface morphologies for (a-b) $CeO_2(111)$, (c) $CeO_2(110)$, and (d) $CeO_2(100)$ surfaces. (b) Octahedral oxygen coordination for Pd^{4+} environment formed by oxygen atoms O1-O6, with O7 moving away from the Pd metal center (compared to the adjacent O8 atom). (Figures adapted from Mayernick *et al.*, Ref. 14)

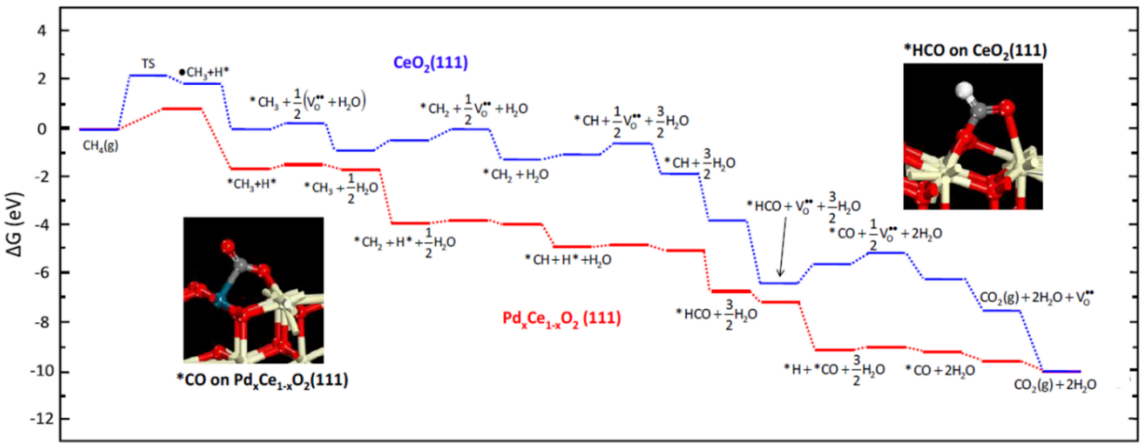

Figure 1-4. Free energy reaction diagrams for CH_4 oxidation over (blue) clean CeO2(111) and (red) $Pd_xCe1_{-x}O_\delta$. (Adapted from Mayernick *et. al.*, Ref. 90)

Although the above studies underscore the importance of strong Pd-ceria interactions, the structure and nature of the active site under reaction conditions is still not well understood. The above work indicates that an incorporated Pd^{4+} is essential to providing a low methane activation. However, Boronin *et al.*[99] reported XPS and XRD results consistent with stable Pd^{2+} states in $Pd_xCe_{1-x}O_\delta$ opposed to Pd^{4+} states, in agreement with the surface structure reported by Colussi *et al.*[13] Despite this evidence, neither investigation conducted structure characterizations under reaction conditions and, therefore, cannot evaluate the possibility that transient Pd^{4+} states play a role in the activation mechanism. Furthermore, the above DFT studies only consider a single Pd atom incorporation site, while the actual system likely features Pd-ceria mixing at the cluster-oxide interface. The kinetic and thermodynamic driving forces inducing such mixing must be understood to better select catalyst synthesis, pre-treatment, and operating conditions for optimizing performance. This motivates the work presented in this dissertation, wherein multi-scale computational approaches are developed and employed to address the complex nature of phase formation in oxide-supported Pd catalysts.

1.3. Hypotheses and Research Objectives

Previous studies motivate the general hypothesis that *unique cluster-support interactions characteristic of mixed surface oxides in $Pd_{1-x}Ce_xO_\delta$ create stable and active sites toward catalytic hydrocarbon activation*. The following research questions and specific hypotheses will be investigated:

1) Under what operating conditions (*i.e.* temperature and oxygen partial pressure) does the surface morphology transition from a supported Pd cluster to a mixed Pd/Ce surface oxide? Does this transition occur during the catalytic cycle? *Hypothesis: Under reaction conditions ($T \sim 500$ K, $P_{O2} \sim 10^{-2}$ atm), dynamic Pd oxidation state transitions allow for facile oxygen exchange upon hydrocarbon activation. The feasibility of these transitions is controlled by operating conditions.*

2) What are the kinetic and thermodynamic driving forces that lead to Pd incorporation at the cluster-support interface? How does this affect catalysis? *Hypothesis: Restructuring of the metal-support interface occurs during the catalytic cycle, and is induced by highly oxidizing conditions. This forms unique mixed-metal oxide phases affecting the performance of Pd/CeO_2 catalysts.*

3) How does phase formation in Pd/ceria catalysts under reaction conditions affect overall stability and activity? *Hypothesis: The incorporation of Pd atoms in the ceria lattice yields meta-stable Pd^{4+} states that, although thermodynamically less stable than Pd^{2+} states, are catalytically active. Pd^{4+}states exist on the surface under reaction conditions, and their meta-stable nature yields highly*

reactive sites for surface reduction processes (i.e. hydrocarbon activation).

A multi-scale computational approach is utilized to investigate these hypotheses. To complement DFT and to extend accessible simulation scales, we first develop a ReaxFF force-field parameterized and validated from DFT data gathered specifically for Ce/Pd/O/C/H systems. With the optimized ReaxFF potential, we implement reactive molecular dynamics (RMD) and Monte Carlo (MC) simulations in tandem with DFT calculations to characterize particle-surface interactions responsible for activating combustion reaction pathways, as well as to model the dynamic restructuring of the Pd/ceria surface during reaction. Along with developing a ReaxFF interaction potential for Pd/ceria/hydrocarbon systems, we develop a ReaxFF-based Grand Canonical Monte Carlo scheme (GC-MC), which will enable simulations featuring the exchange of oxygen, hydrogen, and carbon between the Pd/CeO_2 surface and a gas phase reservoir of reactant species. This approach can assess phase transformations induced by the reactant gas phase, thus modeling the state of the surface while in thermodynamic equilibrium with a gas phase reservoir. This establishes surface composition and morphology as a function of reactant chemical potentials, providing relevant surface models for subsequent reactivity analyses. As such, the following research objectives are set to develop the necessary simulation methods and to address the above hypotheses and research questions:

1) Optimize Pd/O/C/H interaction parameters for ReaxFF against a training set populated with DFT data of bulk formation energies, surface energies, adsorption energies, and activation barriers. (Chapters 2-4) Combine the Pd/O/C/H parameters with existing parameter sets describing oxide supports. (Ti/O in Chapters 5, and Ce/O in Chapter 7)

2) Develop a Grand Canonical Monte Carlo (GC-MC) simulation method for ReaxFF that can treat phase transformations in the catalyst bulk and surface induced by exposure to the reactant gas phase environment. (Chapters 2-3)
3) Apply the developed ReaxFF interaction potentials and GC-MC method to model phase formation in unsupported Pd clusters. Typical Pd-phases formed under operating conditions are oxides, hydrides, and carbides. (Chapters 2-4)
4) Extend the phase formation investigations to oxide-supported Pd systems. Typical Pd supports are TiO_2 and CeO_2. (Chapters 5-7)
5) Conduct multi-scale investigation of hydrocarbon activation at the Pd/CeO_2 interface. (Chapters 6-7)

1.4. Computational Methods

DFT methods can calculate the ground state electronic structure and energy of a system as a function of nuclear coordinates, allowing one to determine the preferred reaction path by identifying optimal structures on the DFT calculated potential energy surface (PES). Thus, the utility of DFT lies in its ability to accurately describe the energetics of reactive bond breaking/forming events, which reveals important aspects of the underlying electronic structure, such as oxidation states in atoms, orbital occupancies in molecules, and electronic band structures in solids. *Ab initio* thermodynamics uses statistical mechanics to extend DFT to high temperature and pressure descriptions, which allows one to calculate free energies to assess the stability the catalyst surface as a function

of chemical environment. Such knowledge is a powerful tool for determining preferred reaction paths over catalytic surfaces, and for building a fundamental understanding of the electronic driving forces behind catalytic mechanisms.

The computational expense of DFT and *ab initio* thermodynamics limits investigations to highly idealized models, such as the single crystal surfaces and small clusters, that only approximate the complex geometry of actual systems. These methods are also limited in their ability to consider dynamic structural transitions at a metal-oxide interface. Although it is difficult to characterize long range and dynamic effects using QM, it becomes possible with the use of empirical force-fields that are based on classical principles and therefore have a relatively low computational expense. The ReaxFF potential is designed to model bond dissociation and formation, and can therefore be implemented in reactive molecular dynamics (RMD) and Monte Carlo (MC) simulations that are capable of describing the dynamic nature of a catalyst at longer length and time scales (up to ~10^4 atoms and ~1 ns). Studies utilizing these methods can systematically probe catalytically interesting properties of supported metal-oxide systems that arise from structural irregularities and dynamic effects of surface reconstruction at interfaces.

1.4.1. Density Functional Theory (DFT)

This section will briefly outline the central concepts behind DFT, and will discuss how the theory can be utilized to characterize and design heterogeneous catalysts at the atomic level. Only the central ideas underlying the theory will be reviewed, and for a more complete discussion of DFT and its implementation, we refer the reader to the introductory

DFT textbook by D. Sholl and J. Steckel.[100] Density functional theory is rooted in quantum mechanics, and is capable of calculating the ground state energy of a system of interacting electrons and nuclei.[101] The principle equation of quantum mechanics, the Schrödinger equation, is reproduced below in its time-independent, non-relativistic form:

$$\hat{H}\psi(r_1, \dots r_n) = E\psi(r_1, \dots r_n)\ , \tag{1}$$

where E is the energy of the system and ψ is the wavefunction expressed as a function of electronic coordinates, r_i. The Hamiltonian operator, $\hat{H}$, for a chemical system under the Born–Oppenheimer approximation (in which all atomic nuclei are assumed to be stationary) consists of three terms: the kinetic term, the external potential term resultant from electrostatic interaction between electrons and atomic nuclei with charge Z_α, and the electron-electron electrostatic interaction term.

$$\hat{H} = \sum_i^n \left(-\frac{1}{2}\nabla_i^2 - \sum_\alpha \frac{Z_\alpha}{r_i}\right) + \sum_{i=1}^n \sum_{j=i+1}^n \frac{1}{|r_j - r_i|}\,. \tag{2}$$

The energy of a state specified by the wavefunction, $\psi(r_1, \dots r_n)$, is given by the expectation value of $\hat{H}$, which is calculated from the equation:

$$\langle E \rangle = \int \psi^*(r_1, \dots r_n)\hat{H}\psi(r_1, \dots r_n)\, dr. \tag{3}$$

Hence, the total energy of a system can be determined from the above equation once the ground state wavefunction is known. Solving the Schrödinger equation, however, is a difficult task due to the magnitude of computational power required to obtain an approximate solution to the equation for a many-bodied system. An exact solution to a many-bodied Schrodinger equation is impossible to achieve analytically, and it is therefore necessary to find methods, such as DFT, that achieve approximate solutions.

DFT hinges on the Hohenberg-Kohn theorem,[102] which states that there is a unique one-to-one mapping between the all-electron wavefunction and the electron density distribution, $\rho(r)$. This allows the Hamiltonian to be formally re-cast as a functional of the electron density distribution. The kinetic, potential, and total energy can be determined from $\rho(r)$, which is expressed in the following equation:

$$E[\rho(r)] = T[\rho(r)] + V_{ee}[\rho(r)] + V_{eN}[\rho(r)] + V_{xc}[\rho(r)] + E_{nuclei}, \quad (4)$$

where the total energy functional is split into contributions from kinetic energy (T), electron-electron (V_{ee}) and electron-nuclei (V_{eN}) electrostatic interactions, electron exchange and correlation (V_{xc}), and nuclei-nuclei electrostatic repulsion (E_{nuclei}). Building on the Hohenberg-Kohn theorem, the Kohn-Sham (KS) equations[103] describe single-electron wavefunctions, $\varphi_i(r)$, satisfying the Schrödinger with the Hamiltonian re-cast in terms of the electron density function:

$$(-\frac{1}{2}\nabla_i^2 + v_{Ne} + v_{ee} + v_{xc})\,\varphi_i(r) = \varepsilon_i\varphi_i(r) \quad ; \quad \rho(r) = \sum_i^n |\varphi_i(r)|^2 \quad , \quad (5)$$

where again the potential energy contributions are divided into terms representing electron-nuclei electrostatics, electron-electron electrostatics, and electron exchange-correlation. Electron exchange is a quantum mechanical property that requires the wavefuction of a fermionic system to be anti-symmetric. This is commonly known as the Pauli Exclusion Principle, which forbids that any two electrons have the same set of quantum numbers. Electron correlation arises from the instantaneous coupling of electronic motion, which is not reflected in the space-time averaged nature of $\rho(r)$. Both terms are formally derived from a fully-interacting multi-electron wavefunction approach, and as such their proper mathematical expression in the formalism of density functional theory is unknown. The

approximate forms typically employed are derived from the theory of an ideal electron gas, often containing tunable parameters based on empirical observations.

DFT significantly reduces the computational requirements for approximating a solution to the Schrödinger equation by reworking the problem in terms of finding an average electron density, as opposed to finding coupled solutions for numerous individual electron wavefunctions. Solutions to the Kohn-Sham equations, in principle, provide detailed information regarding the electronic structure and energy of a system as a function of nuclei positions, thus yielding the zero-Kelvin potential energy surface (PES). By locating minima and maxima on the potential energy surface, it is possible to determine optimal structures of reactant, product, and transition states along with the corresponding reaction energies and barriers. The solutions also reveal important aspects of the underlying electronic structure, such as oxidation states in atoms, orbital occupancies in molecules, and electronic band structures in solids. Such knowledge is a powerful tool for determining preferred reaction paths over catalytic surfaces, and for building a fundamental understanding of the electronic driving forces behind catalytic mechanisms. This information is invaluable for optimizing the design of heterogeneous catalysts.

1.4.2. *Ab Initio* Thermodynamics

The formalism of *ab initio* thermodynamics uses statistical mechanics to extend DFT calculations to pressures and temperatures that reflect actual operating conditions. Understanding the relative stability of possible surface structures under these conditions is vital to building a fundamental understanding of catalytic activity. This section only briefly

outlines the central ideas behind *ab initio* thermodynamics, following the presentation methodology outlined in the introductory textbook by D. Sholl and J. Steckel.[104]

The DFT method discussed in the previous section allows one to calculate the ground state energy and optimal structure of a system at *zero* temperature and pressure. It follows that DFT analyses of surface structures and reaction mechanisms are only valid for high temperature and pressure effects are negligible in the appropriate thermodynamic expressions. This approximation is valid for systems in which entropic and pressure contributions are not significant, such as highly ordered bulk structures and single crystal surfaces. It is, however, not sufficient for discerning the energetically favored structure in systems that have considerable differences in entropy, or systems in equilibrium with a reservoir of gaseous species. In these cases, the thermodynamic stability of a surface is subject to the equilibrium of many adsorption, migration, and desorption events. This is modeled thermodynamically by a g*rand canonical ensemble*, in which a system is able to exchange particles with an external reservoir while maintaining a constant chemical potential.

The thermodynamic stability of a system is dependent on the grand canonical free energy, which is given by the formula:

$$\Omega = E - TS - \sum_i N_i \mu_i \ , \qquad (6)$$

where E is the internal energy of the system (given by the zero-Kelvin electronic energy calculated by DFT), T is temperature, S is entropy, N_i is the number of atoms removed from the gas phase reservoir, and μ_i is the chemical potential of the gas phase species. The free energy difference between structures is given by the difference in Ω; the most stable structure will correspond to the structure with the lowest grand canonical free energy. The

gas phase chemical potential for an ideal gas is given by the formula:

$$\mu_i(T,p) = E_i^{DFT} + [\mu_i^o(T,p^o) - \mu_i(T=0)] + kTln(p_i/p_i^o)\,, \quad (7)$$

where the degree sign denotes a reference pressure and the bracketed term represents the difference between the chemical potential at zero Kelvin and at the temperature of interest, which is readily computed from statistical mechanical arguments and can be found in various thermodynamic tables available in the literature (such as the NIST-JANAF thermochemical tables).[105] Using these equations, one can plot the free energy of a structure as a function of temperature and partial pressure, which can in turn be used to construct phase diagrams at catalytically relevant temperatures and pressures.

Consider, for example, the free energy change for the formation of a surface metal-oxide phase, where a metal surface is in contact with a pure oxygen gas phase. The entropy term is negligible for the solid surface compared to the contributions of the electronic internal energy and gas phase entropy. This is a valid approximation for ordered systems with minimal configurational variation. Combining equations 6 and 7 above, and neglecting configurational entropy, yields the free energy change:

$$\Delta\Omega\,(T,P) =$$

$$E_{oxide}^{DFT} - E_{metal}^{DFT} - N_O\,\frac{1}{2}[E_{O2}^{DFT} + [\mu_{O2}^o(T,p^o) - \mu_{O2}(T=0K)] + kTln(p_{O2}/p_{O2}^o)], \quad (8)$$

where the first two terms on the right side of the equation correspond to the DFT energies of the oxide and clean metal surfaces, N_O corresponds to the number of oxygen atoms in the oxide, and the final bracketed term corresponds to the chemical potential of O_2 in the gas phase at *P* and *T*. The half factor accounts for the substitution relating gas phase molecular oxygen to atomic oxygen: $\mu_O = \frac{1}{2}\mu_{O2}$. This equation allows one to determine the

conditions under which the surface oxide phase will be thermodynamically preferred (*i.e.* the conditions that yield a negative free energy change). This formalism is powerful for identifying surface structures responsible for high catalytic activity under conditions that correspond more closely to those found in typical experimental setups.

1.4.3. Atomistic Simulations *via* Reactive Force-Fields: ReaxFF

Quantum mechanical (QM) techniques, such as DFT and *ab initio* thermodynamics, provide a powerful means for exploring the activity, stability, and efficiency of candidate catalyst designs. Unfortunately, the computational cost inherent to QM level calculations severely limits system sizes (to ~100 atoms) and time scales (to ~femtoseconds). This limitation excludes QM-based methods from considering the full dynamics of particle/support interactions, such as surface diffusion and local configuration changes that are key factors in determining the activity of the catalyst. QM structure and energy data can be used to train empirical force-fields (FF) that are able to reproduce near QM accuracy for modeling the dynamics of bond formation and dissociation at lower computational cost. Hence, this method trades accuracy for a significantly lowered computational expense, making it possible to model systems that are orders of magnitude larger than those accessible by QM. Atomistic force-field methods utilize empirically determined inter-atomic potentials in conjunction with classical principles to calculate system energy as a function of atomic positions. Electronic contributions, such as bond energy and partial charge, are captured implicitly, therefore eliminating the need for explicit and expensive QM calculations.

ReaxFF utilizes bond-order/bond-length relationships in conjunction with polarizable charge descriptions to describe both reactive and non-reactive interactions between every atom in a system. This allows ReaxFF to accurately model both covalent and electrostatic interactions for a diverse range of materials, and in particular makes it well suited for studies in heterogeneous catalysis. The potential uses bond-length/bond-order relationships to determine bond energy as a function of inter-atomic distances. The viability of bond-length/bond-order based force-fields was initially demonstrated by J. Tersoff for Si-based systems[106] and by W. Brenner for carbon/hydrogen systems.[107] ReaxFF extended the bond-length/bond-order formalism to better describe long range covalent interactions characteristic in transition state structures, allowing the force-field to faithfully predict reaction barriers. This was initially demonstrated through application to hydrocarbon systems,[108, 109] and has since been expanded to include metals,[110-116] and oxides.[117-122]

The ReaxFF description has no predefined connectivity requirements between atoms, the potential is capable of describing bond formation and dissociation in covalent systems, which is necessary for modeling reactive events in computer simulations. The effect of electrostatic interactions is described in the ReaxFF potential *via* a variable-charge electrostatic description that computes the partial charge of individual atoms from a self-consistent electron equilibration method (EEM).[123] The general form of the ReaxFF potential is shown below:

$$E_{system} = E_{bond} + E_{val} + E_{tors} + E_{over} + E_{under} + E_{vdWaals} + E_{Coulomb} . \quad (9)$$

E_{bond} is a continuous function of inter-atomic distance and describes the energy associated

with forming covalent bonds between atoms. E_{val} and E_{tors} are the energies associated with three-body valence angle strain and four-body torsional angle strain. E_{over} and E_{under} are energy penalties that prevent the over and under coordination of atoms based on atomic valences (e.g. a stiff energy penalty is applied if a carbon atom forms more than four bonds). These terms are a function of bond-order, which is in turn calculated from inter-atomic distance using the equation:

$$BO_{ij} = BO_{ij}^{\sigma} + BO_{ij}^{\pi} + BO_{ij}^{\pi\pi} = exp\left[p_{bo1}\left(\frac{r_{ij}}{r_o^{\sigma}} \right)^{p_{bo2}} \right] + exp\left[p_{bo3}\left(\frac{r_{ij}}{r_o^{\pi}} \right)^{p_{bo4}} \right] + exp\left[p_{bo5}\left(\frac{r_{ij}}{r_o^{\pi\pi}} \right)^{p_{bo6}} \right], \quad (10)$$

where BO is the bond-order between atoms i and j, r_{ij} is inter-atomic distance, r_o terms are equilibrium bond lengths, and p_{bo} terms are empirical parameters. In this work, interaction parameters are derived empirically using a previously developed[124, 125] single-parameter error minimization scheme. Equation 10 is a continuous function of inter-atomic distance, and contains no discontinuities through transitions between σ, π, and $\pi\pi$ bond character. This yields a differentiable potential energy surface, which is required for the direct calculation of inter-atomic forces. $E_{Coulomb}$ and $E_{vdWaals}$ are electrostatic and dispersive contributions calculated between all atoms, regardless of connectivity and bond-order. The specific form of each term in the ReaxFF potential shown in Equation 9 can be found in Ref.[108]

1.5. Summary of Chapters

In this dissertation, a multi-scale DFT/ReaxFF computational methodology is developed to model phase formation affecting activity and stability of Pd/ceria catalysts. Chapters 2-3 report the initial development of ReaxFF interaction parameters for Pd/O/C/H systems. These chapters additionally report the development of Monte Carlo techniques for ReaxFF that are utilized to assess the thermodynamic stability of surface phases as a function of the operating conditions. Oxide, hydride, and carbide phases can readily form under typical catalytic operating conditions, where each phase exhibits unique catalytic characteristics. Understanding the formation of such phases, therefore, is essential for understanding reaction mechanisms at the atomic level. The ReaxFF interaction potential is first parameterized to treat Pd metal and PdO_δ oxide systems in Chapter 2. Additionally in this chapter, a hybrid Grand Canonical Monte Carlo/Molecular Dynamics (GC-MC/MD) simulation method is developed and applied to investigate oxide formation in Pd surfaces and clusters.

This method is extended to the formation of palladium hydride in Chapter 3, where Pd/H interaction parameters are additionally developed. Palladium is an exceptional hydrogen storage material, and as such there is great interest in thermodynamic and kinetic influences driving Pd hydride formation. The GC-MC/MD method is employed in conjunction with MD simulations to assess the Pd cluster size-dependence of hydride formation in surface and bulk phases. Chapter 4 reports the development of Pd/C/H interaction parameters, which are employed to assess the competitive formation of hydride and carbide phases upon exposure to a gas phase populated with hydrocarbon reactants.

This has implications for the use of Pd as a selective hydrogenation catalyst, as the formation of a subsurface carbide yields selective hydrogenation, while the formation of a subsurface hydride yields highly active, yet unselective, hydrogenation sites on the Pd surface. Together, Chapters 2-4 demonstrate the capability of ReaxFF for modeling phase formation in unsupported Pd clusters.

The ReaxFF methods developed in Chapters 2-4 are extended to address phase formation in oxide-supported Pd clusters in Chapter 5. This chapter reports work conducted in collaboration experimental lab of Prof. M. Batzill, investigating the atomistic processes of Pd-sintering and hydride formation on a hydroxylated TiO_2 surface. This study employed scanning tunneling microscopy experiments (STM), DFT calculations, kinetic Monte Carlo simulations, and ReaxFF GC-MC simulations. Experiments determine that the formation of small clusters stable at room temperature is achieved on the hydroxylated surface, while much larger clusters are formed under the same conditions on a hydroxyl-free surface. DFT shows that this is a consequence of stronger binding of Pd-atoms adjacent to hydroxyls and increased surface diffusion barriers for Pd-atoms on the hydroxylated surface. DFT, kinetic Monte Carlo, and ReaxFF-GCMC simulations show that Pd-clusters larger than single Pd monomers can adsorb the hydrogen from the oxide surface and form Pd-hydrides. This chapter demonstrates the extension of the developed ReaxFF-MC methods to supported Pd systems, as well as demonstrates the multi-scale application of QM and classical scale simulation techniques complementing experimental observations.

Chapters 6 and 7 report the multi-scale investigation of hydrocarbon activation over Pd/ceria catalysts, utilizing both DFT and ReaxFF methodologies developed in the previous chapters. Chapter 6 contains a DFT-based *ab initio* thermodynamics investigation

of the role site stability plays in methane activation on $Pd_xCe_{1-x}O_\delta$ surfaces. This chapter demonstrates that rapid C-H activation on $Pd_xCe_{1-x}O_\delta$ catalysts results from the emergent behavior of the doped oxide, enabling dynamic $Pd^{4+} \leftrightarrow Pd^{2+}$ transitions during operation. The stability of the active Pd^{4+} state is dependent on temperature and oxygen pressure, requiring an analysis that combines reaction kinetics and thermodynamic stability to derive an expression for the apparent methane activation barrier. The derived expression accounts for the stability of the Pd^{4+} state, demonstrating that Pd^{4+} are metastable under reaction conditions. Hence, they offer lower methane activation barriers compared to more stable (and therefore less reactive) Pd^{2+} states. The Pd^{4+} state is stabilized by the incorporation of Pd in the fluorite lattice structure of CeO_2, which in turn provides unique methane activation chemistry from the $Pd_xCe_{x-1}O_\delta$ mixture.

These findings are extended to larger system models in Chapter 7, which reports an investigation combining DFT, ReaxFF/GC-MC, and ReaxFF/RMD methods to assess thermodynamic and kinetic driving forces affecting phase formation and activity at the Pd/ceria interface. This chapter utilizes the larger size scale available to ReaxFF to model supported Pd clusters. The results demonstrate that Pd-incorporated sites are exposed when a Pd cluster is partially embedded in the ceria surface. The GC-MC method demonstrates that embedded Pd clusters undergo oxidation at the Pd/ceria interface more readily than analogous supported Pd clusters, and RMD simulations demonstrate that such sites are active toward methane dissociative adsorption. DFT calculations on smaller embedded-cluster models corroborate the ReaxFF findings, demonstrating that Pd^{4+} states are stable in PdO_x clusters under ambient conditions. Together, these results demonstrate the emergent behavior of the Pd/ceria system leading to enhanced catalytic performance, in

which the ceria lattice stabilizes active Pd^{4+} sites at the metal-oxide interface.

Final conclusions and recommendations for future studies are provided in Chapter 8. Additionally, two appendices are included in this dissertation that contain work and research investigations that are not directly related to Pd/ceria catalysis, but are included for completeness. Appendix A contains a book chapter overviewing the application of computational methods to supported metal-oxide catalysis. This chapter was written by T.P.S., and appears in the book *Computational Catalysis*.[95] Finally, Appendix B contains a study conducted in collaboration with the Rioux Lab, which utilizes the ReaxFF GC-MC/MD method to identify Pd/Ar interaction sites on the surface of Pd clusters.

1.6. References

1. E. Aneggi, C. de Leitenburg, G. Dolcetti and A. Trovarelli, Catalysis Today Catalytic Control of Diesel Exhaust Emissions **114** (1), 40-47 (2006).
2. R. Burch, P. K. Loader and F. J. Urbano, Catal. Today **27** (1–2), 243-248 (1996).
3. L.-h. Xiao, K.-p. Sun, X.-l. Xu and X.-n. Li, Catal. Commun. **6** (12), 796-801 (2005).
4. S. Colussi, A. Gayen, J. Llorca, C. de Leitenburg, G. Dolcetti and A. Trovarelli, Ind. Eng. Chem. Res. **51** (22), 7510-7517 (2012).
5. S. Specchia, E. Finocchio, G. Busca, P. Palmisano and V. Specchia, J. Catal. **263** (1), 134-145 (2009).
6. L. Shi, W. Chu, F. Qu and S. Luo, Catal. Lett. **113** (1), 59-64 (2007).
7. T. Kuznetsova, V. Sadykov, L. Batuev, E. Moroz, E. Burgina, V. Rogov, V. Kriventsov and D. Kochubey, Journal of Natural Gas Chemistry **15**, 149-163 (2006).
8. C. Bozo, N. Guilhaume, E. Garbowski and M. Primet, Catal. Today **59** (1-2), 33-45 (2000).
9. C. Bozo, N. Guilhaume and J.-M. Herrmann, J. Catal. **203** (2), 393-406 (2001).
10. M. A. Malecka, L. Kepinski and W. Mista, Applied Catalysis B: Environmental **74** (3-4), 290-298 (2007).
11. G. Picasso, M. Gutierrez, M. P. Pina and J. Herguido, Chem. Eng. J. **126** (2-3), 119-130 (2007).

12. M. Cargnello, J. J. D. Jaén, J. C. H. Garrido, K. Bakhmutsky, T. Montini, J. J. C. Gámez, R. J. Gorte and P. Fornasiero, Science **337** (6095), 713-717 (2012).
13. S. Colussi, A. Gayen, M. F. Camellone, M. Boaro, J. Llorca, S. Fabris and A. Trovarelli, Angew. Chem. Int. Ed. **48** (45), 8481-8484 (2009).
14. G. Jacobs, R. A. Keogh and B. H. Davis, J. Catal. **245** (2), 326-337 (2007).
15. X. Wang and R. J. Gorte, Appl. Catal. A: Gen. **224** (1-2), 209-218 (2002).
16. Q. Zhuang, Y. Qin and L. Chang, Applied Catalysis **70** (1), 1-8 (1991).
17. E. Nikolla, J. Schwank and S. Linic, J. Catal. **250**, 85-93 (2007).
18. H.-L. Chen, S.-H. Liu and J.-J. Ho, J. Phys. Chem. B **110**, 14816-14823 (2006).
19. Y. Matsumura, W.-J. Shen, Y. Ichihashi and H. Ando, Catal. Lett. **68** (3), 181-183 (2000).
20. W.-J. S. Y. Matsumura, PCCP **2** (7), 1519-1522 (2000).
21. A. Yee, S. J. Morrison and H. Idriss, J. Catal. **186** (2), 279-295 (1999).
22. J. Lahiri, A. Mayernick, S. L. Morrow, B. E. Koel, A. C. T. van Duin, M. J. Janik and M. Batzill, J. Phys. Chem. C **114** (13), 5990-5996 (2010).
23. H. Idriss, Platinum Met. Rev. **48**, 105-115 (2004).
24. D. Mei, N. A. Deskins, M. Dupuis and Q. Ge, Journal of Physical Chemistry C **112** (11), 4257-4266 (2008).
25. D. Mei, N. Aaron Deskins and M. Dupuis, Surf. Sci. **601** (21), 4993-5001 (2007).
26. R. Burch, A. Goguet and F. C. Meunier, Applied Catalysis a-General **409**, 3-12 (2011).
27. Y. Chen, H. Wang, R. Burch, C. Hardacre and P. Hu, Faraday Discuss. **152** (0), 121-133 (2011).
28. A. Goguet, F. C. Meunier, D. Tibiletti, J. P. Breen and R. Burch, The Journal of Physical Chemistry B **108** (52), 20240-20246 (2004).
29. C. M. Y. Yeung, F. Meunier, R. Burch, D. Thompsett and S. C. Tsang, The Journal of Physical Chemistry B **110** (17), 8540-8543 (2006).
30. G. Jacobs and B. H. Davis, Appl. Catal. A: Gen. **284** (1–2), 31-38 (2005).
31. D. Pierre, W. Deng and M. Flytzani-Stephanopoulos, Top. Catal. **46** (3), 363-373 (2007).
32. X. G. Wang, R.J.; Wagner, J.P., J. Catal. **212**, 225-230 (2002).
33. X. Wang, J. A. Rodriguez, J. C. Hanson, D. Gamarra, A. Martinez-Arias and M. Fernandez-Garcia, J. Phys. Chem. B **110**, 428-434 (2006).
34. C.-H. Lin, C.-L. Chen and J.-H. Wang, J. Phys. Chem. C **115** (38), 18582-18588 (2011).
35. R. Burch, PCCP **8** (47), 5483-5500 (2006).
36. T. Bunlesin, E. S. Putna and R. J. Gorte, Catal. Lett. **41** (1), 1-5 (1996).
37. M. Boaro, C. de Leitenburg, G. Dolcetti and A. Trovarelli, J. Catal. **193** (2), 338-347 (2000).
38. D. Teschner, A. Wootsch, O. Pozdnyakova-Tellinger, J. Krohnert, E. M. Vass, M. Havecker, S. Zafeiratos, P. Schnorch, P. C. Jentoft, A. Knop-Gericke and R. Schlogl, J. Catal. **249** (2), 318-327 (2007).
39. V. Shapovalov and H. Metiu, J. Catal. **245** (1), 205-214 (2007).
40. S. H. Oh and G. B. Hoflund, J. Phys. Chem. A **110**, 7609-7613 (2006).
41. H. Wang and W. F. Schneider, Catal. Today **165** (1), 49-55 (2011).

42. R. B. Getman and W. F. Schneider, ChemCatChem **2** (11), 1450-1460 (2010).
43. W.-J. Zhu, J. Zhang, X.-Q. Gong and G. Lu, Catal. Today **165** (1), 19-24 (2011).
44. H. W. Jen, G. W. Graham, W. Chun, R. W. McCabe, J. P. Cuif, S. E. Deutsch and O. Touret, Catal. Today **50** (2), 309-328 (1999).
45. G. W. Graham, H. W. Jen, R. W. McCabe, A. M. Straccia and L. P. Haack, Catal. Lett. **67**, 99-105 (2000).
46. E. Aneggi, M. Boaro, C. d. Leitenburg, G. Dolcetti and A. Trovarelli, J. Alloys Compd. **408-412**, 1096-1102 (2006).
47. A. Trovarelli, C. d. Leitenburg, M. Boaro and G. Dolvetti, Catal. Today **50**, 353-367 (1999).
48. M. K. Debe, Nature **486** (7401), 43-51 (2012).
49. S. McIntosh, J. M. Vohs and R. J. Gorte, Electrochem. Solid-State Lett. **6** (11), A240-A243 (2003).
50. S. McIntosh and R. J. Gorte, Chem. Rev. **104** (10), 4845-4865 (2004).
51. R. J. Gorte, J. M. Vohs and S. McIntosh, Solid State Ionics **175**, 1-6 (2004).
52. S. An, C. Lu, W. L. Worrell, R. J. Gorte and J. M. Vohs, Solid State Ionics **175**, 135-138 (2004).
53. M. Gong, X. Liu, J. Trembly and C. Johnson, J. Power Sources **168** (2), 289-298 (2007).
54. J.-H. Wang, M. Liu and M. C. Lin, Solid State Ionics **177**, 939-947 (2006).
55. A. Borodziński and G. C. Bond, Catalysis Reviews **50** (3), 379-469 (2008).
56. A. Borodziński and G. C. Bond, Catalysis Reviews **48** (2), 91-144 (2006).
57. M. Boronat, F. Illas and A. Corma, J. Phys. Chem. A **113** (16), 3750-3757 (2009).
58. P. Concepción, S. Carrettin and A. Corma, Appl. Catal. A: Gen. **307** (1), 42-45 (2006).
59. N. Khan, S. Shaikhutdinov and H. Freund, Catal. Lett. **108** (3), 159-164 (2006).
60. W. Ludwig, A. Savara, K.-H. Dostert and S. Schauermann, J. Catal. **284** (2), 148-156 (2011).
61. M. W. Tew, M. Janousch, T. Huthwelker and J. A. van Bokhoven, J. Catal. **283** (1), 45-54 (2011).
62. P. A. Deshpande, M. S. Hegde and G. Madras, AlChE J. **56** (5), 1315-1324 (2010).
63. Z.-P. Liu and P. Hu, J. Am. Chem. Soc. **125** (7), 1958-1967 (2003).
64. G. Jacobs, S. Ricote, U. M. Graham, P. M. Patterson and B. H. Davis, Catal. Today **106** (1-4), 259-264 (2005).
65. J. H. Holles, R. J. Davis, T. M. Murray and J. M. Howe, J. Catal. **195** (1), 193-206 (2000).
66. J. A. Farmer and C. T. Campbell, Science **329** (5994), 933-936 (2010).
67. G. B. Hoflund, H. A. E. Hagelin, J. F. Weaver and G. N. Salaita, Appl. Surf. Sci. **205** (1-4), 102-112 (2003).
68. W.-J. Shen and Y. Matsumura, J. Mol. Catal. A: Chem. **153** (1-2), 165-168 (2000).
69. H. Gabasch, K. Hayek, B. Klötzer, W. Unterberger, E. Kleimenov, D. Teschner, S. Zafeiratos, M. Hävecker, A. Knop-Gericke, R. Schlögl, B. Aszalos-Kiss and D. Zemlyanov, J. Phys. Chem. C **111** (22), 7957-7962 (2007).

70. S. Laursen and S. Linic, Journal of Physical Chemistry C **113** (16), 6689-6693 (2009).
71. A. D. Mayernick and M. J. Janik, J. Phys. Chem. C **112** (38), 14955-14964 (2008).
72. H. Borchert, Y. Borchert, V. V. Kaichev, I. P. Prosvirin, G. M. Alikina, A. I. Lukashevich, V. I. Zaikovskii, E. M. Moroz, E. A. Paukshtis, V. I. Bukhtiyarov and V. A. Sadykov, J. Phys. Chem. B **109**, 20077-20086 (2005).
73. Z.-P. Liu, S. J. Jenkins and D. A. King, Phys. Rev. Lett. **94** (19), 196102 (2005).
74. Z. Yang, G. Luo, Z. Lu, T. K. Woo and K. Hermansson, J. Phys.: Condens. Matter **20** (3), 035210 (2008).
75. L. Szabova, M. F. Camellone, M. Huang, V. Matolin and S. Fabris, J. Chem. Phys. **133** (23), 234705-234711 (2010).
76. M. Nolan, S. Grigoleit, D. C. Sayle, S. C. Parker and G. W. Watson, Surf. Sci. **576**, 217-229 (2005).
77. M. Nolan, S. C. Parker and G. W. Watson, Surf. Sci. **595**, 223-232 (2005).
78. S. Bernal, J. J. Calvino, M. A. Cauqui, J. M. Gatica, C. Larese, J. A. Perez Omil and J. M. Pintado, Catal. Today **50** (2), 175-206 (1999).
79. B. Wang, D. Weng, X. Wu and J. Fan, Catal. Today **153** (3-4), 111-117 (2010).
80. A. D. Mayernick and M. J. Janik, J. Chem. Phys. **131** (8), 084701-084712 (2009).
81. K. Reuter, D. Frenkel and M. Scheffler, Phys. Rev. Lett. **93** (11), 116105 (2004).
82. J. F. Weaver, J. A. Hinojosa Jr, C. Hakanoglu, A. Antony, J. M. Hawkins and A. Asthagiri, Catal. Today **160** (1), 213-227 (2011).
83. H. Zhang, J. Gromek, G. Fernando, H. Marcus and S. Boorse, Journal of Phase Equilibria **23** (3), 246-248 (2002).
84. J. Rogal, K. Reuter and M. Scheffler, Phys. Rev. B **69** (7), 075421 (2004).
85. J. Klikovits, E. Napetschnig, M. Schmid, N. Seriani, O. Dubay, G. Kresse and P. Varga, Phys. Rev. B **76** (4), 045405 (2007).
86. J. A. Rodriguez, X. Wang, J. C. Hanson, G. Liu, A. Iglesias-Juez and M. Fernandez-Garcia, J. Chem. Phys. **119**, 5659-5669 (2003).
87. X. Wang, J. A. Rodriguez, J. C. Hanson, D. Gamarra, A. Martinez-Arias and M. Fernandez-Garcia, J. Phys. Chem. B **109**, 19595-19603 (2005).
88. G. Zhou, P. R. Shah, T. Kim, P. Fornasiero and R. J. Gorte, Catal. Today **123** (1-4), 86-93 (2007).
89. L. M. Misch, J. A. Kurzman, A. R. Derk, Y.-I. Kim, R. Seshadri, H. Metiu, E. W. McFarland and G. D. Stucky, Chem. Mater. **23** (24), 5432-5439 (2011).
90. A. D. Mayernick and M. J. Janik, J. Catal. **278** (1), 16-25 (2011).
91. M. L. Drummond, B. G. Sumpter, W. A. Shelton and J. Z. Larese, J. Phys. Chem. C **111** (2), 966-976 (2007).
92. R. B. Getman, Y. Xu and W. F. Schneider, J. Phys. Chem. C **112** (26), 9559-9572 (2008).
93. H. Wang and W. F. Schneider, J. Chem. Phys. **127** (6), 064706 (2007).
94. D. R. Mullins and S. H. Overbury, Surf. Sci. **511** (1-3), L293-L297 (2002).
95. T. P. Senftle, A. C. T. van Duin and M. J. Janik, in *Computational Catalysis* (The Royal Society of Chemistry, 2014), pp. 157-191.

96. M. Cargnello, V. V. T. Doan-Nguyen, T. R. Gordon, R. E. Diaz, E. A. Stach, R. J. Gorte, P. Fornasiero and C. B. Murray, Science **341** (6147), 771-773 (2013).
97. K. R. Priolkar, B. Parthasarathi, P. R. Sarode, M. S. Hegde, S. Emura, R. Kumashiro and N. P. Lalla, Chem. Mater. **14**, 2120-2128 (2002).
98. M. D. Krcha, A. D. Mayernick and M. J. Janik, J. Catal. **293** (0), 103-115 (2012).
99. R. V. Gulyaev, T. Y. Kardash, S. E. Malykhin, O. A. Stonkus, A. S. Ivanova and A. I. Boronin, Phys. Chem. Chem. Phys. **16** (26), 13523-13539 (2014).
100. D. S. Sholl and J. A. Steckel, *Density Functional Theory: A Practical Introduction*. (Wiley, 2009).
101. W. Kohn, A. D. Becke and R. G. Parr, The Journal of Physical Chemistry **100** (31), 12974-12980 (1996).
102. P. Hohenberg and W. Kohn, Physical Review **136** (3B), B864-B871 (1964).
103. W. Kohn and L. J. Sham, Physical Review **140** (4A), A1133-A1138 (1965).
104. A. E. Baber, A. J. Gellman, D. S. Sholl and E. C. H. Sykes, J. Phys. Chem. C **112** (30), 11086-11089 (2008).
105. J. W. Hudgens, J. M. Pettibone, T. P. Senftle and R. N. Bratton, Inorg. Chem. **50** (20), 10178-10189 (2011).
106. J. Tersoff, Phys. Rev. Lett. **61** (25), 2879-2882 (1988).
107. D. W. Brenner, Phys. Rev. B **42** (15), 9458-9471 (1990).
108. A. C. T. van Duin, S. Dasgupta, F. Lorant and W. A. Goddard III, J. Phys. Chem. A **105** (41), 9396-9409 (2001).
109. K. Chenoweth, A. C. T. van Duin and W. A. Goddard, J. Phys. Chem. A **112** (5), 1040-1053 (2008).
110. K. D. Nielson, A. C. T. van Duin, J. Oxgaard, W.-Q. Deng and W. A. Goddard, J. Phys. Chem. A **109** (3), 493-499 (2004).
111. J. Ludwig, D. G. Vlachos, A. C. T. van Duin and W. A. Goddard, The Journal of Physical Chemistry B **110** (9), 4274-4282 (2006).
112. C. F. Sanz-Navarro, P.-O. Astrand, D. Chen, M. Ronning, A. C. T. van Duin, T. Jacob and W. A. Goddard, J. Phys. Chem. A **112** (7), 1392-1402 (2008).
113. C. F. Sanz-Navarro, P.-O. Åstrand, D. Chen, M. Rønning, A. C. T. van Duin and W. A. Goddard, J. Phys. Chem. C **114** (8), 3522-3530 (2010).
114. M. R. LaBrosse, J. K. Johnson and A. C. T. van Duin, J. Phys. Chem. A **114** (18), 5855-5861 (2010).
115. A. C. T. van Duin, V. S. Bryantsev, M. S. Diallo, W. A. Goddard, O. Rahaman, D. J. Doren, D. Raymand and K. Hermansson, J. Phys. Chem. A **114** (35), 9507-9514 (2010).
116. T. T. Järvi, A. C. T. van Duin, K. Nordlund and W. A. Goddard, J. Phys. Chem. A **115** (37), 10315-10322 (2011).
117. A. C. T. van Duin, A. Strachan, S. Stewman, Q. Zhang, X. Xu and W. A. Goddard, J. Phys. Chem. A **107** (19), 3803-3811 (2003).
118. J. Quenneville, R. S. Taylor and A. C. T. van Duin, J. Phys. Chem. C **114** (44), 18894-18902 (2010).
119. A. C. T. van Duin, B. V. Merinov, S. S. Jang and W. A. Goddard, J. Phys. Chem. A **112** (14), 3133-3140 (2008).

120. A. C. T. van Duin, B. V. Merinov, S. S. Han, C. O. Dorso and W. A. Goddard, J. Phys. Chem. A **112** (45), 11414-11422 (2008).
121. M. Aryanpour, A. C. T. van Duin and J. D. Kubicki, J. Phys. Chem. A **114** (21), 6298-6307 (2010).
122. S. Monti, A. C. T. van Duin, S.-Y. Kim and V. Barone, J. Phys. Chem. C **116** (8), 5141-5150 (2012).
123. W. J. Mortier, S. K. Ghosh and S. Shankar, J. Am. Chem. Soc. **108** (15), 4315-4320 (1986).
124. A. C. T. van Duin, J. M. A. Baas and B. van de Graaf, J. Chem. Soc., Faraday Trans. **90** (19), 2881-2895 (1994).
125. D. Raymand, A. C. T. van Duin, M. Baudin and K. Hermansson, Surf. Sci. **602** (5), 1020-1031 (2008).

Chapter 2
Development of a ReaxFF Potential for Pd/O and Application to Palladium Oxide Formation

This chapter is published as: T. P. Senftle, R. J. Meyer, M. J. Janik and A. C. T. van Duin, *Journal of Chemical Physics* **139** (4), 044109-044115 (2013).

Abstract

Oxide formation on palladium surfaces impacts the activity and selectivity of Pd-based catalysts, which are widely employed under oxygen rich operating conditions. To investigate oxidation processes over Pd catalysts at time and length scales inaccessible to quantum based computational methods, we have developed a Pd/O interaction potential for the ReaxFF reactive force field. The parameters of the ReaxFF potential were fit against an extensive set of quantum data for both bulk and surface properties. Using the resulting potential, we conducted molecular dynamics simulations of oxide formation on Pd(111), Pd(110), and Pd(100) surfaces. The results demonstrate good agreement with previous experimental observations; oxygen diffusion from the surface to the subsurface occurs faster on the Pd(110) surface than on the Pd(111) and Pd(100) surfaces under comparable conditions at high temperatures and pressures. Additionally, we developed a ReaxFF-based hybrid grand canonical Monte Carlo/molecular dynamics (GC-MC/MD) approach to assess the thermodynamic stability of oxide formations. This method is used to derive a theoretical phase diagram for the oxidation of Pd_{935} clusters in temperatures ranging from 300 K to 1300 K and oxygen pressures ranging from 10^{-14} atm to 1 atm. We observe good agreement between experiment and ReaxFF, which validates the Pd/O interaction potential

and demonstrates the feasibility of the hybrid GC-MC/MD method for deriving theoretical phase diagrams. This GC-MC/MD method is novel to ReaxFF, and is well suited to studies of supported-metal-oxide catalysts, where the extent of oxidation in metal clusters can significantly influence catalytic activity, selectivity, and stability.

2.1. Introduction

Catalytic applications featuring late transition metals often employ oxygen rich operating conditions that are capable of oxidizing the metal catalyst. This leads to the formation of surface and bulk oxide phases with catalytic properties that differ greatly from the parent metal.[1-7] This is particularly important in palladium-based systems, which are well known oxidation catalysts used industrially for automotive exhaust treatment,[8-10] CO conversion to CO_2,[11-17] and hydrocarbon oxidation.[17-21] To optimize catalyst performance, it is necessary to understand the stability of oxide surface phases as a function of temperature, pressure, and gas phase composition, as well as the dynamic transition between oxide phases that may occur during catalytic operation.

Numerous experimental and theoretical studies have characterized oxide formation on Pd single-crystal surfaces.[1,7,22-33] Intuitively, oxide formation typically occurs after the initial adsorption and dissociation of oxygen molecules on the surface, followed by the growth of 2-dimensional surface oxides, and the subsequent formation of a bulk oxide. The extent of oxidation on the surface and in the bulk is governed by both kinetic and thermodynamic influences. Lundgren *et al.*[22] combined *in situ* surface x-ray diffraction with *ab initio* thermodynamics to demonstrate that, on the Pd(100) surface, both a *p(2×2)*

adsorbate phase and a 2D $(\sqrt{5}\times\sqrt{5})R27^{o}$ surface oxide phase can be kinetically stable, and that their presence on the surface hinders the formation of the thermodynamically favored bulk oxide. Similarly, Salmeron and co-workers compared theoretical and experimental phase diagrams of Pd(111) derived from *ab inito* thermodynamics and photoemission spectroscopy to demonstrate the kinetic stability of a subsurface oxide phase that prevents further oxidation of the bulk.[28] Recently, Westerström *et al.*[31] utilized *in situ* x-ray diffraction and density functional theory (DFT) to demonstrate that bulk oxidation on Pd(110) does *not* proceed through a kinetically stable surface phase, resulting in rapid bulk oxidation compared to other low-index Pd surfaces. Using a combination of scanning tunneling microscopy (STM), low energy electron diffraction (LEED), and temperature programmed decomposition (TPD), Han *et al.*[34,35] observed a similar trend in affinity toward oxide formation over Pd single crystal surfaces: Pd(110) > Pd(100) > Pd(111). Since catalytic behavior is strongly impacted by the extent of oxidation on the surface and in the bulk, these findings underscore the necessity to thoroughly investigate both kinetic and thermodynamic influences when characterizing oxide formation. This has motivated the work presented here, in which we have developed an empirical reactive force-field (ReaxFF) for Pd/O that, through molecular dynamics (MD) and Monte Carlo (MC) simulations, can help examine oxidization processes on the atomic scale.

Atomistic modeling is a useful method for analyzing the kinetic and thermodynamic properties of oxidation processes during catalytic operation.[1,36-38] The studies mentioned above illustrate how quantum results can be extended to describe ambient conditions through the formalism of *ab initio* thermodynamics.[23,32,39] Unfortunately, the computational expense inherent to quantum mechanical simulations

limits such studies to small (~100 atoms) and highly idealized (periodic) system models. It also precludes direct dynamic studies, as *ab initio* MD is limited to ~fs-ps timescales. Alternatively, empirical force-field methods offer a computationally inexpensive means for modeling processes that occur over larger length and time scales. Although still unable to reach macroscopic time and length scales, these methods can help bridge the size gap between experimental and theoretical studies.

Empirical force-field methods feature inter-atomic potentials that contain parameters optimized against experimental or quantum data. The ReaxFF force-field used here incorporates bond order descriptions in the inter-atomic potential to capture the reaction energetics of covalent interactions. This eliminates pre-defined atomic connectivity required in non-reactive force fields, enabling the potential to describe bond dissociation and formation during reactive events. The viability of bond-length/bond-order based force-fields was initially demonstrated by Tersoff for Si-based systems[40] and by Brenner for hydrocarbon systems.[41] ReaxFF incorporates an extended bond-length/bond-order formalism to better describe long range covalent interactions characteristic in transition state structures, allowing the force-field to describe reaction barriers. This was initially demonstrated through application to hydrocarbon systems,[42,43] and has since been expanded to include metals[44-52] and oxides.[53-58] The transferability of ReaxFF makes it a logical choice for studying oxidation processes; it can describe O_2 adsorption from the gas phase, dissociation on the metal surface, and diffusion into the bulk metal. Herein we derive and validate ReaxFF parameters for describing the interaction between palladium and oxygen in gas, surface, and bulk phases. We apply the resulting potential in molecular dynamics (MD) and Monte Carlo simulations of the oxidation process, which involves

oxygen migration between gas, surface, and bulk phases.

Though MD methods are useful for modeling the dynamics of oxide formation, they are often unable to reach thermodynamic equilibrium within computationally tractable time scales (~1 ns for ReaxFF). Simulations at high temperatures and pressures can overcome kinetic barriers in shorter timescales, but will allow high energy processes that are not thermodynamically feasible under ambient conditions. Monte Carlo methods can circumvent this limitation by sampling the configurational energetics of the system and reproducing a Boltzmann thermal distribution of states that fluctuate around thermodynamic equilibrium. In particular, Grand Canonical Monte Carlo (GC-MC) methods are aptly suited to model the thermodynamics of sorption processes.[59-63] In such simulations, atoms are stochastically exchanged between the system and a gas phase reservoir at constant chemical potential. The system equilibrates when the chemical potential of the system is equal to that of the gas phase reservoir, thus determining the equilibrium concentration of sorbate atoms and the corresponding phase structure. This method is used in this work to derive a theoretical oxidation phase diagram in *T,P* space for large $Pd_{n>300}$ clusters, which is beyond the computational expense of *ab initio* methods.

GC-MC studies have been conducted previously to model sorption in multi-component systems. Ray and co-workers demonstrated the multi-component GC-MC method, in which atoms are exchanged between a gas phase reservoir and a metal lattice, in their work modeling Pd bulk[61] and Pd clusters.[60,62] A similar study was conducted by Debiaggi and co-workers,[64] demonstrating the formation of a PdH subsurface phase prior to the formation of a bulk hydride in Pd nanoclusters. Additionally, Valentini *et al.* employed GC-MC via ReaxFF to investigate oxygen adsorption on the Pt(111) surface.[65]

The direct GC-MC methods employed in these studies, however, cannot be applied to model bulk oxidation because the transition from pure metal to bulk metal-oxide requires a significant rearrangement of the metal lattice. Hybrid Monte Carlo techniques offer a solution to this issue by combining MC configuration steps with a MD relaxation of forces.[66-70] Hybrid-MC/MD was first implemented in ReaxFF by Chenoweth *et al*.,[70] who employed atom swaps in an NVT ensemble to investigate the structure of molybdenum-doped vanadium oxide surfaces. Building on this method, we have developed a hybrid GC-MC/MD method for ReaxFF that uses GC-MC to add, remove, and move oxygen atoms until thermodynamic equilibrium with an oxygen reservoir is reached, and uses MD to relax the system as oxygen atoms are incorporated in the metal lattice in both surface and bulk sites. This scheme is capable of modeling structural rearrangements inherent to the formation of the oxide. Although the GC-MC/MD methodology p is tailored to oxidation processes, the formalism is generally applicable to other multi-component systems.

2.2. Theory and Methods

2.2.1. ReaxFF Background

ReaxFF utilizes bond-order/bond-length relationships in conjunction with polarizable charge descriptions to describe covalent, Coulomb, and van der Waals interactions between atoms. The general form of the ReaxFF potential is shown below:

$$E_{system} = E_{bond} + E_{val} + E_{tors} + E_{over} + E_{under} + E_{vdWaals} + E_{Coulomb}, \qquad (1)$$

where E_{system} is the total potential energy of the system. E_{bond} describes the energy

associated with forming covalent bonds between atoms; E_{val} and E_{tors} are the energies associated with three-body valence angle strain and four-body torsional angle strain. These terms are a function of bond-order, which is in turn calculated from inter-atomic distance using the equation:

$$BO_{ij} = BO_{ij}^{\sigma} + BO_{ij}^{\pi} + BO_{ij}^{\pi\pi} = exp\left[p_{bo1}\left(\frac{r_{ij}}{r_o^{\sigma}}\right)^{p_{bo2}} \right] + exp\left[p_{bo3}\left(\frac{r_{ij}}{r_o^{\pi}}\right)^{p_{bo4}} \right] + exp\left[p_{bo5}\left(\frac{r_{ij}}{r_o^{\pi\pi}}\right)^{p_{bo6}} \right], \quad (2)$$

where BO is the bond-order between atoms i and j, r_{ij} is inter-atomic distance, r_o terms are equilibrium bond lengths, and p_{bo} terms are empirical parameters. Equation 2 is a continuous function of inter-atomic distance, and contains no discontinuities through transitions between σ, π, and $\pi\pi$ bond character. This yields a differentiable potential energy surface, which is required for the direct calculation of inter-atomic forces. E_{over} and E_{under} are energy penalties that prevent the over and under coordination of atoms based on atomic valences. $E_{Coulomb}$ and $E_{vdWaals}$ are electrostatic and dispersive interactions, respectively, calculated between all atom pairs regardless of connectivity. These two terms are bond-order independent and are calculated directly from inter-atomic distances. Electrostatic interactions are described via a variable-charge electrostatic description that computes the partial charge of individual atoms from a self-consistent electron equilibration method (EEM).[71] The exact functional forms of each term in the ReaxFF potential are described in detail in a previous publication.[42] In this study, system-specific parameters contained in the ReaxFF potential were optimized against a DFT training set populated with bulk, surface, and gas phase data for palladium and oxygen. The optimization technique consisted of a previously developed[72,73] single-parameter error minimization scheme.

2.2.2. ReaxFF Grand Canonical Monte Carlo

Using the Pd/O potential, we implemented a hybrid Grand Canonical-Monte Carlo/Molecular Dynamics (GC-MC/MD) method in the $TV\mu_{O2}N_{Pd}$ ensemble with constant temperature (T), volume (V), oxygen chemical potential (μ_{O2}), and number of Pd atoms (N_{Pd}). Possible MC moves include: (1) inserting an oxygen atom into the system at a random position, (2) removing a randomly selected oxygen atom from the system, or (3) moving an oxygen atom to a new random position in the system. Coordinates for O-insertion and O-move steps were chosen randomly such that any unoccupied position in the simulation box could be selected. At equilibrium, the Monte Carlo procedure must maintain a detail-balance, in which the probability of any transition is equal to the probability of the reverse transition.[63,74,75] This is demonstrated in the probability balance:

$$P_1^{Boltz} P_{1\to2}^{select} P_{1\to2}^{accept} = P_2^{Boltz} P_{2\to1}^{select} P_{2\to1}^{accept}, \tag{3}$$

where P^{Boltz} is the Boltzmann probability that a microstate is occupied, P^{select} is the probability that a transition type is selected, and P^{accept} is the probability that the transition is accepted. In the above equation, we ensure that P^{select} is equal on both sides by generating move types with an equal frequency. The probability of accepting a MC step is derived from the remaining Boltzmann terms, yielding the following acceptance criteria for particle insertion, deletion, or displacement during a Monte Carlo transition:

$$P_{insert}^{accept} = min\left[1, \frac{V}{\Lambda^3 (N+1)} \exp[-\beta (E_2 - E_1 - \mu_{res})\right], \tag{4}$$

$$P_{remove}^{accept} = min\left[1, \frac{N\Lambda^3}{V} \exp[-\beta (E_2 - E_1 + \mu_{res})\right], \tag{5}$$

$$P_{move}^{accept} = min\left[1, \exp[-\beta\left(E_2 - E_1\right)\right], \quad (6)$$

where N is the number of exchangeable particles in the system before the MC move, V is the volume of the system, Λ is the thermal de Broglie wavelength of the exchanged particle, β is the Boltzmann factor given by $\beta = 1/k_bT$, E_1 and E_2 are the potential energies calculated as a function of particle configurations in the system before and after the MC move, and μ_{ref} is the chemical potential of the particle reservoir. In this study, μ_{ref} for oxygen is related to T and P by the following equation:

$$\mu_O\left(T,P\right) = \frac{1}{2}\mu_{O2}\left(T,P\right) = \frac{1}{2}\left[\mu_{ref}\left(T,P^o\right) + k_bT\,Ln\left(\frac{P}{P^o}\right) - E_d\right], \quad (7)$$

where $\mu_{O2}(T,P^o)$ is the experimentally determined chemical potential of O_2 at T and P^o available from published thermodynamic tables,[76] and E_d is the zero-Kelvin bond dissociation energy of O_2. Since the ReaxFF parameters are derived from DFT values for oxygen adsorption calculated relative to gas phase O_2, the DFT calculated value of 142.1 kcal mol^{-1} was used for E_d to remain consistent with the ReaxFF training, despite the well documented DFT overestimation of the O_2 bond strength. Using the DFT value for E_d introduces uncertainty in the location of the oxidation phase boundaries determined from MC. We estimate that DFT errors in O_2 binding could shift the resultant oxidation boundaries to lower temperatures by as much as ~200 K and to higher pressures by as much as an order of magnitude. This uncertainty should be taken into account for quantitative comparisons with experiment, but does not affect qualitative conclusions drawn from the results.

In our hybrid method, we introduce an energy minimization step after each MC

trial move. This step is necessary to allow the rearrangement of metal atoms when forming an oxide. Pure GC-MC simulations of solid-oxide formation without an energy minimization step will suffer from low acceptance rates because the majority of the system is occupied by metal atoms and is inaccessible to inserted oxygen atoms. An energy minimization step will alleviate this issue by relaxing the energy of the system prior to applying Equations 4-6, but will introduce a bias in the MC algorithm that must be accounted for in the acceptance probabilities to maintain detail-balance. This was demonstrated by Lachet *et al.*,[63] who employed a biased GC-MC method to simulate the adsorption of xylene molecules in zeolites. They demonstrate that the bias introduced by the energy minimization step can be countered by replacing the system volume, V, in Equations 4 and 5 with an *accessible* volume, V_{acc}, which reflects the volume accessible to the MC-inserted atom. Herein, the accessible volume is calculated by subtracting the volume occupied by Pd metal atoms from the total volume:

$$V_{acc} = V - N_{metal} \frac{4}{3} \pi r_{metal}^3 , \tag{8}$$

where N_{metal} is the number of metal atoms and r_{metal} is the atomic radius of the metal atom (for Pd, r_{metal} = 1.39 *Å*). In this study, the energy minimization step consists of a conjugant gradient (CG) geometry optimization, with a convergence criterion of 0.5 kcal mol^{-1} between subsequent CG steps. The convergence criterion affects the accessible volume, since the CG algorithm determines how close an inserted O atom can be placed to any Pd atom. In the limit of an extremely loose criterion, an inserted O atom can be placed within the atomic radii of the Pd atoms, resulting in larger accessible volumes and lower MC acceptance rates as these structures would be very high in energy. Conversely, employing

a tight convergence criterion will decrease the accessible volume, but will increase the computational expense of each MC trial move. The 0.5 kcal mol^{-1} convergence criteria was chosen because it provides a reasonable tradeoff, in which the CG converges in a reasonable timeframe, while still preventing inserted O atoms from being placed in high energy regions within the atomic radius of a Pd atom. We tested tighter and looser convergence criteria, which impacted the computational time required for the MC run to reach equilibrium, but did not significantly impact the final equilibrium values.

The final MC algorithm consists of the following steps: (1) execute MC move, (2) relax atomic forces by conjugate gradient energy minimization, (3) accept or reject the MC move and geometry resulting from relaxation using Equations 4-6 above, (4) iterate until the system energy converges at equilibrium. The converged system reflects the formation of an oxide in equilibrium with a gas phase at the temperature and pressure specified by the reference chemical potential, $\mu_{ref}(T,P)$.

2.2.3. ReaxFF Molecular Dynamics

MD simulations in this study were conducted in the NVT ensemble using the velocity Verlet method[77] with a time step of 0.25 fs. Temperature control was maintained using a Berendsen thermostat[78] with a damping constant of 100 fs. Energy minimization via a conjugate gradient relaxation of forces was conducted prior to each MD run to eliminate simulation artifacts that can arise from high energy contacts initially present in the starting geometry.

2.2.4. QM Method

Density functional calculations were completed in the Vienna *ab initio* simulation package (VASP).[79,80] The exchange-correlation functional was treated with the Perdew-Wang (PW91) version of the generalized gradient approximation (GGA).[81] Atomic core regions were represented using the projector augmented wave method,[82] with valence configurations of $4d^{10}$ for Pd atoms and $2s^2 2p^4$ for O atoms. Plane-wave basis sets were truncated at 400 eV for surface calculations and 600 eV for bulk structures. A convergence criterion of atomic forces less than 0.05 eV $Å^{-1}$ was employed for all structural optimizations. The Monkhorst-Pack (MP) formulation[83] was used to sample the Brillouin zone of all periodic calculations. A *7×7×1* MP k-point spacing was used for Pd surface calculations in a *2×2×6* periodic cell including a 15 Å vacuum layer between periodic images in the z-direction perpendicular to the surface. The bottom three Pd layers were held fixed during structural optimizations to simulate the underlying bulk. A *6×6×6* MP k-point spacing was used for bulk Pd and PdO, where minimal orthogonal unit cells were employed. Clusters were modeled in a *45*Å × *45*Å × *45*Å periodic box with the gamma point considered. Transition states for oxygen dissociation were identified using the climbing image nudged elastic band (CI-NEB) procedure as implemented in VASP,[84] and were conducted in a *3×3×6* periodic cell to minimize interactions across periodic images.

2.3. Results and Discussion

2.3.1. Force Field Development

2.3.1.1. Palladium-Palladium Metal Interactions.

The Pd atom and Pd-Pd interaction parameters listed in Table 2-1 were obtained by optimizing the ReaxFF potential against a training set of 85 data points consisting of both bulk and surface DFT data. We first optimized bulk formation energies calculated as a function of lattice compression and expansion for fcc, bcc, simple cubic, and diamond structure phases of Pd. This enables the potential to properly describe bulk Pd-Pd interactions in numerous configurations and chemical environments. Energetically unfavorable phases that are not experimentally viable, such as simple cubic and diamond, were included in the training to ensure that the potential will not improperly favor these high energy phases. The resulting expansion-compression energy curves, shown in Figure 2-1, demonstrate that the potential correctly discerns energy differences separating bulk Pd phases. ReaxFF predicts that the bcc phase is 1.61 kcal mol^{-1} higher in energy than the fcc phase, which agrees with the DFT value of 0.92 kcal mol^{-1}. The potential yields cubic and diamond phases that are 19.43 and 28.19 kcal mol^{-1} higher in energy, respectively, compared to the fcc phase, in reasonable agreement with the respective DFT values of 11.06 kcal mol^{-1} and 21.91 kcal mol^{-1}. Agreement between DFT and ReaxFF for high energy phases and at densities far from equilibrium is less important for capturing correct Pd-Pd interaction behavior, as long as these phases and densities are unrealizable under relevant simulation conditions. Finally, the potential yields a cohesion energy of -87.7 kcal

mol^{-1}, in agreement with the DFT value of -89.8 kcal mol^{-1}, and the experimental value of -89.7 kcal mol^{-1}.[85,86]

The expansion-compression curves in Figure 3-1 can be used to determine structural properties that are directly comparable with experimental results, such as the fcc lattice constant, the density, and the bulk modulus of Pd metal. The ReaxFF potential predicts an equilibrium lattice constant of 3.97 Å for the fcc phase, which is in good agreement with the respective DFT and experimental[87] values of 3.95 Å and 3.89 Å. The ReaxFF lattice spacing yields a density of 11.3 g/cm^3, in agreement with the experimental[86,87] value of 12.0 g/cm^3. The bulk modulus of fcc Pd can be determined from the expansion-compression curve using the Birch-Murnaghan equation of state for crystalline solids,[88] as shown in the insets of Figure 2-1. A least squares regression of the third order Birch-Murnaghan equation yields a bulk modulus of 140.1 GPa from the ReaxFF data and 144.2 GPa from the DFT data. Both of these values are in reasonable agreement with the experimental value of 180.8 GPa.[86,87] The above comparisons between ReaxFF, DFT, and experiment are summarized in Table 2-2.

Pd-Pd interaction parameters were also optimized to reproduce DFT surface energies for Pd(111) and Pd(100) surfaces. Surface energies for converged 12-layer slab models normalized by the number of surface atoms, calculated with the formula: $\sigma_{surf} = ½ (E_{slab,n} - n\, E_{bulk})$, are shown in Table 2-3, along with literature comparisons. For Pd(111), Pd(100), and Pd(110), ReaxFF predicts surface energies of 10.71 kcal mol^{-1}, 13.95 kcal mol^{-1}, and 20.77 kcal mol^{-1}, respectively, in reasonable agreement with our respective DFT values of 12.97 kcal mol^{-1} , 17.44 kcal mol^{-1}, and 25.26 kcal mol^{-1}. The results are also in agreement with the previously reported DFT values of 12.91 kcal mol^{-1}, 17.06 kcal mol^{-1},

and 24.91 kcal mol^{-1}.[89] Despite having not been explicitly optimized against data for the Pd(110) surface, ReaxFF is in qualitative agreement with DFT and literature results for this surface, predicting Pd(110) to be significantly higher in energy than the Pd(100) surface and Pd(111) surfaces.

The Pd-Pd training set contains structures that sample a range of chemical environments, thus allowing the potential to describe Pd-Pd interactions in structures that are not explicitly considered during parameter training. Figure 2-2 contains relative DFT and ReaxFF cluster energies for Pd_n clusters with n ranging from 6 to 236 atoms, where the relative cluster energy was calculated using the formula: $E_{rel} = E_{cluster,n} / n - E_{bulk}$. Although these structures were not contained in the training set, the potential performs well, yielding energies within ~5 kcal mol^{-1} of the DFT value for cluster sizes larger than 48 atoms and within ~3 kcal mol^{-1} for clusters larger than 135 atoms. Larger deviations occur for smaller clusters, with a deviation of ~7 kcal mol^{-1} for cluster sizes between 19 and 43 atoms. The large deviation of ~12 kcal mol^{-1} for the 6 atom cluster demonstrates the limitation of the ReaxFF potential for describing small ($n < 15$) gas phase clusters. For this reason, we restrict our analysis in the following sections to cluster sizes larger than 43 atoms.

In addition to cluster formation, we compared the performance of ReaxFF for describing the formation of vacancies in the fcc lattice, which was not included in the parameter fitting process. The potential yields a vacancy formation energy of 41.1 kcal mol^{-1}, in reasonable agreement with the DFT value of 29.8 kcal mol^{-1} and the empirical value of 33.21 kcal mol^{-1} (estimated from the experimental melting point of Pd metal[90,91]). These comparisons demonstrate the strengths and limitations of the Pd-Pd potential for

describing both surface and bulk properties in structures that are not present in the 85 point training set described above.

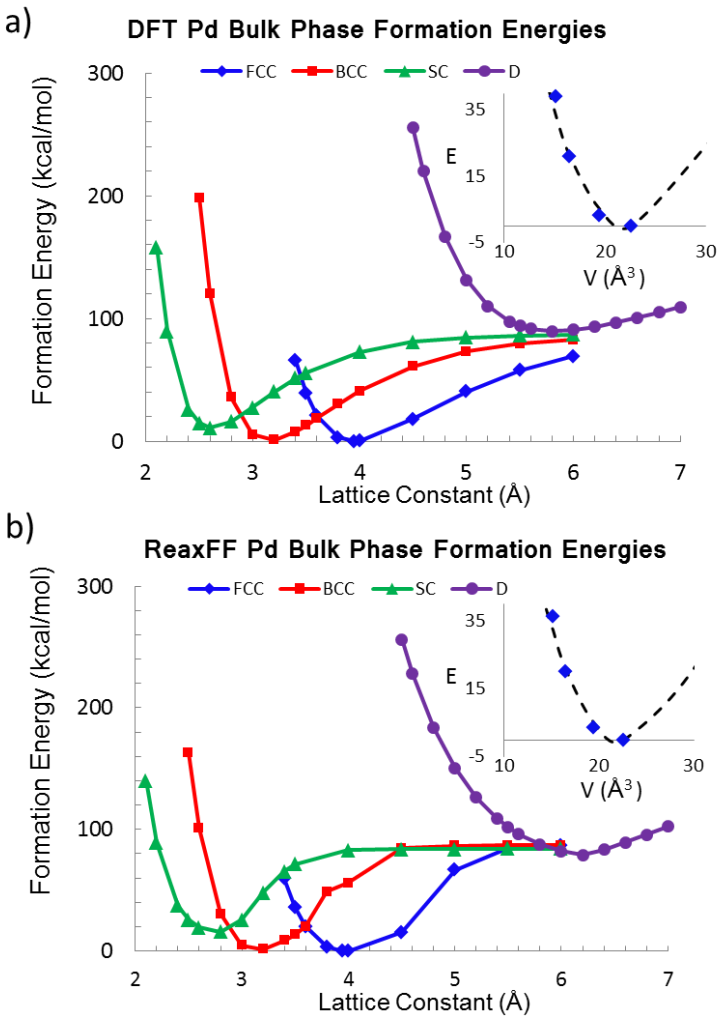

Figure 2-1. (a) DFT and (b) ReaxFF expansion-compression curves for fcc, bcc, simple cubic, and diamond structures of bulk Pd. (Insets) Birch-Murnaghan equation of state fit to the minima of the DFT and ReaxFF bulk fcc curves.

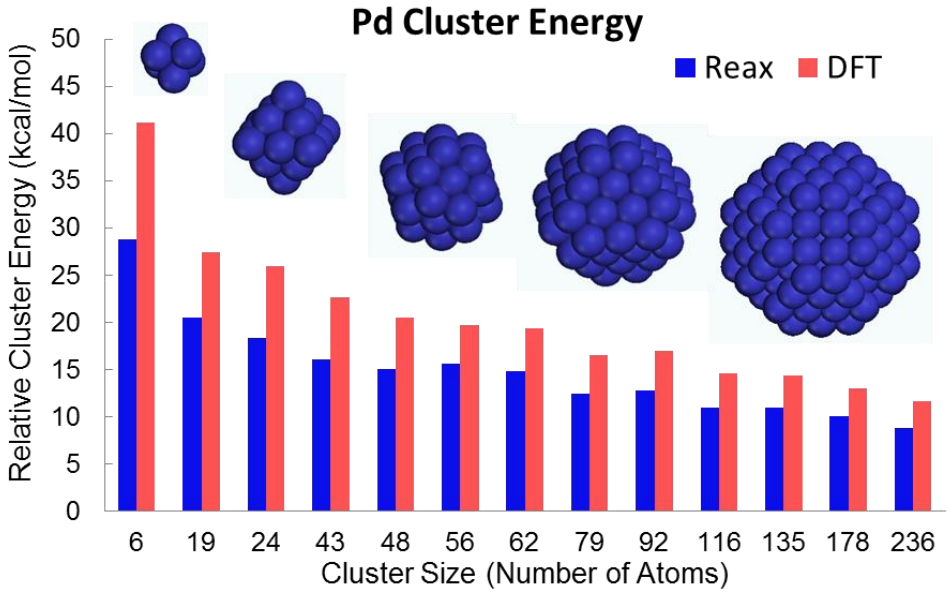

Figure 2-2. ReaxFF and DFT cluster energies per Pd atom relative to the fcc bulk. (Insets) Structures of 6, 24, 48, 92, and 236 atom clusters.

2.3.1.2. Palladium-Oxygen Interactions.

A 49 point DFT training set consisting of bulk, surface, and adsorption data was used to optimize the Pd-O interaction parameters shown in Table I. The oxygen atom and O-O interaction parameters were derived in a previous study.[92] Expansion-compression curves were obtained for bulk palladium(II) oxide (PdO) and palladium(IV) oxide (PdO_2). The most stable phase, PdO, has a tetragonal lattice with a Pd square-planar oxygen coordination. The experimental lattice constants are $a=b=3.03$ *Å* and $c=5.33$ *Å*.[93] The PdO_2 phase is thermally unstable under ambient conditions,[94] and is included in the parameterization process to help diversify the DFT training set. To model PdO_2, we constructed an orthogonal unit cell with an octahedral oxygen coordination surrounding each Pd atom. The unit cells for both phases are shown in Figure 2-3 with the corresponding

expansion-compression curves. The results in the figure show good agreement between ReaxFF and DFT. For PdO, ReaxFF predicts equilibrium lattice spacing of a=b=3.06 *Å* and c=5.53 *Å*, which agrees with both the DFT values of a=b=3.07 *Å* and c=5.52 *Å*, and the experimental values listed above. These lattice constants yield a density of 7.81 g/cm^3, in reasonable agreement with the experimental value of 8.28 g/cm^3. For PdO_2, ReaxFF predicts equilibrium lattice constants of a=b=4.62 *Å* and c=3.24 *Å*, which is consistent with the DFT values of a=b=4.59 *Å* and c=3.22 *Å*. ReaxFF predicts zero-Kelvin formation energies (calculated relative to Pd-fcc and gas phase O_2) of -25.09 kcal mol^{-1} and -22.63 kcal mol^{-1} for PdO and PdO_2, respectively, which agrees with the respective DFT values of -24.32 kcal mol^{-1} and -25.74 kcal mol^{-1}. This demonstrates that the potential is capable of describing Pd-O interactions in bulk phases near equilibrium densities. Deviation in the PdO energy-volume curve occurs at densities far from equilibrium, where the energies are significantly higher (~35 kcal mol^{-1} or greater) than the equilibrium value. It is more important for ReaxFF to correctly reproduce the equilibrium volume and formation energy. Correspondingly, deviations at higher energies are acceptable as long as the corresponding energies are high enough to ensure that such structures are not accessible under the simulation conditions of interest.

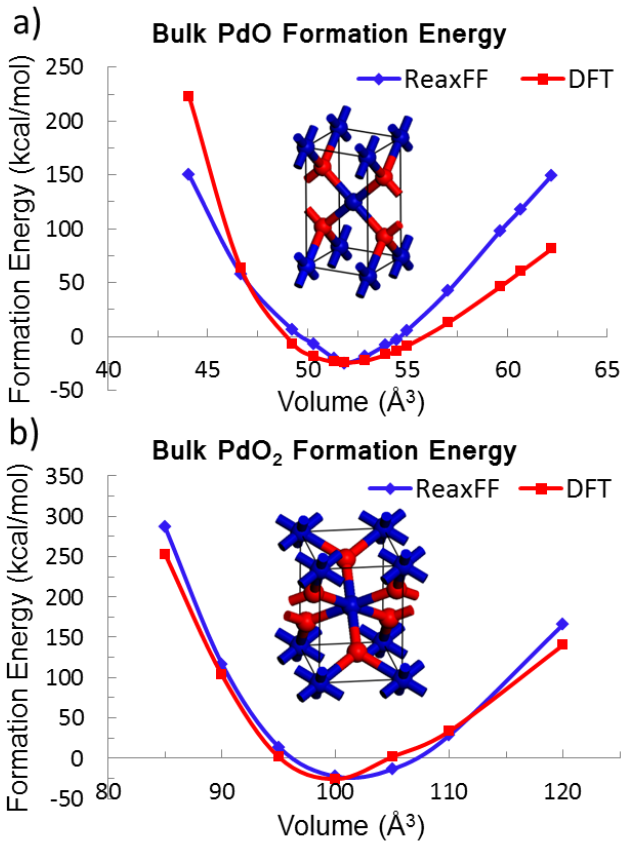

Figure 2-3. ReaxFF and DFT cluster energies per Pd atom relative to the fcc bulk. (Insets) Structures of 6, 24, 48, 92, and 236 atom clusters.

The ReaxFF potential was also optimized to describe Pd-O interactions in surface structures. First, the parameters were fit to DFT relative surface formation energies for PdO(100), PdO(101), PdO(110), PdO(111), and PdO(001). Relative surface formation energies were calculated with the formula $E_{rel} = E_{slab,(PdO)n} / n - E_{PdO,bulk}$, where $E_{slab,(PdO)n}$ is the energy of the surface slab model consisting of n PdO units and $E_{PdO,bulk}$ is the reference energy of one PdO unit in the optimized bulk PdO structure. In order to use this energy reference, our slab models required stoichiometric amounts of Pd and O. Accordingly, the models feature one Pd-terminated side and one O-terminated side, or one Pd terminated side and one PdO terminated side for the PdO(100) surface; resulting in a

surface energy averaged over both Pd and O terminations. The results shown in Table 2-4 demonstrate qualitative agreement between ReaxFF and DFT in predicting the relative stability of each surface. The ReaxFF values for surface energy are linked to bulk formation energies, which causes the accuracy of ReaxFF's description of PdO surface formation energies to trade off with the accuracy of its description of the PdO bulk formation energy. In this instance, we chose to tolerate the potential's tendency to systematically under predict surface energies in order to correctly predict the bulk oxide formation energy.

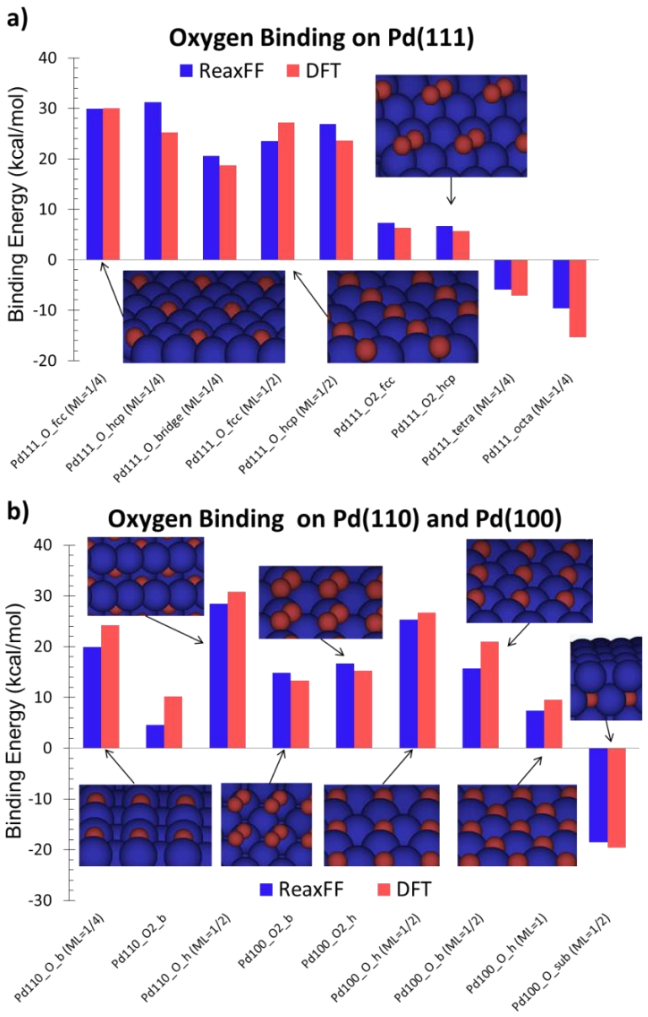

Figure 2-4. ReaxFF and DFT surface binding energies for oxygen on (a) Pd(111), (b) Pd(110) and Pd(100).

The Pd/O interaction parameters were additionally trained against DFT data for oxygen adsorption and dissociation on Pd(111), Pd(110), and Pd(100). Adsorption data for both chemisorbed O_2 molecules and dissociated oxygen atoms were included in the training set. Binding energies were calculated relative to the clean surface and a gas phase O_2 molecule, and were normalized by the number of oxygen atoms in the cell: $E_{bind} = (E_{clean} - E_{O/Pd\text{-}surf}) / n_o + ½ E_{O2}$. The *2×2* periodic cells employed resulted in either 0.25 mono-layer, 0.5 mono-layer, or 1.0 mono-layer coverage, depending on the number of adsorbed oxygen atoms contained in the cell. This ensures that the potential can properly describe interactions between adsorbed oxygen atoms on the Pd surface at variable coverages.

The adsorption data presented in Figure 2-4 demonstrate the feasibility of the ReaxFF potential, which qualitatively reproduces numerous oxygen binding trends predicted by DFT. ReaxFF correctly predicts that oxygen will bind less strongly to both the Pd(111) and Pd(100) surfaces as oxygen coverage increases. For the Pd(111)-fcc site, the ReaxFF binding energy decreases from 29.93 kcal mol^{-1} at 0.25 ML to 23.48 kcal mol^{-1} at 0.5 ML, in agreement with the respective DFT values of 30.05 kcal mol^{-1} and 27.18 kcal mol^{-1}. Similarly for the Pd(111)-hcp site, ReaxFF yields binding energies of 31.20 kcal mol^{-1} at 0.25 ML and 26.82 kcal mol^{-1} at 0.5 ML, which correspond to the DFT values of 25.21 kcal mol^{-1} at 0.25 ML and 23.64 kcal mol^{-1} at 0.5 ML. These numbers are in agreement with DFT energies reported previously by Todorova *et al.*,[95] who calculated binding energies of 34 kcal mol^{-1} and 28 kcal mol^{-1} for the fcc and hcp sites, respectively at 0.25 ML, and binding energies of 26 kcal mol^{-1} and 21 kcal mol^{-1} at 0.5 ML. On the Pd(100) surface, ReaxFF yields a binding energy of 25.35 kcal mol^{-1} at 0.5 ML and 7.36 kcal mol^{-1} at 1 ML, in agreement with the respective DFT values of 26.75 kcal mol^{-1} and

9.57 kcal mol^{-1}. These energies are also in agreement with the DFT values of 24.7 kcal mol^{-1} and 7.9 kcal mol^{-1} reported by Zhang e*t al.* [96]. On Pd(111) tetrahedral and octahedral subsurface sites, ReaxFF yields binding energies of -5.90 kcal mol^{-1} and -9.67 kcal mol^{-1}, respectively. This is in qualitative agreement with the respective DFT values of -7.15 kcal mol^{-1} and -15.35 kcal mol^{-1}, as well as the previously reported[97] DFT values of -8.5 kcal mol^{-1} and -17.9 kcal mol^{-1}. For O_2 binding on the Pd(111) surface, ReaxFF yields binding energies of 7.29 kcal mol^{-1} and 6.64 kcal mol^{-1} on the fcc and hcp sites, respectively, in agreement the DFT values of 6.29 kcal mol^{-1} and 5.65 kcal mol^{-1}. These numbers are also in agreement with those reported by Honkala *et al.*,[98] who calculated DFT adsorption energies of 6.5 kcal mol^{-1} and 6.1 kcal mol^{-1} for O_2 adsorption on the analogous fcc and hcp sites. These data are summarized in Table 2-5, together with the appropriate literature comparisons where available.

We note that ReaxFF does not correctly reproduce the relative stability of an oxygen atom adsorbed on fcc and hcp sites. This is a result of the weighting scheme used during parameter optimization, which minimizes the overall deviation between DFT and ReaxFF. Here, we prefer that the potential is within ~5 kcal mol^{-1} for both sites with the reverse stability ordering, as opposed to having the ordering correct with a larger overall deviation. Furthermore, experimental and theoretical examples exist in the literature showing that the hcp site may be preferred over the fcc site, despite contrary DFT evidence. Using ion-scattering experiments, Steltenpohl and Memmel found that the hcp site is preferred over the fcc site.[99] German *et al.* show that the hcp/fcc preference can be dependent on the DFT method and functional employed; they found that the hcp site is ~3 kcal mol^{-1} more stable than the fcc site when using a converged cluster model of the

Pd(111) surface with the PBE0 functional.[100] Still, the majority of evidence in the literature supports the conclusion that the fcc site is preferred, suggesting that these examples are anomalous. Ultimately, training ReaxFF to correctly reproduce the hcp/fcc trend entails a significant increase in the overall deviation between ReaxFF and DFT, which is not justified since the hcp/fcc site preference is not a principle interest of this study.

Finally, the potential was trained to reproduce O_2 dissociation barriers, which were obtained by CI-NEB for both DFT and ReaxFF. The initial and final structures used in the CI-NEB simulations were chosen from high symmetry sites to provide plausible O_2 dissociation paths that could be used to compare analogous DFT and ReaxFF barriers. Figure 2-5 shows the resulting ReaxFF dissociation paths over the Pd(111), Pd(100), and Pd(110) surfaces, which yield barriers of 19.2 kcal mol^{-1}, 20.4 kcal mol^{-1}, and 17.2 kcal mol^{-1}, respectively. This compares well with our respective DFT barriers of 17.1 kcal mol^{-1}, 17.8 kcal mol^{-1} for Pd(111) and Pd(100); and the barrier of 16 kcal mol^{-1} calculated by P. Junell *et al.* for Pd(110).[101] The reaction paths over Pd(100) and Pd(110) were not explicitly contained in the training set, demonstrating the transferability of the potential for describing barriers not considered in the training process.

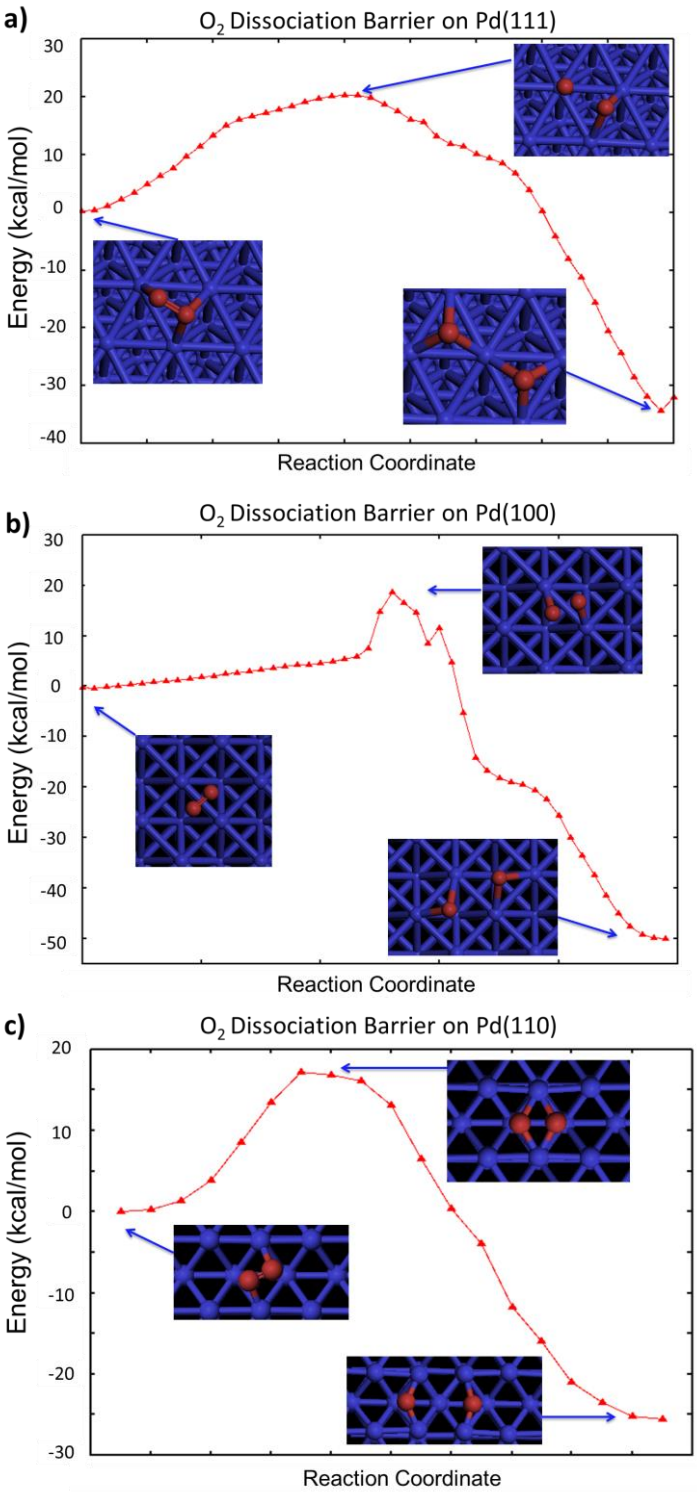

Figure 2-5. ReaxFF O_2 dissociation barrier over (a) the Pd(111) surface, (b) the Pd100 surface, and (c) the Pd(110) surface. (Insets) Initial structure, transition state, and final structure.

Table 2-1. ReaxFF parameters optimized from DFT training set for Pd-Pd and Pd-O terms

Atom	r_o	η	χ	γ	r_{vdW}	ϵ_{vdw}	α	γ_{vdW}
Pd	1.8582	6.6477	5.5005	1.0000	2.0113	0.2465	12.5712	6.0083
O[a]	1.245	8.3122	8.5000	1.0898	2.389	0.1000	9.7300	13.8449
Bond	D_e^{σ}	$p_{be,1}$	$p_{ovun,1}$	$p_{be,2}$	$p_{bo,1}$	$p_{bo,2}$		
Pd-Pd	90.7003	-0.1661	0.2578	3.0618	-0.0914	5.4665		
Pd-O	56.7412	0.7149	0.1000	11.9839	-0.3000	4.7089		
Off-Diagonal	r^{σ}	R_{vdW}	γ	ϵ^{σ}				
Pd-O	1.7139	1.661	10.6568	0.2237				
Valence Angle	θ_o	k_a	k_b	$p_{val,2}$				
Pd-Pd-O	55.7429	4.8907	3.9242	1.0000				
Pd-O-Pd	53.8540	30.0000	2.0649	1.7008				
O-Pd-O	0.0100	30.0000	8.0000	2.4156				
Pd-O-O	90.0000	30.0000	1.6813	1.9155				
Torsion Angle	V_1	V_2	V_3	$P_{tor,1}$	$P_{tor,2}$			
Pd-O-O-Pd	1.7276	50.0000	0.0100	-2.5000	-1.0000			

a) Oxygen atom parameters from ref. [92]

Table 2-2. Properties of bulk-fcc Pd metal from ReaxFF, DFT, and experiment

Property	**ReaxFF**	**DFT**	**Experimental**
Lattice Constant (Å)	3.97	3.95	3.89[86, 87]
Density (g/cm^3)	11.3	11.5	12.0[86, 87]
Bulk Modulus (GPa)	140.1	144.2	180.8[86, 87]
Cohesion Energy (kcal mol^{-1})	-87.7	-89.8	-89.7[85, 86]
Vacancy Energy (kcal mol^{-1})	41.1	29.8	32.3[90, 91]

Table 2-3. Pd surface energies (per surface Pd atom)

Surface	**ReaxFF(kcal mol^{-1})**	**DFT (kcal mol^{-1})**	**Lit. DFT (kcal mol^{-1})**
111	10.71	12.97	12.91[89]
100	13.95	17.44	17.06[89]
110	20.77	25.26	24.91[89]

Table 2-4. Relative PdO surface energies

PdO Surface	**ReaxFF (kcal mol^{-1})**	**DFT (kcal mol^{-1})**
100	4.60	7.01
110	12.27	14.05
111	4.01	6.94
001	12.81	14.65
101	11.45	13.65

Table 2-5. Oxygen binding energies on Pd(111), Pd(100), and Pd(110)

Adsorption Site	ReaxFF (kcal mol^{-1})	DFT (kcal mol^{-1})	Literature (kcal mol^{-1})
111-fcc (1/4 ML)	29.93	30.05	34[95]
111-hcp (1/4 ML)	31.20	25.21	28[95]
111-bridge (1/4 ML)	20.55	18.72	22[95]
111-fcc (1/2 ML)	23.48	27.18	26[95]
111-hcp (1/2 ML)	26.82	23.64	21[95]
111-O_2 fcc	7.29	6.29	6.5[98]
111-O_2 hcp	6.64	5.65	6.1[98]
111-tetra (1/4 ML)	-5.90	-7.15	-8.5[97]
111-octa (1/4 ML)	-9.67	-15.35	-17.9[97]
100-hollow (1/2 ML)	25.35	26.75	24.7[96]
100-hollow (1 ML)	7.36	9.57	7.9[96]
100-bridge (1/2 ML)	15.74	20.98	18.5[96]
100-octa (1/2 ML)	-18.52	-19.60	-
100-O_2 bridge	14.83	13.38	-
100-O_2 hollow	16.67	15.34	-
110-bridge (1/4 ML)	19.91	24.21	-
110-hollow (1/2 ML)	28.46	30.79	-
110-O_2 bridge	4.65	10.26	-

Table 2-6. Structural properties of 3-nm and 2-nm Pd clusters

3-nm Cluster	**111**	**110**	**100**
Nr. of Facets	8	12	6
Area (per facet, Å^2)	82.57	44.67	55.33
Surface Atoms (per facet)	7	1	4
Edge Atoms (per facet)	3-(100), 3-(110)	2-(111), 2-(100)	-
Corner Atoms (per facet)	6	4	8
Step Sites (per facet)	-	-	12
2-nm Cluster	**111**	**110**	**100**
Nr. of Facets	8	12	6
Area (per facet, Å^2)	44.73	7.95	11.17
Surface Atoms (per facet)	3	-	-
Edge Atoms (per facet)	3-(100)	-	-
Corner Atoms (per facet)	6	4	4
Step Sites (per facet)	-	-	8

2.3.2. MD Simulations of Palladium Oxide Formation

The Pd/O interaction parameters developed above were implemented in 250 ps NVT simulations of oxide formation on Pd surfaces and clusters. The experimental results discussed in the introduction suggest that oxidation of the bulk below Pd(111)[28] and Pd(100)[22] is kinetically hindered by surface and subsurface oxide phases, whereas Pd(110)[31] readily forms a bulk oxide. We conducted MD simulations to determine if this behavior is reproduced by the ReaxFF Pd/O interaction potential. Pd clusters were also included in the analysis, as many Pd catalysts feature Pd clusters dispersed on oxide supports, rather than perfect single-crystal surfaces. The Pd(111), Pd(110), and Pd(100) surface models consist of periodic surfaces with surface vectors chosen as near to 20 Å×20 Å as possible depending on Pd-Pd spacing. Each slab model is 10 Pd layers thick, with periodic images in the z-direction separated by 100 *Å* of vacuum space that is populated with O_2 molecules. Each simulation began with 40 O_2 molecules in the gas phase above the surface. The Pd(111), Pd(100), and Pd(110) slabs consist of 640, 500, and 400 atoms, respectively. The ratio of Pd to O atoms will affect the overall amount of oxygen that can be absorbed by each surface. Since we are interested in comparing oxidation rates, we chose O/Pd ratios that are well below the stoichiometric 1:1 ratio characteristic of bulk PdO, thus ensuring that the metal never becomes saturated with oxygen atoms. This, in conjunction with the high simulation temperatures and pressures, allows us to simulate an oxidation process that is kinetically limited, as opposed to thermodynamically limited. As such, the dimensions of the simulation cells were chosen such that each Pd surface has an equal number of Pd layers exposed to a comparable O_2 environment, allowing for a direct

comparison of the relative oxidation kinetics on each surface. The populations of O_2 molecules and O atoms either present in the gas phase, adsorbed on the Pd surface, or absorbed in the bulk were recorded at 25 fs intervals. The resulting species population plots for each simulation are shown in Figure 2-6 for surface simulations and in Figure 2-7 for cluster simulations; and the structures of the cluster and surface models are shown in Figure 2-8 and Figure 2-9, respectively.

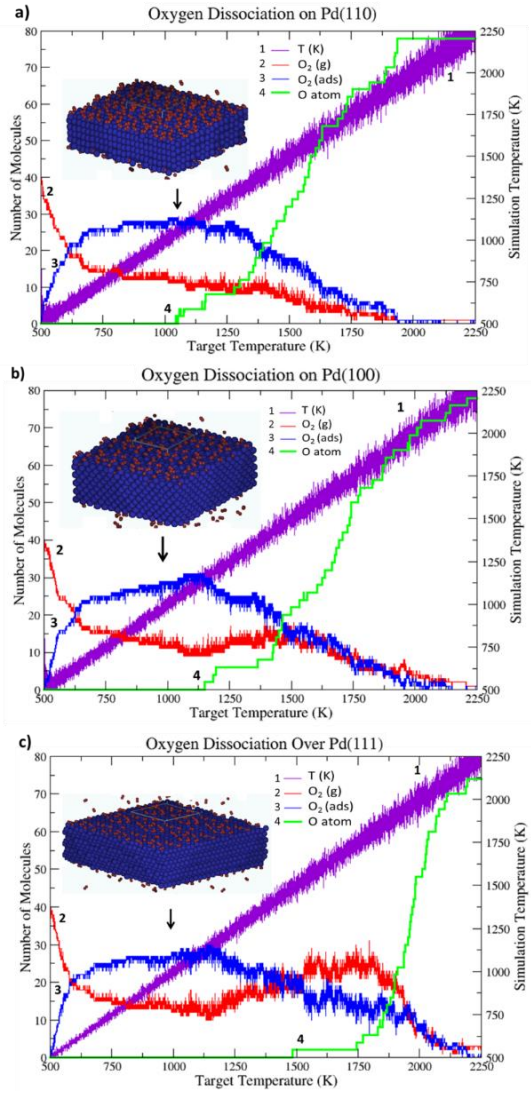

Figure 2-6. Temperature ramped NVT simulation of O_2 dissociation and oxide formation on (a) Pd(110), (b) Pd(100), and (c) Pd(111) surfaces. (Insets) Periodic surface structure at 1000 K.

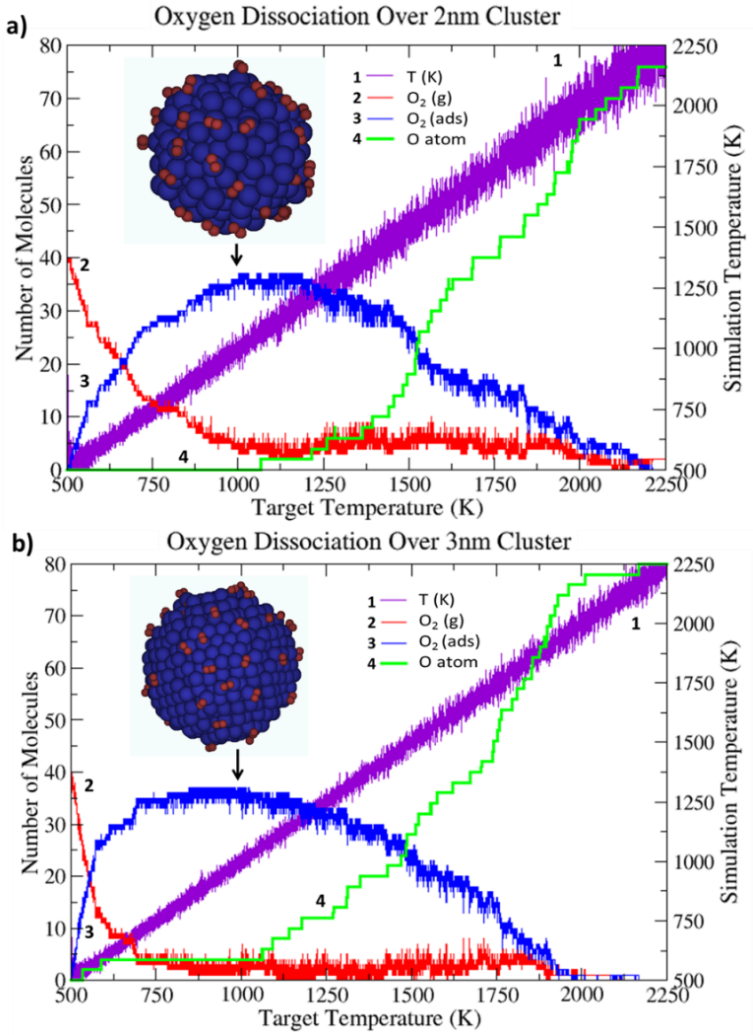

Figure 2-7. Temperature ramped NVT simulation of O_2 dissociation and oxide formation on (a) 2-nm diameter Pd_{321} cluster, and (b) 3-nm diameter Pd_{935} cluster. (Insets) Surface at 1000 K.

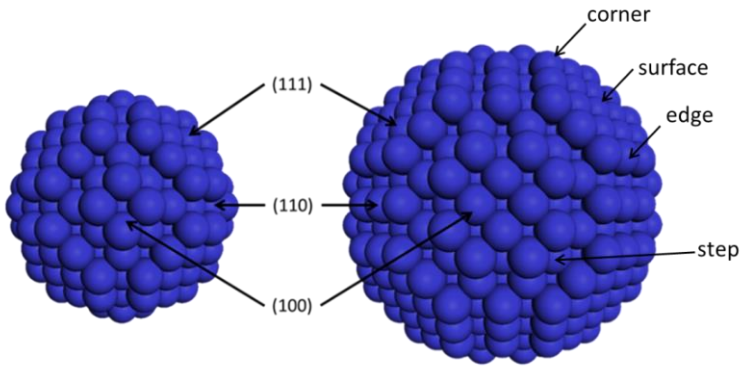

Figure 2-8. Structure of the (left) 2-nm and (right) 3-nm Pd clusters.

Both temperature-ramp and fixed-temperature simulations were employed to assess reactivity toward O_2 dissociation and oxide formation. In the temperature-ramp simulations, the system temperature was initially set at 500 K and was increased at a rate of 8 K/ps, yielding a final temperature of 2500 K. This results in a pressure range in the gas phase of approximately 15 MPa to 2 MPa depending on the temperature and number of O_2 molecules remaining in the gas phase. The results in Figures 1-6 and 1-7 demonstrate the necessity of high temperature and pressure ranges, as appreciable O_2 dissociation does not occur below ~1000 K and ~7 MPa at these timescales.

The relative activity of each surface toward oxide formation can be assessed by comparing the onset temperature of oxygen dissociation (T_d) for each surface, marked by the appearance of atomic oxygen. As seen in Figure 2-6, the Pd(110) surface dissociates oxygen most readily, with T_d = 1040 K compared to T_d = 1150 K for Pd(100) and T_d = 1490 K for Pd(111). On all the surfaces, O_2 adsorbs at low temperatures until the surface becomes saturated, and either dissociates or desorbs back into the gas phase as temperature increases. The kinetic hindrance of subsurface oxygen migration beneath Pd(111) and Pd(100) surfaces is demonstrated by a pronounced increase in the number of gas phase oxygen molecules as O_2 desorbs back into the gas phase after T_d. This occurs when the surface becomes saturated with oxygen that cannot migrate into the bulk, and therefore desorbs as the temperature increases. Over Pd(110), there is no desorption of O_2 molecules after T_d, indicating that oxygen atoms can rapidly diffuse into the subsurface, thus forming a bulk oxide with little kinetic hindrance in these temperature ranges.

The difference in T_d between the Pd(111) and Pd(100) surface is somewhat

surprising given the similar dissociation barriers shown in Figure 2-5. This difference can be attributed to surface coverage effects. The O_2 dissociation barriers shown in Figure 2-5 were calculated in a *3×3* cell in order to minimize adsorbate-adsorbate interactions affecting the barrier height. These barriers, therefore, correspond to the O_2 activation energy at low coverage. To determine the barriers at higher coverage, we calculated DFT barriers in a *2×2* cell to illustrate the effect of surface coverage on barrier heights. The barrier over Pd(111) increases from 17.1 kcal mol^{-1} at 0.22 ML to 25.14 kcal mol^{-1} at 0.5 ML, while the barrier over Pd(100) remains near ~17 kcal mol^{-1}. Under the simulation conditions presented here, the surface coverage of O_2 prior to the onset of dissociation is high (~0.5 ML), thus the high coverage barriers are more pertinent for comparing dissociation temperatures. The high coverage barriers for dissociation over Pd(100) and Pd(110) are close in magnitude (both near ~17 kcal mol^{-1}), and are significantly lower than that over Pd(111) (~25 kcal mol^{-1}). This explains why dissociation over Pd(110) and Pd(100) begins at similar temperatures (1040 K and 1150 K, respectively) and why Pd(111) has a much higher dissociation temperature (1490 K). A similar trend in coverage dependence was reported for O_2 dissociation on Pt(111) by Miller *et al.*,[102] who found that the O_2 dissociation barrier increased by ~12 kcal mol^{-1} when the coverage is increased from 0.25 ML to 0.5 ML. Also, similar high coverage barriers over Pd(111) have been reported by Eichler *et al.*[103] (~23 kcal mol^{-1} at 0.33 ML), and by Honkala *et al.*[98] (~27 kcal mol^{-1} at 0.5 ML).

Fixed temperature simulations were also conducted to further assess the oxidation affinity of the three Pd surfaces. A temperature of 1400 K was chosen for these simulations, which is high enough to yield oxygen dissociation in the simulation timeframe, but is low

enough to maintain a crystalline metal lattice. The results, shown in Figure 2-9, depict the initial and final structures of each surface after exposure to O_2(g) for the duration of the 250 ps simulation. As seen in Figure 2-9(a), oxygen dissociates over the Pd(111) surface, but, with little subsurface oxygen migration, does not form a bulk oxide. The Pd(100) surface forms a surface oxide with oxygen migrating into the first two subsurface layers, but maintains a pure Pd crystal structure in the bulk. Oxygen rapidly dissociates and migrates into the subsurface over the Pd(110) surface, resulting in a bulk oxide with no crystalline Pd structure remaining in the bulk. The migration of oxygen into the Pd(110) sub-layers leads to a transition in the lattice structure of the bulk, yielding the disordered phase seen in the figure. The fixed cell dimension prohibits the system from relaxing into an ordered PdO crystalline structure. This result demonstrates that the surface structure of crystalline Pd(110) allows oxygen atoms to migrate into the subsurface, which is not seen under comparable conditions for Pd(111) and Pd(100). This trend is the result of two factors. First, the oxygen dissociation barrier is lower over Pd(110) compared to the other two surfaces, which is reflected in the lower value for T_d discussed above. Second, oxygen diffusion into the bulk occurs more rapidly over Pd(110) due to wide surface channels present on the Pd(110) surface, which are easily penetrated by diffusing oxygen compared to the close packed Pd(111) and Pd(100) surfaces.

Additionally, we calculated barriers for O atoms to migrate from a surface hollow site to a subsurface octahedral site over each surface. On the Pd(111) surface, ReaxFF yields a barrier of 65 kcal mol^{-1} for an oxygen atom to migrate from a surface fcc site to a subsurface octahedral site, which is in reasonable agreement with the analogous DFT barrier of 58 kcal mol^{-1} (calculated in a 2×2 periodic cell). On the Pd(100) and Pd(110)

surfaces, the ReaxFF barriers are significantly lower for subsurface migration to octahedral sites at 44 kcal mol^{-1} and 32 kcal mol^{-1}, respectively. This trend is in agreement with the MD results showing that oxygen can diffuse more readily into the Pd(110) surface compared to the Pd(100) and Pd(111) surfaces. These results corroborate the experimental finding, reported by Han *et al.*[34,35], that Pd(110) has a lower subsurface diffusion barrier than Pd(100) and Pd(111).

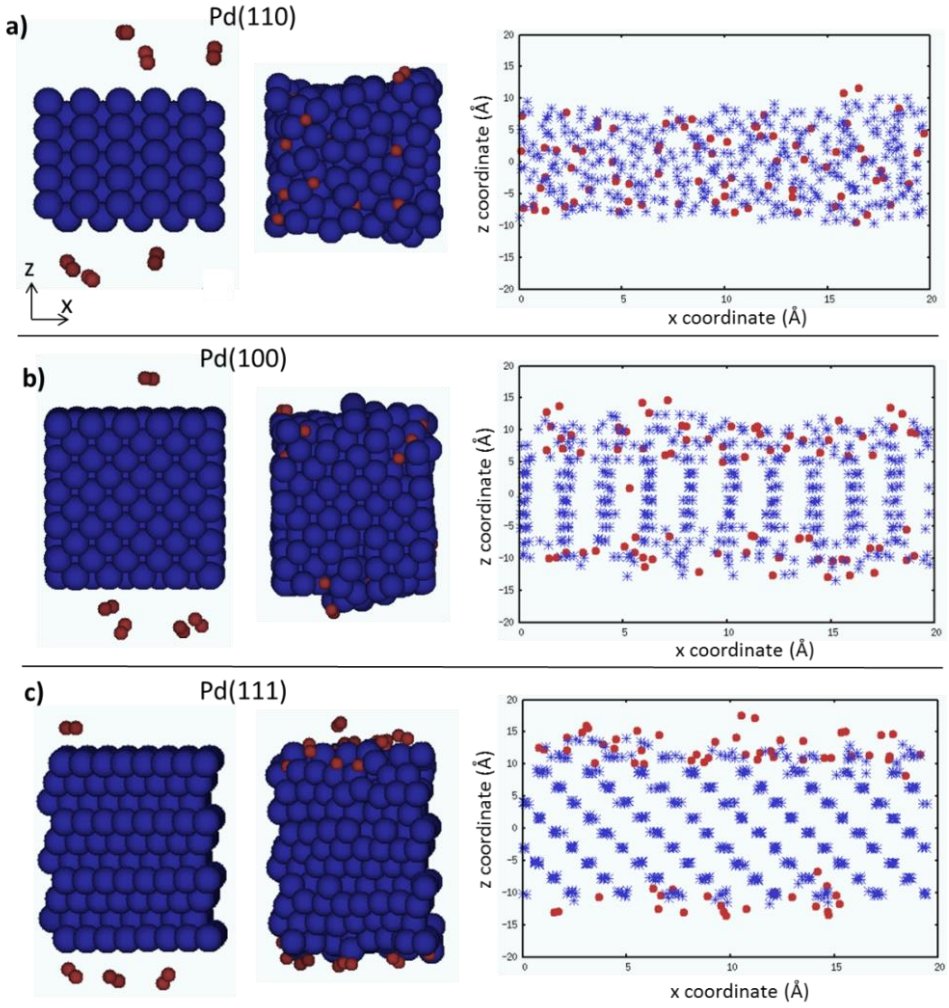

Figure 2-9. NVT simulation of O_2 dissociation at 1400 K on (a) Pd(110), (b) Pd(100), and (c) Pd(111) surfaces. The initial structures are shown on the left and the final structures after 250 ps are shown on the right (note: not all gas phase atoms are shown). Plots represent the final *x* and *z* coordinates of all atoms in the system, (red dots = oxygen atoms, blue stars = Pd atoms).

Since most catalytic applications feature supported metal particles, rather than single crystal surfaces, we conducted similar temperature-ramp NVT analyses of oxidation on Pd clusters. The cluster simulations were conducted with spherical 2-nm diameter (321 atoms) and 3-nm diameter (935 atoms) cluster models constructed from the bulk-fcc phase, which are shown in Figure 2-8. As seen in the figure, both clusters feature significant Pd(111), Pd(100), and Pd(110) facets, as well as numerous step, corner, and edge sites. The structural details of each cluster are summarized in Table 2-6. Each cluster was placed in a $50\text{Å}\times50\text{Å}\times50\text{Å}$ periodic box with the remaining vacuum space occupied by 40 O_2 molecules. The results, shown in Figure 2-7, show that the 2-nm cluster begins to dissociate O_2 at 1070 K and allows a negligible amount of oxygen molecules to desorb back to the gas phase at high temperatures. Similar results are found for the 3-nm cluster, which begins to rapidly dissociate O_2 at 1060 K and does not allow oxygen to desorb from the surface. This is qualitatively comparable to the performance of the Pd(110) surface, suggesting that oxide diffusion into the bulk is less kinetically hindered on clusters in this size range than for close packed single-crystal surfaces under comparable temperature and pressure conditions. Similar to the Pd(110) surface, rapid oxidation in the bulk phase is the result of two factors. First, the cluster surfaces contain under-coordinated Pd atoms on corner, step, and edge sites resulting in low O_2 dissociation barriers, allowing the surface to rapidly saturate with oxygen atoms. For example, we calculated a ReaxFF dissociation barrier of 12 kcal mol^{-1} over a corner site on the 2-nm cluster, which is even lower than the dissociation barrier over Pd(110). Second, the cluster surface is less closely packed, allowing oxygen atoms to readily diffuse into the bulk. Here, we calculated a subsurface migration barrier from a step site to a subsurface octahedral site of 26 kcal mol^{-1}, which

again is significantly lower than the analogous barrier on the single-crystal surfaces.

The kinetic behavior observed in these MD simulations suggests that surface oxide phases do not limit bulk oxidation in clusters at high temperatures. These results, however, are limited to high temperatures and pressures to allow oxidation to occur on an accessible timescale. As such, the results cannot conclusively demonstrate a lack of kinetic hindrance for the analogous process at low temperatures. Nevertheless, the MD simulations suggest that oxidation over clusters is qualitatively similar to the Pd(110) surface, which is experimentally[31] shown to form a bulk oxide without kinetic hindrance. It is therefore important to also assess the thermodynamic stability of bulk and surface oxide phases over Pd clusters at lower temperatures and pressures, which is addressed in Section 2.3.3.

2.3.3. Grand Canonical Monte Carlo Simulations of Palladium Oxide Formation

The MD results in Section 2.3.2 underscore the importance of investigating the thermodynamic stability of oxide formations in Pd clusters at temperatures and pressures typically employed during oxidation catalysis. For this reason, we applied a hybrid GC-MC/MD method to determine the extent of surface and bulk oxidation in Pd clusters as a function of temperature and oxygen partial pressure. Each simulation began with a 3-nm diameter Pd_{935} cluster in a $50\mathring{A}\times50\mathring{A}\times50\mathring{A}$ box. Oxygen atoms were added, moved, and removed from the system until the energy of the system converged such that the total system energy varied less than 20 kcal mol^{-1} over the final 1000 MC trial moves. This is demonstrated in Figure 2-10, which depicts the convergence of both oxygen concentration and system energy (calculated relative to the clean Pd cluster and the oxygen chemical

potential) for simulations at 500 K with varying oxygen pressures. As seen in the figure, the number of MC iterations (defined as an attempted move, as opposed to an accepted move) required to reach equilibration is typically between 15,000 and 25,000 for this system, depending on temperature and pressure.

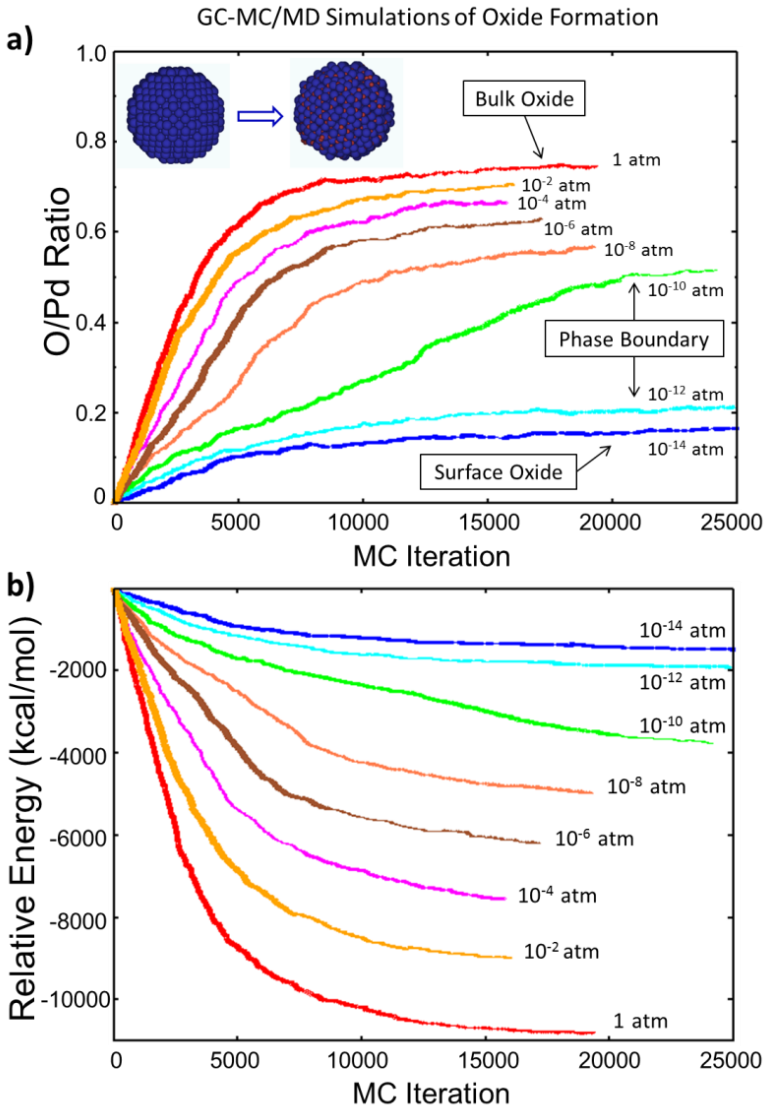

Figure 2-10. (a) Ratio of oxygen to palladium atoms and (b) relative energy ($E_{relative} = E_{system,n_o} - E_{clean} - n_o\mu_{ref}$) of the system during a grand canonical Monte Carlo simulation of PdO formation on a 3-nm diameter Pd_{935} cluster at T = 500 K and $P = 10^{-14}$ atm (dark blue), $P = 10^{-12}$ atm (light blue), $P = 10^{-10}$ atm (green), $P = 10^{-8}$ atm (orange), $P = 10^{-6}$ atm (brown), $P = 10^{-4}$ atm (magenta), $P = 10^{-2}$ atm (yellow), P = 1 atm (red). (Insets) Initial and final structure after GC-MC at 500 K and 1 atm.

A total of 34 GC-MC/MD simulations were conducted to sample the oxidation phase space at temperatures ranging from 300 K to 1300 K and oxygen pressures ranging from 10^{-14} atm to 1 atm. The degree of oxidation was determined by the final O/Pd ratio of the equilibrated system. As expected, the O/Pd ratio decreases as the oxygen pressure is lowered, and increases as the temperature is lowered. Figure 2-10 shows a clear distinction between bulk and surface oxidation, indicated by the pronounced increase in converged O/Pd ratios that occurs between 10^{-10} atm and 10^{-12} atm.

To further analyze the structure of the oxide phases, we used the atomic coordinates of the equilibrated systems to calculate the radial distribution of oxygen atoms in the cluster. By analyzing the radial distribution of oxygen atoms in the cluster, we determined whether oxidation occurred primarily on the particle surface or throughout the particle bulk. This is demonstrated in Figure 2-11, which shows the final structure and corresponding radial distribution of oxygen atoms from the center of the cluster (r=0) at 1 atm over a range of temperatures. As seen in Figure 2-11(a-b), simulations under oxidizing conditions (300 K - 800 K, 1 atm) yield a nearly uniform oxygen density throughout the particle. Figure 2-11(d) shows the oxygen distribution at 1 atm and 1200 K, where oxygen atoms adsorb on the surface, but not in the bulk. Figure 2-11(c) shows the onset of bulk oxidation at 1000 K and 1atm, which lies near the phase boundary between bulk and surface oxidation. Similar plots were used to classify the final structure of each MC simulation as (1) bulk oxide, (2) surface oxide, or (3) Pd metal. Surface oxides were defined broadly to include varying coverages of chemisorbed oxygen. Adsorbed oxygen atoms almost always rearranged surface Pd atoms forming a surface oxide, so we did not differentiate between surface adsorption and surface oxidation. These distinctions were used to estimate the

boundaries of an oxidation phase diagram, shown in Figure 2-12, which predicts the *T*,*P* regions in which a surface oxide phase is thermodynamically stable on a 3-nm Pd cluster.

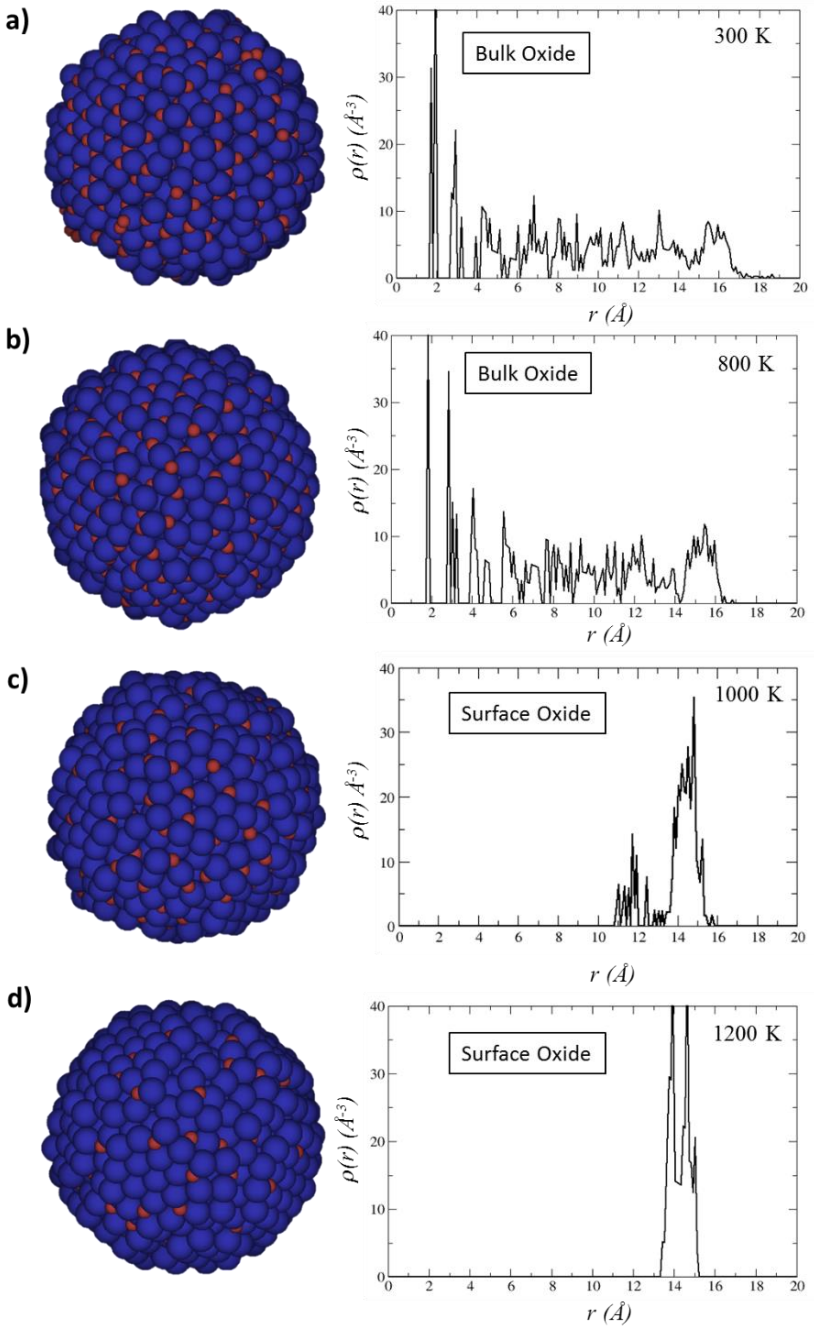

Figure 2-11. Final structure and radial distribution of oxygen atoms relative to the center of the Pd cluster after Grand Canonical Monte Carlo simulations of oxide formation at P = 1 atm and T = (a) 300 K, (b) 800 K, (c) 1000 K, and (d) 1200 K.

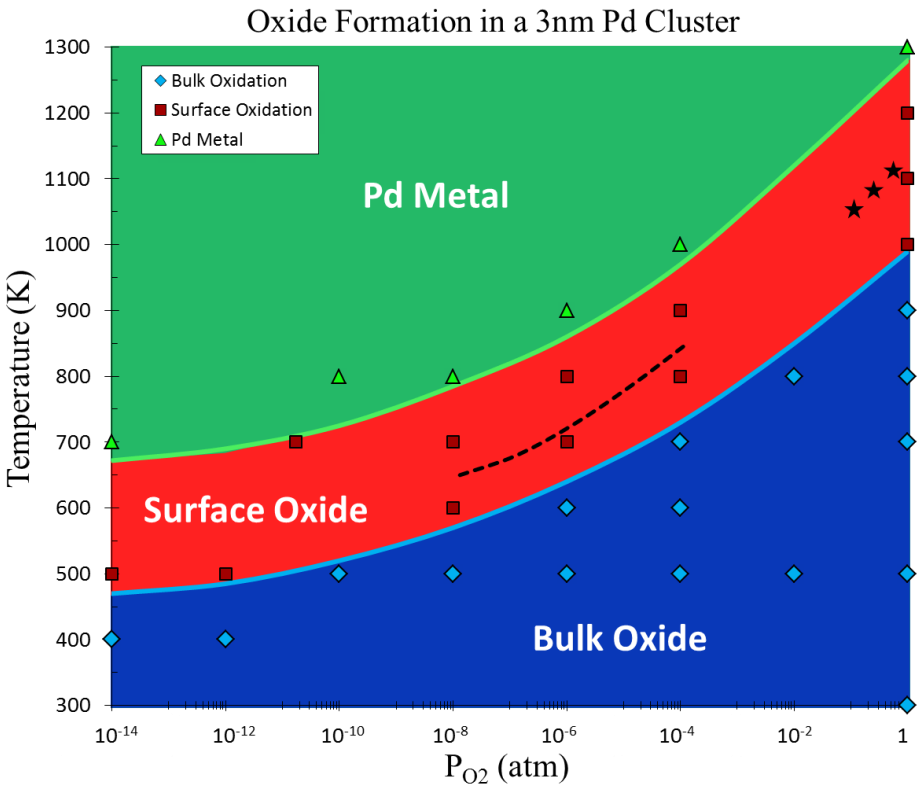

Figure 2-12. Phase diagram derived from ReaxFF GC-MC/MD simulations of oxide formation in a 3-nm diameter Pd cluster. The points indicate the temperature and pressure of each GC-MC simulation, from which the phase boundaries are estimated. The dashed black line indicates the bulk Pd→PdO transition reproduced from ref.[28], which was calculated from experimental enthalpies and heat capacities. The stars indicate experimentally observed bulk Pd→PdO transitions at 0.1 atm/1050 K, 0.5 atm/1085 K, and 0.9 atm/1125 K.[104]

The phase boundaries predicted by the ReaxFF GC-MC/MD method for the 3-nm cluster are similar to the experimental and *ab initio* phase diagrams for the Pd(111) surface determined by Ketteler *et al.*[28] and for the Pd(100) surface determined by Lundgren *et al.*[22] Both contain thermodynamically stable surface oxide phases in *T,P* regions similar to those predicted by ReaxFF. The phase diagram derived from the ReaxFF GC-MC method also compares favorably with experimentally observed bulk Pd→PdO phase boundaries. These comparisons are demonstrated by the dotted black line in Figure 2-12, which represents the bulk Pd → PdO phase boundary derived by Ketteler *et al.* [28] from experimental enthalpies

and heat capacities. Additionally, the ReaxFF phase diagram is in agreement with bulk Pd → PdO phase transitions observed experimentally by Zhang *et al.*, which are marked in Figure 2-12 by black stars.[104] The uncertainty introduced by the inaccuracy of DFT for describing O_2 systematically shifts the GC-MC/MD boundaries to lower temperatures; the actual boundary may lie at higher temperatures. This indicates that the cluster forms an oxide more readily than the single crystal surfaces and the Pd bulk, which is expected since the cluster surface exposes under-coordinated Pd atoms at corner and edge sites that serve as nucleation sites for oxide growth. The agreement between experimental, *ab initio*, and ReaxFF phase diagrams validates the Pd/O interaction potential, and demonstrates the applicability of the hybrid MD/GC-MC method for assessing the thermodynamic properties of large (~1000 atom), non-periodic systems.

2.4. Conclusion

Oxide formation on noble metal surfaces, such as palladium, plays an important role in numerous industrial catalytic operations. To investigate the dynamics of oxidation processes on Pd surfaces and clusters, we derived a ReaxFF interaction potential for Pd/O from an extensive set of DFT data for both bulk and surface properties. Using this potential, we conducted NVT molecular dynamics simulations of oxide formation on Pd(111), Pd(110), and Pd(100). These results, while limited to high temperatures, are in agreement with previous experimental observations,[34] predicting that oxygen migration into the subsurface of Pd(110) is less kinetically hindered than Pd(111) and Pd(100). Our MD results similarly suggest that oxide formation in Pd clusters is qualitatively comparable to

Pd(110); although the lack of kinetic hindrance in clusters cannot be conclusively demonstrated by high temperature simulations. Building on this kinetic result, we introduced a hybrid GC-MC/MD approach to assess the thermodynamic stability of oxide formation on Pd clusters. Using this method, we derived a theoretical phase diagram for oxidation in spherical 3-nm diameter Pd_{935} clusters. The corroboration between experiment and ReaxFF both validates the Pd/O interaction potential, and demonstrates the feasibility of the hybrid GC-MC/MD method. The formalism of the hybrid GC-MC/MD method is transferrable to other multi-component systems, and is capable of deriving theoretical phase diagrams that are either in temperature and pressure ranges inaccessible to experimental methods, or are too large or irregular to treat with *ab initio* methods in a computationally tractable timescale.

2.5. Acknowledgements

This research was supported by funding from the National Science Foundation grant: CBET-1032979. R.J.M. acknowledges funding from NSF grant: CHEM-1026717.

2.6. References

1. E. Lundgren, G. Kresse, C. Klein, M. Borg, J. N. Andersen, M. De Santis, Y. Gauthier, C. Konvicka, M. Schmid and P. Varga, Physical Review Letters **88** (24), 246103 (2002).
2. W. X. Li, L. Österlund, E. K. Vestergaard, R. T. Vang, J. Matthiesen, T. M. Pedersen, E. Lægsgaard, B. Hammer and F. Besenbacher, Physical Review Letters **93** (14), 146104 (2004).

3. J. Gustafson, A. Mikkelsen, M. Borg, J. N. Andersen, E. Lundgren, C. Klein, W. Hofer, M. Schmid, P. Varga, L. Köhler, G. Kresse, N. Kasper, A. Stierle and H. Dosch, Physical Review B **71** (11), 115442 (2005).
4. P. Kostelník, N. Seriani, G. Kresse, A. Mikkelsen, E. Lundgren, V. Blum, T. Šikola, P. Varga and M. Schmid, Surface Science **601** (6), 1574-1581 (2007).
5. C. Dri, C. Africh, F. Esch, G. Comelli, O. Dubay, L. Kohler, F. Mittendorfer, G. Kresse, P. Dudin and M. Kiskinova, The Journal of Chemical Physics **125** (9), 094701 (2006).
6. J. Klikovits, M. Schmid, L. R. Merte, P. Varga, R. Westerström, A. Resta, J. N. Andersen, J. Gustafson, A. Mikkelsen, E. Lundgren, F. Mittendorfer and G. Kresse, Physical Review Letters **101** (26), 266104 (2008).
7. J. Klikovits, E. Napetschnig, M. Schmid, N. Seriani, O. Dubay, G. Kresse and P. Varga, Physical Review B **76** (4), 045405 (2007).
8. H. W. Jen, G. W. Graham, W. Chun, R. W. McCabe, J. P. Cuif, S. E. Deutsch and O. Touret, Catalysis Today **50** (2), 309-328 (1999).
9. H. S. Gandhi, G. W. Graham and R. W. McCabe, Journal of Catalysis **216** (1–2), 433-442 (2003).
10. T. Kobayashi, T. Yamada and K. Kayano, Appl. Catal. B-Environ. **30** (3-4), 287-292 (2001).
11. M.-F. Luo, Z.-Y. Hou, X.-X. Yuan and X.-M. Zheng, Catalysis Letters **50** (3), 205-209 (1998).
12. T. Engel and G. Ertl, J. Chem. Phys. **69** (3), 1267-1281 (1978).
13. B. C. Sales, J. E. Turner and M. B. Maple, Surface Science **114** (2-3), 381-394 (1982).
14. E. M. Stuve, R. J. Madix and C. R. Brundle, Surface Science **146** (1), 155-178 (1984).
15. Y. Xu, J. Q. Ma, Y. F. Xu, L. Xu, H. X. Li and H. Li, RSC Adv. **3** (3), 851-858 (2013).
16. R. Toyoshima, M. Yoshida, Y. Monya, K. Suzuki, B. S. Mun, K. Amemiya, K. Mase and H. Kondoh, J. Phys. Chem. Lett. **3** (21), 3182-3187 (2012).
17. G. B. Hoflund, H. A. E. Hagelin, J. F. Weaver and G. N. Salaita, Applied Surface Science **205** (1-4), 102-112 (2003).
18. J. F. Weaver, J. A. Hinojosa Jr, C. Hakanoglu, A. Antony, J. M. Hawkins and A. Asthagiri, Catalysis Today **160** (1), 213-227 (2011).
19. A. D. Mayernick and M. J. Janik, The Journal of Physical Chemistry C **112** (38), 14955-14964 (2008).
20. A. D. Mayernick and M. J. Janik, Journal of Catalysis **278** (1), 16-25 (2011).
21. M. Li, D. Weng, X. D. Wu, J. Wan and B. Wang, Catalysis Today **201**, 19-24 (2013).
22. E. Lundgren, J. Gustafson, A. Mikkelsen, J. N. Andersen, A. Stierle, H. Dosch, M. Todorova, J. Rogal, K. Reuter and M. Scheffler, Physical Review Letters **92** (4), 046101 (2004).
23. J. Rogal, K. Reuter and M. Scheffler, Physical Review B **69** (7), 075421 (2004).

24. M. Todorova, E. Lundgren, V. Blum, A. Mikkelsen, S. Gray, J. Gustafson, M. Borg, J. Rogal, K. Reuter, J. N. Andersen and M. Scheffler, Surface Science **541** (1–3), 101-112 (2003).
25. E. H. Voogt, A. J. M. Mens, O. L. J. Gijzeman and J. W. Geus, Surface Science **373** (2-3), 210-220 (1997).
26. G. Zheng and E. I. Altman, Surface Science **462** (1-3), 151-168 (2000).
27. G. Zheng and E. I. Altman, Surface Science **504** (1-3), 253-270 (2002).
28. G. Ketteler, D. F. Ogletree, H. Bluhm, H. J. Liu, E. L. D. Hebenstreit and M. Salmeron, J. Am. Chem. Soc. **127** (51), 18269-18273 (2005).
29. J. A. Hinojosa Jr and J. F. Weaver, Surface Science **605** (19–20), 1797-1806 (2011).
30. H. H. Kan, R. B. Shumbera and J. F. Weaver, Surface Science **602** (7), 1337-1346 (2008).
31. R. Westerström, C. J. Weststrate, J. Gustafson, A. Mikkelsen, J. Schnadt, J. N. Andersen, E. Lundgren, N. Seriani, F. Mittendorfer, G. Kresse and A. Stierle, Physical Review B **80** (12), 125431 (2009).
32. N. Seriani, J. Harl, F. Mittendorfer and G. Kresse, The Journal of Chemical Physics **131** (5), 054701 (2009).
33. H. Gabasch, W. Unterberger, K. Hayek, B. Klotzer, E. Kleimenov, D. Teschner, S. Zafeiratos, M. Havecker, A. Knop-Gericke, R. Schlogl, J. Y. Han, F. H. Ribeiro, B. Aszalos-Kiss, T. Curtin and D. Zemlyanov, Surface Science **600** (15), 2980-2989 (2006).
34. J. Y. Han, D. Y. Zemlyanov and F. H. Ribeiro, Surface Science **600** (13), 2752-2761 (2006).
35. J. Y. Han, D. Y. Zemlyanov and F. H. Ribeiro, Surface Science **600** (13), 2730-2744 (2006).
36. K. Reuter and M. Scheffler, Physical Review Letters **90** (4), 046103 (2003).
37. K. Reuter, D. Frenkel and M. Scheffler, Physical Review Letters **93** (11), 116105 (2004).
38. K. Reuter and M. Scheffler, Physical Review B **68** (4), 045407 (2003).
39. K. Reuter and M. Scheffler, Physical Review B **65** (3), 035406 (2001).
40. J. Tersoff, Physical Review Letters **61** (25), 2879-2882 (1988).
41. D. W. Brenner, Physical Review B **42** (15), 9458-9471 (1990).
42. A. C. T. van Duin, S. Dasgupta, F. Lorant and W. A. Goddard III, The Journal of Physical Chemistry A **105** (41), 9396-9409 (2001).
43. K. Chenoweth, A. C. T. van Duin and W. A. Goddard, The Journal of Physical Chemistry A **112** (5), 1040-1053 (2008).
44. K. D. Nielson, A. C. T. van Duin, J. Oxgaard, W.-Q. Deng and W. A. Goddard, The Journal of Physical Chemistry A **109** (3), 493-499 (2005).
45. J. Ludwig, D. G. Vlachos, A. C. T. van Duin and W. A. Goddard, The Journal of Physical Chemistry B **110** (9), 4274-4282 (2006).
46. C. F. Sanz-Navarro, P.-O. Astrand, D. Chen, M. Ronning, A. C. T. van Duin, T. Jacob and W. A. Goddard, The Journal of Physical Chemistry A **112** (7), 1392-1402 (2008).

47. C. F. Sanz-Navarro, P.-O. Åstrand, D. Chen, M. Rønning, A. C. T. van Duin and W. A. Goddard, The Journal of Physical Chemistry C **114** (8), 3522-3530 (2010).
48. M. R. LaBrosse, J. K. Johnson and A. C. T. van Duin, The Journal of Physical Chemistry A **114** (18), 5855-5861 (2010).
49. A. C. T. van Duin, V. S. Bryantsev, M. S. Diallo, W. A. Goddard, O. Rahaman, D. J. Doren, D. Raymand and K. Hermansson, The Journal of Physical Chemistry A **114** (35), 9507-9514 (2010).
50. T. T. Järvi, A. C. T. van Duin, K. Nordlund and W. A. Goddard, The Journal of Physical Chemistry A **115** (37), 10315-10322 (2011).
51. J. E. Mueller, A. C. T. van Duin and W. A. Goddard, Journal of Physical Chemistry C **114** (11), 4939-4949 (2010).
52. J. E. Mueller, A. C. T. van Duin and W. A. Goddard, The Journal of Physical Chemistry C **114** (12), 5675-5685 (2010).
53. A. C. T. van Duin, A. Strachan, S. Stewman, Q. Zhang, X. Xu and W. A. Goddard, The Journal of Physical Chemistry A **107** (19), 3803-3811 (2003).
54. J. Quenneville, R. S. Taylor and A. C. T. van Duin, The Journal of Physical Chemistry C **114** (44), 18894-18902 (2010).
55. A. C. T. van Duin, B. V. Merinov, S. S. Jang and W. A. Goddard, The Journal of Physical Chemistry A **112** (14), 3133-3140 (2008).
56. A. C. T. van Duin, B. V. Merinov, S. S. Han, C. O. Dorso and W. A. Goddard, The Journal of Physical Chemistry A **112** (45), 11414-11422 (2008).
57. M. Aryanpour, A. C. T. van Duin and J. D. Kubicki, The Journal of Physical Chemistry A **114** (21), 6298-6307 (2010).
58. S. Monti, A. C. T. van Duin, S.-Y. Kim and V. Barone, The Journal of Physical Chemistry C **116** (8), 5141-5150 (2012).
59. S. C. James, J. Hamilton and W. G. Wolfer, Chemical Engineering Science **68** (1), 250-257 (2012).
60. M. W. Lee, R. J. Wolf and J. R. Ray, Journal of Alloys and Compounds **231** (1–2), 343-346 (1995).
61. R. J. Wolf, M. W. Lee, R. C. Davis, P. J. Fay and J. R. Ray, Physical Review B **48** (17), 12415-12418 (1993).
62. R. J. Wolf, M. W. Lee and J. R. Ray, Physical Review Letters **73** (4), 557-560 (1994).
63. V. Lachet, A. Boutin, B. Tavitian and A. H. Fuchs, Faraday Discussions **106** (0), 307-323 (1997).
64. M. Ruda, E. A. Crespo and S. R. d. Debiaggi, Journal of Alloys and Compounds **495** (2), 471-475 (2010).
65. P. Valentini, T. E. Schwartzentruber and I. Cozmuta, Surface Science **605** (23–24), 1941-1950 (2011).
66. S. Duane, A. D. Kennedy, B. J. Pendleton and D. Roweth, Physics Letters B **195** (2), 216-222 (1987).
67. U. H. E. Hansmann, Y. Okamoto and F. Eisenmenger, Chemical Physics Letters **259** (3-4), 321-330 (1996).
68. B. Mehlig, D. W. Heermann and B. M. Forrest, Physical Review B **45** (2), 679-685 (1992).

69. B. M. Forrest and U. W. Suter, Molecular Physics **82** (2), 393-410 (1994).
70. K. Chenoweth, A. C. T. van Duin and W. A. Goddard III, Angewandte Chemie International Edition **48** (41), 7630-7634 (2009).
71. W. J. Mortier, S. K. Ghosh and S. Shankar, J. Am. Chem. Soc. **108** (15), 4315-4320 (1986).
72. A. C. T. van Duin, J. M. A. Baas and B. van de Graaf, Journal of the Chemical Society, Faraday Transactions **90** (19), 2881-2895 (1994).
73. D. Raymand, A. C. T. van Duin, M. Baudin and K. Hermansson, Surface Science **602** (5), 1020-1031 (2008).
74. N. Metropolis, A. W. Rosenbluth, M. N. Rosenbluth, A. H. Teller and E. Teller, The Journal of Chemical Physics **21** (6), 1087-1092 (1953).
75. D. Frenkel and B. Smit, *Understanding molecular simulation : from algorithms to applications*. (Academic Press, San Diego, 2002).
76. M. W. Chase and National Institute of and Technology, *NIST-JANAF thermochemical tables*. (American Chemical Society, Washington, D.C., 1998).
77. L. Verlet, Physical Review **159** (1), 98-103 (1967).
78. H. J. C. Berendsen, J. P. M. Postma, W. F. v. Gunsteren, A. DiNola and J. R. Haak, The Journal of Chemical Physics **81** (8), 3684-3690 (1984).
79. G. Kresse and J. Furthmuller, Computational Materials Science **6**, 15-50 (1996).
80. G. Kresse and J. Furthmuller, Physical Review B **54** (16), 11169-11186 (1996).
81. J. P. Perdew, J. A. Chevary, S. H. Vosko, K. A. Jackson, M. R. Pederson, D. J. Singh and C. Fiolhais, Physical Review B **46** (11), 6671 (1992).
82. G. Kresse and D. Joubert, Physical Review B **59** (3), 1758 LP - 1775 (1999).
83. H. J. Monkhorst and J. D. Pack, Physical Review B **13** (12), 5188 LP - 5192 (1976).
84. G. Henkelman, B. P. Uberuaga and H. Jonsson, J. Chem. Phys. **113** (22), 9901-9904 (2000).
85. J. H. Li, Y. Kong, H. B. Guo, S. H. Liang and B. X. Liu, Physical Review B **76** (10), 104101 (2007).
86. D. R. Lide, *Handbook of Chemistry and Physics: A Ready Reference Book of Chemical and Physical Data.* (CRC Press, New York, 2004).
87. C. Kittel, *Introduction to solid state physics*. (Wiley, Hoboken, NJ, 2013).
88. F. Birch, Physical Review **71** (11), 809-824 (1947).
89. N. E. Singh-Miller and N. Marzari, Physical Review B **80** (23), 235407 (2009).
90. S. M. Foiles, M. I. Baskes and M. S. Daw, Physical Review B **33** (12), 7983-7991 (1986).
91. V. International Conference on, M. Interstitials in and A. Seeger, (North Holland Pub. Co.; Wiley Interscience Division, John Wiley, Amsterdam; New York, 1970).
92. D. Raymand, A. C. T. van Duin, D. Spångberg, W. A. Goddard Iii and K. Hermansson, Surface Science **604** (9–10), 741-752 (2010).
93. A. G. Christy and S. M. Clark, Physical Review B **52** (13), 9259-9265 (1995).
94. S. F. Matar, G. Demazeau, M. H. Möller and R. Pöttgen, Chemical Physics Letters **508** (4–6), 215-218 (2011).
95. Y. Zhang, V. Blum and K. Reuter, Physical Review B **75** (23), 235406 (2007).

96. N. Lopez, Z. Łodziana, F. Illas and M. Salmeron, Physical Review Letters **93** (14), 146103 (2004).
97. M. Todorova, K. Reuter and M. Scheffler, Physical Review B **71** (19), 195403 (2005).
98. W. Dong, V. Ledentu, P. Sautet, A. Eichler and J. Hafner, Surface Science **411** (1–2), 123-136 (1998).
99. A. Steltenpohl and N. Memmel, Surface Science **443** (1–2), 13-18 (1999).
100. E. D. German, M. Sheintuch and A. M. Kuznetsov, The Journal of Physical Chemistry C **113** (34), 15326-15336 (2009).
101. P. Junell, K. Honkala, M. Hirsimäki, M. Valden and K. Laasonen, Surface Science **546** (2–3), L797-L802 (2003).
102. D. J. Miller, H. Oberg, L. A. Naslund, T. Anniyev, H. Ogasawara, L. G. M. Pettersson and A. Nilsson, The Journal of Chemical Physics **133** (22), 224701-224707 (2010).
103. B. Hammer, L. B. Hansen and J. K. Nørskov, Physical Review B **59** (11), 7413-7421 (1999).
104. H. Zhang, J. Gromek, G. Fernando, H. Marcus and S. Boorse, Journal of Phase Equilibria and Diffusion **23** (3), 246-248 (2002).

Chapter 3
A ReaxFF Investigation of Hydride Formation in Palladium Nanoclusters *via* Monte Carlo and Molecular Dynamics Simulations

This chapter is published as: T. P. Senftle, M. J. Janik and A. C. T. van Duin, *Journal of Physical Chemistry C* **118** (9), 4967-4981 (2014).

Abstract

Palladium can readily dissociate and absorb hydrogen from the gas phase, making it applicable in hydrogen storage devices, separation membranes, and hydrogenation catalysts. To investigate hydrogen transport properties in Pd on the atomic scale, we derived a ReaxFF interaction potential for Pd/H from an extensive set of quantum data for both bulk and surface properties. Using this potential, we employed a recently developed hybrid grand canonical-Monte Carlo/molecular dynamics (GC-MC/MD) method to derive theoretical hydrogen absorption isotherms in Pd bulk crystals and nanoclusters for hydrogen pressures ranging from 10-1 atm to 10-14 atm, and at temperatures ranging from 300 K to 500 K. Analysis of the equilibrated cluster structures reveals the contributing roles of surface, subsurface, and bulk regions during the size-dependent transition between the solid solution α phase and the hydride β phase. Additionally, MD simulations of the dissociative adsorption of hydrogen from the gas phase were conducted to assess size-dependent kinetics of hydride formation in Pd clusters. Hydrogen diffusion coefficients, apparent diffusion barriers, and pre-exponential factors were derived from MD simulations of hydrogen diffusion in bulk Pd. Both the thermodynamic results of the GC-MC/MD method and the kinetic results of the MD simulations are in agreement with experimental

values reported in the literature, thus validating the Pd/H interaction potential, and demonstrating the capability of the GC-MC and MD methods for modeling the complex and dynamic phase behavior of hydrogen in Pd bulk and clusters.

3.1. Introduction

Palladium can dissociate and absorb hydrogen from the gas phase, making it an extensively studied medium for application in hydrogen storage devices,[1-4] hydrogen separation membranes,[5-7] and hydrogenation catalysts.[8-13] Hydrogen can be incorporated in bulk palladium in two distinct PdH_x phases, called the α phase and the β phase, which differ in hydrogen concentration.[14] At low hydrogen concentrations ($\sim x<0.1$), the α phase consists of a solid solution in which hydrogen atoms occupy random interstitial octahedral sites in the fcc lattice of palladium. As the hydrogen concentration increases ($\sim x>0.6$), a transition to the β phase occurs, marked by an increase in the fcc lattice constant. The structures of the solid solution α phase and the hydride β phase only differ by the hydrogen concentration and the fcc lattice constant. This phase change displays a characteristic plateau on a pressure-composition isotherm caused by the miscibility gap (MG) separating the low concentration α phase and the high concentration β phase. The extent of the MG and its location on the pressure-composition isotherm, namely its dependence on temperature and pressure, varies between bulk and cluster systems, and is additionally affected by cluster size[15-17] and preparation method.[18] The effects of temperature, pressure, cluster size, and preparation method must be understood to optimize the design of Pd-based processes for hydrogen separation, storage, and catalysis.

Hydrogen sorption by Pd surfaces, clusters, and bulk has been investigated extensively in numerous experimental and theoretical studies.[19-36] Compared to the bulk, Pd clusters display a narrower MG characterized by an increased maximum hydrogen concentration in the α phase, a decreased minimum concentration in the β phase, and an increased slope in the isotherm-plateau connecting the phases. The MG continually narrows with decreasing cluster size,[37-39] and in some cases closes completely,[15,16] indicating that there may be a critical cluster size below which the phase change does not occur. Using x-ray diffraction (XRD), Pundt and co-workers[15] found that the phase transition occurs in 6.0 nm clusters and does not occur in 3.8 nm clusters, where both clusters were stabilized by a surfactant shell. Similarly, Konopsky *et al.*[16] demonstrated by observing photonic crystal surface waves (PC SWs) that, when supported on Ta_2O_5/SiO_2, the phase transition occurs in 6.0 nm clusters and does not occur in 2.0 nm clusters.

The existence of a MG in small clusters and the impact of surface stabilizers or supports remains an open question. Ingham *et al*.[17] measured lattice expansions via *in situ* XRD and found that the MG remains open for naked 6.1 nm, 3.0 nm, and 1.7 nm clusters supported on a weakly interacting Si/SiO_2 substrate. They contend that the increased solubility of the α phase, and thus the narrowing of the MG, is the result of surface interactions affecting the hydrogen absorption capability of the underlying bulk-like core region of the cluster, and that the nature of the surfactant, polymer, or support used to stabilize the cluster alters these surface interactions; this explains why the MG closes in studies conducted on small clusters with strongly interacting stabilizers. The impact of the cluster stabilizer is further demonstrated by Suleiman *et al.*,[18] who found that the MG in polymer stabilized clusters occurs over a wider pressure range than in the analogous

surfactant stabilized clusters, which is related to differing mechanical stain imparted on the cluster lattice by the stabilizers. Additionally, Wilde *et al.*[40] utilized a nuclear reaction analysis (NRA) technique to differentiate between hydrogen uptake in surface, subsurface, and bulk sites, showing that the increased solubility of the α phase consists of H atoms absorbed in the cluster's bulk-like core volume. This demonstrates that the narrowing of the MG in clusters cannot be attributed solely to additional surface and subsurface sites available in clusters compared to the bulk, as had been previously proposed.[37,41]

These results, among numerous others, demonstrate the complex nature of hydride formation in Pd clusters, and underscore the necessity of an atomic level understanding of the hydride formation process. Herein, we describe the development of an empirical reactive force-field, using the ReaxFF formalism,[42] for Pd/H. We have employed this potential in grand canonical Monte Carlo (GC-MC) simulations to derive theoretical hydrogen absorption isotherms in Pd bulk and clusters (sizes ranging from 1.0 nm to 2.0 nm), and have analyzed the resulting structural properties to assess the role of surface, subsurface, and bulk hydrogen adsorption sites. Additionally, we have conducted molecular dynamics simulations to investigate the initial kinetics of hydrogen uptake from the gas phase by Pd clusters, and the concentration dependence of hydrogen diffusion in bulk Pd. Together, these simulations enable us to assess both the thermodynamic and kinetic properties of hydride formation in palladium on the atomic scale. Furthermore, the Pd/H parameters developed here are fully transferable with previously developed Pd/O parameters,[43] making the future extension to Pd/O/H and Pd/C/O/H descriptions straightforward.

3.2. Theory and Methods

3.2.1. ReaxFF Potential

Empirical force-field methods, such as ReaxFF, are computationally inexpensive compared to direct quantum methods, enabling studies to reach larger length and time scales. These methods can help bridge the size gap between macroscopic experimental investigations and studies utilizing quantum calculations. The ReaxFF potential[42] is a reactive force field comprised of bond-order/bond-length relationships[44,45] combined with polarizable charge descriptions[46] to describe covalent, Coulomb, and van der Waals interactions between atoms in a system. It was originally developed to treat hydrocarbon systems,[42,47] and has been extended to model multi-phase interfaces,[48-50] including dissociative H_2 adsorption on Pt[51] and Fe.[52] ReaxFF is well suited for investigations of hydride formation in Pd, as the Pd/H parameters developed here are transferable between gas and surface species, allowing the potential to model hydrogen dissociation and absorption across the gas/surface interface.

The details of the ReaxFF potential have been described previously,[42] and are only briefly restated here. Covalent terms in the interaction potential, such as bond-energy, 3-body valence angle strain, and 4-body torsion angle strain, are calculated as an explicit function of bond order, which is in turn calculated from inter-atomic distance using the equation:

$$BO_{ij} = BO_{ij}^{\sigma} + BO_{ij}^{\pi} + BO_{ij}^{\pi\pi} = exp\left[p_{bo1}\left(\frac{r_{ij}}{r_o^{\sigma}}\right)^{p_{bo2}} \right] + exp\left[p_{bo3}\left(\frac{r_{ij}}{r_o^{\pi}}\right)^{p_{bo4}} \right] + exp\left[p_{bo5}\left(\frac{r_{ij}}{r_o^{\pi\pi}}\right)^{p_{bo6}} \right] \quad , \quad (1)$$

where BO_{ij} is the bond-order between atoms i and j, r_{ij} is inter-atomic distance, r_o terms are

equilibrium bond lengths, and p_{bo} terms are empirical parameters fit to experimental or quantum data. This bond-length/bond-order formalism produces smooth transitions between σ, π, and $\pi\pi$ bond character, and can thus be used in simulations involving bond dissociation and formation during reactive events. Additionally, electrostatic and dispersive interactions are calculated between all atom pairs from inter-atomic distances, regardless of bond-order. Electrostatic interactions are treated with a self-consistent electron equilibration method (EEM). This method determines atomic partial charges from the system configuration; the partial charges are then employed in a shielded Coulombic potential.[46] In this study, the ReaxFF parameters unique to Pd/H interactions were derived using a previously developed single-parameter optimization scheme,[53] which minimizes deviation between ReaxFF and quantum data in a training set populated with bulk, surface, and gas phase data for palladium and hydrogen. The contents of this training set and the parameter optimization process are described in Section 2.3.1.

3.2.2. Monte Carlo Method

We implement a recently developed[43] hybrid grand canonical Monte Carlo/molecular dynamics (GC-MC/MD) method to investigate hydrogen absorption in Pd clusters and bulk. For cluster simulations, the GC-MC/MD method is employed in a $TV\mu_{H2}N_{Pd}$ ensemble with constant temperature (T), volume (V), hydrogen chemical potential (μ_{H2}), and number of Pd atoms (N_{Pd}). Cluster simulations do not require a variable system volume because the cluster can expand into a surrounding vacuum space to accommodate absorbed hydrogen atoms in the metal lattice, which is not possible in

periodic bulk simulations. For periodic bulk simulations, a $TP\mu_{H2}N_{Pd}$ ensemble, with constant pressure and variable volume, is required to allow for lattice expansion upon hydrogen uptake. Hence, we have extended the previously reported GC-MC/MD method to include stochastic volume changes in a fixed pressure ensemble, similar to the GC-MC methods employed to investigate Pd/H systems by Ray and co-workers[54,55] and by Debiaggi and co-workers.[56-58] The following MC moves are available in the $TV\mu_{H2}N_{Pd}$ ensemble: (1) insertion of a hydrogen atom into the system at a random position, (2) deletion of a randomly selected hydrogen atom from the system, or (3) displacement of a hydrogen atom to a new random position in the system. The same MC moves are available in the $TP\mu_{H2}N_{Pd}$ ensemble, with the addition of a volume-change MC move that allows the system volume to cubically expand or contract by a randomly selected amount.

The following acceptance criteria, derived from detail-balance Boltzmann relationships,[59,60] were applied for atom insertion, deletion, displacement, or volume-change moves during a Monte Carlo step:

$$\mathrm{P}_{insert}^{accept} = \min\left[1, \frac{V}{\Lambda^3\left(N+1\right)}\exp\left[-\beta(E_2 - E_1 - \mu_{res})\right]\right] \quad , \tag{2}$$

$$\mathrm{P}_{delete}^{accept} = \min\left[1, \frac{N\Lambda^3}{V}\exp\left[-\beta(E_2 - E_1 + \mu_{res})\right]\right] \quad , \tag{3}$$

$$\mathrm{P}_{displace}^{accept} = \min\left[1, \exp\left[-\beta(E_2 - E_1)\right]\right] \quad , \tag{4}$$

$$\mathrm{P}_{volume}^{accept} = \min\left[1, \exp\left[-\beta\left((E_2 - E_1) + P(V_2 - V_1) - k_b T \ln\left(\frac{V_2}{V_1}\right)\right)\right]\right] \quad , \tag{5}$$

where N is the number of exchangeable atoms in the system before the MC move, Λ is the

thermal de Broglie wavelength of the exchanged atom, β is the Boltzmann factor given by $\beta = 1/(k_bT)$, E_1 and E_2 are the potential energies calculated as a function of atom configurations in the system before and after the MC move, V_1 and V_2 are the system volumes before and after a volume-change MC move, P is pressure, and μ_{res} is the chemical potential of the hydrogen reservoir. The gas phase pressures considered here are on the order of ~1 atm and are not large enough to significantly affect the bulk system volume through mechanical stress, and thus the PV term in Equation 5 is negligible. In this study, μ_{res} for hydrogen is related to T and P by the following equation:

$$\mu_{res}(T,P) = \frac{1}{2}\left[\mu_{H_2}(T,P^o) + k_b T \ln\left(\frac{P}{P^o}\right) - E_d \right] \quad , \tag{6}$$

where $\mu_{H2}(T, P^o)$ is the experimentally determined chemical potential of H_2 at T and P^o available from published thermodynamic tables,[61] and E_d is the zero-Kelvin bond dissociation energy of H_2. Since the Pd/H ReaxFF parameters were derived from DFT-PW91 values for hydrogen adsorption energies that were calculated relative to gas phase H_2, the DFT-PW91 H_2 dissociation energy of 105.1 kcal mol^{-1} was used for E_d to remain consistent with the DFT values used for ReaxFF training. We note that the PW91 functional used here yields values for hydrogen binding that are typically higher than those observed experimentally,[20,21,32,35] which will shift palladium hydride phase boundaries predicted by our GC-MC/MD method to lower hydrogen pressures. This systematic error does not affect qualitative conclusions drawn from the results presented herein, but must be taken into account for quantitative comparisons to experimental values. The relative extent and impact of this deviation is discussed in detail in Section 2.3 where appropriate.

As discussed in a previous publication,[43] the GC-MC/MD method introduces a

MD-based energy minimization step after each MC trial move to allow a structural relaxation in the system prior to applying the acceptance criteria in Equations 2-5. This additional step reduces the number of MC iterations required to reach equilibrium compared to pure GC-MC simulations; the energy minimization step prevents hydrogen atoms from being placed in high energy locations occupied by metal atoms, thus increasing MC acceptance rates. Here, we employ a conjugate gradient (CG) relaxation of forces, with a convergence criterion of 0.5 kcal mol^{-1} between subsequent CG steps. The 0.5 kcal mol^{-1} convergence criteria was selected because it is tight enough to prevent inserted H atoms from being placed within the atomic radius of any Pd atom, and is loose enough to converge in a reasonable timeframe. Tighter and looser convergence criteria impact the computational time required for the MC run to reach equilibrium, but do not significantly impact the final equilibrium values.

3.2.3. Quantum Method

The Vienna *ab initio* simulation package (VASP) was employed for all density functional theory (DFT) calculations.[62,63] The generalized gradient approximation (GGA) was used to treat the exchange-correlation functional, as implemented by the Perdew-Wang formulation (PW91).[64] Plane-wave basis sets were employed in all calculations, and were truncated at 450 eV for periodic surface calculations and 725 eV for bulk calculations. The atomic force convergence criterion for all structural optimizations was 0.05 eV $Å^{-1}$. The projector augmented wave method[65] (PAW) was employed to represent core electron regions with valence configurations of $4d^{10}$ for Pd atoms and $1s^1$ for H atoms. The

Monkhorst-Pack[66] (MP) Brillouin zone sampling method was utilized for periodic calculations. Pd surface calculations used a *3×3×1* MP k-point spacing in a 4-layer *3×3* periodic cell with a 20 Å vacuum layer separating images perpendicular to the surface. The bottom two Pd layers were fixed during structural optimizations, while the top two surface layers were allowed to relax. A *7×7×7* MP k-point spacing was used for bulk PdH_x calculations with a *2×2×2* fcc lattice in a triclinic $\alpha = \beta = \gamma = 60^{o}$ unit cell (containing 8 Pd atoms, and x=1 to x=8 H atoms). Cluster and molecule calculations were conducted in a *45*Å × *45*Å × *45*Å periodic box, in which the Γ point was considered. The climbing image nudged elastic band (CI-NEB) method[67] was used to identify transition states for hydrogen migration.

3.3. Results and Discussion

3.3.1. Pd/H Force-field Development

A DFT training set consisting of bulk formation energies, surface adsorption energies, and transition state barriers was used to optimize the Pd/H interaction parameters shown in Table 3-1. These parameters were used in conjunction with previously published Pd/Pd[43] and H/H[50] interaction parameters, which are also provided in Table 3-1. The ReaxFF general parameters and the entire Pd/H parameter set are provided in ReaxFF input format in the Supporting Material online. Again, the Pd/H parameters provided here are fully transferable with the previous Pd/O parameter set,[43] which will allow for the direct extension to a Pd/O/H description.

Table 3-1. ReaxFF Parameters for Pd/H Interactions.

Atom	r_o	η	χ	γ	r_{vdW}	ϵ_{vdw}	α	γ_{vdW}	$p_{ov/un}$
Pd[a]	1.8582	6.6477	5.5005	1.0000	2.0113	0.2465	12.57	6.008	-13.00
H[b]	0.8930	9.6093	3.7248	0.8203	1.3550	0.0930	8.22	33.289	-19.45

Bond	D_e^σ	$p_{be,1}$	p_{cov}	$p_{be,2}$	$p_{bo,1}$	$p_{bo,2}$
Pd-Pd[a]	90.7003	-0.1661	0.2578	3.0618	-0.0914	5.4665
H-H[b]	153.3934	-0.4600	0.7300	6.2500	-0.0790	6.0552
Pd-H	67.5406	0.6327	0.2077	0.7493	-0.0547	4.0000

Off-Diagonal	r^σ	R_{vdW}	γ	ϵ^σ
Pd-H	1.5714	1.1103	13.0000	0.1445

Angle	θ_o	k_a	k_b	$p_{val,1}$	$p_{val,2}$
Pd-Pd-H	40.0354	9.2882	8.0000	1.0000	2.7288
Pd-H-Pd	0.9367	12.0943	6.6344	1.0000	1.0115
H-Pd-H	25.6680	10.1984	7.6844	1.0000	1.2474
Pd-H-H	83.9156	13.0474	0.9983	1.0000	3.1381

a) Palladium atom parameters from Ref. [43] ; b) Hydrogen parameters from Ref. [50]

b) units: r terms in $Å$;γ terms in $Å^{-1}$; ϵ, D and k_a in kcal mol^{-1}; η and χ in eV; θ in degrees; k_b in (1/radians)^2 ; all other terms are dimensionless

Bulk Hydride. The ReaxFF potential was trained to reproduce hydrogen adsorption behavior in bulk palladium. Palladium readily forms two phases upon exposure to hydrogen: a low concentration α phase and a high concentration β phase. Both phases consist of H atoms absorbed interstitially in Pd fcc-octahedral sites, and vary only in concentration and fcc lattice parameter. The Pd/H interaction parameters were trained to correctly reproduce bulk properties related to this phase behavior. The potential was trained to reproduce lattice expansion upon hydride formation by fitting against a DFT energy-volume curve for two stoichiometric PdH structures, shown in Figure 3-1. One is the energetically favored NaCl-type structure, in which H atoms occupy octahedral sites in a fcc Pd lattice. The other is a simple cubic structure, where a single H atom is placed in the center of a cubic Pd unit cell. Although the cubic structure is high in energy and is not experimentally realizable, it is included to diversify the ReaxFF training set to ensure that

the potential does not improperly favor such high energy structures. For the NaCl-type structure, ReaxFF predicts an equilibrium lattice spacing of 4.24 Å and a corresponding formation energy of -2.56 kcal mol^{-1}, compared to our DFT values of 4.15 Å and -3.04 kcal mol^{-1} and the DFT values reported by Grönbeck and Zhdanov[34] of 4.11 Å and -5.3 kcal mol^{-1}. The equilibrium lattice spacing predicted by DFT for the high concentration β phase is longer than the experimental[17,31] value of ~4.02 Å. This variation can be attributed to the PW91 functional, which yields an elongated Pd fcc lattice spacing of 3.97 Å compared to the experimental[68] value of 3.89 Å. To account for phase behavior arising from varying hydrogen concentrations, the potential was additionally optimized against DFT formation energies for bulk PdH_x with x ranging from 0.125 to 1.0, where the formation energy is calculated relative to gas phase H_2 and a PdH_0 bulk where all H atoms have been removed (*i.e.* an expanded Pd-fcc lattice). The results, shown in Figure 3-2, demonstrate good agreement between ReaxFF and DFT. Both ReaxFF and DFT predict that the formation energy remains near -9 kcal mol^{-1} for concentrations less than x=0.5, and that the formation energy becomes significantly less favorable as additional hydrogen is added to the Pd lattice.

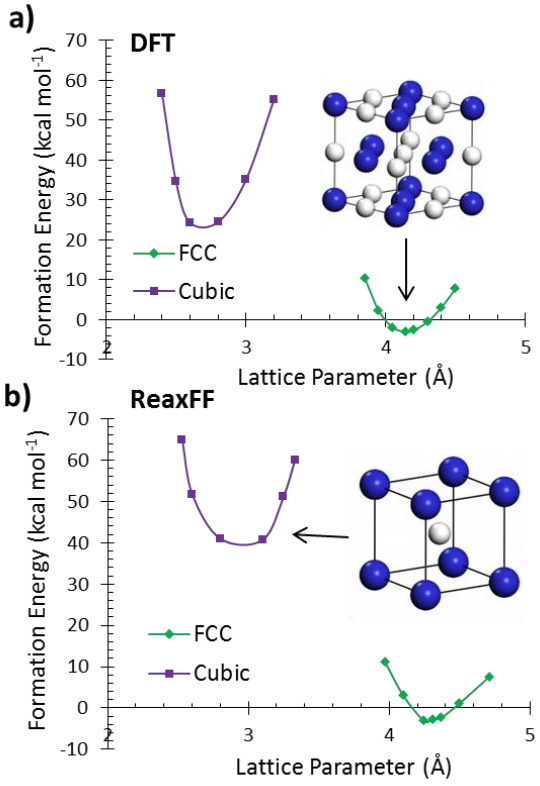

Figure 3-1. Bulk lattice expansion-compression curves for fcc and cubic PdH phases calculated with (a) DFT and (b) ReaxFF. (Insets) The structures of the (a) NaCl-type PdH phase and the (b) cubic PdH phase.

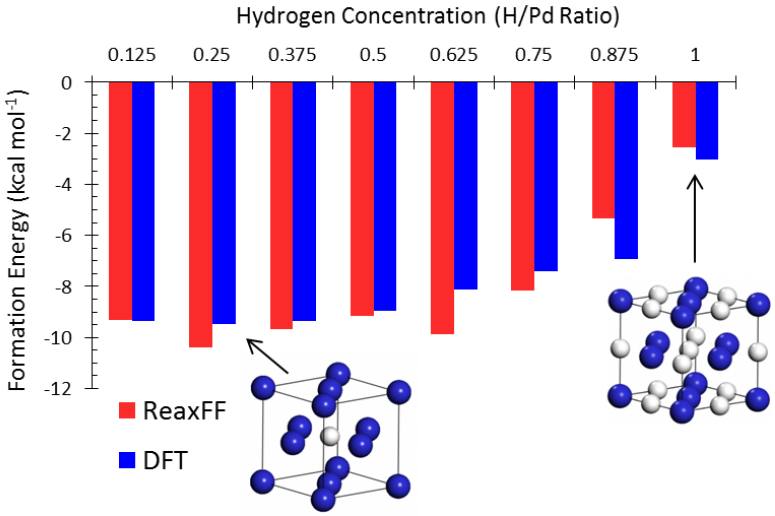

Figure 3-2. DFT and ReaxFF PdH_x formation energies for hydrogen concentrations varying from x=0.125 to x=1. Energies are calculated relative to the PdH_x (x = 0) structure (*i.e.* – an expanded Pd-fcc structure) and gas phase hydrogen.

Surface Adsorption Energies. The Pd/H interaction parameters were optimized for hydrogen adsorption on Pd(111), Pd(110), and Pd(100) surface and subsurface sites. Adsorption energies were calculated relative to the clean surface and a gas phase H_2 molecule:

$$E_{ads} = E_{clean} + N_H\,(\tfrac{1}{2}\,E_{H2}) - E_{H/Pd\text{-}surf} \quad , \tag{7}$$

where E_{clean} is the energy of the clean Pd surface, N_H is the number of H atoms in the cell, E_{H2} is the energy of a gas phase H_2 molecule, and $E_{H/Pd\text{-}surf}$ is the energy of the H-adsorbed surface. Adsorption models including one adsorbed H atom resulted in a 0.11 mono-layer (ML) coverage in the 3×3 periodic cell. We also included surface models with two H atoms adsorbed in adjacent hollow sites, resulting in a 0.22 ML coverage. This ensures that the potential can properly describe interactions between adsorbed hydrogen atoms on the Pd surface, allowing the potential to properly describe variable hydrogen coverages.

The resulting adsorption data, summarized in Figure 3-3, demonstrate the feasibility of the ReaxFF potential for describing hydrogen adsorption on Pd surface, subsurface, and bulk sites. At 0.11 ML, the potential yields binding energies of 16.15 kcal mol^{-1} and 16.82 kcal mol^{-1} for adsorption in fcc and hcp hollow sites, respectively, compared to the DFT values of 17.67 kcal mol^{-1} and 16.54 kcal mol^{-1}. There is a repulsive interaction between H atoms adsorbed in adjacent fcc-fcc or hcp-hcp sites, reflected by lower binding energies per H atom; the respective ReaxFF adsorption energies are 28.36 kcal mol^{-1} (14.18 kcal mol^{-1} per H atom) and 28.35 kcal mol^{-1} (14.17 kcal mol^{-1} per H atom). These energies are in agreement with our respective DFT values of 30.72 kcal mol^{-1} and 30.71 kcal mol^{-1}, and with those reported by Lopez *et al.*[32], who calculated DFT-PW91 adsorption energies for fcc hollow sites of 15.45 kcal mol^{-1} and 28.59 kcal mol^{-1} (14.29

kcal mol^{-1} per H atom) at 0.22 ML and 0.66 ML coverage, respectively. As stated in Section 2.2.2, the PW91 functional generally over-binds hydrogen on the Pd surface compared to experimental data, which is evident in the experimental fcc hollow site binding energies of 10.75 kcal mol^{-1} per H atom at low coverage and 9.23 kcal mol^{-1} per H atom at high coverage.[20,21] This systematic error is on the order of ~5 kcal mol^{-1}, and can be empirically corrected by adjusting the ground state energy of H_2 to fit experimental data. We did not apply this correction, since a change in the gas phase H_2 energy reference will not affect qualitative adsorption trends.

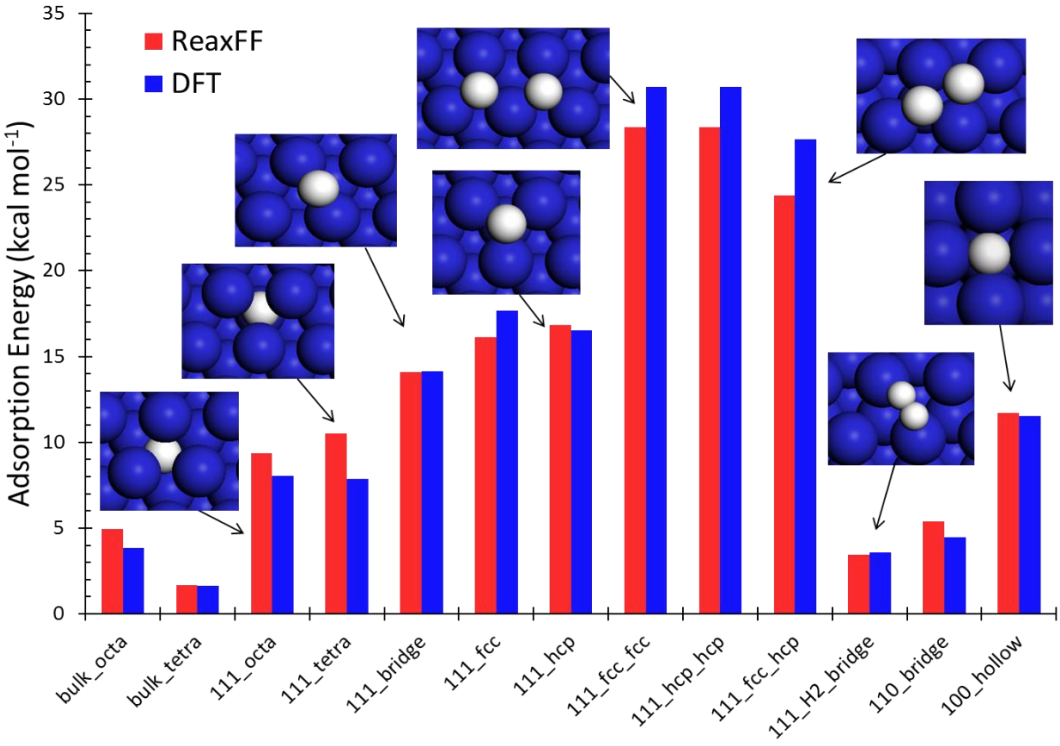

Figure 3-3. Hydrogen adsorption energies in Pd bulk and on Pd(111), Pd(110), and Pd(100) surfaces. (Insets) Optimized structures for H adsorption at the indicated surface sites.

Dissociation and Migration Barriers. In order to model the kinetic properties of hydride formation, the ReaxFF potential was trained to reproduce DFT-NEB barriers for hydrogen dissociation, surface to subsurface migration, and bulk diffusion. The ReaxFF potential energy surfaces for these processes are shown in Figure 3-4. As seen in Figure 3-4(a), ReaxFF predicts that H_2 dissociation on the Pd(111) surface proceeds through a physisorbed H_2 precursor state that has an adsorption energy of 7.81 kcal mol^{-1} relative to the gas phase, which precedes a dissociation barrier of 4.93 kcal mol^{-1}. The stability of the H_2 physisorbed state is reflected in the DFT data shown in Figure 3, in which we identified a local energy minimum for H_2 adsorption on a bridge site. This dissociation path is in qualitative agreement with the DFT-PW91 dissociation path reported by Lopez *et al*.[32] and reproduced in Figure 3-4(a), which shows a precursor state with an adsorption energy of 7.1 kcal mol^{-1} and a corresponding dissociation barrier of 2.1 kcal mol^{-1}. Figure 3-4(b) shows the ReaxFF barrier for H migration from a surface fcc hollow site to a subsurface octahedral site. ReaxFF predicts a subsurface diffusion barrier of 11.71 kcal mol^{-1}, in agreement with our DFT barrier of 10.42 kcal mol^{-1}. Finally, the potential was trained to reproduce the diffusion barrier for H migration in bulk Pd from an octahedral site to a tetrahedral site. The potential predicts adsorption energies of 4.95 kcal mol^{-1} and 1.67 kcal mol^{-1} in bulk octahedral and tetrahedral sites, respectively, in agreement with the respective DFT values of 3.86 kcal mol^{-1} and 1.64 kcal mol^{-1}. As seen in Figure 3-4, the potential yields a barrier of 6.38 kcal mol^{-1}, in agreement with the DFT barrier of 5.12 kcal mol^{-1}. These data for adsorption and migration in bulk Pd are also in agreement with the DFT barrier of 5.07 kcal mol^{-1} reported by Grönbeck and Zhdanov,[34] and the experimental diffusion barrier of 5.85 kcal mol^{-1} reported by Hara *et al.*[28] Together, the agreement

between ReaxFF and DFT for surface and bulk data demonstrates the Pd/H potential's ability to properly model hydrogen dissociation and migration on the Pd surface, migration from Pd surface sites to subsurface sites, and diffusion in bulk Pd.

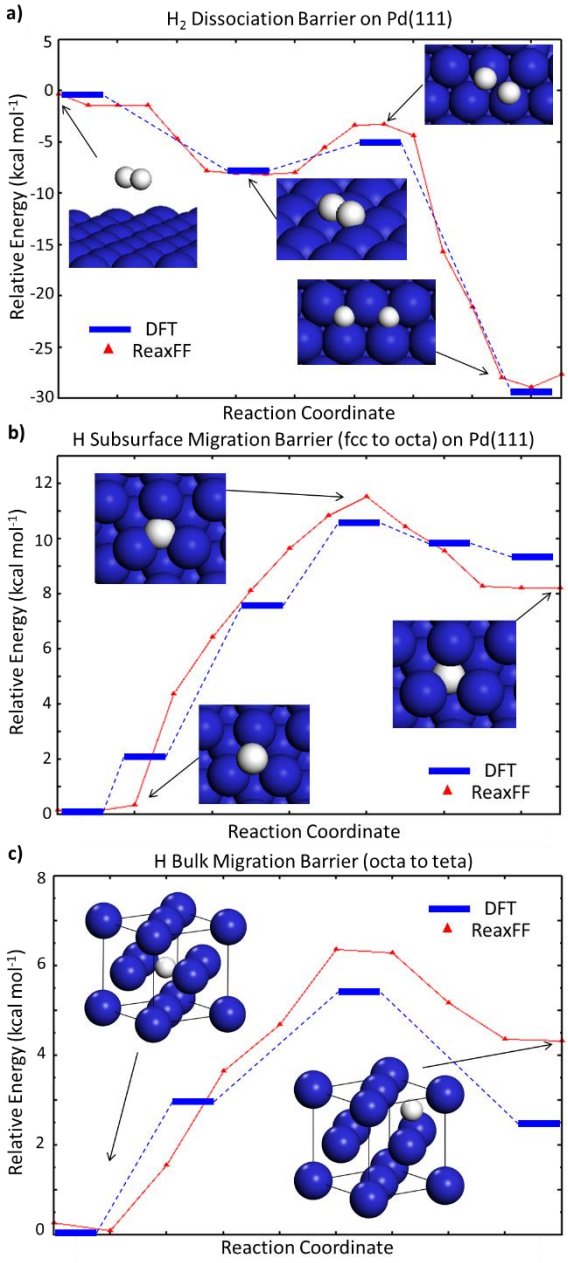

Figure 3-4. DFT (blue) and ReaxFF (red) activation barriers for (a) H_2 dissociation on the Pd(111) surface (DFT potential energy surface reproduced from Ref.[32]), (b) H migration from a Pd(111) surface fcc site to a subsurface octahedral site, and (c) H migration from an octahedral site to a tetrahedral site in the bulk. (Insets) Initial structures, transition states, and final structures.

3.3.2. Monte Carlo Simulations of Palladium Hydride Formation

We applied the optimized Pd/H potential in GC-MC/MD simulations to assess the extent of hydrogen uptake in Pd bulk and clusters as a function of hydrogen pressure and temperature. Each Pd cluster simulation began with a clean Pd cluster in a $50\text{Å}\times50\text{Å}\times50\text{Å}$ simulation box. Three spherical Pd cluster models of varying size were studied, and were constructed from the optimized fcc bulk structure. The clusters were approximately 1.0 nm, 1.5 nm, and 2.0 nm in diameter, and consisted of 43, 135, and 321 Pd atoms, respectively. A geometry optimization of the Pd clusters prior to the GC-MC/MD simulations was not necessary, as hydrogen induced restructuring of the cluster will occur during the MD relaxation steps of the simulation. Bulk simulations were initiated from an orthogonal fcc lattice consisting of 108 Pd atoms with an optimized Pd-Pd lattice spacing. The GC-MC/MD algorithm added, moved, and removed hydrogen atoms until the system reached thermodynamic equilibrium, at which point the chemical potential of hydrogen in the simulation box and the hydrogen reservoir are equal. For cluster simulations, equilibrium is reached when the system energy and the number of hydrogen atoms converges, as seen in Figure 3-5(a). Figure 3-5(b) shows the same equilibration for bulk simulations, in which the system volume must also converge. As seen in the figure, the MC simulations typically required between 5,000 and 10,000 MC iterations to converge, and were considered converged if the total energy fluctuation normalized by the number of Pd atoms in the system was less than ~5 kcal mol^{-1} over the final 1000 MC iterations. The converged system reflects the equilibrium hydrogen concentration and phase structure at the temperature and pressure specified by the chemical potential of the hydrogen reservoir.

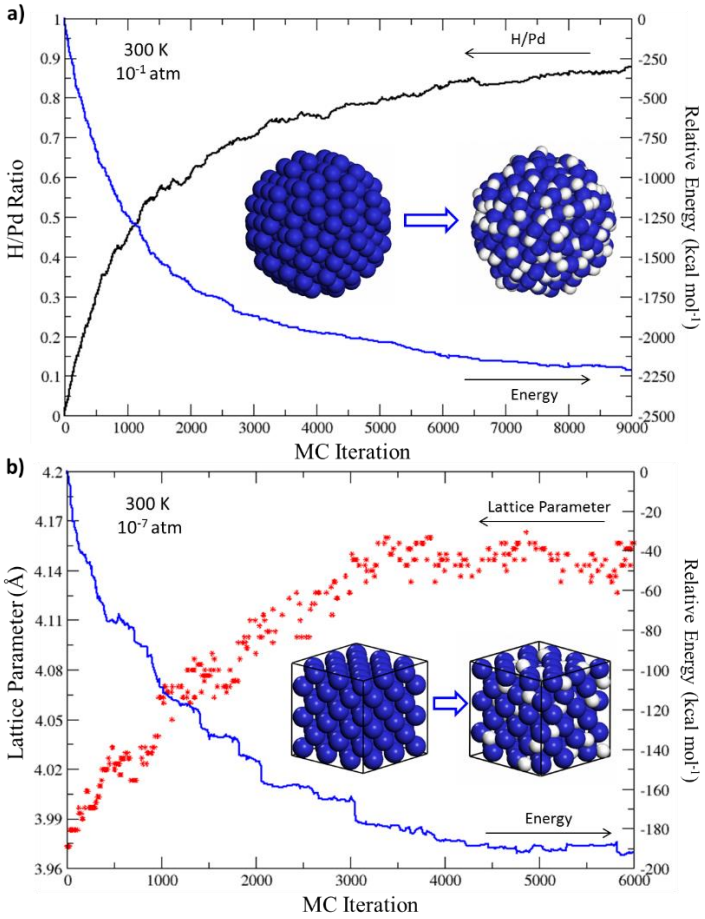

Figure 3-5. Equilibration of GC-MC/MD with (a) varying H/Pd ratio in a 2.0 nm Pd cluster at 300 K and 10^{-1} atm, and with (b) varying volume in Pd bulk at 300 K and $P_{H2} = 10^{-7}$ atm.

Surface, Subsurface, and Bulk Hydrogen Loading. The GC-MC/MD method was used to assess the degree of hydrogen loading at surface, subsurface, and bulk-like sites in the Pd clusters. For each cluster, GC-MC/MD simulations were conducted at 300 K and at pressures ranging from 10^{-14} atm to 10^{-1} atm. We analyzed the final structure of each simulation to assess the degree of hydride formation in the surface, subsurface, and bulk-like regions of the Pd cluster as a function of hydrogen pressure. First, we calculated the radial distribution of hydrogen atoms in each cluster from the final atomic coordinates of the equilibrated system. Figure 3-6 shows the local density of hydrogen atoms as a function

of radial distance from the center (r=0) of a 2.0 nm cluster at varying H_2 pressures. As expected, the H/Pd ratio progressively increases as the hydrogen pressure is increased; surface sites are first occupied at low hydrogen pressures, followed by subsurface sites, and then bulk sites. The figure shows the onset of hydrogen uptake in the bulk-like region of the cluster at 10^{-11} atm, and the formation of the hydride phase by 10^{-9} atm. This demonstrates the enhanced hydrogen binding of the Pd surface compared to the bulk, in agreement with experimental results[37,69] and with previous MC results obtained by Wolf *et al.*[55] and by Ruda *et al.*[57]

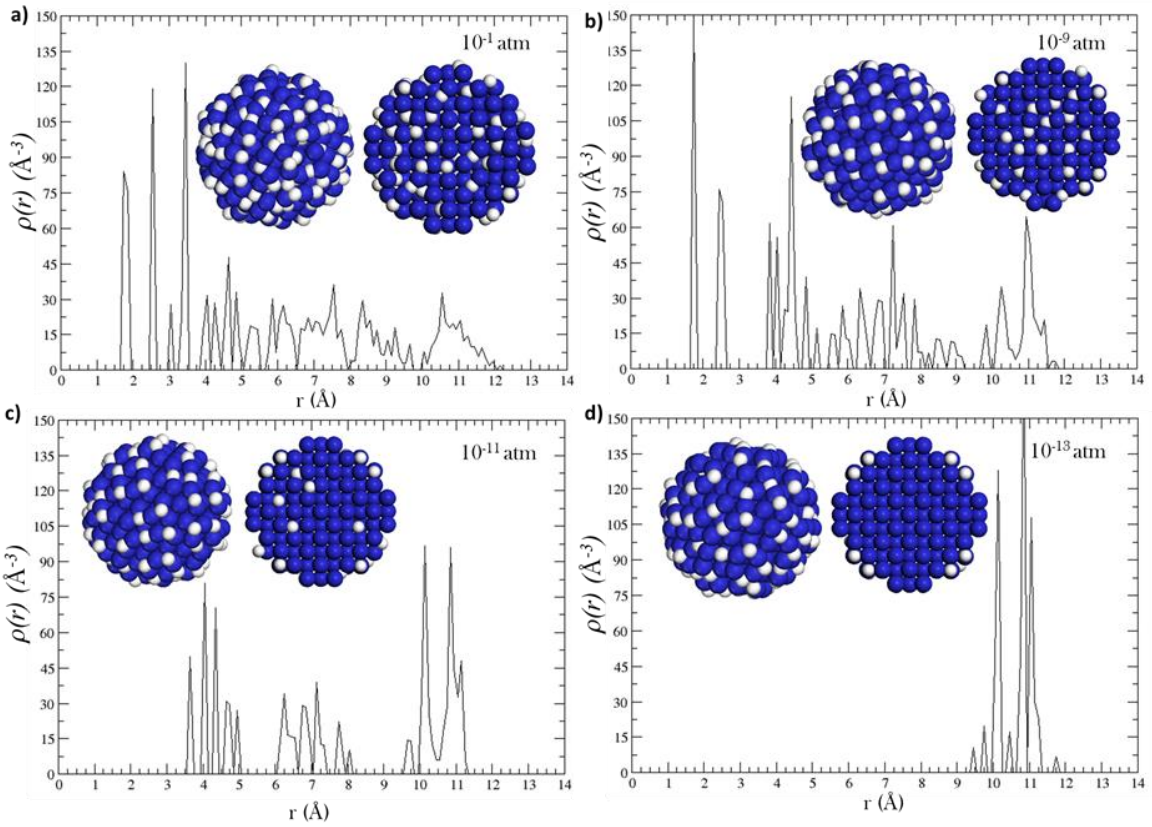

Figure 3-6. Final structure and local hydrogen densities relative to the center of the Pd cluster after GC-MC/MD simulations at T = 300 K and P = (a) 10^{-1} atm, (b) 10^{-9} atm, (c) 10^{-11} atm, and (d) 10^{-13} atm. (Insets) Whole structure (left) and cross section (right) of the final cluster structures after GC-MC/MD.

To further assess whether a phase transition occurs in the cluster, we determined the number of hydrogen atoms in the surface and bulk-like regions of the cluster by radially integrating the local hydrogen densities. This results in the data shown in Figure 3-7, which shows the total number of hydrogen atoms within a specified radius from the cluster center. As seen in the figure, there is a clear distinction between hydrogen loading in the bulk-like region and the surface regions. The distinction between surface and subsurface regions is less clear due to the fact that the cluster models are not perfectly spherical and contain corner, edge, and facet sites that slightly vary in distance from the cluster center, which can be seen in the insets of Figure 3-7. This makes it difficult to distinguish between atoms adsorbed in the subsurface layer and atoms adsorbed on surface sites that are closer to the cluster center. Nevertheless, there is still a clear distinction between the bulk and surface regions, which is demonstrated by the pronounced increase in the number of hydrogen atoms near the surface of each cluster, marked by a dashed line in the figure. Using this distinction, the H/Pd ratio in the bulk-like region of each cluster can be determined as a function of pressure, thus deriving absorption isotherms that reflect hydrogen uptake in the cluster's bulk-like region. This allows for the varying phase behaviors of the bulk and surface regions to be assessed independently, as will be discussed in the following section.

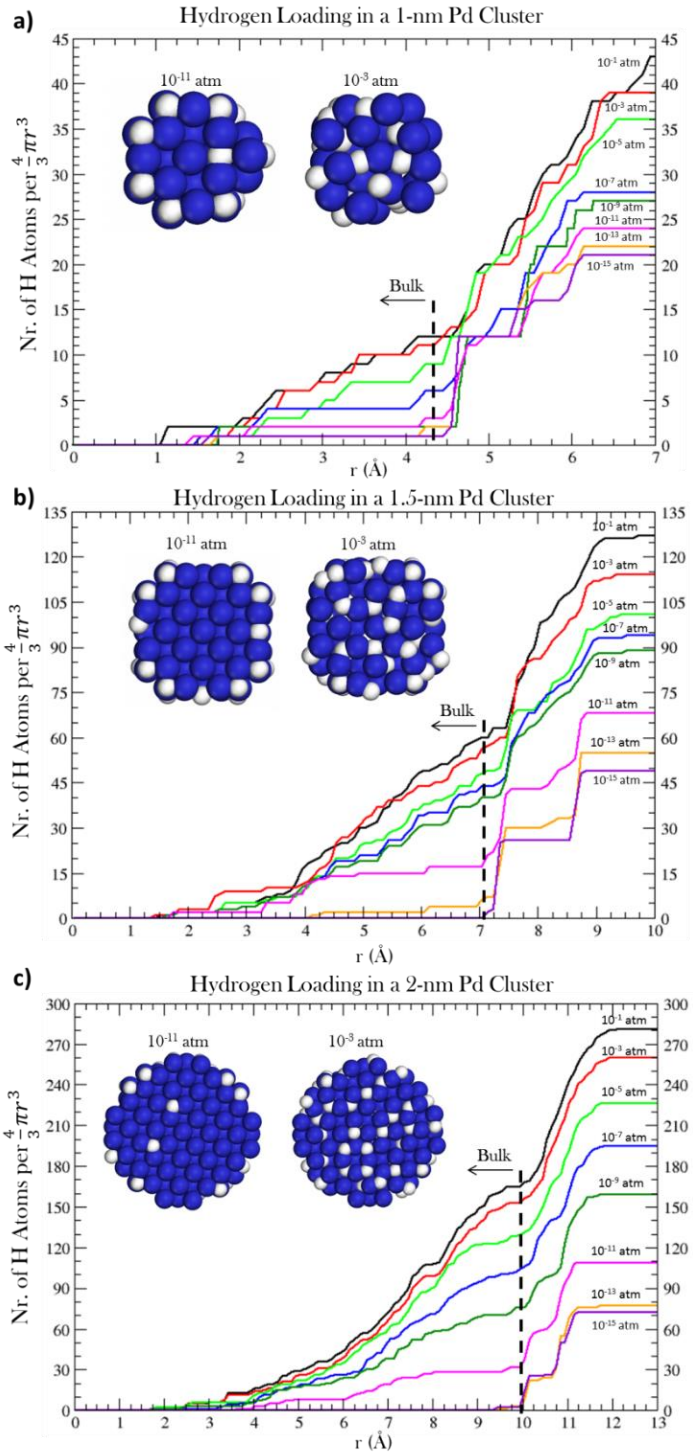

Figure 3-7. Radial distribution of hydrogen atoms in (a) a 1.0 nm Pd cluster, (b) a 1.5 nm Pd cluster, and (c) a 2.0 nm Pd cluster after GC-MC/MD simulations at 300 K and at $P = 10^{-15}$ atm (purple), $P = 10^{-13}$ atm (orange), $P = 10^{-11}$ atm (magenta), $P = 10^{-9}$ atm (dark green), $P = 10^{-7}$ atm (blue), $P = 10^{-5}$ atm (light green), $P = 10^{-3}$ atm (red), $P = 10^{-1}$ atm (black). (Insets) Cross section of the center of the cluster exposing a (100) facet after GC-MC/MD at 10^{-11} atm and 10^{-3} atm.

Hydrogen Absorption Isotherms. Hydrogen absorption isotherms are shown in Figure 3-8(a) for bulk simulations at varying temperatures, and in Figure 3-8(b-c) for cluster simulations with varying cluster sizes. As seen in Figure 3-8(a), the bulk simulations yield a clear plateau characteristic of the α to β phase transition at 300 K, 400 K, and 500 K. At 300 K, the simulations yield a maximum H/Pd ratio in the α phase, α_{max}, of 0.02, and a minimum H/Pd ratio in the β phase, β_{min}, of 0.54, in agreement with the respective experimental values of α_{max} = 0.03 and β_{min} = 0.55 reported by Yamauchi *et al.*[22] for hydrogen uptake in Pd-black at 303 K. At 400 K and 500 K, α_{max} increases to 0.06 and 0.07, respectively, and β_{min} decreases to 0.50 and 0.47, respectively. This qualitatively reproduces the experimentally observed MG narrowing with increasing temperature. We note that the isotherm-plateau predicted by ReaxFF occurs at pressures much lower than those determined experimentally,[22,26] which is caused by the over-prediction of the hydrogen binding energy noted in the previous sections. At 300 K, the GC-MC/MD method predicts a plateau at P_{H2} ~5.5×10^{-11} atm, as opposed to the experimentally observed plateau near ~10^{-3} atm. Using Equation 6, these two hydrogen pressures at 300 K result in chemical potentials of μ_H= -63.2 kcal mol^{-1} and μ_H= -58.3 kcal mol^{-1}, respectively. This is within the ~5 kcal mol^{-1} over-binding error of the DFT-PW91 method used to train the ReaxFF potential, thus accounting for the discrepancy in plateau pressures. As stated above, the disparity between the hydrogen binding energies predicted by ReaxFF and experiment is the result of a systematic error in the hydrogen energy reference, and does not impact relative trends in hydrogen binding.

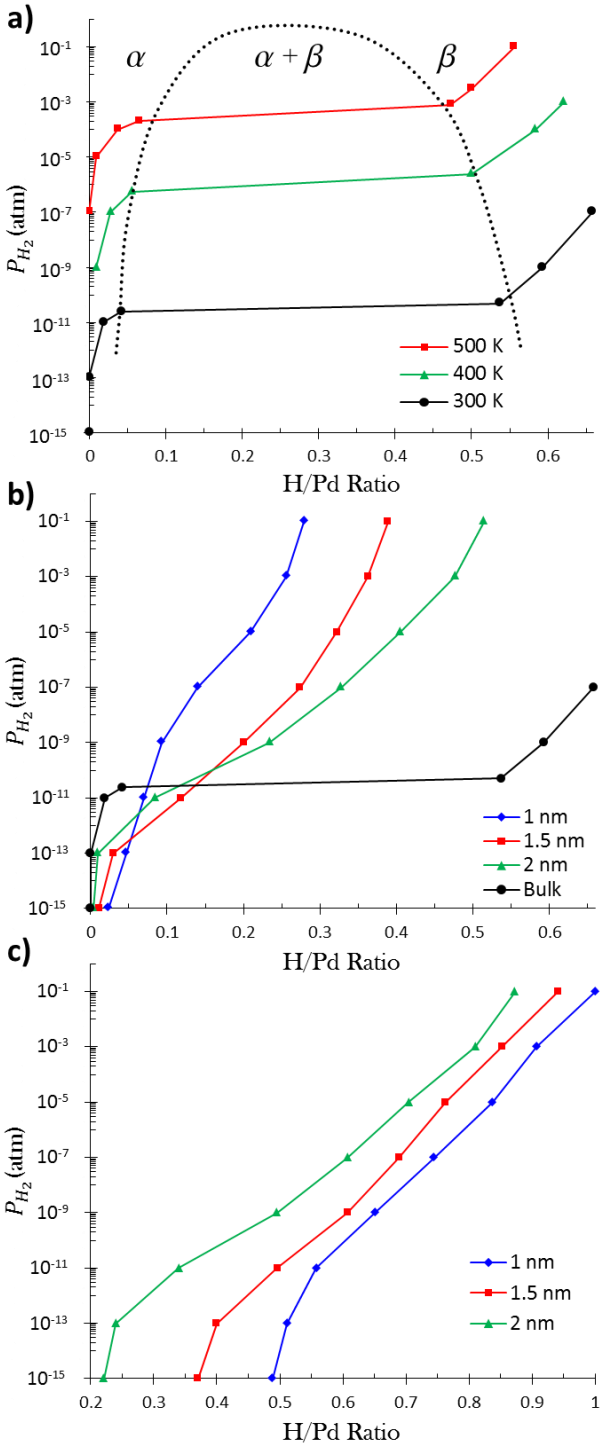

Figure 3-8. Hydrogen absorption isotherms for (a) Pd bulk, (b) the bulk-like region of Pd clusters at 300 K, and (c) the entire Pd cluster (including hydrogen in both bulk and surface regions) at 300 K. The dashed line in (a) is an estimated delineation of the α-β phase boundary.

Absorption isotherms for 1.0 nm, 1.5 nm, and 2.0 nm Pd clusters are shown in Figure 3-8(b-c). The H/Pd ratios shown in Figure 3-8(b) were derived using the radial distribution data shown in Figure 3-7, and reflect the number of hydrogen atoms in the bulk-like region of the cluster divided by the total number of Pd atoms in the cluster. The clusters display an increased hydrogen concentration in the solid solution α phase, and a decreased hydrogen concentration in the hydride β phase compared to the bulk. As cluster size decreases, the α phase concentration increases and the β phase concentration decreases, resulting in a narrowed MG and a sloped plateau connecting the phases, in agreement with experimental observations.[15,22,26,37] Although the cluster plateaus are sloped and narrowed compared to the bulk, each plateau retains a clear inflection point indicative of a α to β phase transition. Figure 3-8(c) shows the total H/Pd ratios, which reflect hydrogen uptake by both the surface and bulk-like regions of each cluster. As seen in the figure, there is a high affinity for adsorption on the cluster surface, making it difficult to discern the isotherm-plateau behavior observed in the bulk-like region. This suggests that the cluster surface becomes saturated with adsorbed hydrogen at low hydrogen pressures, and the surface remains covered despite any phase transition in the bulk-like region below. Figure 3-8(b) correspondingly shows that the phase transition occurs in the bulk-like region of the clusters, indicating that the narrowing MG with decreasing cluster size is not simply the result of an increased ratio of surface to bulk sites, in agreement with the experimental observations of Eastman *et al.*[31] and of Wilde *et al.*[40]

Lattice Expansion. In addition to an increased H/Pd ratio, the α to β transition is principally marked by an increased Pd-Pd lattice spacing. To investigate this behavior, we determined the average Pd-Pd lattice spacing for each cluster as a function of hydrogen

pressure, as shown in Figure 3-9. This was accomplished by calculating the Pd-Pd radial pair distribution function, *g(r)*, from the final atomic coordinates of the equilibrated GC-MC/MD cluster simulations. As seen in the figure, the peaks in the pair distribution function retain the characteristic fcc lattice spacing of the clean cluster, and broaden at higher hydrogen pressures. As such, the equilibrium fcc lattice spacing was approximated by taking the weighted average over the first *g(r)* peak. The resulting lattice spacings, shown in Figure 3-9, demonstrate a discernible increase in the fcc lattice constant as H_2 pressure increases, indicating that the phase transition occurs in all three clusters. The maximum lattice spacing of the α phase increases and the minimum lattice spacing of the β phase decreases with decreasing cluster size. This is in agreement with the experimental XRD trend in lattice expansion reported by Ingham *et al.*,[17] who likewise found that the phase transition occurs in naked clusters that are as small as ~1.7 nm in diameter. The lattice parameters for bulk simulations are also summarized in Table 3-2, which contains the minimum and maximum lattice parameters obtained for the α and β phases at 300 K, 400 K, and 500 K. The minimum bulk lattice parameter of the β phase decreases with increasing temperature, indicating the closure of the MG as the system approaches the critical temperature. As expected, the maximum and minimum lattice parameters in the clusters approach the values obtained for the bulk as cluster size increases.

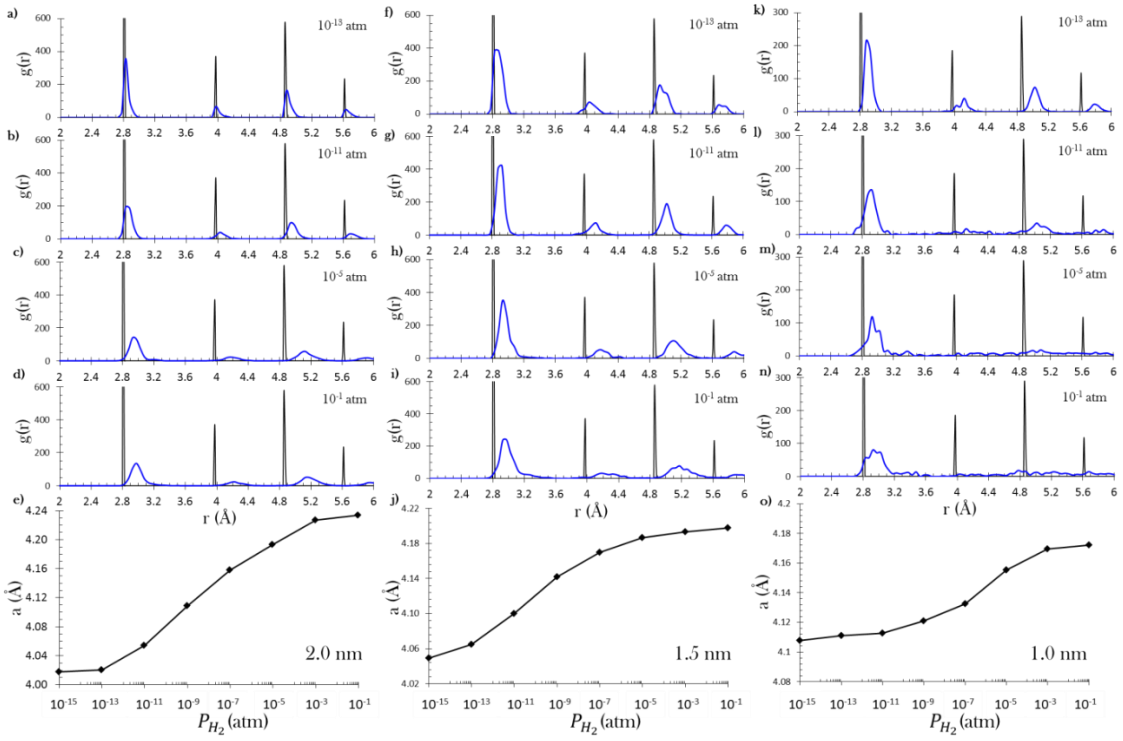

Figure 3-9. Pd-Pd pair distribution functions, *g(r)*, after GC-MC/MD equilibration in a (a-d) 1.0 nm cluster, a (h-i) 1.5 nm cluster, and a (m-n) 2.0 nm cluster. The *g(r)* represented by a black line corresponds to the Pd-Pd pair distribution of the clean cluster prior to GC-MC/MD. (e,j,o) Average fcc lattice constants derived from pair distribution functions for (e) the 1.0 nm cluster, (j) the 1.5 nm cluster, and (o) the 2.0 nm cluster.

Table 3-2. Maximum and minimum recorded H/Pd ratios and lattice parameters in bulk simulations at 300 K, 400 K, and 500 K.

300 K	**P_{H2} (atm)**	**H/Pd Ratio**	**Lattice Parameter (Å)**
α	1×10^{-13}	0.0	3.97
α_{max}	2.4×10^{-11}	0.02	3.99
β_{min}	5×10^{-11}	0.54	4.15
β	1×10^{-1}	0.88	4.24
400 K	**P_{H2} (atm)**	**H/Pd Ratio**	**Lattice Parameter (Å)**
α	1×10^{-9}	0.0	3.97
α_{max}	5.5×10^{-7}	0.06	3.99
β_{min}	2.5×10^{-6}	0.51	4.13
β	1×10^{-1}	0.66	4.18
500 K	**P_{H2} (atm)**	**H/Pd Ratio**	**Lattice Parameter (Å)**
α	1×10^{-7}	0.0	3.97
α_{max}	2×10^{-4}	0.07	3.99
β_{min}	8×10^{-4}	0.47	4.12
β	1×10^{-1}	0.56	4.16

Discussion. These results help clarify the role of surface and bulk-like regions during hydride formation in Pd clusters. We observe that the phase transition occurs in the bulk-like region of Pd clusters, and that the MG remains open for naked clusters as small as 1.0 nm in diameter. This supports the conclusion of both Wilde *et al.*,[40] who found that the enhanced hydrogen uptake in the solid solution phase occurs in the bulk-like region (as opposed to at surface sites), and with Eastman *et al.*,[31] who found that the narrowing MG in clusters cannot be attributed to a varying phase behavior in the surface/subsurface region. It also supports the conclusions of Ingham *et al.*,[17] who argue that the closing of the MG in small clusters reported in the literature[15,16] is the result of surface strain affecting absorption in the bulk-like region of the clusters.

Our results show that the surface of the Pd cluster becomes saturated with hydrogen even at low pressures, and that the experimental trends related to cluster size are retained when these sites are excluded from the absorption isotherms, indicating that the size-dependent absorption behavior is associated with the bulk-like region of the cluster, in agreement with Wilde *et al*.[40] Although increased uptake occurs in the cluster bulk, it can be attributed to the effects of adsorbate bonding at the cluster surface. Ingham *et al.*[17] posit that Pd-Pd bonds between the surface and bulk-like region are weakened by Pd-adsorbate bonds on the surface. As surface Pd atoms form bonds to adsorbates, fewer electrons are available to fill Pd-Pd bonding orbitals between surface and subsurface Pd atoms. Such weakening of subsurface Pd-Pd bonds allows the bulk region to more easily expand to accommodate hydrogen absorption, thus making hydrogen absorption in the bulk more favorable. Since smaller clusters have a larger surface to volume ratio, this effect becomes

increasingly more important as cluster size decreases, leading to a narrowed MG for smaller clusters. This effect will be magnified by strongly interacting cluster-stabilizers,[18] such as polymer matrices, surfactants, and oxide supports, thus leading to the complete closure of the MG in small clusters. The agreement between the literature and the results of the MC simulations demonstrates the applicability of the Pd/H potential, as well as the feasibility of the GC-MC/MD method for investigating the thermodynamic stability of hydride phases in Pd bulk and clusters.

3.3.3. Molecular Dynamics Simulations of Hydrogen Dissociation and Diffusion

In addition to thermodynamic properties, the kinetics of hydrogen uptake and diffusion have been extensively investigated,[3,5,28,29,70-73] as a detailed understanding of hydrogen transport properties in Pd is essential to designing Pd-based devices with optimal absorption-desorption kinetics. The Pd/H potential developed here utilizes hydrogen parameters that are invariant between hydrogen in the gas phase, adsorbed on the surface, or dissolved in the bulk. This allows the potential to model dissociative hydrogen adsorption and diffusion into the bulk, which can help assess the kinetic properties of hydrogen transport at an atomistic level. To demonstrate this, we applied the Pd/H potential in molecular dynamics simulations to investigate the kinetics of hydrogen uptake by clusters of varying size, as well as to derive diffusion coefficients for hydrogen diffusion in the bulk at varying concentrations and temperatures. These results are compared to experimental studies, demonstrating the capabilities and limitations of the Pd/H potential for describing kinetics. MD simulations in this study were conducted in the NVT ensemble

using the velocity Verlet method[74] with a time step of 0.25 fs. A Berendsen thermostat[75] with a damping constant of 100 fs maintained temperature control throughout the simulation.

H_2 Dissociation and Absorption in Pd Clusters. To model the kinetics of hydrogen dissociation and absorption in clusters, we conducted MD simulations for a duration of 250 ps, in which each simulation began with a H_2 gas phase surrounding a single Pd cluster. This was conducted for three spherical cluster sizes: a 1.0 nm cluster consisting of 43 Pd atoms, a 1.5 nm cluster consisting of 135 Pd atoms, and a 2.0 nm cluster consisting of 321 Pd atoms. The ratio of Pd to H atoms in the simulation cell affects the overall amount of hydrogen that can be absorbed by the clusters. Correspondingly, we populated each simulation cell with a stoichiometric 1:1 Pd/H ratio to ensure that the cluster can become saturated with H atoms. Also, the pressure of hydrogen in the gas phase affects the kinetics of hydrogen absorption. Therefore, the dimensions of the simulation cells were chosen such that each Pd cluster was exposed to an equivalent initial hydrogen pressure. The initial simulation pressure was estimated from the number of hydrogen molecules in the gas phase using the ideal gas law, yielding a pressure of ~5.4 MPa in cubic simulation cells with side-lengths of 38 Å, 56 Å, and 75 Å for the 1.0 nm, 1.5 nm, and 2.0 nm clusters, respectively. A temperature of 1250 K was employed for all simulations, which was selected because it is high enough to allow rapid dissociation and diffusion in the timeframe of the simulation, yet is still below the melting point of Pd metal. The populations of H_2 molecules and H atoms either present in the gas phase or adsorbed on the Pd cluster were recorded at 25 fs intervals, allowing the hydride formation process to be tracked as a function of simulation time.

Hydride formation in Pd clusters proceeds through a core-shell mechanism, in which a hydride shell forms at the surface and progresses toward the center of the cluster.[29] Hydride formation is limited by hydrogen diffusion through the hydride shell to the metallic core, and the size-dependent kinetics described by this model have been investigated theoretically by Zhdanov *et al.*[70] and experimentally by Langhammer *et al.*[29] Zhdanov *et al.* used Monte Carlo simulations to demonstrate a power-law relationship relating the time required to reach hydrogen saturation when forming a hydride phase to cluster size: $t_{1/2} \sim d^Z$, where $t_{1/2}$ is half the time required to reach saturation in the cluster, d is the cluster diameter, and Z is a proportionality constant. They predict that $Z = 2.0$ in the ideal case of diffusion limited hydride formation, and that Z increases to as much as 3.0 depending on diffusion dynamics and cluster geometry. This is corroborated by the experimental results of Langhammer *et al.*, who compared hydride formation rates in samples containing clusters with average diameters of 1.81 nm, 2.47 nm, and 5.35 nm, finding that $Z = 2.9$ at 303 K.

We conducted MD simulations, summarized in Figure 3-10, to determine if the power law relation for the size-dependent kinetics of hydrogen absorption is retained by the Pd/H potential. Since these simulations were conducted at high temperatures, we expect that the small dissociation barrier (~2 kcal mol^{-1}) will be readily overcome, and that the higher subsurface diffusion barrier (~10 kcal mol^{-1}) will be rate limiting. As seen in the figure, the Pd/H potential yields a value of Z=1.92, in agreement with the power-law scaling predicted by Zhdanov *et al.* This supports the core-shell model for hydride formation in clusters, in which the rate limiting step is hydrogen diffusion to the metallic core through a growing hydride surface shell.

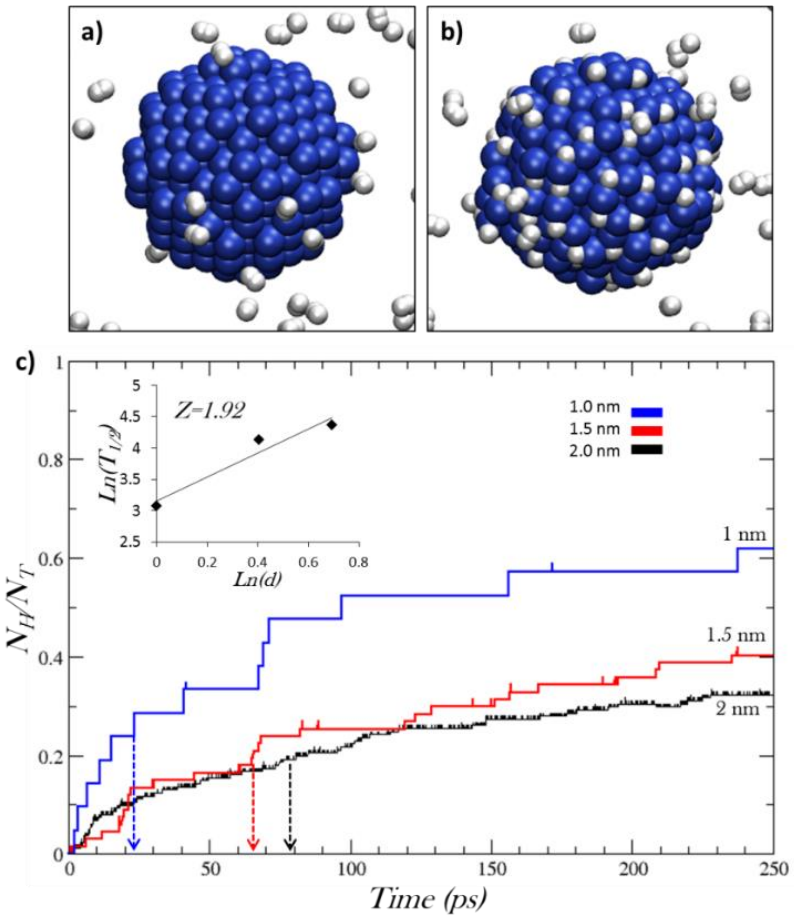

Figure 3-10. (a) Initial and (b) final structure of a 250 ps NVT-MD simulation of hydrogen adsorption at 1250 K in a 2.0 nm cluster. (c) Number of hydrogen atoms adsorbed from the gas phase normalized by the total number of hydrogen atoms. Arrows mark the time required to reach half of the final hydrogen saturation point, $t_{1/2}$. (Inset) $t_{1/2}$ plotted against cluster diameter.

Hydrogen Diffusion in Bulk Pd. To derive diffusion coefficients for hydrogen diffusion in bulk Pd, we conducted NVT-MD simulations in which hydrogen was initially loaded in a fcc lattice at varying concentrations. The simulation box consisted of 256 Pd atoms in a cubic cell with periodic boundary conditions in all three directions. Octahedral sites were randomly populated with 8, 64, or 128 H atoms, yielding H/Pd ratios of 0.03, 0.25, and 0.5, respectively. A conjugate gradient energy minimization was performed prior to each simulation to allow the simulation cell size and hydrogen coordinates to relax, thus mitigating simulation artifacts caused by high energy contacts in the initial geometry.

Diffusion coefficients were calculated from the average mean-square displacement (MSD) of hydrogen atoms, which was determined from the atomic coordinates of the system that were archived after every 0.025 ps. Diffusion coefficients were calculated from the slope of the MSD curve using the well-known relation: $MSD = 6Dt$, where D is the diffusion coefficient and t is time. This is summarized in Figure 3-11 for all three hydrogen concentrations at 500 K, 550 K, 650 K, and 750 K. The apparent diffusion barrier can be determined using an Arrhenius relationship: $D = D_o \, Exp[-E_d / (RT)]$, where D is the diffusion coefficient determined from the MSD data, D_o is the Arrhenius pre-exponential factor, E_d is the apparent diffusion barrier, R is the gas constant, and T is temperature. This is demonstrated in Figure 3-12, where a linear regression was employed to determine the pre-exponential factor and hydrogen diffusion barrier at each concentration. The results, tabulated in Table 3-3 along with experimental comparisons, show that the diffusion barrier increases from 6.87 kcal mol^{-1} at $H/Pd = 0.03$, to 7.55 kcal mol^{-1} and 8.32 kcal mol^{-1} at $H/Pd = 0.25$ and 0.5, respectively. As shown in Figure 3-12, the diffusion coefficients increase with decreasing hydrogen concentration, moving toward the experimentally determined[28] dilute limit shown in the figure. Despite approaching the experimentally determined dilute limit, the Pd/H potential still systemically under-predicts hydrogen diffusion coefficients compared to the experimental barriers reported Hara *et al.*[28] However, the magnitude of this deviation can be attributed to the fact that ReaxFF over-predicts the hydrogen diffusion barrier, shown in Figure 3-4, by ~2 kcal mol^{-1}, which is within the expected accuracy of the ReaxFF method. The agreement between ReaxFF and experiment demonstrates that the Pd/H potential can be used to derive hydrogen diffusion properties in bulk Pd over a variety of temperatures and concentrations.

Together, the MD results presented above demonstrate that the ReaxFF potential can accurately represent the interaction between hydrogen and Pd both at the gas/surface interface and in the bulk. This demonstrates the capabilities of the potential for investigating the kinetic properties of hydrogen uptake and diffusion.

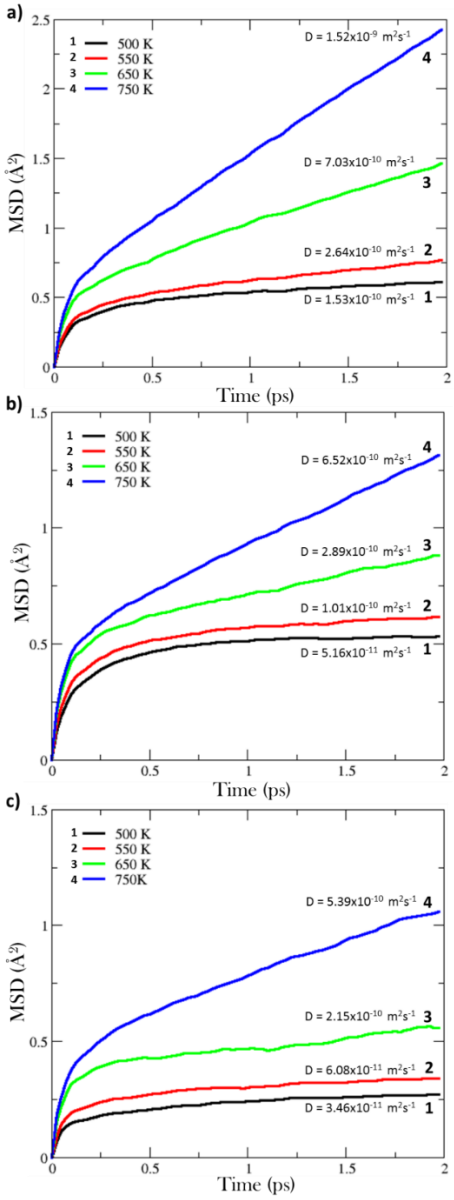

Figure 3-11. Mean-square displacements of hydrogen during MD-NVT simulations of PdH_x bulk for (a) $x = 0.03$, (b) $x = 0.25$, and (c) $x = 0.5$.

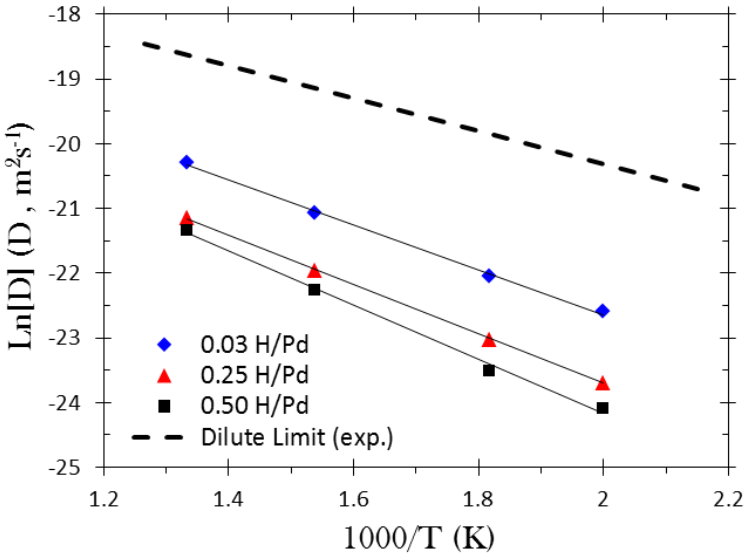

Figure 3-12. Arrhenius relationship between diffusion coefficients and temperature obtained from MD-NVT simulations at varying hydrogen concentrations. The dashed line shows the experimental dilute limit reported in Ref. [28]

Table 3-3. Activation barriers (E_d) and pre-exponential factors (D_0) for hydrogen diffusion.

H/Pd	E_d (kcal mol^{-1})	D_0 (10^{-6} m^2 s^{-1})
0.5	8.32	0.137
0.25	7.55	0.102
0.03	6.87	0.144
0.02-0.05 (500 kPa)[a]	*6.26*	*0.553*
0.04[a]	*5.86*	*0.385*
Dilute Limit[a]	*5.04*	*0.240*

a) Experimental barriers and pre-exponentials from Ref. [28]

3.4. Conclusion

Palladium can readily dissociate and absorb hydrogen from the gas phase, making it a candidate for use in hydrogen storage devices, separation membranes, and hydrogenation catalysts. Optimizing the design of these devices requires an extensive knowledge of both kinetic and thermodynamic influences affecting hydrogen transport at

the atomistic scale. To aid this effort, we derived a ReaxFF interaction potential for Pd/H from an extensive set of DFT data for both bulk and surface properties. Using this potential, we conducted GC-MC/MD simulations to derive theoretical hydrogen absorption isotherms in Pd bulk and clusters, thus assessing the contributing roles of surface, subsurface, and bulk regions during the size-dependent transition between the solid solution α phase and the hydride β phase. We determined that the narrowing hydrogen miscibility gap in Pd clusters of decreasing size is related to an increased solubility in the bulk-like region of the cluster, and that the miscibility gap remains open for naked clusters at small as 1.0 nm in diameter, in agreement with previous experimental observations.[17] Additionally, we conducted NVT simulations of the dissociative adsorption of hydrogen from the gas phase, and of hydrogen diffusion in the bulk. The size-dependent kinetics of hydrogen absorption from the gas phase, as well as bulk diffusion coefficients, determined from these simulations are in agreement with experimental results,[28,29] demonstrating the capability of the ReaxFF potential for modeling hydrogen transport between gas and solid phases. The corroboration between experiment and ReaxFF both validates the Pd/H interaction potential for treating the complex phase behavior of PdH, as well as demonstrates the ability of ReaxFF to assess thermodynamic and kinetic influences on phase behavior at the atomic scale through GC-MC and MD methods.

3.5. Acknowledgements

This research was supported by funding from the National Science Foundation grant: CBET-1032979.

3.6 References

1. M. Yamauchi and H. Kitagawa, Synth. Met. **153** (1–3), 353-356 (2005).
2. M. Yamauchi, H. Kobayashi and H. Kitagawa, ChemPhysChem **10** (15), 2566-2576 (2009).
3. C. Lebouin, Y. Soldo, S. A. Grigoriev, M. Guymont and P. Millet, Int. J. Hydrogen Energy **38** (2), 966-972 (2013).
4. Y. E. Cheon and M. P. Suh, Angew. Chem. Int. Ed. **48** (16), 2899-2903 (2009).
5. W. D. Michalak, J. B. Miller, D. R. Alfonso and A. J. Gellman, Surf. Sci. **606** (3–4), 146-155 (2012).
6. P. Kamakoti, B. D. Morreale, M. V. Ciocco, B. H. Howard, R. P. Killmeyer, A. V. Cugini and D. S. Sholl, Science **307** (5709), 569-573 (2005).
7. Ø. Hatlevik, S. K. Gade, M. K. Keeling, P. M. Thoen, A. P. Davidson and J. D. Way, Sep. Purif. Technol. **73** (1), 59-64 (2010).
8. A. Borodziński and G. C. Bond, Catalysis Reviews **48** (2), 91-144 (2006).
9. A. Borodziński and G. C. Bond, Catalysis Reviews **50** (3), 379-469 (2008).
10. C. l. Chizallet, G. t. Bonnard, E. Krebs, L. Bisson, C. c. Thomazeau and P. Raybaud, J. Phys. Chem. C **115** (24), 12135-12149 (2011).
11. D. Teschner, J. Borsodi, A. Wootsch, Z. Révay, M. Hävecker, A. Knop-Gericke, S. D. Jackson and R. Schlögl, Science **320** (5872), 86-89 (2008).
12. D. Teschner, J. Borsodi, Z. Kis, L. Szentmiklósi, Z. Révay, A. Knop-Gericke, R. Schlögl, D. Torres and P. Sautet, J. Phys. Chem. C **114** (5), 2293-2299 (2010).
13. W. Ludwig, A. Savara, R. J. Madix, S. Schauermann and H.-J. Freund, J. Phys. Chem. C **116** (5), 3539-3544 (2012).
14. L. L. Jewell and B. H. Davis, Appl. Catal. A: Gen. **310** (0), 1-15 (2006).
15. M. Suleiman, N. M. Jisrawi, O. Dankert, M. T. Reetz, C. Bähtz, R. Kirchheim and A. Pundt, J. Alloys Compd. **356–357** (0), 644-648 (2003).
16. V. N. Konopsky, D. V. Basmanov, E. V. Alieva, S. K. Sekatskii and G. Dietler, Appl. Phys. Lett. **100** (8), 083108-083104 (2012).
17. B. Ingham, M. F. Toney, S. C. Hendy, T. Cox, D. D. Fong, J. A. Eastman, P. H. Fuoss, K. J. Stevens, A. Lassesson, S. A. Brown and M. P. Ryan, Phys. Rev. B **78** (24), 245408 (2008).
18. M. Suleiman, J. Faupel, C. Borchers, H. U. Krebs, R. Kirchheim and A. Pundt, J. Alloys Compd. **404–406** (0), 523-528 (2005).
19. R. J. Behm, K. Christmann and G. Ertl, Surf. Sci. **99** (2), 320-340 (1980).
20. H. Conrad, G. Ertl and E. E. Latta, Surf. Sci. **41** (2), 435-446 (1974).
21. T. Engel and H. Kuipers, Surf. Sci. **90** (1), 162-180 (1979).
22. M. Yamauchi, R. Ikeda, H. Kitagawa and M. Takata, J. Phys. Chem. C **112** (9), 3294-3299 (2008).
23. W. Dong and J. Hafner, Phys. Rev. B **56** (23), 15396-15403 (1997).
24. W. Dong, V. Ledentu, P. Sautet, A. Eichler and J. Hafner, Surf. Sci. **411** (1–2), 123-136 (1998).
25. Y. Zhao and D. Tian, Computational and Theoretical Chemistry **991** (0), 40-43 (2012).

26. S. Kishore, J. A. Nelson, J. H. Adair and P. C. Eklund, J. Alloys Compd. **389** (1–2), 234-242 (2005).
27. M. Moreno, F. J. Ibañez, J. B. Jasinski and F. P. Zamborini, J. Am. Chem. Soc. **133** (12), 4389-4397 (2011).
28. S. Hara, A. Caravella, M. Ishitsuka, H. Suda, M. Mukaida, K. Haraya, E. Shimano and T. Tsuji, Journal of Membrane Science **421–422** (0), 355-360 (2012).
29. C. Langhammer, V. P. Zhdanov, I. Zorić and B. Kasemo, Phys. Rev. Lett. **104** (13), 135502 (2010).
30. V. Srivastava and R. Balasubramaniam, Materials Science and Engineering: A **304–306** (0), 897-900 (2001).
31. J. A. Eastman, L. J. Thompson and B. J. Kestel, Phys. Rev. B **48** (1), 84-92 (1993).
32. N. Lopez, Z. Łodziana, F. Illas and M. Salmeron, Phys. Rev. Lett. **93** (14), 146103 (2004).
33. S. Wilke, D. Hennig, R. Löber, M. Methfessel and M. Scheffler, Surf. Sci. **307–309, Part A** (0), 76-81 (1994).
34. H. Grönbeck and V. P. Zhdanov, Phys. Rev. B **84** (5), 052301 (2011).
35. M. Johansson, E. Skúlason, G. Nielsen, S. Murphy, R. M. Nielsen and I. Chorkendorff, Surf. Sci. **604** (7–8), 718-729 (2010).
36. A. Shabaev, D. A. Papaconstantopoulos, M. J. Mehl and N. Bernstein, Phys. Rev. B **81** (18), 184103 (2010).
37. C. Sachs, A. Pundt, R. Kirchheim, M. Winter, M. T. Reetz and D. Fritsch, Phys. Rev. B **64** (7), 075408 (2001).
38. K. Tanaka, Catal. Today **154** (1–2), 105-112 (2010).
39. A. Pundt, M. Suleiman, C. Bähtz, M. T. Reetz, R. Kirchheim and N. M. Jisrawi, Materials Science and Engineering: B **108** (1–2), 19-23 (2004).
40. M. Wilde, K. Fukutani, M. Naschitzki and H. J. Freund, Phys. Rev. B **77** (11), 113412-113416 (2008).
41. T. Mütschele and R. Kirchheim, Scripta Metallurgica **21** (2), 135-140 (1987).
42. A. C. T. van Duin, S. Dasgupta, F. Lorant and W. A. Goddard III, J. Phys. Chem. A **105** (41), 9396-9409 (2001).
43. T. P. Senftle, R. J. Meyer, M. J. Janik and A. C. T. van Duin, J. Chem. Phys. **139** (4), 044109-044115 (2013).
44. D. W. Brenner, Phys. Rev. B **42** (15), 9458-9471 (1990).
45. J. Tersoff, Phys. Rev. Lett. **61** (25), 2879-2882 (1988).
46. W. J. Mortier, S. K. Ghosh and S. Shankar, J. Am. Chem. Soc. **108** (15), 4315-4320 (1986).
47. K. Chenoweth, A. C. T. van Duin and W. A. Goddard, J. Phys. Chem. A **112** (5), 1040-1053 (2008).
48. S. Monti, A. C. T. van Duin, S.-Y. Kim and V. Barone, J. Phys. Chem. C **116** (8), 5141-5150 (2012).
49. J. Quenneville, R. S. Taylor and A. C. T. van Duin, J. Phys. Chem. C **114** (44), 18894-18902 (2010).
50. D. Raymand, A. C. T. van Duin, D. Spångberg, W. A. Goddard Iii and K. Hermansson, Surf. Sci. **604** (9–10), 741-752 (2010).

51. J. Ludwig, D. G. Vlachos, A. C. T. van Duin and W. A. Goddard, The Journal of Physical Chemistry B **110** (9), 4274-4282 (2006).
52. C. Zou, A. T. Duin and D. Sorescu, Top. Catal. **55** (5-6), 391-401 (2012).
53. A. C. T. van Duin, J. M. A. Baas and B. van de Graaf, J. Chem. Soc., Faraday Trans. **90** (19), 2881-2895 (1994).
54. R. J. Wolf, M. W. Lee, R. C. Davis, P. J. Fay and J. R. Ray, Phys. Rev. B **48** (17), 12415-12418 (1993).
55. R. J. Wolf, M. W. Lee and J. R. Ray, Phys. Rev. Lett. **73** (4), 557-560 (1994).
56. E. A. Crespo, S. Claramonte, M. Ruda and S. R. de Debiaggi, Int. J. Hydrogen Energy **35** (11), 6037-6041 (2010).
57. M. Ruda, E. A. Crespo and S. R. d. Debiaggi, J. Alloys Compd. **495** (2), 471-475 (2010).
58. E. A. Crespo, M. Ruda and S. Ramos de Debiaggi, Int. J. Hydrogen Energy **33** (13), 3561-3565 (2008).
59. N. Metropolis, A. W. Rosenbluth, M. N. Rosenbluth, A. H. Teller and E. Teller, J. Chem. Phys. **21** (6), 1087-1092 (1953).
60. D. Frenkel and B. Smit, *Understanding molecular simulation : from algorithms to applications*. (Academic Press, San Diego, 2002).
61. M. W. Chase, S. National Institute of and Technology, *NIST-JANAF thermochemical tables*. (American Chemical Society ; American Institute of Physics for the National Institute of Standards and Technology, [Washington, D.C.]; Woodbury, N.Y., 1998).
62. G. Kresse and J. Furthmuller, Computational Materials Science **6**, 15-50 (1996).
63. G. Kresse and J. Furthmuller, Phys. Rev. B **54** (16), 11169-11186 (1996).
64. J. P. Perdew, J. A. Chevary, S. H. Vosko, K. A. Jackson, M. R. Pederson, D. J. Singh and C. Fiolhais, Phys. Rev. B **46** (11), 6671 (1992).
65. G. Kresse and D. Joubert, Phys. Rev. B **59** (3), 1758 LP - 1775 (1999).
66. H. J. Monkhorst and J. D. Pack, Phys. Rev. B **13** (12), 5188 LP - 5192 (1976).
67. G. Henkelman, B. P. Uberuaga and H. Jonsson, J. Chem. Phys. **113** (22), 9901-9904 (2000).
68. D. R. Lide, (CRC Press, New York, 2004).
69. D. M. Cox, P. Fayet, R. Brickman, M. Y. Hahn and A. Kaldor, Catal. Lett. **4** (4-6), 271-278 (1990).
70. V. P. Zhdanov and B. Kasemo, Chem. Phys. Lett. **460** (1–3), 158-161 (2008).
71. D. Matsumura, Y. Okajima, Y. Nishihata and J. i. Mizuki, J. Alloys Compd. **509** (0), S849-S852 (2011).
72. J. H. He, D. L. Knies, G. K. Hubler, K. S. Grabowski, R. J. Tonucci and L. F. Dechiaro, Appl. Phys. Lett. **101** (15), 153103 (2012).
73. G. L. Holleck, The Journal of Physical Chemistry **74** (3), 503-511 (1970).
74. L. Verlet, Physical Review **159** (1), 98-103 (1967).
75. H. J. C. Berendsen, J. P. M. Postma, W. F. v. Gunsteren, A. DiNola and J. R. Haak, J. Chem. Phys. **81** (8), 3684-3690 (1984).

Chapter 4
Determining *in situ* Phases of a Nanoparticle Catalyst *via* Grand Canonical Monte Carlo Simulations with the ReaxFF Potential

This chapter is published as: T. P. Senftle, A. C. T. van Duin and M. J. Janik, *Catalysis Communications* **52** (0), 72-77 (2014).

Abstract

Catalyst design requires a detailed understanding of the structure of the catalyst surface as a function of varying reaction conditions. Here we demonstrate the capability of a grand canonical Monte Carlo/molecular dynamics (GC-MC/MD) method utilizing the ReaxFF potential to predict nanoparticle structure and phase stability as a function of temperature and pressure. This is demonstrated for Pd nanoparticles, which readily form oxide, hydride, and carbide phases under reaction environments, impacting catalytic behavior. The approach presented here can be extended to other catalytic systems, providing a new tool for exploring the effects of reaction conditions on catalyst activity, selectivity, and stability.

4.1. Introduction

The rational design of catalytic systems featuring nano-sized metal particles requires knowledge of the active surface phase under operating conditions.[1] In particular, the reactant gas phase can rearrange the metal lattice, forming unique surface, subsurface, and bulk phases.[1, 2] The chemical properties of such phases will differ from those of the parent metal, affecting the selectivity and activity of the catalyst.[1-7] Quantum mechanical

(QM) computational methods, such as density functional theory (DFT), can model the phase stability of the catalyst through the formalism of *ab initio* thermodynamics.[6, 8-12] The computational expense of QM methods, however, limits QM studies to highly idealized catalyst models. This has motivated the use of empirical force fields, such as ReaxFF,[13] that are computationally inexpensive compared to QM, therefore helping to close the size and pressure gap between macroscopic experimental techniques and quantum-scale computational methods.

Herein, we demonstrate how the ReaxFF potential can be employed in hybrid grand canonical Monte Carlo/molecular dynamics (GC-MC/MD) simulations to determine the structure and stability of nanoparticle phases as a function of temperature and gas phase composition under reaction conditions. Phase reconstruction under operating conditions is a particular concern for Pd-based systems, which are industrially relevant oxidation[14-16] and hydrogenation catalysts.[5-7] Pd catalysts form oxide phases when employed under oxidizing conditions,[3,4,17] and form complex hydride/carbide phases when used to hydrogenate unsaturated hydrocarbons.[5-7] We will highlight two GC-MC/MD studies; one assessing oxide formation in a Pd cluster as a function of oxygen pressure and temperature, and the other assessing carbide and hydride formation under varying hydrogen/hydrocarbon ratios in the gas phase. Together, these studies demonstrate the capabilities of the ReaxFF potential and the GC-MC/MD method for modeling *in situ* behavior in catalytic systems.

4.2. Theory and Methods

4.2.1. ReaxFF Potential

The ReaxFF potential[13] is a reactive force field comprised of bond-order/bond-length relationships[18,19] combined with polarizable charge descriptions[20] to describe covalent, Coulomb, and van der Waals interactions between atoms in a system. The bond-length/bond-order formalism yields a differentiable potential energy surface through reactive events, thus allowing for reactive molecular dynamics (RMD). As illustrated in Figure 4-1, the transferability of the ReaxFF potential offers a unique capability for modeling catalyst behavior as a function of reaction conditions, since the same set of parameters can be employed in both GC-MC/MD simulations assessing *in situ* stability and in RMD simulations assessing kinetics.

The ReaxFF parameters unique to Pd/O and Pd/H interactions used herein were derived previously in Ref.[21] and in Ref.[22], respectively. We refer the reader to these publications and the references therein for detailed discussions of the accuracy of the ReaxFF method and the parameter optimization process. The Pd/C/H potential parameters were similarly derived from a training set of ~40 data points consisting of C_xH_y adsorption energies at various surface, subsurface, and bulk Pd sites. Generally, the Pd/C/H ReaxFF parameters reproduce the adsorption energies in the training set to within an average of ~5 kcal mol^{-1}. ReaxFF and DFT adsorption energies on the energetically favored Pd(111) surface are briefly summarized in the supporting material.

4.2.2. Grand Canonical Monte Carlo

The previously developed[21] hybrid grand canonical-Monte Carlo/molecular dynamics (GC-MC/MD) method is well suited for investigating phase behavior, as it can model uptake of gas phase species in a solid. Atoms are stochastically exchanged between the system and a gas phase reservoir at constant chemical potential, $\mu_{res}(T,P)$, until the system reaches equilibrium with the gas phase reservoir. Here, the GC-MC/MD method is employed in a ($TVN_{Pd}\mu_{res}$) ensemble with constant temperature (T), volume (V), chemical potential of all species in the reservoir (μ_{res}), and number of Pd atoms (N_{Pd}). MC moves include insertion, deletion, or displacement of an atom other than Pd. The acceptance criteria for each move type is derived from detail-balance Boltzmann relationships,[23] and are related to the temperature and pressure of the gas phase through the chemical potential of the reservoir, $\mu_{res}(T,P)$. Additionally, the GC-MC/MD method includes a MD-based energy minimization step after each MC move prior to applying the acceptance criteria. The bias toward acceptance introduced by the MD relaxation step is mitigated by excluding the volume occupied by Pd metal atoms from the total system volume definition utilized in the Boltzmann acceptance criteria, as described in Ref.[21]. This additional step allows for structural relaxation of the metal lattice necessary for forming new phases. Thus, the structure after GC-MC/MD reflects the stable phase in equilibrium with the gas phase at the temperature and pressure set by $\mu_{res}(T,P)$.

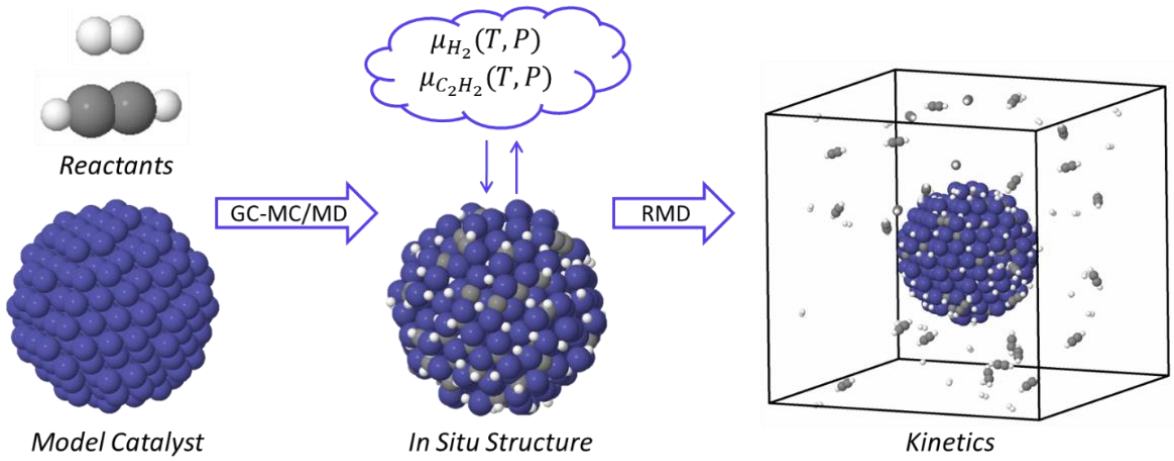

Figure 4-1. Scheme for using GC-MC/MD and RMD in tandem.

4.3. Results and Discussion

Here we highlight two GC-MC/MD studies used to explore phase formation in Pd nanoparticles. The first assesses oxidation in a 3 nm Pd cluster as a function of oxygen pressure and temperature. The second demonstrates multi-species GC-MC/MD, in which both carbon and hydrogen atoms are exchanged with a hydrogen/hydrocarbon reservoir, showing the dependence of carbide/hydride formation on the ratio of reactant partial pressures in the gas phase.

4.3.1. Oxide Formation in Pd

Oxide formation on palladium surfaces impacts the activity and selectivity of Pd-based catalysts, which are widely employed under oxygen rich operating conditions. Our recent study[21] applied the hybrid GC-MC/MD method to determine the extent of surface and bulk oxidation in Pd clusters. Oxygen atoms were added, moved, and removed from a

3 nm Pd cluster until the O:Pd ratio and total energy of the system converged. This method was repeated at varying temperatures and pressures to derive a theoretical phase diagram for the oxidation of Pd clusters in temperatures ranging from 300 K to 1300 K and oxygen pressures ranging from 10^{-14} atm to 1 atm, which is summarized in Figure 4-2.

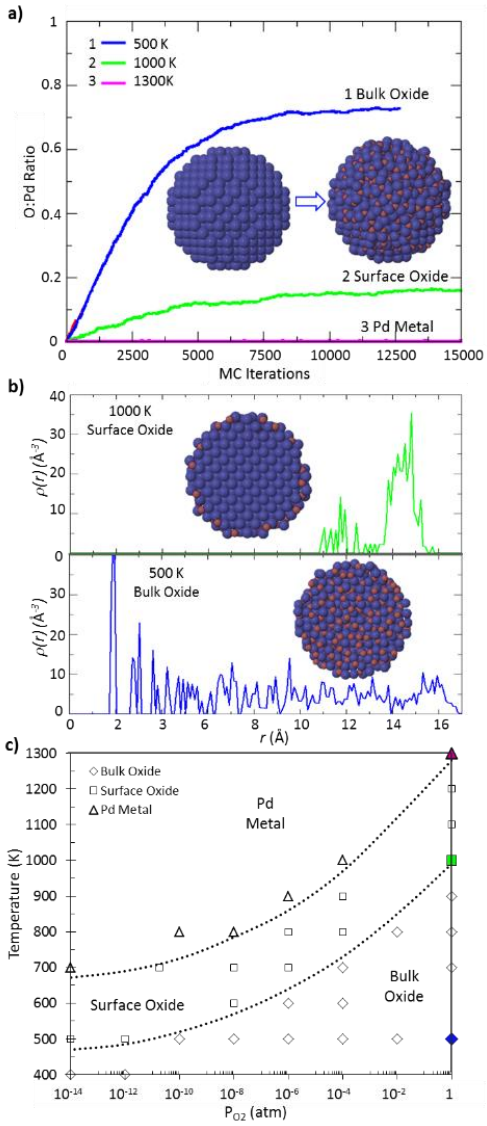

Figure 4-2. (a) GC-MC/MD results for oxide formation in a 3 nm Pd cluster at P_{O2} = 1 atm. (b) Radial oxygen distribution, insets show center cross sections. (c) Oxidation phase diagram, data points represent separate GC-MC/MD simulations. The dotted boundaries represent estimated delineations between the oxidation phases, and the filled data points correspond to the simulations in (a) and (b). (Data adapted from Ref.[21])

Figure 4-2(a) reflects the convergence of O:Pd ratios in GC-MC/MD simulations at P_{O2} = 1 atm that correspond to three oxidation phases in the Pd cluster: (1) a bulk oxide at 500 K, (2) a surface oxide at 1000 K, and (3) Pd metal (no oxidation) at 1500 K. Intuitively, the phase transition between surface and bulk oxidation is marked by an increased O:Pd ratio. Additionally, the radial distribution of oxygen atoms in the cluster was analyzed to assess the extent of oxidation in surface and bulk regions of the cluster, which is demonstrated Figure 4-2(b). The radial distribution was calculated from the atomic coordinates of the final structure of the GC-MC/MD simulation, and represents the average number of oxygen atoms located at a specified radius, *r*, from the center of the cluster (r = 0). The radial distribution of oxygen atoms was determined for varying temperatures and oxygen pressures, allowing the thermodynamically stable phase to be determined for the specified oxygen pressure and temperature.

Together, these data can be used to estimate oxidation phase boundaries, which are shown in the phase diagram in Figure 4-2(c). In Figure 4-2(c), each data point corresponds to a separate GC-MC/MD simulation for which the final structure was classified as either (1) a bulk oxide, (2) a surface oxide, or (3) Pd metal. The phase boundaries predicted by the ReaxFF GC-MC/MD method for the 3 nm cluster are similar to the experimental and *ab initio* phase boundaries reported by Ketteler *et al.* in *Ref.*[24] and by Lundgren *et al.* in Ref.[25] for single crystal Pd surfaces, as well as the experimentally observed bulk Pd→PdO phase boundaries reported by Zhang *et al*. in Ref.[26]. The ability to predict oxidation phase boundaries is instrumental to catalysis studies, as the degree of surface oxidation affects catalytic activity; which is experimentally demonstrated for methane combustion by Su *et al*. in Ref.[27] and for CO oxidation by Toyoshima *et al*. in Ref.[28].

4.3.2. Carbide and Hydride Formation in Pd

The GC-MC/MD method can also model the formation of multi-species phases that occur when the gas phase is composed of varying reactant compositions. Numerous studies suggest that the formation of a subsurface carbide phase enhances the selectivity of Pd catalysts toward hydrogenation. Teschner *et al.*, using *in situ* x-ray photoelectron spectroscopy, found that a subsurface carbide phase is stable at low H:C ratios, yielding selective hydrogenation of 1-pentyne.[5-7] Total, unselective hydrogenation occurs at high H:C ratios after the subsurface carbide decomposes. They propose that the carbide phase separates bulk and surface hydrogen phases, thus inhibiting the more reactive bulk hydrogen from hydrogenating the hydrocarbon species on the surface of the cluster. We conducted GC-MC/MD simulations in which both C and H atoms were exchanged between a 2 nm Pd cluster and a hydrogen/hydrocarbon reservoir at 300 K, where μ_H and μ_C were determined by temperature and partial pressures in the reservoir. Each simulation was terminated after 6500 MC iterations, at which point the MC acceptance rates significantly decrease as the system approaches equilibrium.

Figure 4-3 summarizes the GC-MC/MD results for varying hydrogen and carbon pressures. Figure 4-3(a-b) shows H/C:Pd ratios in simulations at the same hydrogen chemical potential and varying carbon chemical potentials, and *vice versa* in Figure 4-3(b-d). As seen in Figure 4-3(a-b), an increase in μ_C leads to an increase in both carbon *and* hydrogen uptake. Thus, an increase in the hydrocarbon pressure leads to increased hydrogen uptake, which corroborates the experimental finding of Teschner *et al.*, who found that the H:Pd ratio increased from 0.75 after exposure to 1 atm of pure H_2 to 0.87

after hydrogenation events upon subsequent exposure to 1-pentyne.[5] Interestingly, Figure 4-3(c-d) shows that the amount of carbon uptake is minimally affected by an increase in the hydrogen pressure. This can be explained by the radial distribution plots shown in Figures 4-4 and 4-5. Results for low hydrogen pressure (10^{-14} atm) in Figure 4-4 demonstrate that carbon preferentially aggregates in the subsurface region of the particle, and only begins to form surface hydrocarbon species at high hydrocarbon pressures. Figure 4-5 summarizes carbon uptake at the same μ_C values, but at high hydrogen pressures (1 atm). In this case, the carbon still prefers the subsurface region, but forms surface hydrocarbons more readily.

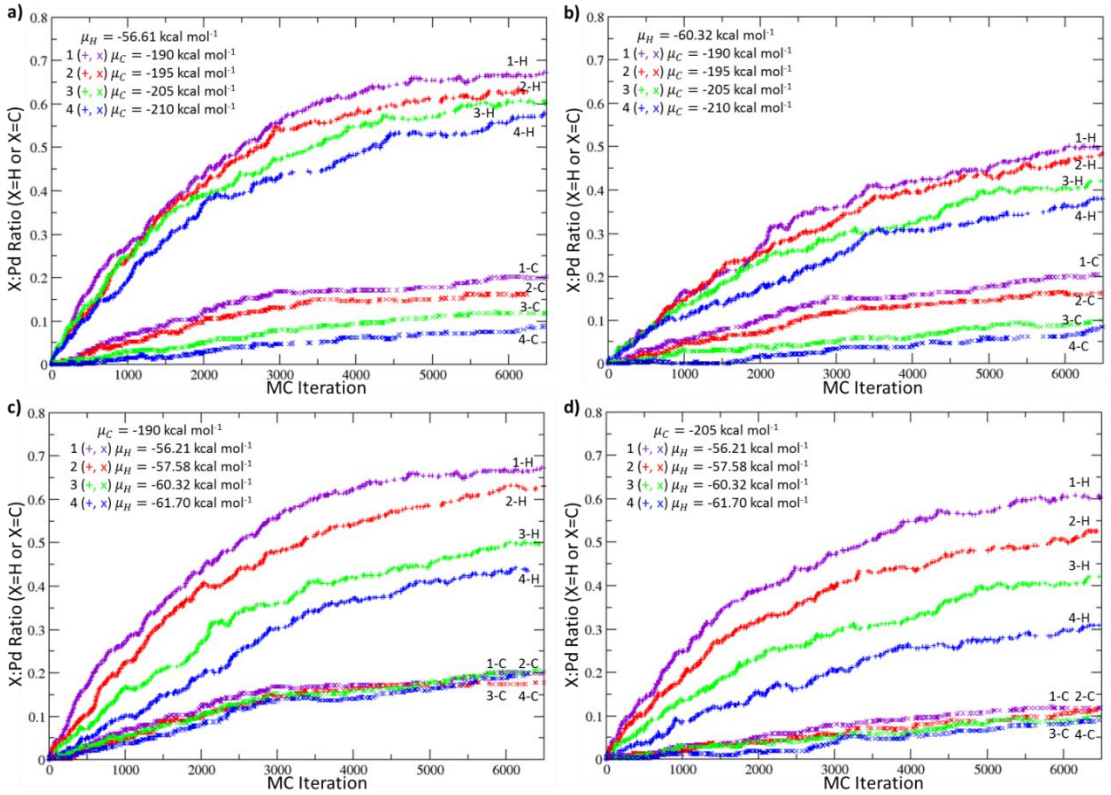

Figure 4-3. GC-MC/MD results for hydrogen and carbon uptake in a 2 nm Pd cluster at 300 K and at constant (a-b) hydrogen chemical potential, or (c-d) carbon chemical potential. "+" symbols represent hydrogen data and "×" symbols represent carbon data.

The amount of carbon uptake in the particle is similar at both high and low hydrogen pressures, but the subsurface carbon phase is destroyed by the formation of surface hydrocarbon species at high hydrogen pressures. GC-MC/MD demonstrates that the subsurface carbon phase segregates surface and bulk hydrogen at low H:C ratios and that the extent of this segregation decreases at higher H:Pd ratios, in agreement with experimental observations.[5-7]

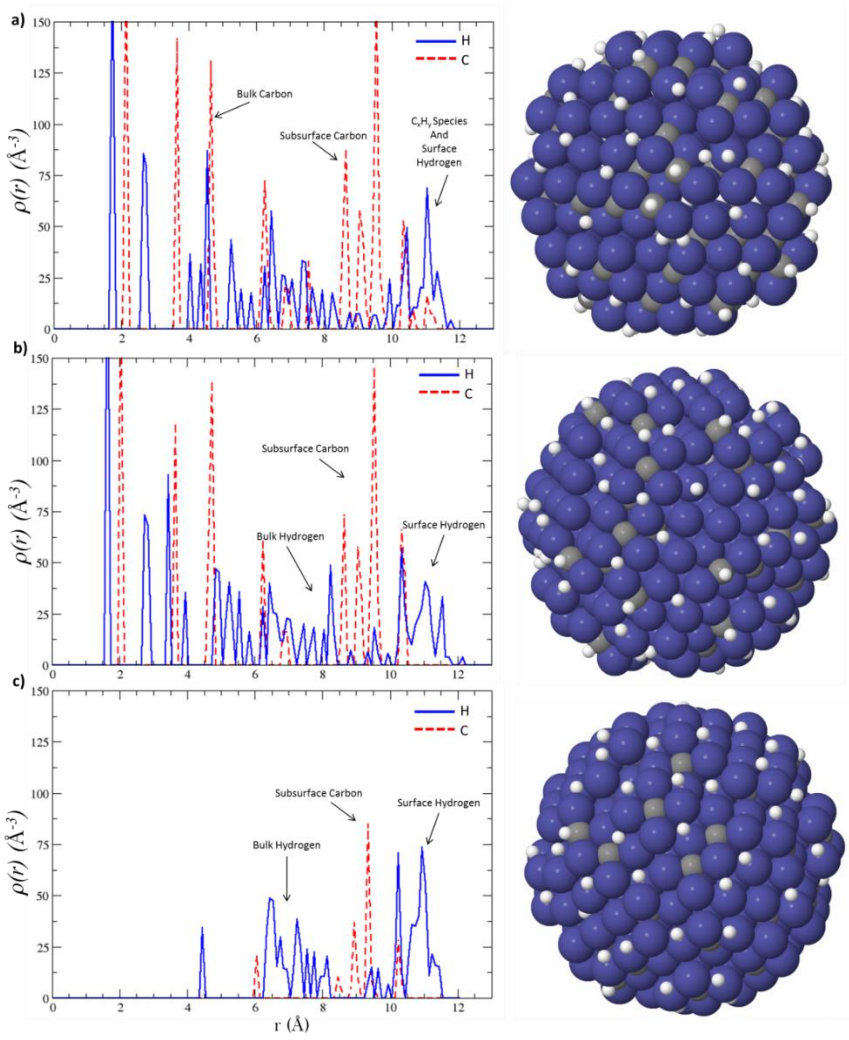

Figure 4-4. Radial distribution of carbon and hydrogen after GC-MC/MD at 300 K, μ_H = -65.82 kcal mol^{-1} (P_{H2}=10^{-14} atm) and (a) μ_C = -190.0 kcal mol^{-1}, (b) μ_C-195.0 kcal mol^{-1}, or (c) μ_C-200.0 kcal mol^{-1}.

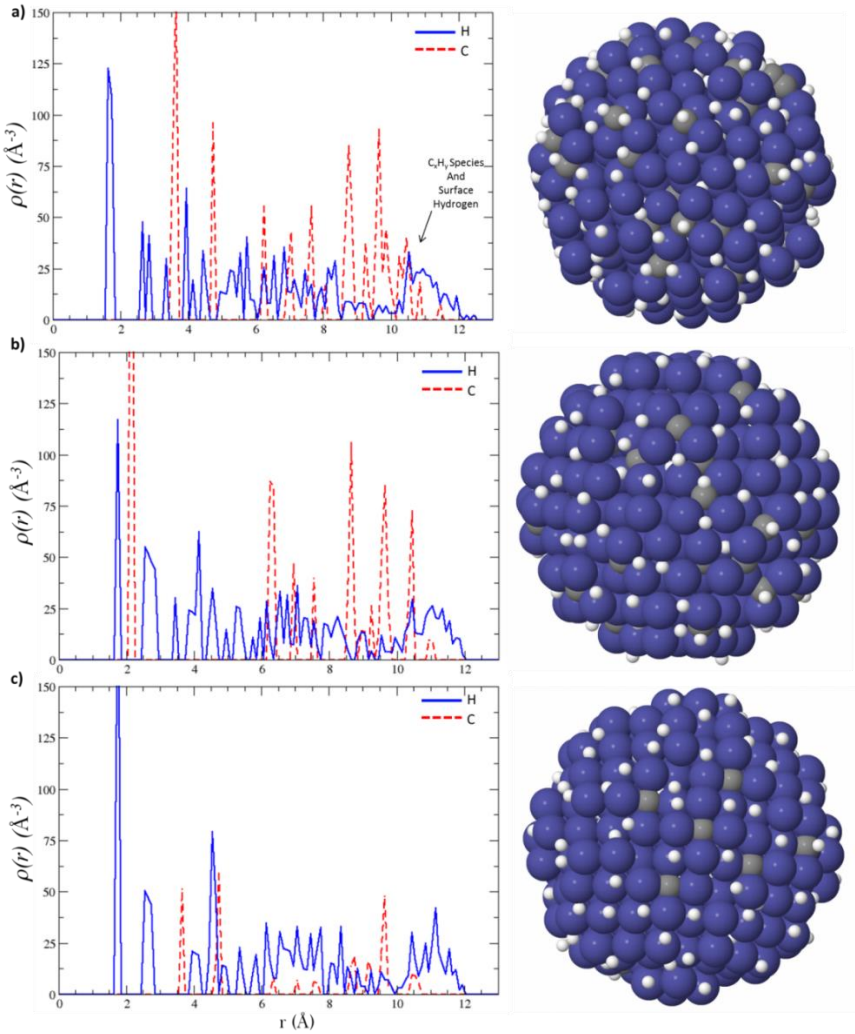

Figure 4-5. Radial distribution of carbon and hydrogen after GC-MC/MD at 300 K, μ_H = -56.21 kcal mol^{-1} (P_{H2}= 1 atm) and (a) μ_C = -190.0 kcal mol^{-1}, (b) μ_C-195.0 kcal mol^{-1}, or (c) μ_C-200.0 kcal mol^{-1}.

4.4. Conclusion

We demonstrated the use of GC-MC/MD via the ReaxFF potential for modeling the structure and stability of phases that form in a Pd catalyst under reaction conditions typical of either oxidation or hydrogenation applications. The agreement between ReaxFF,

ab initio, and experimental observations demonstrates the capability of the GC-MC/MD method for exploring the phase space of a catalyst under reaction conditions. Furthermore, the resultant system structures determined by GC-MC/MD can be utilized in subsequent RMD studies to assess reaction kinetics, or can be used to suggest models that better represent the catalyst surface under reaction conditions for more detailed DFT studies. The formalism presented here, though specifically tailored to Pd systems, can be readily extended to other catalytic systems, providing a new tool for exploring the impact of reaction conditions on catalyst activity, selectivity, and stability.

4.5. Acknowledgements

This research was supported by National Science Foundation grant CBET-1032979.

4.6. References

1. K. Tanaka, Catal. Today **154** (1–2), 105-112 (2010).
2. L. P. Nielsen, F. Besenbacher, E. Laegsgaard and I. Stensgaard, Phys. Rev. B **44** (23), 13156-13159 (1991).
3. A. Hellman, A. Resta, N. M. Martin, J. Gustafson, A. Trinchero, P. A. Carlsson, O. Balmes, R. Felici, R. van Rijn, J. W. M. Frenken, J. N. Andersen, E. Lundgren and H. Grönbeck, J. Phys. Chem. Lett. **3** (6), 678-682 (2012).
4. J. Klikovits, M. Schmid, L. R. Merte, P. Varga, R. Westerström, A. Resta, J. N. Andersen, J. Gustafson, A. Mikkelsen, E. Lundgren, F. Mittendorfer and G. Kresse, Phys. Rev. Lett. **101** (26), 266104 (2008).
5. D. Teschner, J. Borsodi, A. Wootsch, Z. Révay, M. Hävecker, A. Knop-Gericke, S. D. Jackson and R. Schlögl, Science **320** (5872), 86-89 (2008).
6. D. Teschner, J. Borsodi, Z. Kis, L. Szentmiklósi, Z. Révay, A. Knop-Gericke, R. Schlögl, D. Torres and P. Sautet, J. Phys. Chem. C **114** (5), 2293-2299 (2010).

7. E. M. Vass, M. Hävecker, S. Zafeiratos, D. Teschner, A. Knop-Gericke and R. Schlögl, J. Phys.: Condens. Matter **20** (18), 184016 (2008).
8. K. Reuter and M. Scheffler, Phys. Rev. B **65** (3), 035406 (2001).
9. K. Reuter and M. Scheffler, Phys. Rev. Lett. **90** (4), 046103 (2003).
10. C. l. Chizallet, G. t. Bonnard, E. Krebs, L. Bisson, C. c. Thomazeau and P. Raybaud, J. Phys. Chem. C **115** (24), 12135-12149 (2011).
11. N. İnoğlu and J. R. Kitchin, J. Catal. **261** (2), 188-194 (2009).
12. A. D. Mayernick and M. J. Janik, J. Chem. Phys. **131** (8), 084701-084712 (2009).
13. A. C. T. van Duin, S. Dasgupta, F. Lorant and W. A. Goddard III, J. Phys. Chem. A **105** (41), 9396-9409 (2001).
14. G. B. Hoflund, H. A. E. Hagelin, J. F. Weaver and G. N. Salaita, Appl. Surf. Sci. **205** (1-4), 102-112 (2003).
15. R. V. Gulyaev, A. I. Stadnichenko, E. M. Slavinskaya, A. S. Ivanova, S. V. Koscheev and A. I. Boronin, Appl. Catal. A: Gen. **439–440** (0), 41-50 (2012).
16. T. Engel and G. Ertl, J. Chem. Phys. **69** (3), 1267-1281 (1978).
17. J. Y. Han, D. Y. Zemlyanov and F. H. Ribeiro, Surf. Sci. **600** (13), 2730-2744 (2006).
18. D. W. Brenner, Phys. Rev. B **42** (15), 9458-9471 (1990).
19. J. Tersoff, Phys. Rev. Lett. **61** (25), 2879-2882 (1988).
20. W. J. Mortier, S. K. Ghosh and S. Shankar, J. Am. Chem. Soc. **108** (15), 4315-4320 (1986).
21. T. P. Senftle, R. J. Meyer, M. J. Janik and A. C. T. van Duin, J. Chem. Phys. **139** (4), 044109-044115 (2013).
22. T. P. Senftle, M. J. Janik and A. C. T. van Duin, J. Phys. Chem. C (2013).
23. D. Frenkel and B. Smit, *Understanding molecular simulation : from algorithms to applications*. (Academic Press, San Diego, 2002).
24. G. Ketteler, D. F. Ogletree, H. Bluhm, H. J. Liu, E. L. D. Hebenstreit and M. Salmeron, J. Am. Chem. Soc. **127** (51), 18269-18273 (2005).
25. E. Lundgren, J. Gustafson, A. Mikkelsen, J. N. Andersen, A. Stierle, H. Dosch, M. Todorova, J. Rogal, K. Reuter and M. Scheffler, Phys. Rev. Lett. **92** (4), 046101 (2004).
26. H. Zhang, J. Gromek, G. Fernando, H. Marcus and S. Boorse, Journal of Phase Equilibria **23** (3), 246-248 (2002).
27. S. C. Su, J. N. Carstens and A. T. Bell, J. Catal. **176** (1), 125-135 (1998).
28. R. Toyoshima, M. Yoshida, Y. Monya, K. Suzuki, B. S. Mun, K. Amemiya, K. Mase and H. Kondoh, Journal of Physical Chemistry Letters **3** (21), 3182-3187 (2012).

Chapter 5
The influence of hydroxyls on Pd-atom mobility and clustering on rutile TiO_2(011)-2×1

This chapter is published as: R. Addou,* T. P. Senftle,* N. O'Connor, M. J. Janik, A. C. T. van Duin and M. Batzill, *ACS Nano* **8** (6), 6321-6333 (2014).
*Equal author contribution. Contributions are specified at the beginning of each section.

Abstract

Understanding agglomeration of late transition metal atoms, such as Pd, on metal-oxide supports, such as TiO_2, is critical for designing heterogeneous catalysts as well as for controlling metal/oxide interfaces in general. One approach for reducing particle sintering is to modify the metal oxide surface with hydroxyls that decrease ad-atom mobility. We study by scanning tunneling microscopy experiments, density functional theory (DFT) calculations, and Monte Carlo (MC) computer simulations, the atomistic processes of Pd-sintering on a hydroxyl-modified TiO_2(011)-2×1 surface. The formation of small 1- to 3-atom clusters that are stable at room temperature is achieved on the hydroxylated surface, while much larger clusters are formed under the same conditions on a hydroxyl-free surface. DFT shows that this is a consequence of stronger binding of Pd-atoms adjacent to hydroxyls and increased surface diffusion barriers for Pd-atoms on the hydroxylated surface. DFT, kinetic MC, and ReaxFF-based NVT-MC simulations show that Pd-clusters larger than single Pd monomers can adsorb the hydrogen from the oxide surface and form Pd-hydrides. This depletes the surface hydroxyl coverage, thus allowing Pd to more freely diffuse and agglomerate at room temperature. Experimentally this causes a bi-modal cluster size distribution with 1-3 atom clusters prevalent at low Pd coverage, while

significantly larger clusters become dominant at higher Pd concentrations. This study demonstrates that hydroxylated oxide surfaces can significantly reduce Pd-cluster sizes, thus enabling the preparation of surfaces populated with metal clusters comprised of single to few atoms.

5.1. Introduction

Diffusion and agglomeration of metal ad-atoms on oxide-surfaces plays an important role in the creation of nano-particles, and more generally, in the formation of metal/oxide interfaces. The dispersion of transition metals and their agglomeration into clusters on metal oxide supports is of particular interest for the formation of catalytically active metal nanoclusters. Single-atom catalysts,[1-3] as well as cluster-size dependent chemical functionality have been documented.[4] Notably for gold, numerous studies demonstrate a dramatic effect of cluster size on catalytic activity.[5-11] Similarly, Pd-clusters display numerous size dependent chemical properties.[12-17] In addition to catalysis, the agglomeration of metal atoms into clusters also affects the formation of ultra-thin metal coatings on metal oxides. In order to synthesize and maintain small clusters, ad-atom mobility and sintering must be suppressed. For planar model catalysts used in fundamental surface science studies, transition metals are commonly vapor deposited on oxide supports. However, vapor deposition of transition metals at room temperature on oxide supports usually results in nanometer-sized clusters with several hundred atoms, which precludes investigation of very small nanoclusters. In addition, to address the technologically important issue of oxide wetting with metal layers, hydroxylation of oxides has been

suggested as a means for increasing metal binding. [18-20] Thus, both the formation of very small metal clusters, as well as metal coatings, may be controlled by hydroxyls on oxide surfaces. Unfortunately, the fundamental processes governing metal-hydroxyl interactions on oxide surfaces are not well understood. Here we combine scanning tunneling microscopy with computer simulations to investigate the interplay between hydroxyls and transition metal atoms, thus yielding atomic level insight to the effect of oxide hydroxylation on metal cluster formation.

Numerous scanning tunneling microscopy (STM) studies of vapor-deposited metals on planar oxide model systems have contributed to the understanding of metal diffusion and agglomeration.[21-23] The majority of these studies focused on pristine metal oxide surfaces, while some investigated the role of impurities,[24] particularly hydroxyls, on metal cluster formation. Matthey *et al.* investigated the bonding of Au on TiO_2(110) for variously prepared surfaces.[25] For hydroxylated surfaces, an apparent decreased adhesion of Au was found resulting in the formation of large Au-clusters compared to vacuum prepared TiO_2(110) surfaces, which contain O-vacancies. Conversely, hydroxyls on Fe_3O_4 surfaces induced stronger Pd binding and reduced sintering.[26] Previous DFT studies for Ag on hydroxylated alumina[27,28] also suggest that the interaction-strength between the hydroxyl and the transition metal ad-atoms is important for determining the sintering behavior of transition metals.

Here we use STM experiments in conjunction with DFT calculations, kinetic Monte Carlo (kMC) simulations, and ReaxFF-based Monte Carlo simulations to investigate Pd ad-atom behavior on pristine and hydroxylated TiO_2(011)-2×1 surfaces. At low Pd-coverage, the hydroxyl groups effectively suppress surface diffusion, leading to small Pd

clusters that are stable at room temperature. This is contrasted by the formation of large Pd clusters on the pristine surface. Furthermore, simulations show that Pd clusters as small as two atoms can remove hydrogen from the TiO_2(011)-2×1 surface and adsorb it on the Pd clusters. This process is made possible by the known weak binding of hydrogen to the TiO_2(011)-2×1 surface.[29] An obvious consequence of removing the hydroxyls from the TiO_2 surface is that this process also causes the hydrogen induced increased diffusion barriers for Pd ad-atoms to disappear. This then facilitates sintering of Pd to a level similar to that of an initially hydroxyl free surface. Thus at a Pd-coverage that is high enough to remove all the hydroxyls from the TiO_2 surface the sintering and agglomeration of Pd is expected to be undistinguishable or at least very similar to that on an initially hydroxyl-free surface.

Generally, our atomistic studies demonstrate that hydroxyls on oxide surfaces can strongly affect the diffusion and sintering of metals. However, on this particular TiO_2 surface two Pd atoms are sufficient to remove one hydroxyl from the TiO_2 surface and consequently remove the additional Pd-diffusion barrier the hydroxyls introduce. Thus only small Pd-clusters are prevented from sintering. Also note that 2-atom Pd cluster can only adsorb one hydrogen and thus additional hydroxyls at the surface can still prevent diffusion of Pd-atoms from such a Pd_2H cluster. This explains the presence of 2- and 3-atom clusters in STM images on a hydroxylated surface at low coverage. Importantly, the agreement between the experiment and simulation validates our theoretical description, providing rationale for screening methods that could identify metal-oxide systems that may yield high concentrations of small clusters that are resistant to sintering at room temperature.

5.2. Methods

5.2.1. Experimental Methods

**(Note: Experiments performed by R. Addou,
text written by R. Addou and M. Batzill)**

The experiments were carried out in a UHV chamber with a base pressure in the low 10^{-10} Torr range. The chamber is equipped with facilities for substrate cleaning including an ion-gun for ion-sputtering of the sample with 1 keV Ar^+ ions and a radiative BN-sample heater that allows sample heating up to 800 °C. For sample characterization the UHV chamber was equipped with low energy electron diffraction (LEED) and an Omicron variable temperature STM operated at room temperature. The TiO_2 samples used in this study were cleaned by repeated cycles of sputtering and annealing to 650 °C in vacuum. Sample cleanliness was checked by STM prior to Pd deposition. Pd was evaporated from a home built Pd-source consisting of a Pd-wire wrapped around a tungsten wire that could be heated by a direct current. We always deposited Pd with the sample cooled to room temperature. The deposition rate may be estimated from the STM images to ~6×10^{-3} atoms/(nm^2s) which can be expressed as one equivalent-monolayer in ~30 min deposition time.

The samples studied here are rutile TiO_2(011) single crystals purchased from MTI corporation. Unlike the more frequently studied TiO_2(110) surfaces the TiO_2(011) surface reconstructs into a 2×1 superstructure. Furthermore, vacuum prepared surfaces do not exhibit the high density of O-vacancies like the (110) surface. These hydroxyls appear as bright protrusions in empty state STM images. In some samples hydrogen is naturally

present and no additional preparation is required to obtain a high hydrogen coverage. Alternatively atomic hydrogen can be adsorbed at the surface. This has been achieved by utilizing a hot tungsten filament in 2×10^{-6} Torr H_2 background gas and the sample facing the filament. In this way we obtained a maximum coverage of about 0.2 monolayers of hydrogen. Hydrogen can also be removed from the surface by exposure to 10^{-6} Torr O_2 at room temperature. Similar reaction of hydroxyls with O_2 has also been reported for the (110) surface.[3]

5.2.2. DFT Method

The Vienna ab initio simulation package (VASP) was implemented for all DFT calculations.[49,50] The projector augmented wave (PAW) formalization was employed to treat atomic core regions,[51] and valence configurations of $4d^{10}$ for Pd atoms, $2s^2 2p^4$ for O atoms, and $3p^6 3d^2 4s^2$ for Ti atoms. All calculations were spin polarized. The Perdew-Wang (PW91) version of the generalized gradient approximation (GGA) was used to treat the exchange-correlation functional, and plane-wave basis sets were truncated at 450 eV. The TiO_2(011)-2×1 reconstructed surface was modeled in a 2×1 unit cell with three TiO_2 tri-layers perpendicular to the surface, where the topmost tri-layer consisted of the reconstructed surface and bottom tri-layer was fixed during structural optimizations. A 15 Å vacuum layer was included separating periodic images perpendicular to the surface. The convergence criterion for structural optimization was 0.05 eV $Å^{-1}$ for atomic forces in all directions. The Monkhorst-Pack (MP) method[52] was employed to model the first Brillouin zone of all periodic calculations, where a 3×3×1 MP k-point spacing was employed. The

gas phase Pd atom reference for surface binding energies was modeled in a 45Å × 45Å × 45Å periodic box, where solely the Γ point was considered. Transition states for Pd and H diffusion on the TiO_2 surface were identified by the climbing image nudged elastic band (CI-NEB) procedure implemented in VASP.[53]

There is a well-known deficiency in the GGA-PW91 functional for describing localized Ti 3d states that may become partially occupied when the surface is reduced by adsorbed H atoms. This issue can be mitigated by the inclusion of the Hubbard U term, which prevents spurious delocalization of localized states.[54] To assess the impact of this deficiency, we conducted DFT+U calculations with a U value of 4.2 eV[55] applied to the 3d states of all Ti atoms. We found that the inclusion of U value yields similar Pd adsorption energies and higher Pd diffusion barriers. However, the relative trends in diffusion barriers remained the same as those identified when the U value was excluded. On the clean surface, the lowest diffusion barrier for Pd migration in the $[0\bar{1}1]$ direction was 31.9 kcal mol^{-1}, compared to the barrier of 35.0 kcal mol^{-1} on the hydroxylated surface. The difference of 3.1 kcal mol^{-1} yields a diffusion rate in the preferred direction parallel to the zig-zag row ~1.9×10^2 times slower on the hydroxylated surface at 300 K. , in qualitative agreement with the results obtained above without the U term.

5.2.3. kMC Method

DFT energetics were used to derive Pd hopping rates during kMC simulations of Pd cluster formation on the TiO_2 surface. Diffusion rates were derived from harmonic transition state theory, where the activation barrier for each process is determined by cluster

size and whether the move is within a trough or is over the zig-zag row. For moves involving a Pd atom leaving a cluster, the barrier is increased by the sintering energy given by:

$$E_{sinter} = E(Pd_{n-1} + Pd_1) - E(Pd_n) \quad . \tag{1}$$

We applied sintering energies derived from the DFT data for cluster adsorption provided in Table 5-1, where the additional sintering energy was 19.2 kcal mol^{-1} to remove a Pd atom from a Pd_3 cluster and was 15.6 kcal mol^{-1} to remove a Pd atom from a Pd_4 cluster. As seen in the table, there is little difference in adsorption energy per Pd atom between a single Pd monomer and a dimer, so no sintering energy was included in the barrier when a Pd atom is removed from a dimer. Furthermore, we assumed that the sintering energy was constant for Pd clusters larger than four atoms. This results in six processes with unique rates: (1) a move within the trough, or (2) a move over the zig-zag row; each coupled with (1) a move from a monomer or dimer, (2) a move from a Pd_3 cluster, or (3) a move from a $Pd_{n\geq4}$ cluster. Finally, we conducted the simulations at a temperature of 450 K, which is high enough to induce sintering. We assume the usual pre-exponential factor of 10^{13} s^{-1}, which results in the rate constants provided in Table 5-1 for each of the six processes.

During each kMC step, a move is chosen from the following well-known kMC criteria derived from detail-balance relationships:[56]

$$R = \sum_i n_i r_i \tag{2}$$

$$\frac{1}{R}\sum_{i=0}^{k} n_i r_i \geq rand(0,1) > \frac{1}{R}\sum_{i=0}^{k-1} n_i r_i \tag{3}$$

where R is the sum of the rates of all possible processes, r_i is the rate of process i, and n_i is the number of available processes with rate r_i. r_k is the randomly selected rate, from which one of the process with rate r_k is executed. The system time is then updated using the following:

$$t = t + \Delta t \text{, and } \Delta t = -\frac{1}{R}\log[rand(0,1)] \quad (4)$$

where the time step of each move is inversely proportional to the overall rate total, R.

Table 5-1. Rate constants determined from harmonic transition state theory for possible move types during kMC simulations on the clean and hydroxylated TiO_2(011)-(2×1) surface at 450 K.

TiO_2-clean *Move Type*	*Cluster Size (# atoms)*	*Barrier (kcal mol^{-1})*	*Sintering Energy (kcal mol^{-1})*	*Rate Constant (s^{-1})*
In Trough	1 or 2	21.2	-	5.1×10^{2}
In Trough	3	21.2	19.2	2.4×10^{-7}
In Trough	≥4	21.2	15.6	1.3×10^{-5}
Over Row	1 or 2	24.0	-	2.2×10^{1}
Over Row	3	24.0	19.2	1.1×10^{-8}
Over Row	≥4	24.0	15.6	5.8×19^{-7}
TiO_2-(OH) *Move Type*	*Cluster Size (# atoms)*	*Barrier (kcal mol^{-1})*	*Sintering Energy (kcal mol^{-1})*	*Rate Constant (s^{-1})*
In Trough	1 or 2	24.1	-	1.9×10^{1}
In Trough	3	24.1	19.2	9.3×10^{-9}
In Trough	≥4	24.1	15.6	5.2×10^{-7}
Over Row	1 or 2	28.9	-	9.2×10^{-2}
Over Row	3	28.9	19.2	4.3×10^{-11}
Over Row	≥4	28.9	15.6	2.4×10^{-9}

5.2.4. ReaxFF Potential and MC Method

The ReaxFF potential is a classical force-field method that is computationally inexpensive compared ab initio total energy calculations, which enables studies on system models far larger than those typically employed for QM calculations.[57] The combination of both bonding and non-bonding interactions enables the potential to model van der Waals, Coulombic, and covalent interactions during reactive events, thus allowing simulations involving complex metal/oxide/gas interfaces.[58-62] This makes the ReaxFF potential ideal for modeling hydrogen uptake in large (~20 atom) Pd clusters supported on an extensive (~1000 atom) TiO_2 surface. The Ti/O/H,[63] Pd/O,[64] and Pd/H[65] interaction parameters employed here were developed previously. The Pd/O and Pd/H parameters have not been altered, whereas the O-H bond energy term was altered in the Ti/O/H description in order to properly reproduce H atom binding on the TiO_2-2x1 surface. The Ti/O/Pd three-body interaction terms were optimized against a training set consisting of Pd_n (n = 1 to n = 4) cluster adsorption energies on the surface at varying sites.

The optimized ReaxFF potential was employed in NVT-MC simulations in which the number of atoms (N), system volume (V), and system temperature (T) were fixed. Each MC step randomly displaced a H atom to a new location anywhere in the unit cell, and the resulting configuration was accepted or rejected according to the Metropolis probability criterion[56,65] $Prob = \min\left[1, \exp\left[-\beta(E_2 - E_1)\right]\right]$. The system was considered converged if the total system energy did not change by more than 10 kcal mol^{-1} over the final 1000 MC trial iterations. A CG relaxation step prior to applying the Metropolis criterion is often necessary to increase the acceptance rates for 'off-lattice' MC moves in which the

displacement of one atom may require a structural relaxation in the surrounding system. The converged structure at the end of the simulation represents the equilibrated surface structure at the temperature set by the Metropolis criterion (300 K).

5.3. Results

5.3.1. Scanning Tunneling Microscopy Investigation of Pd-cluster Formation

(**Note: Experiments performed by R. A. and text written by R. A. and M. B.)**

Pd-atoms were vapor-deposited on the 2×1 reconstructed rutile TiO_2(011) surface[30-33] held at room temperature. For low doses of Pd, the adsorption structure on a clean TiO_2(011)-2×1 surface is compared to that of a hydroxylated surface in Figure 5-1. In Figure 5-1(a), a hydroxylated surface prior to Pd-deposition is shown. The hydroxyls appear in the STM images as bright protrusions situated slightly off-center of the characteristic zig-zag rows of the TiO_2(011)-2×1. Figure 5-1(b) shows the surface after the deposition of a small amount of Pd on a surface exhibiting hydroxyls, while Figure 5-1(c) shows the same amount of Pd deposited on a nearly hydroxyl-free surface. Clearly, a higher density of clusters is observed in Figure 5-1(b) than in Figure 5-1(c); and consequently the clusters in (b) are smaller than in (c). All the Pd-associated features in Fig.1(b) have similar apparent heights (2.1-3 Å). Only three different lateral sizes are observed. These different sizes are assigned to clusters with one-, two-, or three- Pd atoms. Particularly, the smallest clusters, which may be associated with single Pd-atoms, are situated close to the zig-zag row in STM. Also seen in Figure 5-1(b), an antiphase-domain boundary of the 2×1

reconstruction is visible running from the top to the bottom of the STM image. While we show below that such defects are preferential 'anchor-sites' for larger Pd clusters, for the low Pd density shown in Figure 5-1(b) no statistically significant increased Pd cluster formation along such defects is observed.

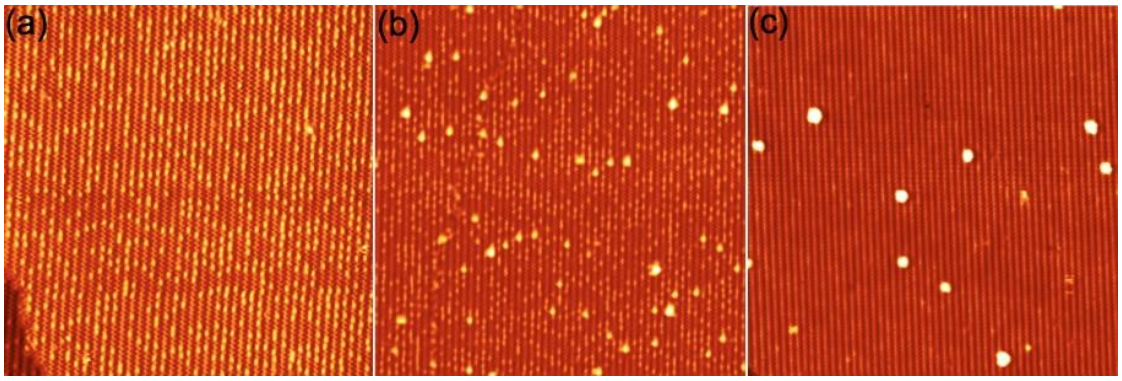

Figure 5-1. STM characterization of TiO_2(011)-2×1 surfaces. (a) a partially hydroxylated TiO_2 surface, with the bright spots indicating individual hydroxyl groups (40×40 nm, V_{bias}= 1.3 V, I_t= 0.4 nA) (b) hydroxylated TiO_2 surface after deposition of small amount of Pd, (50×50 nm, V_{bias}= 1.3 V, I_t= 0.5 nA) and (c) deposition of the same amount of Pd as in (b) on an almost hydroxyl-free surface (50×50 nm, V_{bias}= 1.3 V, I_t= 0.5 nA). The Pd-cluster sizes are small, typically only 1-3 atoms, in (b) compared to much larger clusters in (c).

On the hydroxyl-free surface, the cluster height and lateral dimensions are significantly larger. For an identical Pd amount as for the hydroxylated surface shown in Figure 5-1(b), the cluster heights are mainly in the range of 3.6-6.5 Å, indicating that the clusters are much larger in size and have a 3D-cluster shape that may be as much as three atoms tall. Furthermore, the smaller density of clusters, for nominally the same amount of Pd, also indicates the larger size of the clusters. The differences in size and density of Pd-clusters for the hydroxyl free surface compared to the partially hydroxylated surface suggests that Pd atoms have very different mobility on these two surfaces. An obvious assessment is that on the hydroxylated surface, Pd atoms cannot diffuse over long distances and consequently do not sinter into larger clusters.

Staying with an initially hydroxylated surface, we investigated the cluster evolution as a function of the amount of deposited Pd. A Pd evaporation source with constant Pd flux is used, so that the amount of Pd is proportional to the deposition time. Thus, we consider the deposition-time a measure of the amount of Pd deposited. As noted above, for Pd-deposition time of less than one minute, we observe only clusters of ~ 1-3 atoms in size. For Pd deposition times of 1-3 min, we observe a bimodal cluster-size distribution. In addition to the small clusters, clusters larger and taller are observed with a height of 3-6 Å. These larger clusters are comparable to the clusters observed at low Pd-coverage on the hydroxyl-free surface.

Figure 5-2 shows the cluster densities for the 'small' and 'large' clusters as a function of Pd-deposition time. For very low deposition times, only small clusters are present. With increasing Pd-deposition time, initially the density of both small and large clusters increases. After 2 minutes of deposition, the density of small clusters decreases while the density of large clusters remaining nearly constant. This suggests that the small clusters have been incorporated into the larger clusters. With increasing Pd deposition the clusters continue to grow, though no new large clusters are nucleated once a critical density has been reached. In addition, hydroxyls between the clusters disappear with increasing Pd-deposition. At the point of maximum cluster density, *i.e.* after ~ 3 minutes deposition time, almost no hydroxyls remain at the surface. The absence of hydroxyls can be seen in the higher resolution image shown for 6 minutes deposition time in Figure 5-3(a). Furthermore, the decoration of step edges and antiphase-domain boundaries with larger Pd clusters is seen in Figure 5-3(b) after 20 minutes of deposition time. Step edges that are parallel to the $[0\bar{1}1]$ direction, *i.e.* parallel to the row structure of the surface reconstruction,

show less decoration than step edges that intersect the surface row structure. This indicates that Pd atoms preferentially diffuse along the rows and are anchored at step edges that intersect this diffusion direction. Preferential diffusion along the rows of the reconstruction is consistent with a lower diffusion barrier in this direction in agreement with computed diffusion barriers discussed below. While a preferred diffusion direction is a kinetic effect, the decoration of step edges and antiphase boundaries may indicate that binding at these defects is also enhanced, as has been observed for metal clusters on many other oxide supports.[34-36]

These experimental results suggest the following mechanisms. At low Pd coverage, hydroxyls prevent diffusion of Pd atoms, resulting in small Pd clusters consisting of only 1-3 Pd atoms. Furthermore, the disappearance of hydroxyls from the oxide surface for Pd deposition times longer than ~3 minutes suggests that larger Pd clusters take up hydrogen, which subsequently makes Pd ad-atoms more mobile and facilitates the formation of larger clusters. This uptake of hydrogen by Pd-clusters is confirmed below in computer simulations. The alternative explanation that the deposition of Pd-atoms causes thermal desorption of hydrogen from the TiO_2 surface is unlikely because of the previously reported thermal behavior of hydrogen on this surface. To substantiate the influence of hydroxyls on Pd adsorption we performed a series of computational analyses, which are discussed in the following sections.

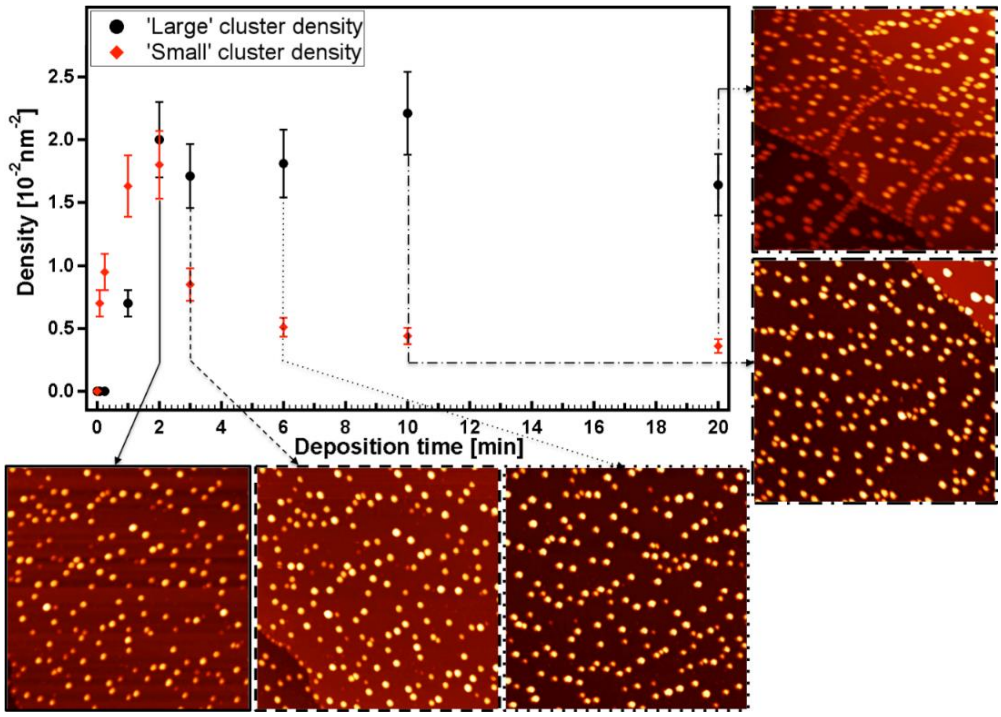

Figure 5-2. Evolution of cluster density as function of deposition time on an initially hydroxylated TiO_2(011)-2×1 surface. We distinguish between small clusters with an estimated 1-3 Pd atoms and larger clusters, whose height suggest at least 2-3 atom-layer height. The density of small clusters is shown as red-diamonds and the cluster density for the larger clusters as black-circles.

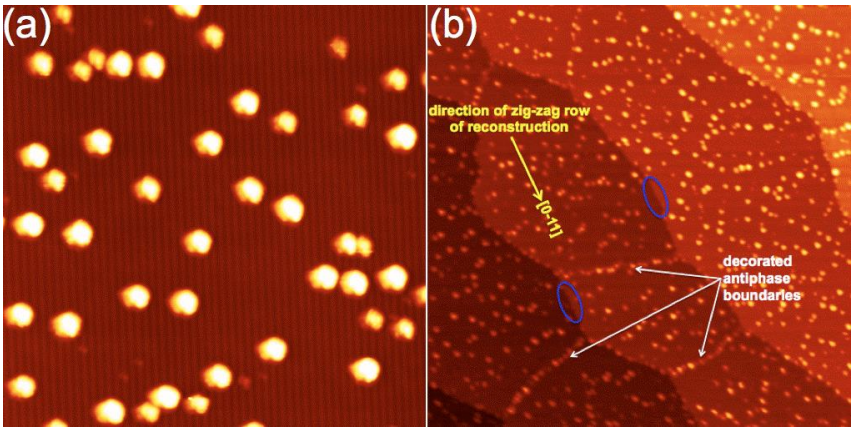

Figure 5-3. A Pd-clusters on a TiO_2(011)-2×1 after long (6 min) Pd-deposition. The surface in (a) was hydroxyl-modified prior to Pd-deposition (50 nm×50 nm, V_{bias}= 1.3 V, I_t= 0.5 nA). No hydroxyls remain at the surface suggesting that the Pd-clusters have absorbed the surface hydrogen. The decoration of antiphase domain boundaries of the 2×1 surface reconstruction by Pd clusters can be observed (white arrows). Also step edges are decorated with Pd, however, steps that are oriented parallel to the row-structure of the surface reconstruction are not decorated (blue ovals) indicating preferential Pd-diffusion in the direction of the Pd-rows.

5.3.2. Simulation of Pd Diffusion Barriers

Both DFT and classical computational techniques are employed to assess the various aspects of Pd diffusion, cluster formation, and hydrogen uptake on the clean and hydroxylated TiO_2(011)-2×1 surface. To determine the effect of adsorbed hydrogen on Pd mobility, DFT calculations are used to derive the potential energy surface for varying Pd diffusion paths over the clean and hydroxylated surfaces. The barriers and adsorption energies derived with DFT calculations are then employed in kinetic Monte Carlo simulations to assess cluster formation rates. Finally, a Ti/O/Pd/H ReaxFF potential is employed in Monte Carlo simulations to assess hydrogen transfer between the TiO_2 surface and Pd clusters of varying size.

DFT calculations were completed on two models of the TiO_2(011)-2×1 surface, consisting of a clean surface (shown in Figure 5-4) and a hydroxylated surface. The clean surface contains characteristic zig-zag rows separated by a trough region containing alternating hollow sites. The unit cell contains two top-oxygen atoms in the zig-zag row (labeled O1 and O2, where O4 is the periodic image of O1), two trough-oxygen atoms (labeled O7 and O8, where O9 is the periodic image of O7), and two bridging-oxygen atoms located on opposites sides of the zig-zag row (labelled O3 and O5, where O6 is the periodic image of O5). The hydroxylated surface model is obtained by adsorbing a single H atom in the unit cell above top-oxygen O1.

On the clean surface, a single Pd atom adsorbs most strongly in the hollow site of the trough between oxygen atoms O6 and O8, with an exothermic adsorption energy of -50.7 kcal mol^{-1} relative to the clean surface and a single gas phase Pd atom. Similarly on

the hydroxylated surface, the Pd atom binds most strongly in the hollow site between oxygen atoms O2 and O6, with an exothermic adsorption energy of -55.3 kcal mol^{-1}. Net diffusion in the [$0\bar{1}1$] direction parallel to the zig-zag row consists of Pd migration between adjacent hollow sites within the same trough, and net diffusion in the [100] direction perpendicular to the zig-zag row consists of Pd migration between adjacent hollow site separated by the row structure. The overall diffusion barrier for each direction can be assessed by determining the minimum energy path for Pd migration between adjacent sites in the trough (represented by green arrows in Figure 5-4) or between adjacent sites separated by the zig-zag row structure (represented by purple arrows).

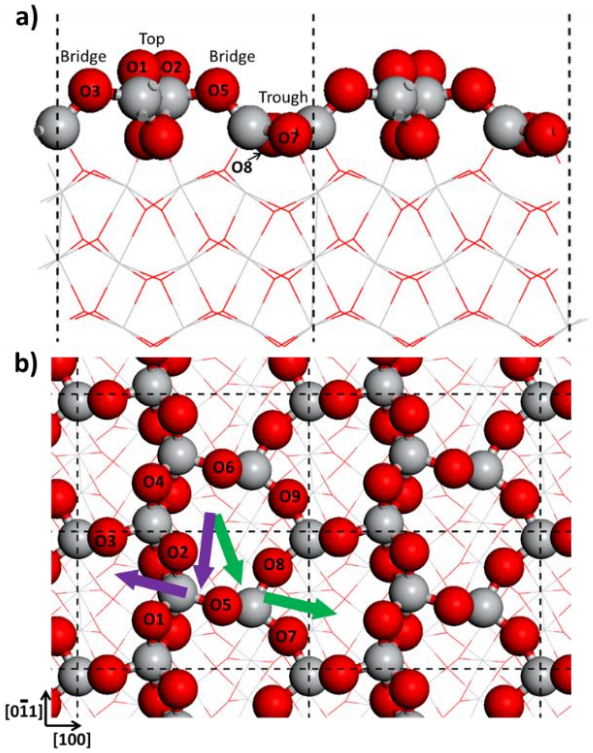

Figure 5-4. (a) Side and (b) top views of the TiO_2(011)-2×1 surface. Surface atoms are represented by spheres and bulk atoms are represented by lines. The dashed lines indicate the unit cell used in all calculations. Purple arrows indicate the Pd diffusion path parallel to the [100] direction traversing the top-oxygens of the zig-zag row. The green arrows indicate the Pd diffusion path traversing trough-oxygens between adjacent hollow sites parallel to the [0-11] direction.

The minimum energy paths for Pd migration on the clean TiO_2 surface are shown in Figure 5-5. As seen in the figure, we identified energy minima within the hollow site between oxygen atoms O2-O8 (Figure 5-5b) and between oxygen atoms O2-O6 (Figure 5-5c) that are 6.3 kcal mol^{-1} and 4.7 kcal mol^{-1} higher in energy than the preferred hollow site (Figure 5-5a), respectively. Figure 5-5d depicts a meta-stable adsorption site between oxygen atoms O8-O5, from which the Pd atom may migrate into the adjacent hollow site within the trough by traversing the bridging oxygen O8, or may migrate over the row by traversing top oxygen atoms O1-O2. The overall activation barriers for these two processes are 21.2 kcal mol^{-1} and 24.0 kcal mol^{-1}, respectively, where the transition state structures identified for these two paths are depicted in the insets of the figure. Using a simple Arrhenius relationship, we approximate that diffusion in the $[0\bar{1}1]$ direction parallel to the zig-zag row is $\sim 1.1\times10^2$ times faster than diffusion in the [100] direction at 300 K, in agreement with the experimental observations described above.

Figure 5-6 depicts the calculated minimum energy paths for Pd migration on the hydroxylated TiO_2 surface. In addition to the preferred adsorption site in the surface hollow between O2-O6 (Figure 5-6a), we identified an energy minimized site in the surface hollow between O2-O8 (Figure 5-6b) that is 4.9 kcal mol^{-1} higher in energy than the preferred site. Again, from this site the Pd atom can migrate to an adjacent hollow site within the trough by traversing trough oxygen O8, or can diffuse into the adjacent trough by traversing top oxygen O2. The transition state structures for each of these paths are shown in the insets of the figure, yielding overall diffusion barriers of 24.1 kcal mol^{-1} and 28.9 kcal mol^{-1} for diffusion in the $[0\bar{1}1]$ direction and [100] direction, respectively. Similar to the clean

surface, diffusion in the [0$\bar{1}$1] direction is preferred, and occurs ~3.1×10^3 times faster at 300 K than diffusion in the [100] direction perpendicular to the zig-zag row. Compared to the clean surface, the diffusion barrier in the [0$\bar{1}$1] direction yields a diffusion rate ~1.3×10^2 times slower than the rate over the analogous path on the clean surface. Likewise, the barrier in the [100] direction yields a diffusion rate ~3.7×10^3 times slower than the analogous rate on the clean surface. These results corroborate the above experimental observations by demonstrating that hydroxyl groups on the TiO_2 surface hinder Pd diffusion rates, thus preventing the agglomeration of Pd atoms into large clusters.

Unlike the clean surface, adjacent hollow sites on the hydroxylated surface are not necessarily equivalent, as the additional hydrogen atom can be adsorbed on either top oxygen O1 or O2, which breaks the symmetry of the unit cell. This is illustrated in the figure, where the most stable site in the adjacent hollow (Figure 5-6c) yields an adsorption energy 14.1 kcal mol^{-1} higher than the preferred site. The equivalent of the optimal adsorption site can be obtained by transferring the adsorbed hydrogen from O1 to O2, which is depicted by the blue dashed line in the figure. The barrier for hydrogen transfer is 17.0 kcal mol^{-1} relative to the structure shown in Figure 5-6c, which is similar to the barrier of 17.3 kcal mol^{-1} for the analogous hydrogen transfer in the absence of adsorbed Pd. The barrier for the reverse hydrogen transfer process is 31.2 kcal mol^{-1}, indicating that adsorbed Pd atoms hinder H diffusion across the TiO_2 surface. Hence, the apparent diffusion barriers for Pd migration consist of the paths shown in green and purple in Figure 5-6.

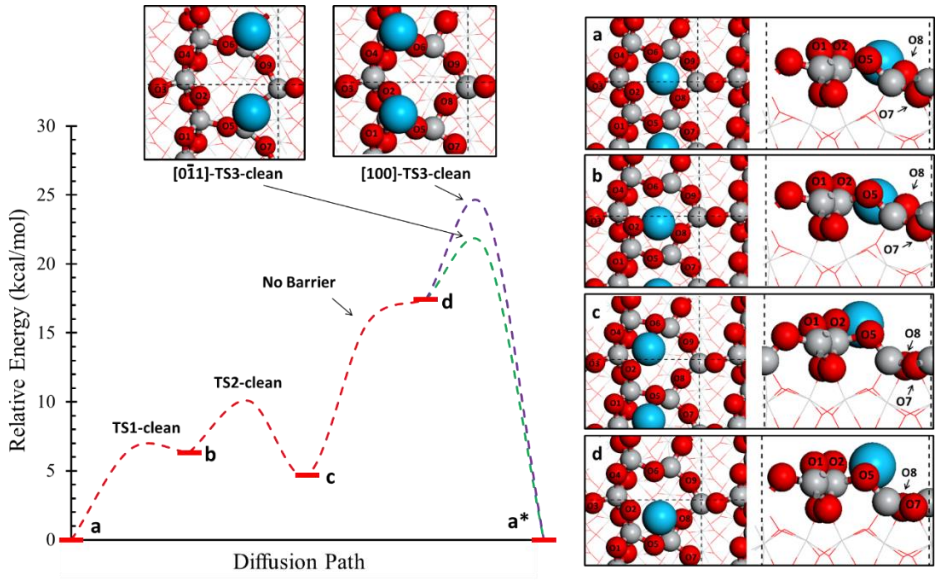

Figure 5-5. Diffusion barrier over the clean TiO_2 surface for Pd migration between hollow sites traversing top-oxygens (purple) and traversing trough-oxygens (green). Energy minimized structures are shown to the right, and transition state structures are shown in the insets above. Symmetrically equivalent positions in adjacent hollow sites are marked with a star.

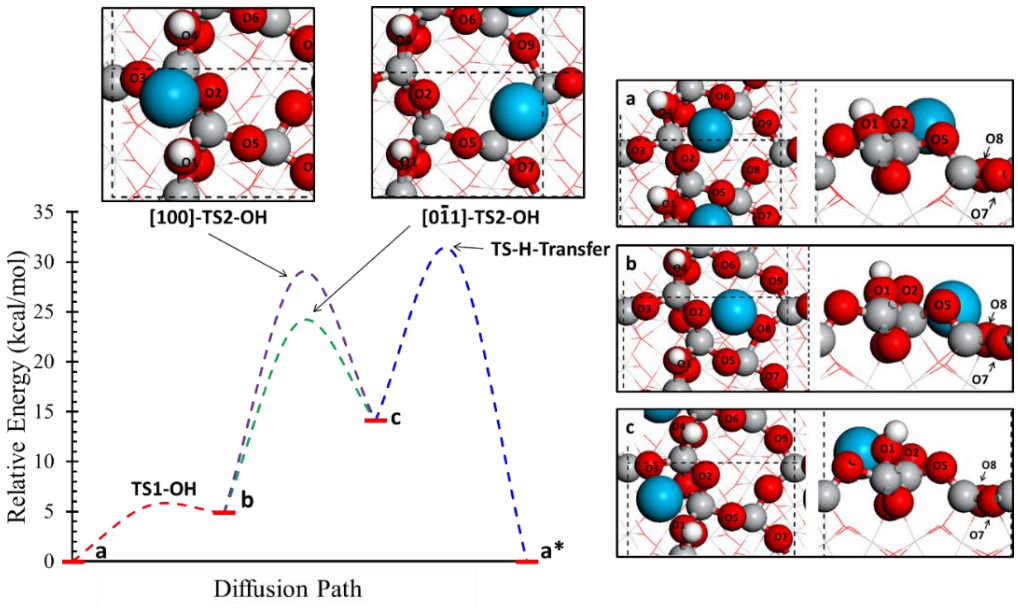

Figure 5-6. Diffusion barrier over the hydroxylated TiO_2-(OH) surface for Pd migration between hollow sites traversing top-oxygens (purple) and traversing trough-oxygens (green). The blue line represents the barrier for a hydrogen transfer from oxygen "O4" to oxygen "O2". Energy minimized structures are shown to the right, and transition state structures are shown in the insets.

5.3.3. Kinetic Monte Carlo Simulation of Pd Sintering

We employed kMC simulations to further assess the impact of hydroxyl groups on Pd cluster formation. These simulations utilize a simple sintering model,[37] in which Pd clusters are considered immobile and cluster growth occurs through the exchange of single Pd atoms between clusters. A similar kMC model was applied by Zhang and Alexandrova[38] to model Pd cluster growth on defective TiO_2(110) surfaces, demonstrating the feasibility of this approach for modeling Pd mobility on titania. To represent the TiO_2(011)-(2×1) surface, we constructed a 2-dimensional lattice, shown in the inset of Figure 5-7a, where every lattice position represents a Pd adsorption site in the preferred hollow position. During the simulation, single Pd atoms are exchanged between hollow sites, and the occupancy at each lattice position represents the cluster size at that adsorption site. The corresponding rate for each move is calculated from harmonic transition state theory, which is described in the methods section along with further details of the kMC method.

To simulate the sintering behavior observed experimentally in Figure 5-1, we performed each kMC simulation with a 100×100 lattice populated with 175 Pd atoms placed in random lattice positions. This lattice size and Pd adsorption density yields a 55 nm × 46 nm surface with a 0.0175 ML coverage of Pd, which is comparable to the experimental STM images shown in Figure 5-1. Each kMC simulation was conducted at 450 K for three seconds, which was sufficient to induce sintering on the clean surface. The results, shown in Figure 5-7, demonstrate that the elevated barriers on the hydroxylated surface effectively prevent cluster growth, as the majority of Pd atoms remain as monomers. Conversely, Pd atoms aggregate into larger Pd clusters on the clean surface,

where only a few Pd atom remain as monomers. The final cluster distributions, shown in Figure 5-7b-c, closely resemble the STM results shown in Figure 5-1, demonstrating the feasibility of the kMC sintering model. Nevertheless, these results are limited in that they assume that all adsorption sites are equivalent, and that the formation of clusters does not affect adsorption energies or barriers in adjacent sites. Furthermore, this model assumes that only Pd monomers are mobile, whereas it is possible that slightly larger Pd clusters (dimers and trimers) are also mobile. We assume that diffusion hindrance observed for Pd monomers will similarly apply to slightly larger clusters, and the qualitative conclusions are not affected. Despite these limitations, this simplified kMC model further illustrates the kinetic effect of surface hydroxyl groups on cluster formation.

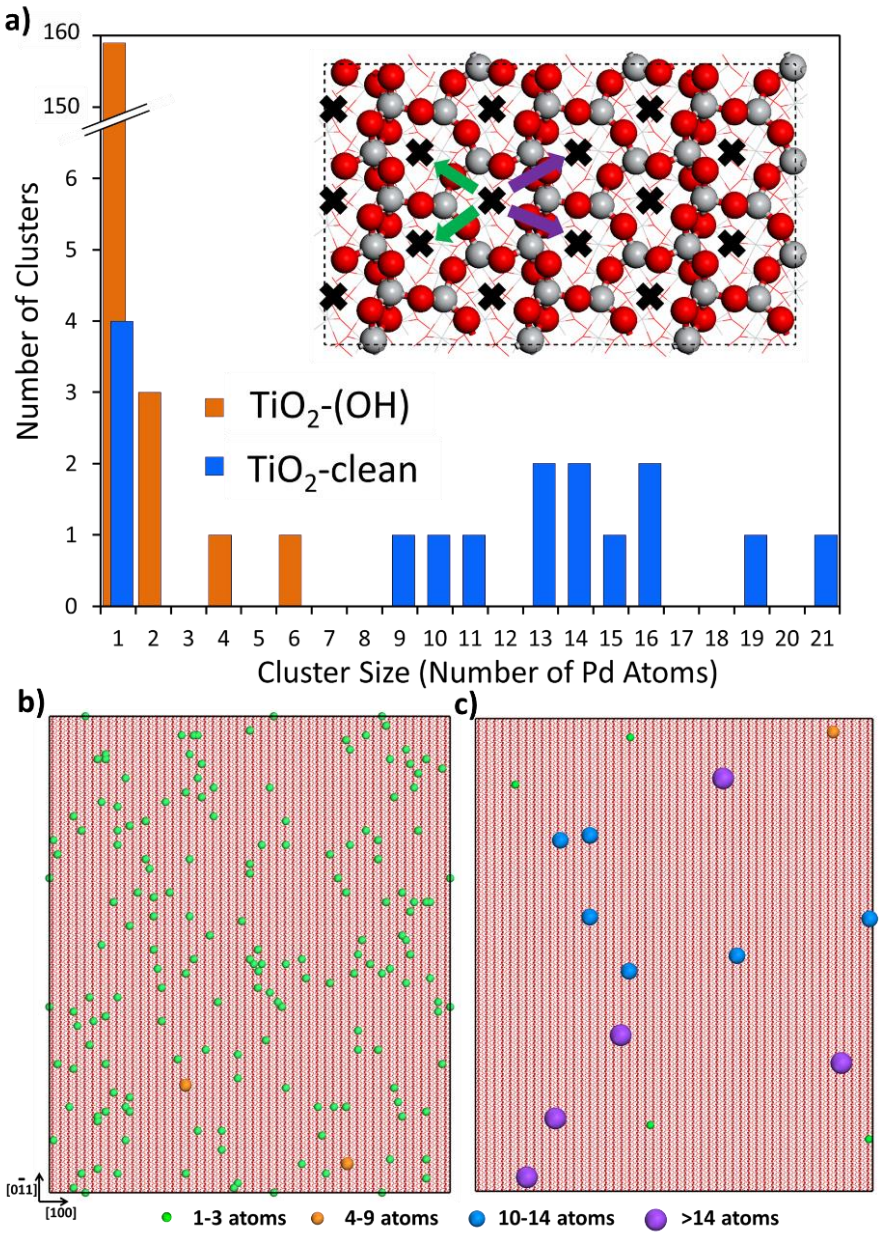

Figure 5-7. (a) Final cluster size distribution after 3 second kMC at 450 K. (b-c) Final cluster distribution projected on to the corresponding 55 nm x 46 nm (b) hydroxylated and (c) clean surfaces. Sphere size and color represents cluster size range: 1-3 atoms (small, green), 4-9 atoms (medium-small, orange), 10-14 atoms (medium-large, blue), and >14 atoms (large, purple).

5.3.4. ReaxFF Simulation of Pd-hydride Formation

Clusters of Pd-hydride may form on the TiO_2 surface, which was suggested in the experimental observation that the coverage of hydroxyl groups significantly decreased with the formation of larger Pd clusters. To investigate the thermodynamic preference for hydrogen to exchange between adsorption sites on the TiO_2 surface and the supported Pd clusters, we conducted MC simulations utilizing ReaxFF interaction parameters for Pd/Ti/O/H. These simulations featured MC steps where H atoms are randomly displaced in a unit cell consisting of a Pd cluster supported on a TiO_2 surface. The initial system, shown in Figure 5-8a, consisted of a 4×8 supercell built from the 2×1 unit cells employed in the DFT calculations. The supercell contains 16 H atoms distributed randomly in the preferred atop sites, yielding a hydrogen coverage of 0.2 ML. Simulations were repeated with varying cluster sizes, where each Pd_n cluster model was structurally optimized by choosing the lowest energy structure after using stochastic MC steps to sample multiple random configurations of the isolated cluster at 300 K. The optimized cluster model was then adsorbed on the TiO_2 surface in a hollow site, and was then further optimized using a conjugant-gradient relaxation of forces.

Using the cluster/surface model, MC steps consisting of a random H atom displacement were executed until the total system energy converged. The probability of accepting the resulting geometry after a MC trial step was determined by the usual Metropolis criteria, and is further described in the methods section. The results, summarized in Figure 5-8, demonstrate that H atoms generally prefer adsorption sites on the Pd cluster. This is demonstrated in Figure 5-8b, where nearly all of the H atoms initially

present on the TiO_2 surface have migrated to the Pd_{20} cluster. Similar results were obtained for smaller clusters, shown in Figure 5-8d, where the final H:Pd ratio in the cluster remains near ~0.6 in all cluster sizes, which is the ratio typically observed in the Pd-hydride phase.[39-42] In simulations with smaller clusters, excess H atoms remained on the TiO_2 surface after the Pd cluster became saturated with hydrogen. Additional DFT calculations were completed to assess H uptake by Pd monomers and dimers. As shown in Figure 5-9, hydrogen adsorption on the Pd dimer is 16.3 kcal mol^{-1} more favorable than H adsorption on the oxide surface, and the migration barrier for a H atom to move from the oxide to the dimer is 25.6 kcal mol^{-1}. This indicates that it is thermodynamically favorable for the Pd dimer to adsorb a hydrogen from an adjacent hydroxyl, but that the kinetics of this process will be slow at room temperature. It is reasonable to assume that this barrier will be significantly lower for migration to larger clusters, since larger clusters have a greater quantity of favorable adsorption sites leading to less constrained migration paths. H adsorption on the Pd monomer was 6.67 kcal mol^{-1} less favorable than adsorption on the oxide, indicating that it is thermodynamically unfavorable for a single Pd atom to remove a surface hydroxyl group.

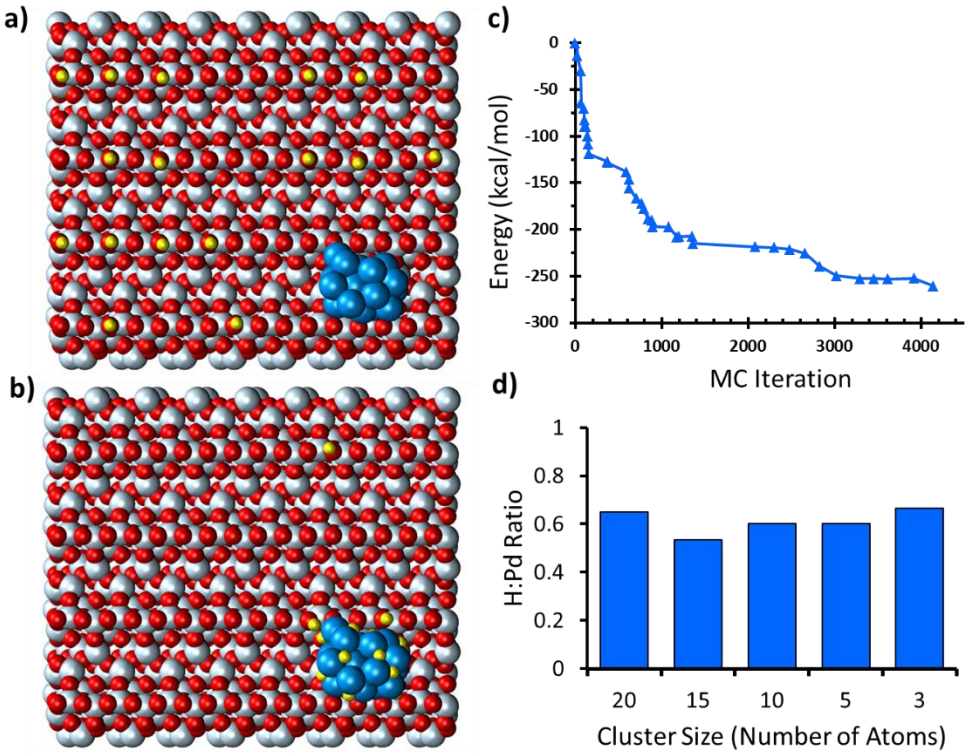

Figure 5-8. (a) Initial and (b) final structure of a NVT-MC simulation of PdH formation initiated from a clean Pd_{20} cluster adsorbed on the TiO_2 surface. (c) Convergence of the total system energy as hydrogen is adsorbed by the Pd cluster. (d) Final H:Pd ratios from converged simulations initiated with Pd_n cluster sizes ranging from $n = 20$ to $n = 3$.

These results corroborate the experimental findings reported above, in which H atoms from hydroxyl groups are absorbed by Pd clusters. The simulations suggest that there is a maximum H:Pd ratio in the clusters similar to that of the Pd-hydride phase (~0.6), and that additional hydrogen will remain on the surface after this limit is reached in the Pd-clusters. Hence, at low Pd deposition times many hydroxyl groups remain on the surface, inhibiting the formation of large Pd clusters. After a critical Pd deposition time, enough Pd clusters are on the surface to remove all hydroxyl groups, thus reducing Pd diffusion barriers leading to the formation of larger clusters.

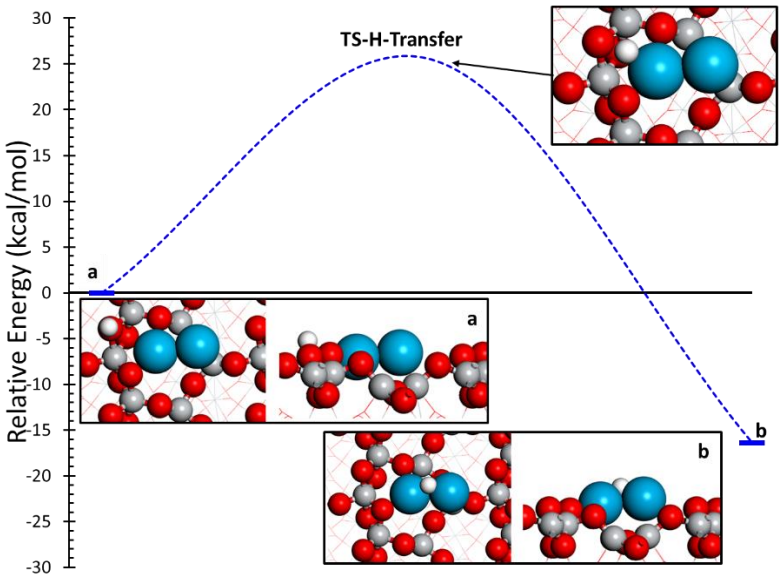

Figure 5-9. DFT minimum energy path for hydrogen transfer from a surface hydroxyl group to a Pd dimer. (Inset) Initial, final, and transition state structures.

5.4. Discussion and Conclusions

The effect of hydroxyl groups on the sintering behavior of Pd clusters adsorbed on a planar rutile-TiO_2(011)-2×1 surface has been investigated with combined experimental and computational techniques. TiO_2 is an important photocatalyst. However, in photocatalytic applications, typical a mixture of anatase and rutile polymorphs are used with the anatase polymorph being more photocatalytically active as a consequence of their bulk properties.[43] Pure rutile-TiO_2, on the other hand, may be used as traditional oxide support in heterogeneous catalysts. In addition to these important applications of TiO_2, the main motivation in using rutile single crystal samples in this study is its use as one of the prototypical surface science model systems for transition metal oxides.[44] Although the gas

phase environment of the samples during our experiments is very different to most applied conditions, it enables detailed sample characterization not otherwise possible. These controlled conditions are needed to correlate experimental findings with computational methods. Thus these kind of model systems are a central part for developing a detailed atomistic understanding of complex surface phenomena and provide important test scenarios for verifying computational methods.

Both experimental observation and theoretical prediction indicate that adsorbed hydroxyl groups anchor Pd ad-atoms, therefore increasing the Pd diffusion barrier and decreasing cluster sintering. Consequently, on the hydroxylated surface only small (1-3 atoms) Pd clusters form at low Pd concentrations, contrary to hydroxyl free surfaces where larger 3-D clusters form at similar Pd concentrations. DFT and ReaxFF results indicate that hydroxyl groups can be transferred from the oxide surface to Pd clusters as small as 2 atoms. The removal of hydrogen from the substrate enables Pd to freely diffuse and subsequently agglomerate into larger clusters. MC simulations indicate that the H:Pd ratio in Pd clusters remains near ~0.65 for all cluster sizes. Hence, a significant number of hydroxyl groups remain on the surface at low Pd deposition times. As the Pd deposition time increases, fewer hydroxyl remain on the surface, which in turn allows small Pd clusters to readily diffuse and agglomerate. This leads to a bimodal cluster size distribution at intermediate deposition times, where enough hydroxyl groups have been adsorbed to allow significant Pd clusters to form, and the remaining hydroxyl groups hinder Pd diffusion allowing small Pd clusters to persist on the surface.

As previous investigations have shown, hydroxyls may affect the sintering of metal clusters differently depending on the metal, the metal oxide support material, and

potentially the crystallographic orientation of the surface. The situation on the TiO_2(110) is somewhat convoluted because adsorption of water in addition of forming hydroxyls also removes surface O-vacancies, which are known to act as anchoring sites for metals.[45,46] Thus the different sintering behavior may be a consequence of fewer O-vacancies rather than hydroxyl formation. This problem is avoided in our experiments because the TiO_2(011)-2×1 is known to exhibit fewer O-vacancies in vacuum prepared surfaces[47] and hydroxyls are formed at the surface by adsorbing atomic-hydrogen.

Our results for Pd on TiO_2(011)-2×1 are similar to results for Pd on Fe_3O_4 that demonstrated suppressed Pd sintering on the hydroxylated surface. As our investigation shows, the mechanism of metal sintering has different contributions. An enhanced binding of ad-atoms to surface sites adjacent to hydroxyl groups and the associated increase in surface diffusion barriers is responsible for the initial suppression of Pd sintering. This metal-hydroxyl interaction will be different for different elements, and in some cases a lower diffusion barrier may result. We speculate that this is possibly the case for Au on the hydroxylated TiO_2(110) surface. The relatively weak adsorption of hydrogen on the TiO_2(011)-2×1 surface and the relatively strong Pd-H bond in the metal hydride explains why hydrogen can be readily removed from the oxide surface by the Pd clusters. The removal of hydroxyls from the surface at high Pd coverage subsequently increases the Pd ad-atom mobility. Consequently, the same cluster size distribution as what was observed on the clean TiO_2(011)-2×1 surface is obtained after the hydroxyl groups have been removed. Thus hydroxyls affect the sintering only at low Pd coverages in the case studied here. Generally, the tendency of metal clusters to absorb hydrogen from the oxide surface negating any ‘anchoring’ effect of small clusters by hydroxyls will depend on the tendency

of the metal to form hydrides and on the hydrogen-oxide bond strength. Other systems may not readily remove hydroxyl groups, and thus a cluster stabilization may be observed at higher metal coverages than those reported here. Therefore a strategy to increase cluster stabilization may be to find oxide supports with strong hydroxyl bonds.

In conclusion, while the complex interactions observed here do not reveal a universal prediction for the role hydroxyls play either enhancing or inhibiting metal sintering, the limited data available suggest that, for Pd, a strong interaction with surface hydroxyls increases diffusion barriers preventing sintering. In general, the agreement between the simulations and the experimental data shows that a good prediction of metal cluster sintering can be obtained by coupled DFT, kMC, and ReaxFF-MC simulations. This is promising for future efforts seeking to computationally screen metal-hydroxyl interactions in different oxide materials. Importantly, in the $Pd/TiO_2(011)$-2×1 system, hydroxylation of the surface enables the formation of room temperature stable single Pd ad-atoms, which without the hydroxyls would sinter into larger 3D clusters. Thus hydroxylation is a viable approach for stabilizing single transition metals on oxide supports.

5.5. Acknowledgement

The authors acknowledge financial support from the National Science Foundation through grant # CBET-1033000.

5.6. References

1. Qiao, B.; Wang, A.; Yang, X.; Allard, L.F.; Jiang, Z.; Cui, Y.; Liu, J.; Li, J.; Zhang, T. *Nat. Chem.* **2011**, *3*, 634-641.
2. Lin, J.; Qiao, B.; Liu, J.; Huang, Y.; Wang, A.; Li, L.; Zhang, W.; Allard, L.F.; Wang, X.; Zhang, T. *Angew. Chem. Int. Ed.* **2012**, *51*, 2920-2924.
3. Yang, X.F.; Wang, A.; Qiao, B.; Li, J.; Liu, J.; Zhang, T. *Acct. Chem. Res.* **2013**, *46*, 1740-1748.
4. Vajda, S.; Pellin, M.J.; Greeley, J.P.; Marshall, C.L.; Curtiss, L.A.; Ballentine, G.A.; Elam, J.W.; Catillon-Mucherie, S.; Redfern, P.S.; Mehmood, F.; Zapol, P. *Nat. Mater.* **2009**, *8*, 213-216.
5. Haruta, M. *Catal. Today* **1997**, *36*, 153-166.
6. Valden, M.; Lai, X.; Goodman, D.W. *Science* **1998**, *281*, 1647-1650.
7. Lemire, C.; Meyer, R.; Shaikhutdinov, Sh,.K.; Freund H.-J. *Surf. Sci.***2004**, *552*, 27-34.
8. Lee, S.; Fan, C.; Wu, T.; Anderson, S.L. *J. Amer. Chem. Soc.* **2004**, *126*, 5682-5683 (2004).
9. Sanchez, A.; Abbet, S.; Heiz, U.; Schneider, W.D.; Haekkinen, H.; Barnett, R.N.; Landman, U. *J. Phys. Chem. A* **1999**, *103*, 9573-9578.
10. Landman, U.; Yoon, B.; Zhang, C.; Heiz, U.; Arenz, M. *Top. Catal.* **2007**, *44*, 145-158.
11. Herzing, A.A.; Kiely, C.J.; Carley, A.F.; Landon, P.; Hutchings, G.J. *Science* **2008**, *321*, 1331- 1335.
12. Kaden, W.E.; Wu, T.; Kunkel, W.A.; Anderson, S.L. *Science* **2009**, *326*, 826-829.
13. Kaden, W.E.; Kunkel, W.A.; Kane, M.D.; Roberts, F.S.; Anderson S.L. *J. Amer. Chem. Soc.* **2010**, *132*, 13097-13099.
14. Kaden, W.E.; Kunkel, W.A.; Roberts, F. S.; Kane, M.; Anderson S.L. *J. Chem. Phys.* **2012**, *136* 204705.
15. Wörz, A.S.; Judai, K.; Abbet, S.; Heiz, U. *J. Amer. Chem. Soc.* **2003**, 125, 7964-7970.
16. Fischer-Wolfarth, J.H.; Farmer, J.A.; Flores-Camacho, J. M.; Genest, A.; Yudanov, I.V.; Rösch, N.; Campbell, C.T.; Schauermann, S.; Freund, H.J. *Phys. Rev. B* **2010**, *81*, 241416 (R).
17. Kunz, S.; Schweinberger, F.F.; Habibpour, V.; Röttgen, M.; Harding, C.; Arenz, M.; Heiz, U. *J. Phys. Chem. C* **2010**, *114*, 1651-1654.
18. Chambers, S. A.; Droubay, T.; Jennison, D. R.; Mattsson, T. R. *Science* **2002** *297*, 827-831.
19. Kelber, J.A.; Niu, C.; Shepherd, K.; Jennison, D.R.; Bogicevic, A. *Surf. Sci.* **2000**, *446*, 76-88.
20. Niu, C.; Shepherd, K.; Martini, D.; Tong, J.; Kelber, J.A.; Jennison, D.R.; Bogicevic, A. *Surf. Sci.* **2000**, *465*, 163-176.
21. Bäumer, M.; Freund, H.J. *Prog. Surf. Sci.* **1999**, *61*, 127-198.
22. Lai, X.; St. Clair, T.P.; Valden, M.; Goodman, D.W. *Prog. Surf. Sci.* **1998**, *59*, 25-52.

23. Dulub, O.; Batzill, M.; Diebold, U.; *Topics Catal.* **2005**; *36*, 65-76.
24. Heemeier, M.; Frank, M.; Libuda, J.; Wolter, K.; Kuhlenbeck, H.; Bäumer, M.; Freund, H. J. *Catal. Lett.* **2000**, *68*, 19-24.
25. Matthey, D.; Wang, J.G.; Wendt, S.; Matthiesen, J.; Schaub, R.; Laegsgaard, E.; Hammer, B.; Besenbacher, F. *Science* **2007**, *315*, 1692-1696.
26. Parkinson, G.S.; Novotny, Z.; Argentero, G.; Schmid, M.; Pavelec, J.; Kosak, R.; Blaha, P.; Diebold, U. *Nat. Mater.* **2013**, *12*, 724-728.
27. Meyer, R.; Ge, Q.; Lockemeyer, J.; Yeates, R.; Lemanski, M.; Reinalda, D.; Neurock, M. *Surf. Sci.* **2007**, *601*, 134-145.
28. Meyer, R.; Lockemeyer, J.; Yeates, R.; Lemanski, M.; Reinalda,D.; Neurock, M. *Chem. Phys. Lett.* **2007**, *449*, 155-159.
29. Tao, J.G.; Cuan, Q.; Gong, X.Q.; Batzill, M. *J. Phys. Chem. C* **2012**, *116*, 20438-20446.
30. Beck, T.J.; Klust, A.; Batzill, M.; Diebold, U.; Di Valentin, C.; Selloni, A. *Phys. Rev. Lett.* **2004**, *93*, 036104.
31. Torrelles, X.; Cabailh, G.; Lindsay, R.; Bikondoa, O.; Roy, J.; Zegenhagen, J.; Teobaldi, G.; Hofer, W.A.; Thornton, G. **2008**, *101*, 185501.
32. Gong, X.Q.; Khorshidi, N.; Stierle, A.; Vonk, V.; Ellinger, C.; Dosch, H.; Cheng, H.Z.; Selloni, A.; He, Y.B.; Dulub, O.; Diebold, U. *Surf. Sci.* **2009** *603*, 138-144.
33. Cuan, Q.; Tao, J.G.; Gong, X.Q.; Batzill, M. *Phys. Rev. Lett.* **2012** *108*, 106105.
34. Højrup Hansen, K.; Worren, T.; Stempel, S.; Lægsgaard, E.; Bäumer, M.; Freund, H. J. Besenbacher, F.; Stensgaard, I. *Phys. Rev. Lett.* **1999**, *83*, 4120-4123.
35. Gong, X.Q.; Selloni, A.; Dulub, O.; Jacobsen, P.; Diebold, U. *J. Amer. Chem. Soc*. **2008**, *130*, 370-381.
36. Dulub, O.; Boatner, L.A.; Diebold, U. *Surf. Sci.* **2002**, *504*, 271-281.
37. Schmidt, A. A.; Eggers, H.; Herwig, K.; Anton, R. *Surf. Sci.* **1996**, *349*, 301-316.
38. Zhang, J.; Alexandrova, A. N. *J. Chem. Phys.* **2011** *135*, 174702.
39. Ingham, B.; Toney, M.F.; Hendy, S.C.; Cox, T.; Fong, D.D.; Eastman, J.A.; Fuoss, P.H.; Stevens, K.J.; Lassesson, A.; Brown S.A.; Ryan, M.P. *Phys. Rev. B* **2008**, *78* 245408.
40. Eastman, J.A.; Thompson, L.J.; Kestel, B. J. *Phys. Rev. B* **1993**, *48*, 84-92.
41. Jewell, L.L.; Davis, B.H. *Appl. Catal. A: Gen.* **2006**, *310*, 1-15.
42. Senftle, T.P.; Janik, M.J.; van Duin, A.C.T. *J. Phys. Chem. C* **2014** *118*, 4967-4981.
43. Luttrell, T.; Halpegamage, S.; Tao, J.G.; Kramer, A.; Sutter, E.; Batzill, M. *Sci. Rep.*, **2014**, *4*, 4043.
44. Diebold, U. *Surf. Sci. Rep.* **2003**, *48*, 53-229.
45. Lee, S.; Fan, C.; Wu, T.; Anderson, S.L. *Surf. Sci.* **2005**, *578*, 5-19.
46. Wendt, S.; Schaub,R.; Matthiesen, J.; Vestergaard, E.K.; Wahlström, E.; Rasmussen, M.D.; Thostrup, P.; Molina, L.M.; Lægsgaard, E.; Stensgaard, I.; Hammer, B.; Besenbacher, F. *Surf. Sci.* **2005**, *598*, 226-245.
47. Dulub, O; Di Valentin, C; Selloni, A; Diebold, U. *Surf. Sci.* **2006**, *600*, 4407-4417.

48. Papageorgiou, A.C.; Beglitis, N.S.; Pang, C.L.; Teobaldi, G.; Cabailh, G.; Chen, Q.; Fisher, A.J.; Hofer, W.; Thornton, G. *Proc. Natl. Acad. Sci. U.S.A.* **2010**, *107*, 2391.
49. Kresse G.; Furthmüller, J. *Comput. Mater. Sci.* **1996**, *6*, 15-50.
50. Kresse G.; Furthmüller, J. *Phys. Rev. B* **1996** *54*, 11169-11186.
51. Kresse, G.; Joubert, D. *Phys. Rev. B* **1999** *59*, 1758-1775.
52. Monkhorst, H. J.; Pack, J. D. *Phys. Rev. B* **1976**, *13*, 5188-5192.
53. Henkelman, G.; Uberuaga, B.P.; Jonsson, H. *J. Chem. Phys.* **2000**, *113*, 9901-9904.
54. Dudarev, S.L.; Botton, G.A.; Savrasov, S.Y.; Humphreys, C.J.; Sutton, A.P. *Phys. Rev. B* **1998**, *57*, 1505-1509.
55. Cococcioni, M.; de Gironcoli, S. *Phys. Rev. B* **2005**, *71*, 035105.
56. Frenkel, D.; Smit, B. *Understanding molecular simulation : from algorithms to applications*. (Academic Press, San Diego, 2002).
57. van Duin, A.C.T.; Dasgupta, S.; Lorant, F.; Goddard III, W. A. *J. Phys. Chem. A* **2001**, *105*, 9396-9409.
58. Lahiri, J.; Mayernick, A.D.; Morrow, S. L.; Koel, B.E.; van Duin, A.C.T.; Janik, M.J.; Batzill, M. *J. Phys. Chem. C* **2009** *114*, 5990-5996.
59. Chenoweth, K.; van Duin, A.C.T.; Persson, P.; Cheng, M.-J.; Oxgaard, J.; Goddard III, W.A. *J. Phys. Chem. C* **2008**, *112*, 14645-14654.
60. Chenoweth, K.; van Duin A.C.T.; Goddard III, W.A. *Angew. Chem. Int. Ed.* **2009**, *48*, 7630-7634.
61. Monti, S.; van Duin, A.C.T.; Kim, S.-Y.; Barone, V. *J. Phys. Chem. C* **2012**, *116*, 5141-5150.
62. Raymand, D.; van Duin, A.C.T.; Spångberg, D.; Goddard III, W.A.; Hermansson, K. *Surf. Sci.* **2010**, *604*, 741-752.
63. Raju, M.; Kim, S.-Y.; van Duin, A.C.T.; Fichthorn, K.A. *J. Phys. Chem. C* **2013**, *117*, 10558-10572.
64. Senftle, T.P.; Meyer, R.J.; Janik, M.J.; van Duin, A.C.T. *J. Chem. Phys.* **2013** *139*, 044109-044115.
65. Metropolis, N.; Rosenbluth, A.W.; Rosenbluth, M.N.; Teller, A.H.; Teller, E. *J. Chem. Phys.* **1953** *21*, 1087-1092.

Chapter 6
The Role of Site Stability in Methane Activation on $Pd_xCe_{1-x}O_\delta$ Surfaces

This chapter is submitted for publication as:
T. P. Senftle, A. C. T. van Duin and M. J. Janik, *ACS Catalysis*

Abstract

Doped metal-oxide catalysts can be optimized by identifying dopant-metal/host-oxide combinations that exhibit synergistic interactions not present in the parent systems. This is exemplified by $Pd_xCe_{1-x}O_\delta$ mixed-oxides that yield methane oxidation rates unobtainable by the separate parent systems. Here we demonstrate rapid C-H activation on $Pd_xCe_{1-x}O_\delta$ catalysts through emergent behavior of the doped oxide that enables $Pd^{4+} \leftrightarrow Pd^{2+}$ transitions not evident in catalysts featuring a PdO_x active phase. $Pd_xCe_{1-x}O_\delta$ surfaces activate methane through hydrogen abstraction over Pd^{4+} surface states, in contrast to the σ-complex activation route favored over PdO_x surfaces. The stability of the active Pd^{4+} state is dependent on temperature and oxygen pressure during catalytic operation, and as such we combine reaction kinetics and thermodynamic stability arguments from density functional theory (DFT) calculations to derive the apparent methane activation barrier. This accounts for varying conditions affecting the stability of the Pd^{4+} state, demonstrating that active Pd^{4+} sites are metastable. These states form under the reaction environment and offer lower methane activation barriers compared to Pd^{2+} states. The Pd^{4+} state is stabilized by the incorporation of Pd in the fluorite lattice structure of CeO_2, which in turn provides unique methane activation chemistry from the $Pd_xCe_{x-1}O_\delta$ mixture. We generalize these results over (*T*,*P*) space by deriving phase boundaries demarcating regions where each Pd

surface oxidation state is thermodynamically stable or kinetically active. The approach presented here can be readily extended to other systems, providing an approach for assessing the interplay between site activity and stability on catalytic surfaces.

6.1. Introduction

Catalysts featuring mixed-metal oxides offer unique opportunities to tune the catalytic properties of the system by selecting metal/oxide combinations tailored to the target reaction process.[1] In such catalysts, dopant transition metal ions are substituted into the lattice structure of a host oxide, resulting in a system with surface chemistry vastly different than the parent systems. Activity, selectivity, and stability may be tuned by searching for metal-dopant/host-oxide combinations that display desired catalytic properties. Hence, understanding chemical interactions between the metal dopant and the host oxide under reaction conditions is paramount to improving the design of a particular catalyst; which in turn may be generalized to offer insight as to how synergistic metal/oxide interactions may be exploited in other catalytic systems.

Doped oxides are of particular interest for catalytic combustion applications seeking efficient and clean utilization of hydrocarbon feedstocks.[2-6] Methane is readily available from natural gas deposits, and as such there is growing research interest in catalysts that can activate methane at low temperatures.[6-10] Catalytic systems featuring Pd supported on CeO_2 demonstrate exceptional activity toward hydrocarbon oxidation, which can be attributed to synergistic Pd-ceria interactions.[5,6,8,9,11-17] The Pd/ceria system exemplifies mixed-metal-oxide catalysis that is enhanced by chemical properties not

available in the parent systems. In this work we use density functional theory (DFT) in conjunction with *ab initio* thermodynamics to investigate methane activation kinetics and site stability on Pd-doped CeO_2 surfaces. This approach can be readily extended to other doped metal-oxide systems, allowing one to identify and exploit emergent catalytic chemistry between metal dopants and oxide supports.

Depending on catalyst preparation, pre-treatment, and reaction environment, Pd can exist on the ceria surface in many morphologies and oxidation states – each with differing catalytic properties. In the metallic state, Pd nanoclusters adsorb as a distribution of particle sizes, exposing distinct sites on surface facets, corners, edges, and terraces. If exposed to oxidizing conditions, Pd-based catalysts can form various PdO_x surface and bulk phases, again with a wide distribution of unique surface sites.[18-20] Pd can incorporate itself in the ceria lattice forming $Pd_xCe_{1-x}O_\delta$ mixed oxides with catalytic properties that vary greatly from supported PdO_x clusters.[21] Since each surface morphology offers distinct catalytic properties, optimizing Pd/CeO_2 catalysts requires a detailed understanding of the structure of the catalyst surface as a function of varying reaction conditions and preparation methods. As such, we combine stability analysis derived from the formalism of *ab initio* thermodynamics with kinetic arguments to better understand how the stability of various Pd/CeO_2 surface morphologies impacts overall catalytic activity.

Numerous studies highlight the importance of the interaction between Pd and the ceria support, suggesting that the Pd/ceria interfacial region offers unique catalytic properties.[5,9,17,22-30] Cargnello *et al.*[6] have reported the synthesis of core-shell style catalysts, in which a Pd cluster is encapsulated by a ceria shell ($Pd@CeO_2$), that demonstrate high methane combustion rates below 400° C. Using kinetic data taken

between 220° to 270° C, the authors demonstrate that the activation barrier over Pd@CeO_2 catalysts is similar in magnitude to barriers over traditional Pd/ceria catalysts with metallic clusters adsorbed on the ceria surface. This suggests that the same low temperature activation site involving a synergistic interaction between Pd and CeO_2 is present on both catalysts. In Pd@CeO_2 catalysts, nearly the entire Pd cluster surface is in contact with the ceria lattice, maximizing the number of active sites compared to traditional Pd/ceria catalysts where such sites are only exposed on the contact line at the metal-cluster/oxide-support boundary. Colussi *et al.*[5,14] reported catalysts featuring highly active $Pd_xCe_{1-x}O_\delta$ mixed oxides prepared with a solution combustion synthesis (SCS) technique, which achieved combustion rates significantly faster than samples prepared by incipient wetness impregnation (IWI). Combined HRTEM and DFT analyses identified stable Pd^{2+} surface states in the SCS samples with Pd atoms incorporated in the CeO_2(110) surface at vacant Ce lattice positions. Such sites were absent in the IWI samples, leading to the conclusion that the incorporated Pd^{2+} states play a key role in increasing catalytic activity toward methane oxidation.

The exceptional activity of ceria-supported Pd catalysts compared to other supports points to an activation mechanism that is fundamentally different than the mechanism over palladium oxide. Activation on PdO_x, which is the widely regarded active phase of palladium for hydrocarbon oxidation, has been extensively investigated both experimentally and computationally.[31-34] These studies demonstrate that the methane activation barrier is lowest on the PdO(101) surface, over which CH_4 forms a precursor σ-complex when adsorbed over exposed Pd atoms that are coordinatively unsaturated (cus-Pd).[33-38] In the precursor state, electrons from C-H bonding orbitals are donated to available

4d states in the exposed metal atom, inducing a back-donation of charge from the metal into the anti-bonding molecular orbitals of CH_4 in the precursor state. This in turn leads to a low 0 K C-H activation barrier (0.65 eV relative to the adsorbed precursor state), as the C-H bonds are destabilized. Over the PdO(100) surface, the methane activation barrier (1.22 eV) is 0.55 eV higher because all exposed Pd atoms reside in saturated square-planar oxygen coordinations that do not allow Pd to strongly interact with methane.[32,33] Since Pd/ceria interactions clearly enhance catalytic activity, ceria must either modulate the σ-complex activation route or offer a fundamentally different route with similar or higher activity than the PdO(101) surface. Experimentally identified structures of $Pd_xCe_{1-x}O_\delta$ clearly indicate that Pd^{2+} exists on the surface in a square-planar coordination environment analogous to the PdO(100) surface,[5,39] suggesting that the σ-complex activation route may not be responsible for the high activity of catalysts containing $Pd_xCe_{1-x}O_\delta$ surface structures.

Previously, our group has demonstrated that Pd atoms incorporated in the CeO_2(111) surface may undergo a facile $Pd^{4+} \rightarrow Pd^{2+}$ transition upon methane activation, leading to a combustion rate many orders of magnitude faster than Pd or PdO surfaces.[9-11] A subsequent *ab initio* thermodynamics investigation suggested that the Pd^{4+} state of a single incorporated Pd atom can be stable under extremely oxidizing conditions; however, this study could not definitively determine if the Pd^{4+} state could exist under typical low temperature combustion conditions.[12] Indeed, Boronin *et al.*[39] reported XPS and XRD results identifying stable Pd^{2+} states in $Pd_xCe_{1-x}O_\delta$, in agreement with the surface structure reported by Colussi *et al.*[5] Despite this evidence demonstrating the stability of the Pd^{2+} surface state, neither investigation conducted structure characterizations under reaction

conditions and, therefore, cannot evaluate the possibility that transient Pd^{4+} states play a role in the activation mechanism.

Although the above studies underscore the importance of strong Pd-ceria interactions, the structure and nature of the active site under reaction conditions is still not well understood. In this work, we use DFT and *ab initio* thermodynamics to examine methane activation over $Pd_xCe_{1-x}O_\delta$ surface models featuring varying Pd oxidation states. We show that the Pd^{2+} surface state is thermodynamically more stable under relevant reaction conditions; nevertheless, a lower apparent barrier is achieved if oxidation of the Pd^{2+} state to a Pd^{4+} state precedes C-H bond activation. Hence, transient Pd^{4+} states play an important role in methane activation over Pd-doped ceria, as incorporation in the ceria lattice enables $Pd^{4+} \leftrightarrow Pd^{2+}$ transitions at the active site yielding rapid catalytic turnover.

6.2. Theory and Methods

6.2.1. DFT Calculations

Electronic Structure Calculations. DFT calculations were completed with the Vienna *ab initio* simulation package (VASP).[40,41] Exchange-correlation energy was calculated with the generalized gradient approximation (GGA), implemented in the Perdew-Wang formulation (PW91).[42] An energy cut-off threshold of 450 eV was employed to truncate plane-wave basis sets. Core electronic regions were represented by the projector augmented wave pseudo potential approximation[43] (PAW), with electronic valence configurations of $5s^25p^66s^24f^15d^1$ for Ce atoms, $4d^{10}$ for Pd atoms, $2s^22p^4$ for O atoms,

$2s^2 2p^2$ for C atoms, and $1s^1$ for H atoms. All calculations were treated as spin polarized, and when appropriate, multiple spin states were tested to ensure that the optimal spin state was identified. Monkhorst-Pack[44] (MP) Brillouin zone sampling was used with a *2×2×1* MP k-point spacing, where a 15 Å vacuum layer separated images perpendicular to the surface. Molecule calculations were conducted in a 15Å × 15Å × 15Å periodic cell at the Γ point. We employed the Hubbard +U correction[45,46] to treat the well documented deficiency of standard DFT when describing localized Ce 4f states that may become occupied during surface reduction processes, such as hydrogen adsorption or oxygen vacancy formation.[11,47,48] We used a correction value of U = 5 eV on Ce 4f states, which was determined by previous studies to yield proper electronic occupations in localized Ce 4f states.[49-52] It is possible that a similar deficiency may affect the occupation and energy of partially localized Pd 4d states, which has been less widely investigated in the literature. As such, we assessed the relative impact differing U values, applied to the 4d states of Pd, have on the results and conclusions obtained herein, which will be further discussed were appropriate. Optimized structures were determined by conjugant gradient structural relaxations employed with an atomic force convergence criterion of 0.05 eV $Å^{-1}$. Coordinates of optimized surface structures and total DFT energies are provided in the Supplemental Information.

$Pd_xCe_{1-x}O_\delta$ Surface Models. We investigate methane activation over ceria (111) and (110) surfaces with Pd atoms substitutionally incorporated in fluorite ceria at Ce lattice positions. The CeO_2(111) surface was modeled with a periodic 13.32 Å × 11.36 Å orthogonal unit cell consisting of three O-Ce-O tri-layers in the z-direction perpendicular to the surface, totaling to 36 Ce atoms and 72 O atoms in the stoichiometric CeO_2(111)

surface, as shown in Figure 6-1. The $Pd_xCe_{36-x}O_{72-y}(111)$ surface models (where *x* equals 1 to 3, and *y* is the number of oxygen vacancies) were constructed by directly substituting Ce surface atoms (labeled Ce1-Ce3 in Figure 6-1) with Pd atoms. Oxygen vacancy formation was treated by successively removing surface oxygen atoms adjacent to incorporated Pd atoms (labeled O1-O7 in Figure 6-1). Vacancy formation energies were calculated for each of the labeled oxygen vacancy sites, where only the energy of the preferred vacancy site is reported. This was repeated for surfaces with multiple oxygen vacancies, where the optimized singly vacant surface served as the starting point for identifying the second oxygen vacancy site, continuing until the number of oxygen vacancies exceeded the number of incorporated Pd atoms by one. The $CeO_2(110)$ surface was modeled with a periodic 10.86 Å × 7.68 Å orthogonal unit cell consisting of five O-Ce-O tri-layers in the z-direction perpendicular to the surface, totaling to 20 Ce atoms and 40 O atoms in the stoichiometric $CeO_2(110)$ surface. Varying oxidation states of the $Pd_2Ce_{18}O_{40-y}(110)$ surface were treated by adding O atoms to the $Pd_2Ce_{18}O_{38}(110)$ surface structure shown in Figure 6-2, which already contains two oxygen vacancies ($y = 2$). The structure in Figure 6-2 was previously identified by Colussi *et al.*[5] with HRTEM experiments, making it a more suitable starting point for modeling varying O vacancy concentrations than the stoichiometric $Pd_2Ce_{18}O_{40}(110)$ surface.

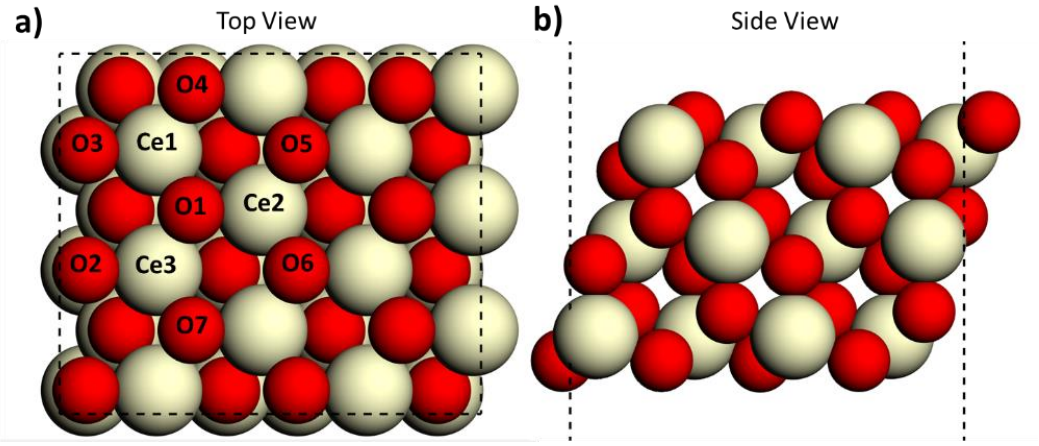

Figure 6-1. (a) Top and (b) side view of the orthogonal $CeO_2(111)$ unit cell. The $Pd_xCe_{1-x}O_\delta(111)$ surface was built by replacing atoms Ce1-Ce3 with Pd atoms and removing atoms O1-O3.

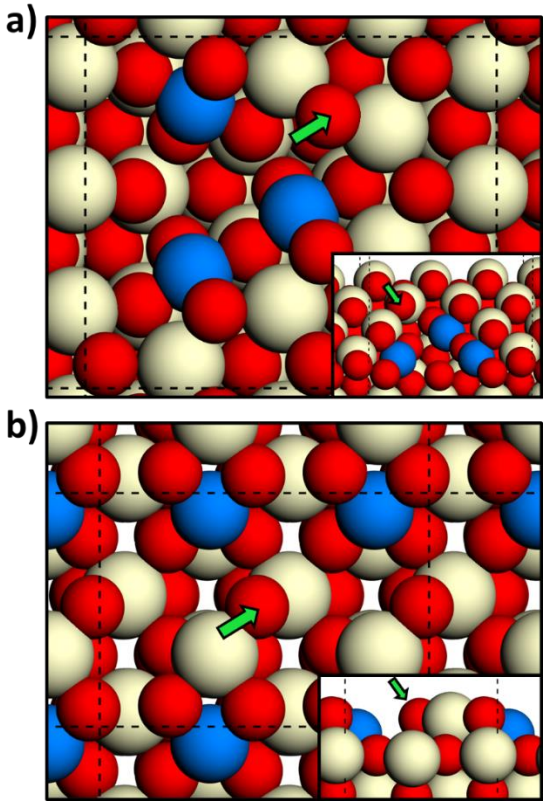

Figure 6-2. (a) The optimized (111)-$3Pd^{2+}$ surface and (b) (110)-$2Pd^{2+}$ surface. (Insets) Side view of each surface. The unit cell is indicated by black dashed lines, and the green arrows indicate the favored hydrogen adsorption site during methane activation.

6.2.2. *ab initio* Thermodynamics

We employ the formalism of *ab initio* thermodynamics[53] to assess the relative stability of varying $Pd^{\delta+}$ incorporated states and Pd^0 adsorbed states as a function of oxygen pressure and temperature. Following the methodology described in previous work,[12] we define the free energy of a Pd/CeO_2 surface relative to fully oxidized PdO_2 and CeO_2 systems. The free energy of Pd-incorporated and Pd-adsorbed surface states are determined by the following formulas, respectively:

$$G_{Surf}^{Pd-Inc} = E_{[N_{Pd}-surf]} + N_{Pd}E_{[CeO_2]} + N_{[O-vac]}\frac{1}{2}\mu_{O_2} - \left(E_{[CeO_2-surf]} + N_{Pd}E_{[PdO_2]}\right) \quad (1)$$

$$G_{Surf}^{Pd-Ads} = E_{[N_{Pd}-surf]} + N_{Pd}\mu_{O_2} - \left(E_{[CeO_2-surf]} + N_{Pd}E_{[PdO_2]}\right) \quad (2)$$

where G_{Surf}^{Pd-Inc} is the free energy of a Pd-incorporated surface and G_{Surf}^{Pd-Ads} is the free energy of a Pd-adsorbed surface. N_{Pd} is the number of Pd atoms in the unit cell, $N_{[O-vac]}$ is the number of surface oxygen vacancies relative to the stoichiometric CeO_2 surface, $E_{[N_{Pd}-surf]}$ is the DFT energy of the Pd-incorporated or Pd-adsorbed surface, $E_{[CeO_2]}$ and $E_{[PdO_2]}$ are the energies of the CeO_2 and PdO_2 bulk references (calculated per stoichiometric formula unit), and $E_{[CeO_2-surf]}$ is the energy of the clean CeO_2 surface. Here we neglect entropy and enthalpy corrections to free energy for bulk and surface structures, as these corrections are negligible.[53] Finally, μ_{O_2} is the chemical potential of the O_2 reference calculated using statistical mechanical arguments for gas phase molecules:

$$\mu_{molecule} = E_{DFT} + E_{ZPV} + H_{thermal} - (S_{trans} + S_{vib} + S_{rot} + S_{elec})T \quad , \quad (3)$$

where E_{DFT} is the electronic ground state energy, E_{ZPV} is zero-point vibrational energy, $H_{thermal}$ is the thermal enthalpy correction, and the *ST* terms are translational, vibrational, rotational, and electronic entropy contributions to the total free energy. Using the above

formulas, we can predict the relative thermodynamic stability of surfaces with varying Pd-dopant morphologies, oxygen vacancy concentrations, and surface oxidation states. Thus, the dominant surface state under operating conditions can be identified as a function of oxygen pressure and temperature.

6.2.3. Calculating Apparent Combustion Rates

We calculate and compare apparent methane activation rates over possible Pd/ceria surface morphologies to identify the favored catalytic surface for methane activation. As shown previously,[9,54] the catalytic combustion of methane on Pd/ceria proceeds through a rate limiting C-H activation step as methane dissociatively adsorbs on the catalyst surface as H* and CH_3* through hydrogen abstraction. Furthermore, the activation barrier for dissociative adsorption can be approximated by calculating the energy of a pseudo-barrier structure consisting of an adsorbed H* atom and a gas phase $\cdot CH_3$ radical above the surface.[9,10] Hence, the pseudo-barrier approximation for methane activation is calculated with the formula:

$$\Delta G_{act} = E_{[surf-H]} + E_{[ZPV-H]} + \mu_{\cdot CH_3} - \left(E_{[surf-clean]} + \mu_{CH_4}\right) \quad , \qquad (4)$$

where $E_{[surf-H]}$ is the energy of the H-adsorbed surface, $E_{[ZPV-H]}$ is the zero-point vibrational energy of the H-adsorbed surface, $E_{[surf-clean]}$ is the energy of the clean surface, $\mu_{CH_4}$is the chemical potential of CH_4 in the gas phase, and $\mu_{\cdot CH_3}$is the chemical potential of the $\cdot CH_3$ radical in the pseudo-transition state. Chemical potentials of CH_4 and $\cdot CH_3$ were calculated as a function of partial pressure and temperature using Equation 3. Translational and rotational contributions in Equation 3 were set to zero for $\cdot CH_3$ in the

pseudo-transition state, as the $\cdot CH_3$ radical has no translational or rotational degrees of freedom in the activated complex over the oxide surface. All pseudo-barriers were calculated with CH_4 and $\cdot CH_3$ molecules treated in simulation cells separate from the oxide surface, unless specifically noted. Additionally, we conducted climbing image nudged elastic band (CI-NEB)[55,56] calculations to identify the true transition state in select cases to validate the pseudo-barrier approach. The magnitude of error introduced by the pseudo-barrier approach does not alter any conclusions, and will be further addressed in the results section.

Apparent Barrier. The thermodynamic stability analysis presented above can be combined with the above barrier calculations to derive an expression for the apparent activation barrier over Pd-incorporated sites in varying oxidation states. Although a particular oxidation state may not be thermodynamically favored, it may offer a lower apparent activation barrier despite forming through an endergonic oxidation step prior to C-H activation. This is demonstrated by the following elementary steps in which a Pd^{n+} incorporated atom is oxidized by gas phase O_2 prior to the dissociative adsorption of methane:

$$\text{A:} \qquad [* Pd^{n+}] + \frac{m}{2} O_2 \rightleftharpoons \left[* Pd^{(n+2m)+}\right] \quad , \tag{5}$$

$$\text{B:} \qquad \left[* Pd^{(n+2m)+}\right] + CH_4 \rightarrow [* (CH_3 + H)] \qquad \text{RDS} \quad , \tag{6}$$

where $[* Pd^{n+}]$ represents a site adjacent to an incorporated Pd atom in the thermodynamically favored $n+$ oxidation state and $\left[* Pd^{(n+2m)+}\right]$ represents the site in a $(n+2m)+$ oxidation state after m oxygen atoms have adsorbed on the surface. The free energy change in Step A is obtained from the free energy of each state calculated by Equation 1:

$$\Delta G_{form} = G_{[Pd^{(n+2m)+}]} - G_{[Pd^{n+}]} = E_{[Pd^{(n+2m)+}]} - \left(E_{[Pd^{n+}]} + \frac{m}{2}\mu_{O_2}\right) + \Delta E_{zpv} \quad . \quad (7)$$

This free energy is related to the equilibrium constant, K_A, of Step A and is then combined with the rate constant of activation Step B, k_b, to yield the rate expression:

$$K_A = exp\left(\frac{-\Delta G_{form}}{RT}\right) = \frac{[*Pd^{(n+2m)+}]}{[*Pd^{n+}]\,P_{O2}^{m/2}} \quad , \quad (8)$$

$$k_B = \frac{kT}{h} exp\left(\frac{-\Delta G_{act}}{RT}\right) \quad , \quad (9)$$

$$r = k_B\left[* Pd^{(n+2m)+}\right] P_{CH_4} = K_A k_B\,[* Pd^{n+}]\,P_{O_2}^{m/2} P_{CH_4} \, . \quad (10)$$

The apparent barrier for activation over incorporated Pd in a particular oxidation state thus consists of the activation barrier summed with the free energy difference compared to the most stable oxidation state:

$$k_{app} = K_A k_B = \frac{kT}{h} exp\left(\frac{-(\Delta G_{act} + \Delta G_{form})}{RT}\right) \quad , \quad (11)$$

$$\Delta G_{app} = \Delta G_{act} + \Delta G_{form} \quad , \quad (12)$$

where k is the Boltzmann constant, h is the Planck constant, ΔG_{form} is the endergonic free energy difference between the $n+$ and $(n+2m)+$ states obtained from Equation 7, and ΔG_{act} is the activation barrier obtained from Equation 4. Since ΔG_{form} depends on μ_{O_2}, the apparent barrier is a function of oxygen pressure, in addition to temperature and methane pressure. This formalism, summarized in Figure 6-3, captures the balance between site activity and stability required to compare the apparent activity of Pd-incorporated sites in varying oxidation states. This allows us to identify less stable oxidation states that are highly reactive and are stable enough to appear as transient active sites, as depicted in Figure 6-3.

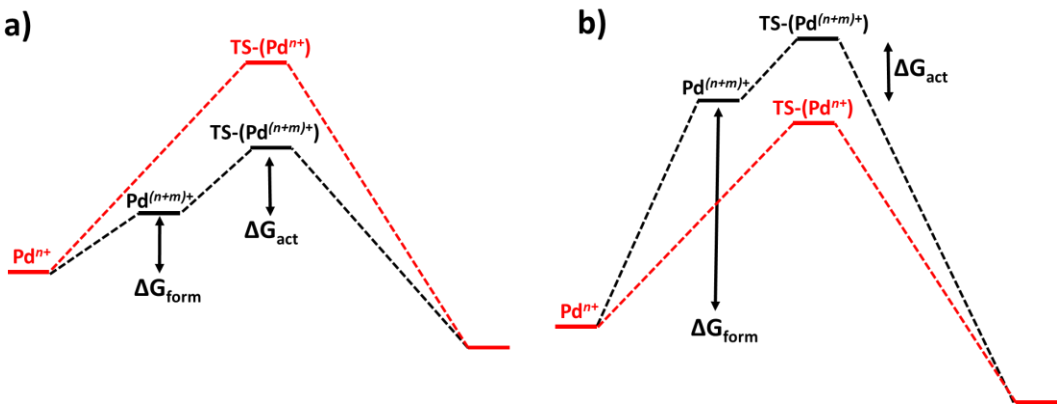

Figure 6-3. Total apparent barrier for CH_4 activation over the thermodynamically favored Pd^{n+} state compared to an oxidized $Pd^{(n+m)+}$ state, where the $Pd^{(n+m)+}$ state yields (a) lower and (b) higher apparent barriers depending on the stability of the $Pd^{(n+m)+}$ state (*i.e.* depending on the magnitude of ΔG_{form}).

6.3. Results

6.3.1. Surface Oxidation States

To identify appropriate models of Pd-incorporated surface states, we assess the effects of oxygen vacancy formation on the oxidation state and local geometry of incorporated Pd atoms in the CeO_2 lattice. As reported by Mayernick *et al.*,[11] direct substitution of a single Pd atom in the stoichiometric CeO_2 surface without oxygen vacancies yields a Pd^{4+} oxidation state, and the formation of an oxygen vacancy results in a $Pd^{4+} \rightarrow Pd^{2+}$ reduction. In the 4+ state, Pd takes an octahedral oxygen coordination characteristic of a d^6 metal center, and in the 2+ state takes a square-planar coordination characteristic of a d^8 metal center. Here we investigate the oxidation behavior and geometry of CeO_2 surface models containing multiple Pd atoms, which better approximate the interfacial region between a partially embedded Pd cluster and the ceria surface. Again,

direct Pd substitution results in octahedral Pd^{4+} states for all surface Pd atoms. Sequential oxygen vacancy formations result in the reduction of adjacent Pd atoms until all Pd atoms are in a square-planar coordination with a 2+ oxidation state. This is demonstrated in Figure 6-2 showing square-planar Pd^{2+} states in the optimized surface structures of both the $Pd_3Ce_{33}O_{69}$(111) and $Pd_2Ce_{18}O_{38}$ (110) surfaces, where the number of oxygen vacancies in each model equals the number of incorporated Pd atoms. The Pd-O bond lengths in the square-planar units range from 1.98 Å to 2.05 Å, comparable to bond distances of 2.06 Å in bulk PdO.[20] Further oxygen removal results in $Ce^{4+} \rightarrow Ce^{3+}$ reductions of two surface Ce atoms adjacent to the oxygen vacancy, as opposed to further reduction of Pd atoms. This was confirmed by Bader[57,58] charge differences showing charge accumulation on Ce atoms adjacent to oxygen vacancy sites.

Since the oxidation state of incorporated Pd atoms is determined by the amount of oxygen present in the surface model, we will refer to Pd and Ce oxidation states to indicate the amount of oxygen in each surface model. Hence, the $Pd_3Ce_{33}O_\delta$(111) surface containing zero, one, two, three, or four oxygen vacancies will be respectively referred to as the (111)-$3Pd^{4+}$, (111)-$1Pd^{2+}$/$2Pd^{4+}$, (111)-$2Pd^{2+}$/$1Pd^{4+}$, (111)-$3Pd^{2+}$, and (111)-$3Pd^{2+}$/$2Ce^{3+}$ surfaces. The same naming convention will be used for all surface models.

6.3.2. Apparent Activation Barriers

Apparent activation barriers were calculated over the $Pd_xCe_{1-x}O_\delta$ (111) and (110) surface models at varying oxidation states using the coupled *ab initio*-thermodynamics/pseudo-barrier approach described above. We calculated the barrier for

activation occurring over every surface oxygen atom in each model, and report here the lowest barrier obtained for each oxidation state. The favored activation sites on the (111)-3Pd^{2+} and (110)-2Pd^{2+} surfaces reside atop oxygen atoms adjacent to two Ce surface atoms that are in turn adjacent to the Pd^{2+} square-planar formation, as indicated in Figure 6-2 by green arrows. The activation site was similar on the remaining surface models, which are provided in Figures S2 and S3 of the Supplemental Information. Attempts to adsorb hydrogen directly on the Pd metal center were unsuccessful, as H migrated to an adjacent oxygen atom in all cases. Furthermore, attempts to locate precursor CH_4 adsorbed states indicated weak interaction between CH_4 and Pd metal centers, with typical exothermic CH_4 adsorption energies less than 0.04 eV relevant to a gas phase CH_4 molecule in a separate simulation cell. The lack of a bound CH_4 precursor indicates that methane does not form an activated σ-complex over $Pd_xCe_{1-x}O_\delta$ surfaces, as it does over cus-Pd atoms on the PdO(101) surface.

The apparent methane activation barrier was determined for each surface oxidation state by either CI-NEB or by using the pseudo-barrier approximation, shown in Equation 4, with H adsorbed on the surface at the optimal site. A CI-NEB transition state search was completed over the (111)-1Pd^{4+}/2Pd^{2+} surface, shown in Figure 6-4, where the CI-NEB search consisted of four equally spaced images between the initial CH_4 state and the (H* + $\cdot CH_3$) pseudo-transition state. The CI-NEB transition state, labeled as point (b) in the figure, has forces converged to within 0.05 eV/Å and was validated by a single imaginary vibrational mode along the reaction coordinate. As seen in the figure, the CI-NEB barrier is 0.04 eV higher in energy than the pseudo-barrier, demonstrating reasonable accuracy in the pseudo-barrier approximation. An equivalent CI-NEB transition state search conducted

over the (111)-3Pd^{2+} surface did not yield a converged transition state structure, and indicated a monotonic rise in the potential energy surface from CH_4 to (H* + ·CH_3). The resulting barriers for each surface oxidation state are reported in Table 6-1, along with barriers reported in the literature for activation over various CeO_2, PdO, and Pd surfaces.

The 0 K barrier over surfaces containing Pd^{4+} states are 0.29 eV, 0.38 eV, and 0.42 eV over the (111)-1Pd^{4+}/2Pd^{2+}, (111)-2Pd^{4+}/1Pd^{2+}, and (111)-3Pd^{4+} surfaces, respectively. These are significantly lower than the 0.68 eV barrier over the (111)-3Pd^{2+} surface, demonstrating the high activity of the Pd^{4+} state. A similar result was obtained for (110)-2Pd^{2+} and (110)-1Pd^{4+}/1Pd^{2+} surfaces, with 0 K barriers of 1.29 eV and 0.05 eV, respectively. The Pd^{4+} state serves as a reduction center facilitating hydrogen abstraction during methane activation. Hence, the additional oxygen atom, coupled with the associated Pd^{4+} center, is highly reactive and can readily activate C-H bonds through hydrogen abstraction.

The additional adsorbed oxygen atom is reactive because it is unstable, which must be accounted for when calculating the total apparent barrier. This is demonstrated in Figure 6-5, which compares the formation energy, activation energy, total apparent barrier, and relative reaction rate for each oxidation state of the $Pd_3Ce_{33}O_\delta$(111) surface. The data in the figure are calculated at T = 400 K, P_{O2} = 0.01 atm, and P_{CH4} = 0.01 atm, which is representative of the low temperature onset of the methane oxidation light-off curve during catalytic combustion.[6] At T = 400 K and P_{O2} = 0.01 atm, the (111)-3Pd^{2+} state is thermodynamically favored and hence has a ΔG_{form} value of zero – in agreement with experimental HRTEM, XPS, and XRD[5,39] observations of the Pd^{2+} state in Pd/Ce mixed

oxides. However, the optimal methane activation rate is achieved over the (111)-1Pd^{4+}/2Pd^{2+} state despite the additional energy required to oxidize the thermodynamically stable (111)-3Pd^{2+} state. This result demonstrates a trade-off between site stability and activity typical in heterogeneous catalysis, where unique catalytic activity can occur near phase boundaries over meta-stable surface states. Although the (111)-1Pd^{4+}/2Pd^{2+} state is less stable than the (111)-3Pd^{2+} state, the uphill free energy 'penalty' required to obtain the Pd^{4+} state (ΔG_{form}) does not outweigh the decrease in ΔG_{act} obtained by forming the Pd^{4+} state (*i.e.* the situation depicted in Figure 6-3a). Comparatively, the free energy penalty required to obtain multiple Pd^{4+} states far outweighs the barrier reduction achieved by the (111)-2Pd^{4+}/1Pd^{2+} and (111)-3Pd^{4+} surfaces, resulting in slower apparent activation rates (as depicted in Figure 6-3b). Hence, the Pd^{4+} state is active in temperature and pressure ranges where the magnitude of ΔG_{form} is smaller than the difference in ΔG_{act} between the Pd^{2+} and Pd^{4+} states. This result is generalized over all temperature and oxygen pressure ranges in the following section.

Table 6-1. Activation barriers, formation energies, total apparent barriers, and relative reaction rates for methane activation over Pd, PdO, CeO_2, and Pd/CeO_2 surfaces.

Surface Model	ΔG_{act} (0 K)	ΔG_{act} (400 K)[a]	ΔG_{form} (400 K)[a]	ΔG_{total} (400 K)[a]	Relative Rate
CeO_2(111)[9]	1.65	2.55[b]	-	2.55	1
Pd*/CeO_2(111)[9]	1.30	2.20[b]	-	2.20	2.6×10^{4}
Pd(111)[32]	0.86	1.76[b]	-	1.76	9.0×10^{9}
Pd(100)[32]	0.73	1.63[b]	-	1.63	3.6×10^{11}
PdO(100)[32]	1.22	2.12[b]	-	2.12	2.6×10^{5}
PdO(101)[32]	0.50	1.40[b]	-	1.40	2.8×10^{14}
O-PdO(101)	0.04[d]	0.94	0.61	1.55	3.7×10^{12}
(111)-3Pd^{4+}	0.42[c]	1.32	1.85	3.17	1.6×10^{-8}
(111)-2Pd^{4+}/1Pd^{2+}	0.38[c]	1.28	0.55	1.83	1.2×10^{9}
(111)-1Pd^{4+}/2Pd^{2+}	0.29[d]	1.19	0.08	1.27	1.2×10^{16}
(111)-3Pd^{2+}	0.68[c]	1.58	-	1.58	1.7×10^{12}
(110)-2Pd^{4+}	0.01[c]	0.91	2.94	3.85	3.8×10^{-17}
(110)-1Pd^{4+}/1Pd^{2+}	0.05[c]	0.95	0.91	1.86	4.0×10^{8}
(110)-2Pd^{2+}	1.29[c]	2.19	-	2.19	3.2×10^{4}

a) T = 400 K, P_{CH4} = 0.01 atm, P_{O2} = 0.01 atm
b) Applied $T\Delta S$ = 0.9 eV correction to 0 K barrier
c) Calculated with the pseudo-barrier approximation
d) Calculated with CI-NEB

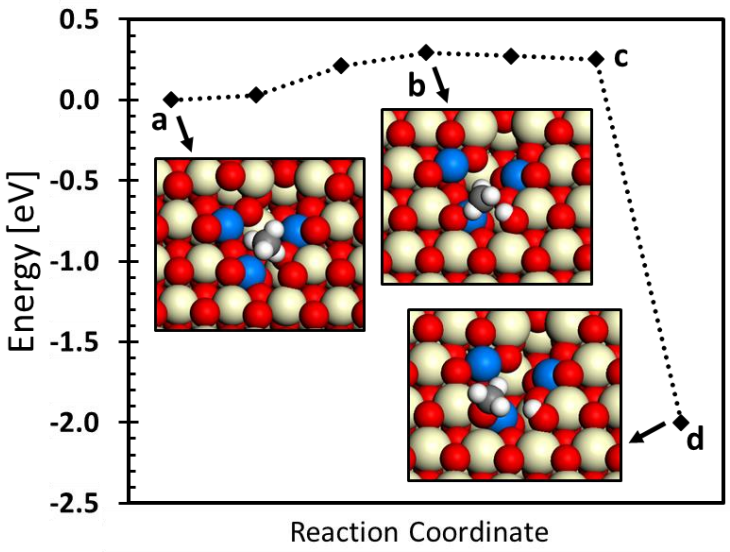

Figure 6-4. Reaction energy diagram for methane activation over the (111)-1Pd^{4+}/2Pd^{2+} surface, where the data points represent (a) the initial CH_4 state, (b) the transition state identified with CI-NEB, (c) the pseudo-transition state consisting of H* and ·CH_3 away from the surface, and (d) the final CH_3* + H* state. The points between (a)-(c) were obtained by CI-NEB with four equally spaced images between the initial state (a) and the pseudo-transition state (c).

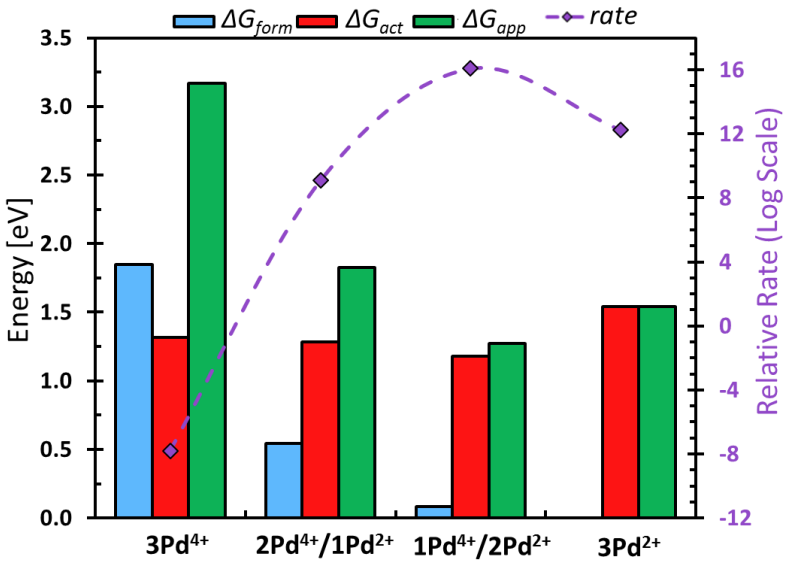

Figure 6-5. Formation energy (blue), activation energy (red), and total barrier (green) for methane activation over the $Pd_xCe_{1-x}O_\delta$(111) surface at varying Pd oxidation states under catalytic combustion conditions (T = 400 K, P_{O2} = 0.01 atm, and P_{CH4} = 0.01 atm). Purple data correspond to relative methane activation rates normalized against the rate over clean CeO_2(111).

6.3.3. Temperature and Pressures Ranges of Stability and Activity

The calculated free energies and apparent barriers presented in the previous section can be generalized to extract boundaries in (*T*,*P*) space demarcating where each oxidation state is thermodynamically stable or kinetically active. This is demonstrated in Figure 6-6a and 5b, where the free energy of each oxidation state of the $Pd_3Ce_{33}O_\delta$(111) surface is plotted against oxygen pressure at 400 K and 700 K, respectively. At 400 K, the (111)-$3Pd^{2+}$ is thermodynamically stable (*i.e.* has the lowest free energy) at oxygen pressures below 1 atm, above which the (111)-$1Pd^{4+}/2Pd^{2+}$ state is stable. At 700 K, the boundary separating the (111)-$3Pd^{2+}$ and (111)-$1Pd^{4+}/2Pd^{2+}$ states shifts to 10^5 atm, and the adsorbed $3Pd^0$ cluster becomes stable at 10^{-7} atm – in agreement with the expectation that Pd is more easily reduced at higher temperatures.

The vertical dashes in Figure 6-6 represent the pressure range at each temperature where the (111)-$1Pd^{4+}/2Pd^{2+}$ state has the lowest apparent barrier despite having a higher free energy than the (111)-$3Pd^{2+}$ state. This region begins when the free energy of the (111)-$3Pd^{2+}$ state is 0.39 eV lower than that of the (111)-$1Pd^{4+}/2Pd^{2+}$ state, at which point the apparent activation barriers over the two states are equal. It then extends to the intersection point where the free energy difference between the states is 0 eV, where the (111)-$1Pd^{4+}/2Pd^{2+}$ state becomes thermodynamically stable. Since the difference in activation energy between the states is independent of temperature and oxygen pressure, the range of free energy difference (0 eV to 0.39 eV) is the same at both 400 K and 700 K, but is shifted to higher oxygen pressures at higher temperatures (Figure 6-6b).

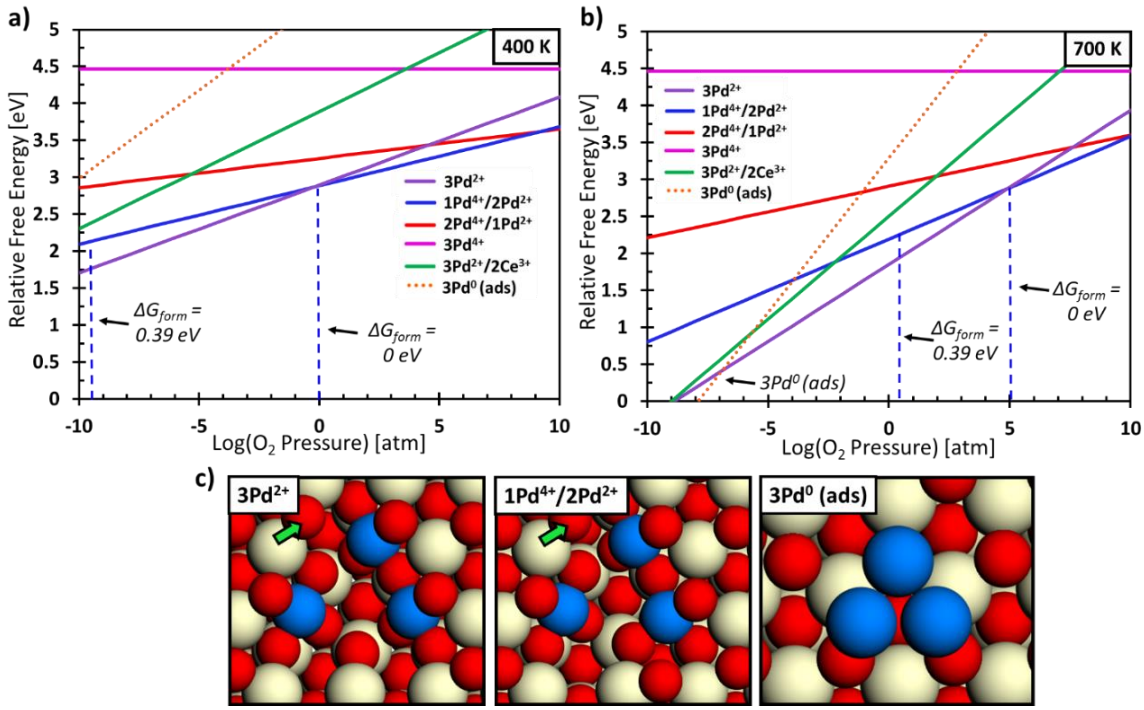

Figure 6-6. Relative free energy of $Pd_xCe_{1-x}O_\delta(111)$ surfaces with varying Pd oxidation states at (a) 400 K and at (b) 700 K. The vertical dashed blue lines indicate the pressure region in which the free energy difference between the (111)-$3Pd^{2+}$ and the (111)-$1Pd^{4+}/2Pd^{2+}$ surface is 0 eV (where the two surface phases are in equilibrium) and 0.39 eV (where the surfaces have the same apparent methane activation barrier). (c) The structure of the three surfaces that can be thermodynamically stable under the shown (*T*,*P*) ranges. Green arrows indicate the favored hydrogen adsorption site during methane activation.

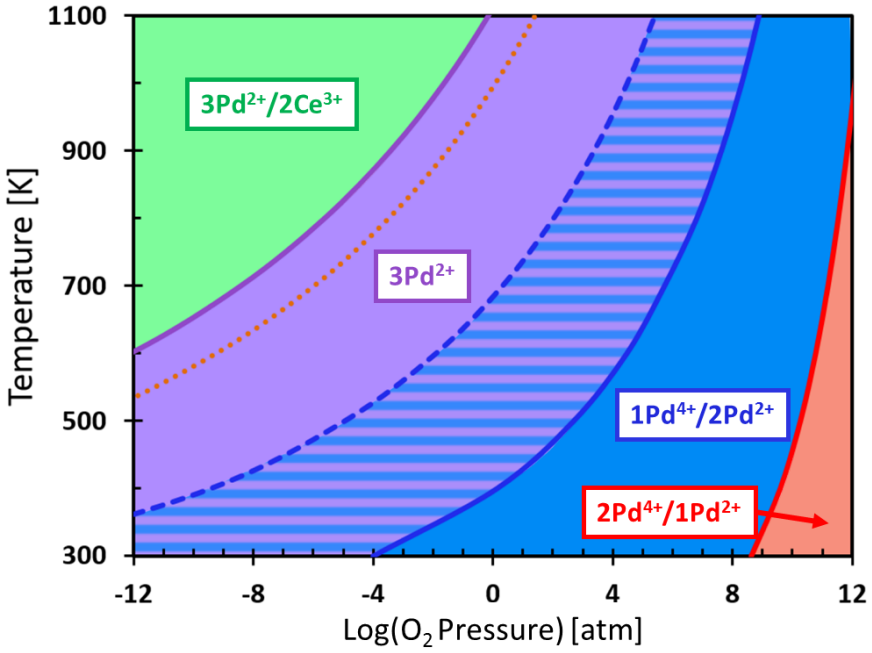

Figure 6-7. Phase diagram describing Pd oxidation states in the $Pd_3Ce_{33}O_\delta(111)$ surface derived from *ab initio* thermodynamics. The solid shaded regions separated by solid colored lines indicate thermodynamically stable regions in (*T*,*P*) space. The striped region and dashed line indicate the region where the $3Pd^{2+}$ surface is thermodynamically stable, yet methane activation is kinetically preferred through the $2Pd^{2+}/1Pd^{4+}$ state. An adsorbed $3Pd^0$ cluster is thermodynamically stable above the orange dotted line.

The boundaries identified in Figure 6-6 are generalized over (*T*,*P*) space in the *ab initio* phase diagram shown in Figure 6-7. In the figure, regions with solid color shading separated by solid lines represent ranges of thermodynamic stability for each oxidation state. At low temperatures and high oxygen pressures, it is thermodynamically favorable for oxygen to adsorb on the oxide surface creating Pd^{4+} states. At high temperatures and low oxygen pressures, it is favorable for oxygen to desorb leaving reduced Pd^{2+} and Ce^{3+} states. The $3Pd^{2+}$ state clearly dominates the room-temperature/low-pressure region, in agreement with HRTEM and XPS investigations identifying stable Pd^{2+} incorporated surface states.[5,39] The adsorbed $3Pd^0$ cluster is stable in the region above the orange dotted line, which reflects the propensity for Pd to migrate from the CeO_2 lattice and sinter into

large metal clusters under reducing conditions.[25] At P_{O2} = 1 atm, the Pd^0 boundary lies near ~1000 K, similar to the experimentally determined PdO → Pd transition at 1050 K for bulk palladium oxide.[59] The purple-blue striped region represents the temperature and pressure ranges where the (111)-3Pd^{2+} state is stable, yet the apparent methane activation barrier is lower over the (111)-1Pd^{4+}/2Pd^{2+} state. This unique kinetic region extends over typical operating conditions for low temperature catalytic combustion, demonstrating that the Pd^{4+} state is likely responsible for the experimentally observed low temperature activity of $Pd_xCe_{1-x}O_\delta$ catalysts.

The same methodology was further applied to the $Pd_xCe_{1-x}O_\delta$(110) surface model, which is summarized in Figure 6-8. The (110)-2Pd^{2+} state, whose structure is identical to the experimentally determined structure reported by Colussi *et al.*[5], is stable over nearly all pressure ranges at low temperatures, in agreement with the HRTEM result identifying the Pd^{2+} incorporated state. The Pd^{4+} state is not stable until unphysically high oxygen pressures are reached, explaining why this state in not observed experimentally under *ex situ* conditions. Nevertheless, the (110)-1Pd^{4+}/1Pd^{2+} state yields a lower apparent barrier than the (110)-2Pd^{2+} state over the majority of the low temperature region, indicating again that the Pd^{4+} state provides a unique active site for low temperature catalytic combustion. Furthermore, the existence of the 'kinetic' region between the Pd^{2+}/Pd^{4+} phase boundaries was also identified for $Pd_xCe_{1-x}O_\delta$(111) surface models with one and two incorporated atoms (provided in Figure S6-4 of the Supporting Information), indicating that this result is general to $Pd_xCe_{1-x}O_\delta$ surface phases, and is not dependent on the particular choice of surface model.

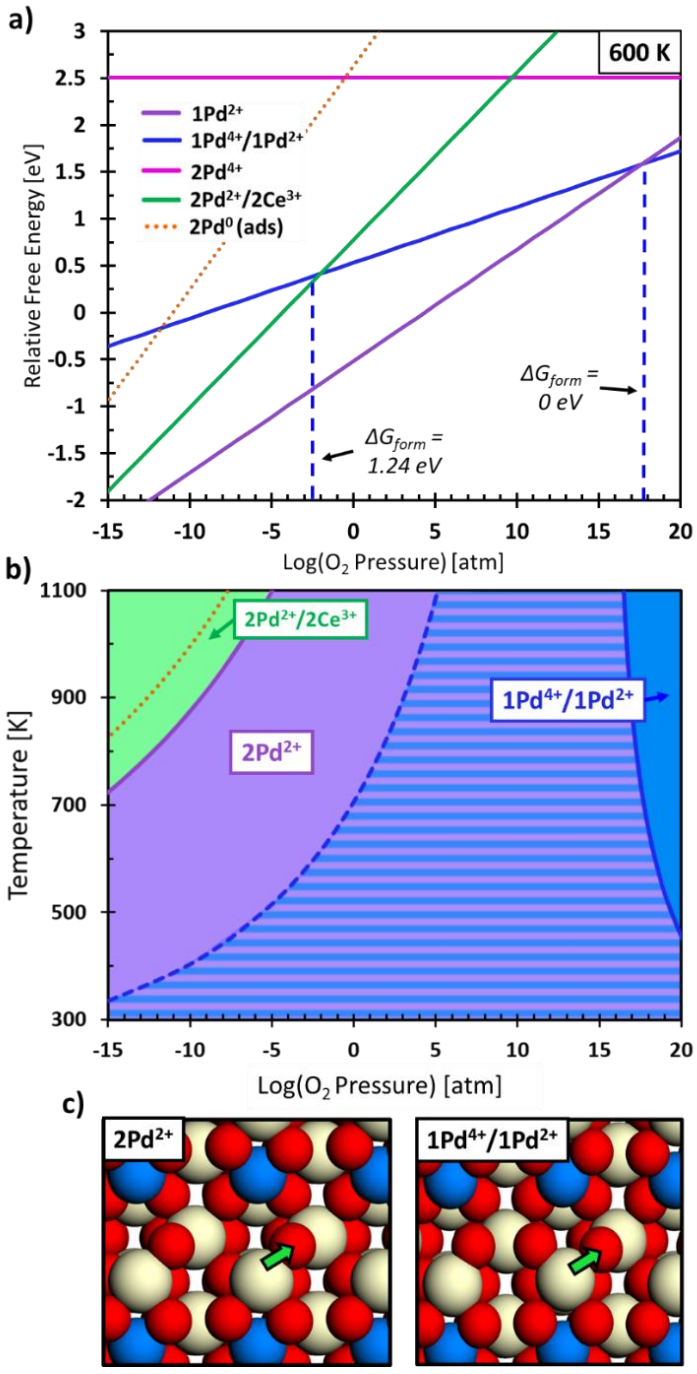

Figure 6-8. (a) Relative free energy of $Pd_2Ce_{18}O_\delta(110)$ surfaces with varying Pd oxidation states at 600 K. (b) Phase diagram describing oxidation states of Pd in the surface. The striped region and dashed line indicate the region where the $2Pd^{2+}$ surface is thermodynamically stable, yet methane activation is still kinetically preferred through the $1Pd^{2+}/1Pd^{4+}$ site. An adsorbed $2Pd^0$ dimer is thermodynamically stable above the orange dotted line. (c) The structure of the relevant surfaces under catalytic combustion conditions. Green arrows indicate the favored hydrogen adsorption site during methane activation.

6.3.4. Electronic Structure upon Hydrogen Abstraction

The active nature of the Pd^{4+} state is further demonstrated by analyzing the density of states (DOS) of the $Pd_xCe_{1-x}O_\delta$ surface upon hydrogen abstraction. Figure 6-9(a-b) shows the total DOS of the (111)-$1Pd^{4+}$/$2Pd^{2+}$ and (111)-$3Pd^{2+}$ surfaces with a single hydrogen adsorbed in the pseudo-transition state structure, where the vertical green line denotes the Fermi level. Over the (111)-$3Pd^{2+}$ surface, hydrogen adsorption leads to a high energy isolated spin state characteristic of a $Ce^{4+} \rightarrow Ce^{3+}$ surface reduction. Orbital imaging of this state further confirms that it corresponds to the 4f state of the surface Ce atom adjacent to the hydrogen adsorption site, shown in the right-side panel of the figure. Over the (111)-$1Pd^{4+}$/$2Pd^{2+}$ surface, hydrogen abstraction reduces a surface Pd atom, which is demonstrated in the figure by the orbital image of the highest energy state below the Fermi level. The highest energy state clearly belongs to a localized Pd 4d state, which resides at a lower energy relative to the vacuum potential reference than the Ce 4f state. The Fermi level of the (111)-$1Pd^{4+}$/$2Pd^{2+}$ surface is 0.34 eV lower in energy than that of the (111)-$3Pd^{2+}$ surface, which approximately corresponds to the difference in activation energies between the two surface states.

This is further demonstrated over the $Pd_2Ce_{18}O_\delta$(110) surface in Figure 6-9(c-d). Similar to the $Pd_3Ce_{33}O_\delta$(111) surface, hydrogen abstraction over the (110)-$2Pd^{2+}$ state induces a high energy single spin state corresponding to an occupied Ce 4f orbital. This state is clearly absent over the (110)-$1Pd^{4+}$/$1Pd^{2+}$ surface, where again the highest occupied state corresponds to a Pd 4d state. In this case, the difference in Fermi level between the (110)-$1Pd^{4+}$/$1Pd^{2+}$ and (110)-$2Pd^{2+}$ is 0.83 eV.

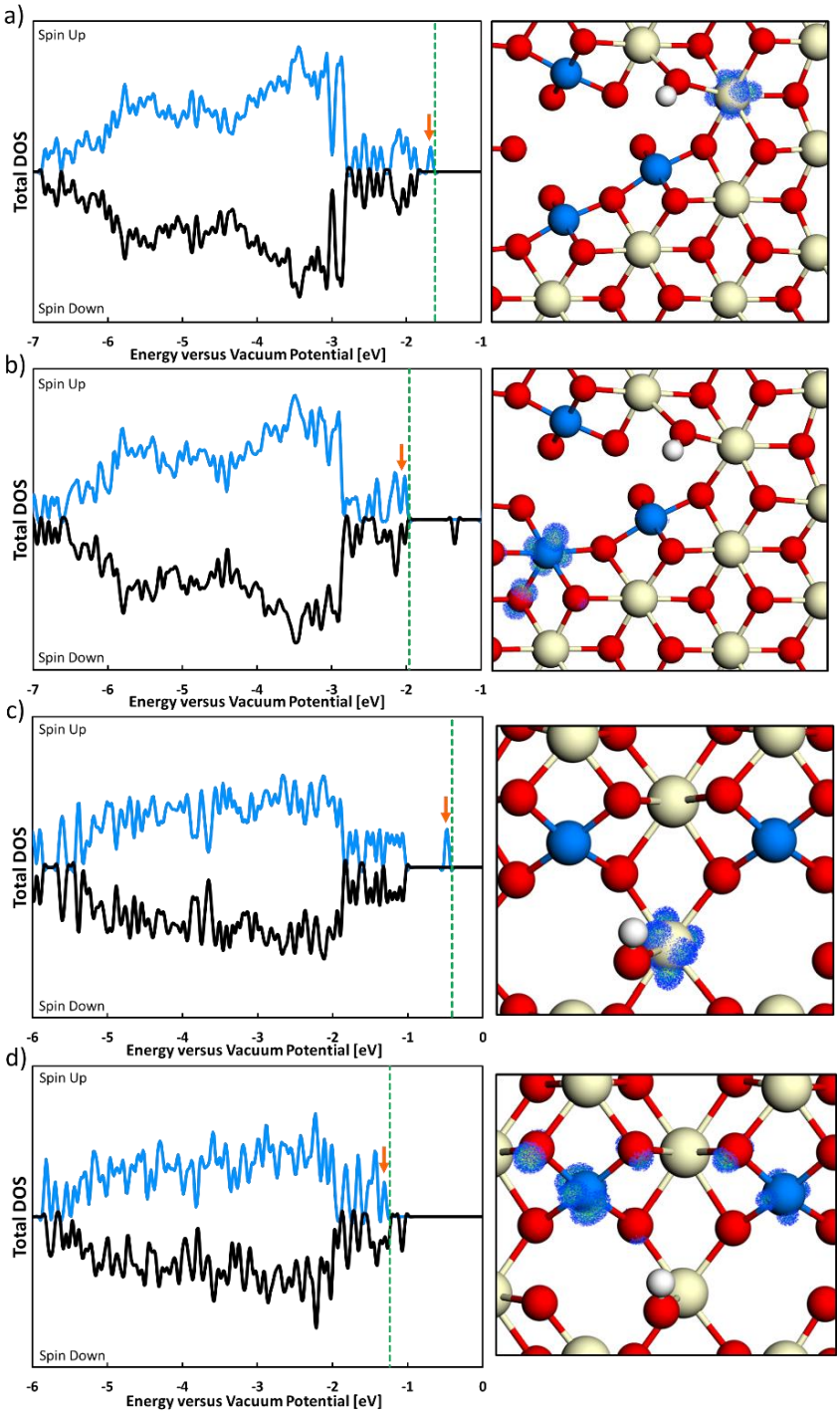

Figure 6-9. Total DOS (left) and orbital image (right) of the hydrogen abstraction process on (a) the (111)-3Pd^{2+} surface, (b) the (111)-2Pd^{2+}/1Pd^{4+} surface, (c) the (110)-2Pd^{2+} surface, and (d) the (110)-1Pd^{2+}/1Pd^{4+} surface. The Fermi level is indicated by the vertical dashed line, and the orange arrow indicates the state imaged in the right-side panels, where only surface layer is shown.

It is clear that additional localized Pd 4d states become occupied after methane activation over Pd^{4+} states. Since DFT does not reliably treat such highly localized states,[33] we investigated how the application of the Hubbard +U correction to Pd 4d states affects the energy of reduced $Pd_xCe_{1-x}O_\delta$ surfaces. We calculated hydrogen and oxygen adsorption energies on the (111)-$1Pd^{4+}$/$2Pd^{2+}$ and (111)-$3Pd^{2+}$ surface states, respectively, at progressively increasing U values ranging from 0 to 7 eV (summarized in Figure S6-1 of the Supplemental Information). We found that there was no net change to the apparent activation barrier as a result of the varying U values, as the changes in the hydrogen and oxygen adsorption energies are offsetting. Increasing the U correction on Pd 4d states increases the reducibility of the surface; thus, the ΔG_{form} contribution to the total apparent barrier increases and the ΔG_{act} contribution decreases. This reflects the previously identified[10,11] correlation between oxygen vacancy formation energy and methane activation barrier on ceria surfaces.

6.4. Discussion

The unique nature of the Pd^{4+} incorporated state in $Pd_xCe_{1-x}O_\delta$ surfaces offers a possible explanation for the observed activity increase in ceria-supported Pd catalysts compared to other supports. The results presented here suggest that the activation route at the Pd/ceria interface is unlike the favored activation mechanism over PdO surfaces. Over PdO(101), the activation path proceeds through an adsorbed precursor state where CH_4 forms an activated σ-complex with under-coordinated cus-Pd atoms exposed on the surface.[33,35] Martin *et al.* demonstrated that the depletion of cus-Pd 5s states in the

PdO(101) surface reduces repulsion from approaching CH_4, inducing a bonding interaction in the precursor σ-complex and a reduced activation barrier. Conversely, on the PdO(100) surface all exposed Pd atoms reside in coordinatively saturated square-planar formations, precluding the formation of the activated precursor state.[38] Here we found that the Pd^{2+} incorporated surface state was thermodynamically favored at typical operating conditions, in agreement with experimental HRTEM, XPS, and XRD observations.[5,39] The stable Pd^{2+} structures identified over a range of Pd surface concentrations and different $Pd_xCe_{1-x}O_\delta$ surface facets all feature stable square-planar configurations. As seen in Figure 6-6, further reducing the Pd^{2+} states to form cus-Pd sites (*i.e.* the (111)-$3Pd^{2+}/2Ce^{3+}$ surface state) does not become thermodynamically favorable until high temperatures are reached – at which point it is more favorable for Pd to egress from the lattice and form adsorbed Pd^0 clusters. Similar to the PdO(100) surface, we did not identify a significant CH_4 interaction with the Pd^{2+} incorporated surface state of $Pd_xCe_{1-x}O_\delta$, as no coordinatively unsaturated Pd atoms are exposed. Rather, the formation of oversaturated Pd^{4+} states leads to a low energy activation route, despite requiring an endergonic oxidation step prior to activation.

Methane activation over these sites proceeds through hydrogen abstraction to a surface oxygen atom adjacent to Pd^{4+}, where DOS analysis confirms that the Pd^{4+} state serves as a reduction center. Activation over the thermodynamically preferred Pd^{2+} state results in a significantly higher barrier because a Ce^{4+} surface atom, rather than a Pd^{4+} atom, is reduced leading to an occupied high-energy 4f state. At 0 K, the CI-NEB barrier over the (111)-$1Pd^{4+}/2Pd^{2+}$ state is 0.29 eV, which is 0.39 eV lower than the pseudo-barrier over the (111)-$3Pd^2$ state and 0.21 eV lower than the barrier over the PdO(101) surface. The resulting apparent rate over the (111)-$1Pd^{4+}/2Pd^{2+}$ site at T = 400 K and P_{O2} = 0.01 atm

is ~10^{16} times faster than the rate over the clean CeO_2(111) surface, ~10^7 times faster than the Pd(111) surface, and ~10^2 times faster than the PdO(101) surface (*i.e.* the experimentally determined active PdO surface during methane oxidation[32]).

The total 0 K activation barrier over the PdO(101) surface (ΔE_{total} = 0.50 eV) is obtained as the sum of the CH_4 adsorption energy to form the σ-complex precursor state relative to the gas phase (ΔE_{ads} = -0.15 eV) and the intrinsic activation barrier to dissociate methane from the precursor state (ΔE_{act} = 0.65 eV).[32] Weaver, Asthagiri, and co-workers[34,35] demonstrate that inclusion of the van der Waals correction, which addresses the well-established deficiency of standard DFT for modeling dispersion interactions, results in significantly stronger CH_4 adsorption (ΔE_{ads} = -0.42 eV) in agreement with experimental TPD adsorption energies. The addition of dispersion corrections also results in a lower activation energy (ΔE_{act} = 0.58 eV), therefore yielding a significantly lower total activation barrier (ΔE_{total} = 0.16 eV) over cus-Pd sites on PdO(101) compared to the uncorrected value. The apparent barrier over the (111)-$1Pd^{4+}$/$2Pd^{2+}$ surface calculated here does not account for dispersion corrections and is therefore more comparable to the uncorrected ΔE_{total} = 0.50 eV barrier over PdO(101), as it is reasonable to expect that dispersion corrections to the adsorbed precursor state will be similar in magnitude over both surfaces.

To test this assumption, we calculated the CH_4 adsorption energy on the (111)-$1Pd^{4+}$/$2Pd^{2+}$ surface using the DFT-D2 dispersion correction scheme introduced by Grimme.[60] We found that the initial CH_4 adsorbed state of the CI-NEB calculation (Figure 6-4) has an adsorption energy of ΔE_{ads} = -0.15 eV relative to gas phase CH_4. The inclusion of dispersive interactions also lower the energy of the pseudo-transition state structure,

yielding a dispersion-corrected total activation barrier of 0.09 eV over the (111)-1Pd^{4+}/2Pd^{2+} state. The dispersion correction systematically affects barriers, and thus it is assumed that this correction will not affect relative reaction rates and barrier differences used to derive the *ab initio* phase diagrams in Figures 6 and 7.

We further investigated whether a Pd^{4+} state may play a role in methane activation on the PdO(101) surface by calculating ΔG_{form}, ΔG_{act}, and ΔG_{app} over the PdO(101) surface where an oxygen atom is adsorbed over an exposed cus-Pd surface atom (referred to here as the O-PdO(101) surface). Computational details regarding calculations over the PdO(101) surface are provided in the Supplemental Information. We found that, at 400 K and P_{O2} = 0.01 atm, ΔG_{form} for this surface is 0.61 eV (shown in Figure S6-5 of the Supplemental Information). This indicates that the O-PdO(101) surface is not thermodynamically stable, in agreement with previous theoretical results reported by Rogal *et al.*[61] for PdO surfaces. The activation barrier, ΔG_{act}, over this surface is 0.04 eV, which was calculated with the CI-NEB as shown in Figure SS-6 of the Supplemental Information. This yields a total apparent barrier for the Pd^{4+} activation route over the O-PdO(101) surface that is higher, albeit similar in magnitude, than activation *via* the σ-complex precursor state on PdO(101). In comparison to Pd-Ce mixed oxide surfaces, the Pd^{4+} state of the O-PdO(101) surface lacks the stabilizing octahedral oxygen coordination offered by Pd incorporation in the fluorite lattice of CeO_2. Activation through the Pd^{4+} state over PdO(101) is therefore only relevant under very oxidizing conditions, as the ΔG_{form} contribution to the total barrier becomes prohibitively high under reducing conditions.

The pseudo-barrier approximation used here may systematically underestimate activation barriers. The CI-NEB results shown in Figure 6-4 and Figure S6-6, however, demonstrate that the pseudo-barrier approximation is reasonable for the $Pd_xCe_{1-x}O_\delta$ surfaces studied herein. Krcha *et al*. further evaluated the magnitude of error introduced by the pseudo-barrier approach, finding that on average the pseudo barrier approximation underestimated the reaction barrier by less than ~0.25 eV.[10] Additionally, it is well-known[62,63] that DFT-GGA overestimates the gas phase O_2 bond energy, with the PW91 functional yielding an $O_2 \rightarrow 2O$ dissociation energy of 6.17 eV compared to the experimental[64] value of 5.15 eV. This leads to a $\frac{1}{2}\mu_{O_2}$ value that is as much as ~0.5 eV too stable, shifting the phase boundaries in Figure 6 to higher oxygen pressures. This error improperly increases ΔG_{form}values required to form the Pd^{4+} state, which in turn increases the total apparent barrier, ΔG_{app}, for activation over Pd^{4+} states. Fortunately, the errors introduced by the pseudo-barrier approximation and overestimation of $\frac{1}{2}\mu_{O_2}$are in opposite directions, leading to a canceling of errors. These errors preclude direct comparison with experimental phase boundaries, but do not affect the conclusion that the Pd^{4+} is active in temperature and pressure regions where the Pd^{2+} state is thermodynamically favored.

The surface models investigated here directly model the $Pd_xCe_{1-x}O_\delta$ mixed oxide surface, but may also represent a reasonable approximation of the interfacial region between a Pd cluster and the ceria support. The work of Cargnello *et al.*[6,22] and Colussi *et al.*[5,14] demonstrate that Pd/ceria morphologies prepared with varying synthesis techniques yield similar activation barriers, but that faster rates are obtained when the degree of Pd-ceria interaction is maximized. We find that Pd incorporation in the ceria lattice leads to a

metastable Pd^{4+} state that is highly active, which can account for the increased activity seen in catalyst preparation methods that induce Pd mixing into the ceria lattice. Although the Pd^{4+} state may also offer an activation path over PdO, as evidenced by the low activation barrier over the O-PdO(101) state, the formation energy of the O-PdO(101) state compared to the (111)-$1Pd^{3+}/2Pd^{2+}$ (0.61 eV versus 0.08 eV at T = 400 K, P_{O2} = 0.01 atm) further emphasizes the important role incorporation in the ceria lattice plays in stabilizing the active Pd^{4+} state. As such, we propose that the Pd^{4+} activation route plays an important role at the interfacial region between Pd clusters and the ceria support, and is not limited to the idealized $Pd_xCe_{1-x}O_\delta$ surface models investigated here. To further explore this possibility, subsequent investigations will directly model the Pd-particle/ceria-surface interface.

6.5. Conclusions

Identifying dopant-metal/host-oxide combinations with unique interactions not present in the parent systems is essential for tuning catalytic performance. Here this is demonstrated for $Pd_xCe_{1-x}O_\delta$ catalysts, which offer unique catalytic activity toward the low temperature oxidation of methane. Pd atoms incorporated in the ceria lattice can take on multiple surface morphologies and oxidation states with varying catalytic properties. To investigate possible activation routes over these surfaces, we utilized DFT calculations to determine apparent methane activation barriers over $Pd_xCe_{1-x}O_\delta$(111) and (110) surfaces. Both the activity and stability of the active state are taken into account using the formalism of *ab initio* thermodynamics. Thus, the resulting apparent barriers reported here account for temperature and oxygen pressure variations affecting the stability of active Pd^{4+} surface

states. The results demonstrate that Pd^{4+} surface states can offer a lower methane activation barrier than analogous Pd^{2+} states under low temperature conditions. Furthermore, the activation route over $Pd_xCe_{1-x}O_\delta$ surfaces is fundamentally different than that of the PdO(101) surface, as CH_4 does not form a precursor σ-complex over incorporated Pd^{2+} metal centers in the $Pd_xCe_{1-x}O_\delta$ surface. The trade-off between state stability and activity was demonstrated in *ab initio* phase diagrams, where we extracted boundaries indicating stability and activity of each oxidation state as a function of temperature and oxygen pressure.

The results lend insight into the high activity of Pd/CeO_2 catalysts for low temperature methane oxidation. In agreement with experimental observations, Pd mixing into the ceria lattice yields high activity attributed to meta-stable Pd^{4+} states. Incorporation in ceria facilitates $Pd^{4+} \leftrightarrow Pd^{2+}$ transitions, as the fluorite lattice allows for Pd atoms to shift between octahedral and square-planar oxygen coordination environments. During low temperature methane oxidation, incorporated Pd sites can be oxidized by reactant O_2, which in turn serve as reduction centers upon methane activation yielding rapid catalytic turnover. As this behavior is unique to the mixed nature of the oxide, it exemplifies how the chemical interactions between metal dopants and host oxides may be exploited to optimize catalyst design.

6.6. Acknowledgments

This research was supported by funding from the National Science Foundation grant CBET-1032979.

6.7. Supplemental Information

Provided in the Supplemental information are calculation results demonstrating the effect of the U correction applied to Pd 4d states; the optimized DFT structures of clean and H-adsorbed $Pd_3Ce_{33}O_\delta(111)$ and $Pd_2Ce_{18}O_\delta(110)$ surfaces; *ab initio* phase diagrams for $Pd_xCe_{36-x}O_\delta(111)$ surfaces (where x = 1 to 2); free energy diagrams for PdO(101) and O-PdO(101) surfaces; the CI-NEB calculation of the methane activation barrier over the O-PdO(101) surface; computational details for PdO(101) surfaces; tabulated entropic contributions to free energies; structural coordinates of surfaces; and DFT total energies.

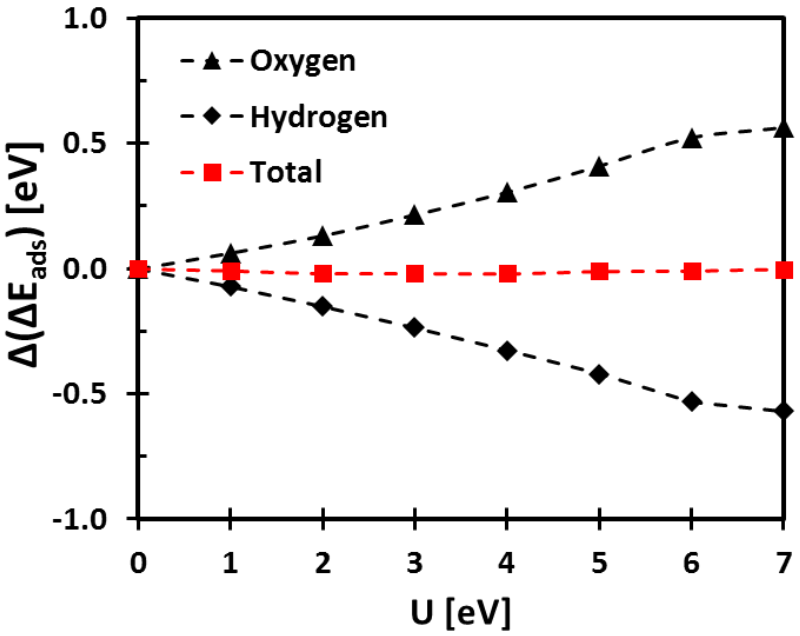

Figure S6-1. Dependence of the calculated oxygen and hydrogen adsorption energies on the (111)-$3Pd^{2+}$ and (111)-$2Pd^{2+}/1Pd^{4+}$ surfaces, respectively, on the U value applied to the 4d states of Pd. The total apparent barrier, ΔG_{app}, is not affected by the choice of U value because changes to ΔG_{form} and ΔG_{act} cancel.

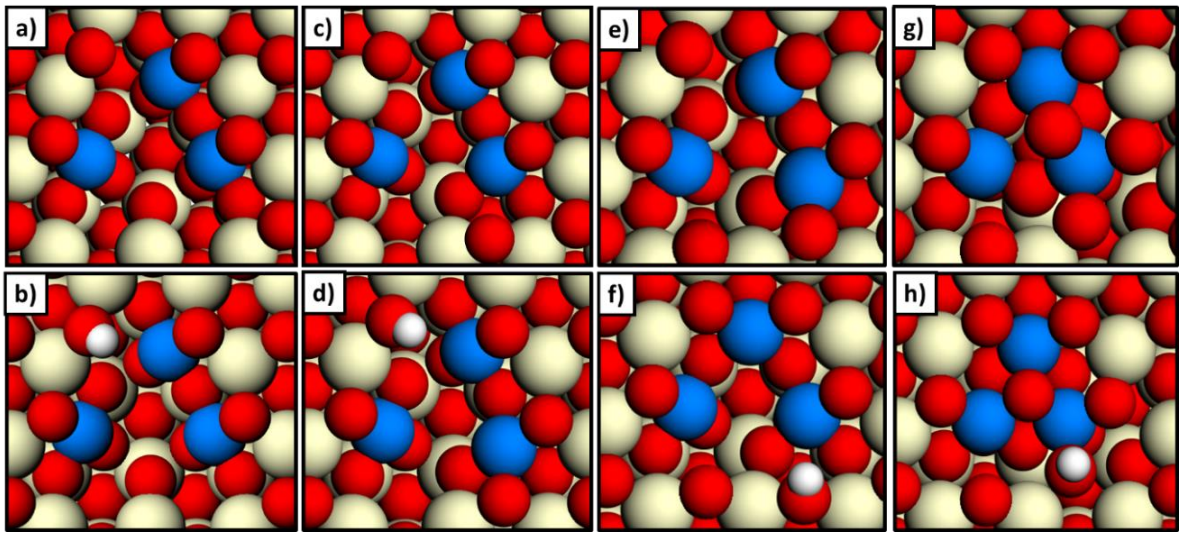

Figure S6-2. DFT optimized structure of clean surfaces (top panels) and hydrogen adsorbed surfaces (bottom panels) of (a-b) $3Pd^{2+}$, (c-d) $1Pd^{4+}/2Pd^{2+}$, (e-f) $2Pd^{4+}/1Pd^{2+}$, and (g-h) $3Pd^{4+}$ incorporated $Pd_3Ce_{33}O_\delta(111)$ surfaces.

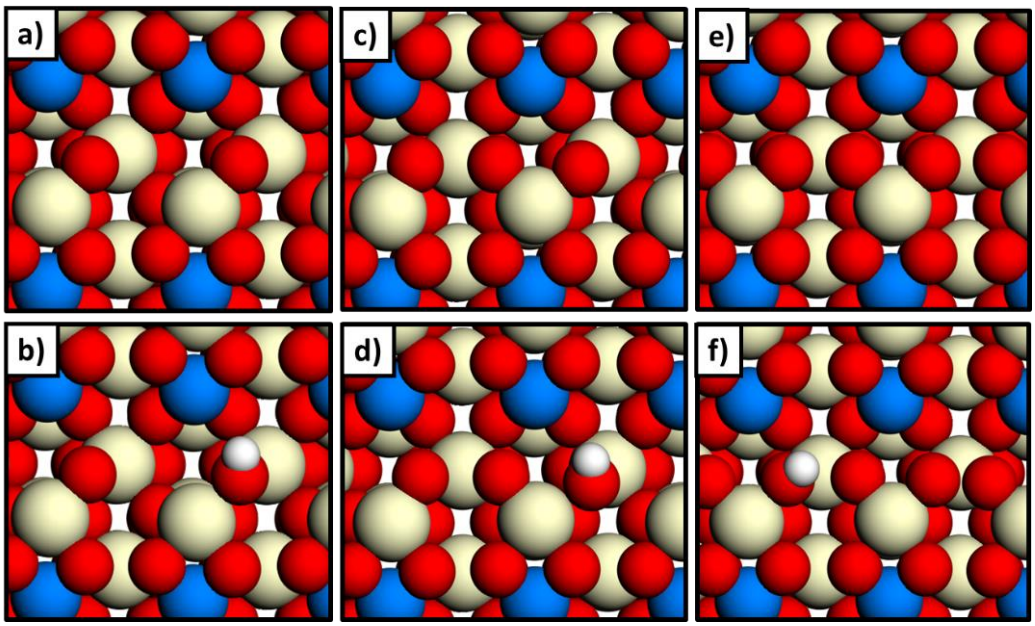

Figure S6-3. DFT optimized structure of clean surfaces (top panels) and hydrogen adsorbed surfaces (bottom panels) of (a-b) $2Pd^{2+}$, (c-d) $1Pd^{4+}/1Pd^{2+}$, and (e-f) $2Pd^{4+}$ incorporated $Pd_2Ce_{18}O_\delta(110)$ surfaces.

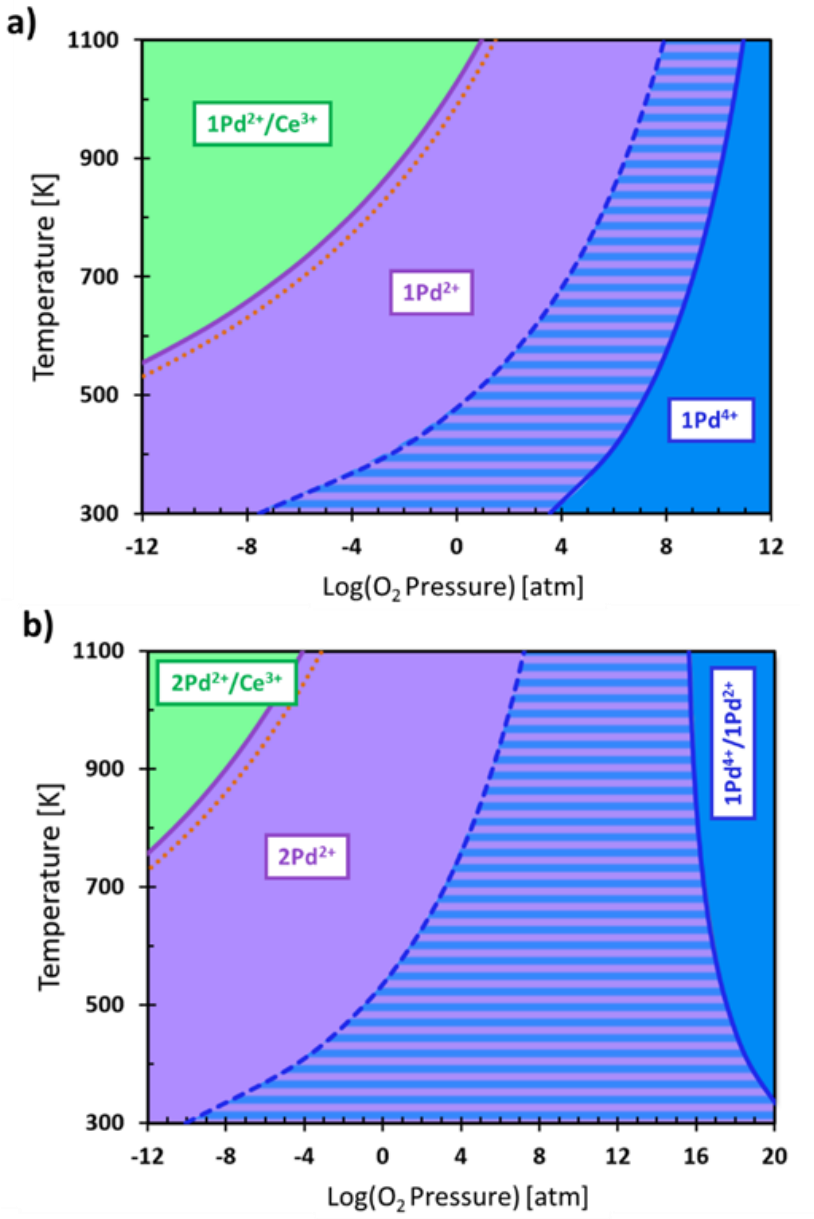

Figure S6-4. Phase diagram describing Pd oxidation states in the $Pd_xCe_{36-x}O_\delta(111)$ surface containing (a) one Pd dopant atom and (b) two dopant atoms per unit cell. The solid shaded regions separated by solid colored lines indicate thermodynamically stable regions in *T*,*P* space. The striped region and dashed line indicate the region where the Pd^{2+} state is thermodynamically stable, but methane activation is still kinetically preferred on the Pd^{4+} state. Adsorbed metallic Pd^0 clusters are thermodynamically stable above the orange dotted line.

The PdO(101) surface was modeled with a periodic 6.314 Å × 6.129 Å orthogonal unit cell consisting of three O-Pd-O tri-layers in the z-direction perpendicular to the surface with a 15 Å vacuum layer separating images perpendicular to the surface. This totals to 12 Pd atoms and 12 O atoms in the stoichiometric PdO(101) surface, as shown in Figure S5a. The O-PdO(101) surface was modeled by adsorbing a single O atom above a cus-Pd atom exposed on the surface, indicated by the green arrow in Figure S5b. Brillouin zone sampling with a *7×7×1* MP k-point spacing was employed, where all other DFT calculation settings were the same as described for calculations on the CeO_2 surface models.

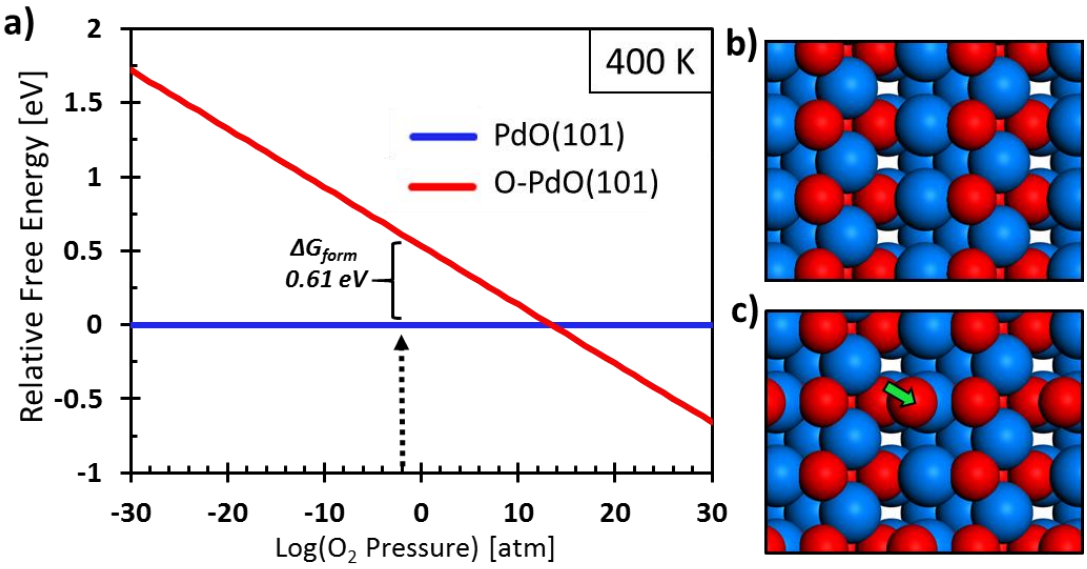

Figure S6-5. (a) Relative free energy diagram at 400 K for the PdO(101) surface with varying oxygen terminations, where the black arrow indicates the oxygen pressure at the conditions reported in Table 6-1. (b-c) DFT optimized structure of the (b) clean PdO(101) surface and (c) O-PdO(101) surface. The green arrow indicates the favored hydrogen adsorption site.

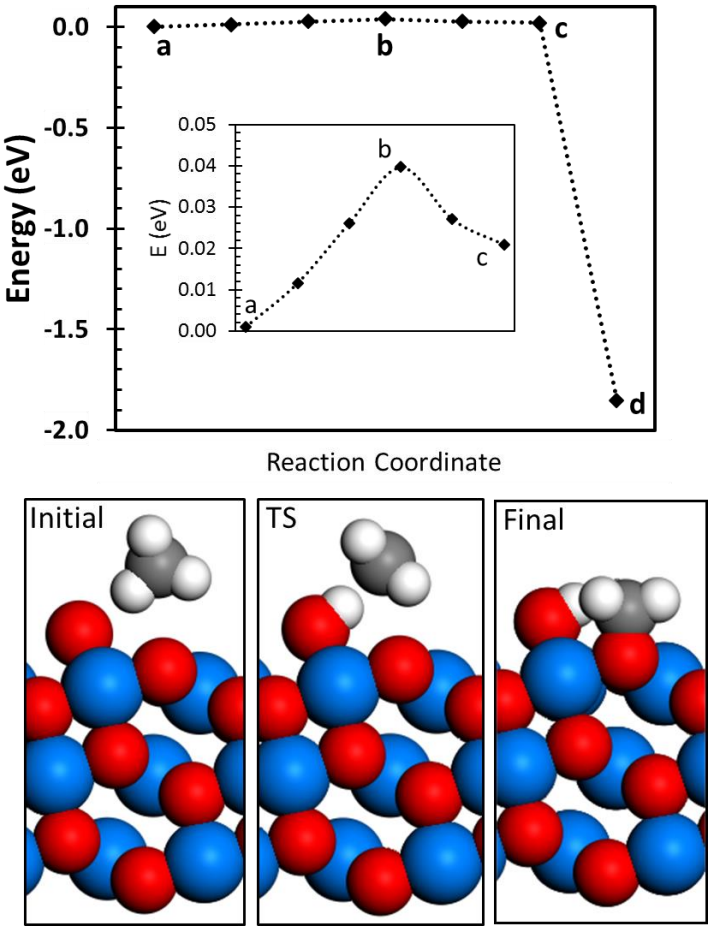

Figure S6-6. Reaction energy diagram for methane activation over the O-PdO(101) surface, where the data points represent (a) the initial $CH_{4(g)}$ state, (b) the transition state identified with CI-NEB, (c) the pseudo-transition state consisting of H* and $\cdot CH_3$ far from the surface, and (d) the final CH_3* + H* state. The points between (a)-(c) were obtained by CI-NEB with four equally spaced images between the initial state (a) and the pseudo-transition state (c). The structures shown respectively correspond to points (a), (b), and (d) in the energy diagram.

6.8. References

1. E. W. McFarland and H. Metiu, Chem. Rev. **113** (6), 4391-4427 (2013).
2. P. Gélin and M. Primet, Applied Catalysis B: Environmental **39** (1), 1-37 (2002).
3. T. V. Choudhary, S. Banerjee and V. R. Choudhary, Appl. Catal. A: Gen. **234** (1–2), 1-23 (2002).
4. D. Ciuparu, M. R. Lyubovsky, E. Altman, L. D. Pfefferle and A. Datye, Catalysis Reviews **44** (4), 593-649 (2002).
5. S. Colussi, A. Gayen, M. F. Camellone, M. Boaro, J. Llorca, S. Fabris and A. Trovarelli, Angew. Chem. Int. Ed. **48** (45), 8481-8484 (2009).
6. M. Cargnello, J. J. D. Jaén, J. C. H. Garrido, K. Bakhmutsky, T. Montini, J. J. C. Gámez, R. J. Gorte and P. Fornasiero, Science **337** (6095), 713-717 (2012).
7. R. J. Farrauto, Science **337** (6095), 659-660 (2012).
8. Y. Zhu, S. Zhang, J.-j. Shan, L. Nguyen, S. Zhan, X. Gu and F. Tao, ACS Catalysis **3** (11), 2627-2639 (2013).
9. A. D. Mayernick and M. J. Janik, J. Catal. **278** (1), 16-25 (2011).
10. M. D. Krcha, A. D. Mayernick and M. J. Janik, J. Catal. **293** (0), 103-115 (2012).
11. A. D. Mayernick and M. J. Janik, J. Phys. Chem. C **112** (38), 14955-14964 (2008).
12. A. D. Mayernick and M. J. Janik, J. Chem. Phys. **131** (8), 084701-084712 (2009).
13. S. Colussi, A. Trovarelli, C. Cristiani, L. Lietti and G. Groppi, Catal. Today **180** (1), 124-130 (2012).
14. S. Colussi, A. Gayen, J. Llorca, C. de Leitenburg, G. Dolcetti and A. Trovarelli, Ind. Eng. Chem. Res. **51** (22), 7510-7517 (2012).
15. L. Adijanto, D. A. Bennett, C. Chen, A. S. Yu, M. Cargnello, P. Fornasiero, R. J. Gorte and J. M. Vohs, Nano Lett. **13** (5), 2252-2257 (2013).
16. X. Wang and R. J. Gorte, Catal. Lett. **73** (1), 15-19 (2001).
17. L. Meng, J.-J. Lin, Z.-Y. Pu, L.-F. Luo, A.-P. Jia, W.-X. Huang, M.-F. Luo and J.-Q. Lu, Applied Catalysis B: Environmental **119–120** (0), 117-122 (2012).
18. E. Lundgren, J. Gustafson, A. Mikkelsen, J. N. Andersen, A. Stierle, H. Dosch, M. Todorova, J. Rogal, K. Reuter and M. Scheffler, Phys. Rev. Lett. **92** (4), 046101 (2004).
19. J. Klikovits, M. Schmid, L. R. Merte, P. Varga, R. Westerström, A. Resta, J. N. Andersen, J. Gustafson, A. Mikkelsen, E. Lundgren, F. Mittendorfer and G. Kresse, Phys. Rev. Lett. **101** (26), 266104 (2008).
20. T. P. Senftle, R. J. Meyer, M. J. Janik and A. C. T. van Duin, J. Chem. Phys. **139** (4), 044109-044115 (2013).
21. K. R. Priolkar, P. Bera, P. R. Sarode, M. S. Hegde, S. Emura, R. Kumashiro and N. P. Lalla, Chem. Mater. **14** (5), 2120-2128 (2002).
22. M. Cargnello, P. Fornasiero and R. J. Gorte, Catal. Lett. **142** (9), 1043-1048 (2012).
23. M. Cargnello, V. V. T. Doan-Nguyen, T. R. Gordon, R. E. Diaz, E. A. Stach, R. J. Gorte, P. Fornasiero and C. B. Murray, Science **341** (6147), 771-773 (2013).

24. R. Craciun, W. Daniell and H. Knözinger, Appl. Catal. A: Gen. **230** (1–2), 153-168 (2002).
25. L. M. Misch, J. A. Kurzman, A. R. Derk, Y.-I. Kim, R. Seshadri, H. Metiu, E. W. McFarland and G. D. Stucky, Chem. Mater. **23** (24), 5432-5439 (2011).
26. L. Meng, A.-P. Jia, J.-Q. Lu, L.-F. Luo, W.-X. Huang and M.-F. Luo, J. Phys. Chem. C **115** (40), 19789-19796 (2011).
27. S. Hinokuma, H. Fujii, M. Okamoto, K. Ikeue and M. Machida, Chem. Mater. **22** (22), 6183-6190 (2010).
28. J. A. Farmer and C. T. Campbell, Science **329** (5994), 933-936 (2010).
29. C. Chen, J. Cao, M. Cargnello, P. Fornasiero and R. J. Gorte, J. Catal. **306** (0), 109-115 (2013).
30. Z. Yang, Z. Lu, G. Luo and K. Hermansson, Phys. Lett. A **369** (1-2), 132-139 (2007).
31. J. H. Guanghui Zhu, Dmitri Yu. Zemlyanov, Fabio H. Ribeiro, J. Phys. Chem. B **109**, 2331-2337 (2005).
32. A. Hellman, A. Resta, N. M. Martin, J. Gustafson, A. Trinchero, P. A. Carlsson, O. Balmes, R. Felici, R. van Rijn, J. W. M. Frenken, J. N. Andersen, E. Lundgren and H. Grönbeck, J. Phys. Chem. Lett. **3** (6), 678-682 (2012).
33. Y.-H. Chin, C. Buda, M. Neurock and E. Iglesia, J. Am. Chem. Soc. **135** (41), 15425-15442 (2013).
34. A. Antony, C. Hakanoglu, A. Asthagiri and J. F. Weaver, J. Chem. Phys. **136** (5), 054702 (2012).
35. J. F. Weaver, C. Hakanoglu, A. Antony and A. Asthagiri, Chem. Soc. Rev. **43** (22), 7536-7547 (2014).
36. J. F. Weaver, C. Hakanoglu, J. M. Hawkins and A. Asthagiri, J. Chem. Phys. **132** (2), - (2010).
37. J. F. Weaver, J. A. Hinojosa Jr, C. Hakanoglu, A. Antony, J. M. Hawkins and A. Asthagiri, Catal. Today **160** (1), 213-227 (2011).
38. N. M. Martin, M. Van den Bossche, A. Hellman, H. Grönbeck, C. Hakanoglu, J. Gustafson, S. Blomberg, N. Johansson, Z. Liu, S. Axnanda, J. F. Weaver and E. Lundgren, ACS Catalysis **4** (10), 3330-3334 (2014).
39. R. V. Gulyaev, T. Y. Kardash, S. E. Malykhin, O. A. Stonkus, A. S. Ivanova and A. I. Boronin, Phys. Chem. Chem. Phys. **16** (26), 13523-13539 (2014).
40. G. Kresse and J. Furthmuller, Comput. Mater. Sci. **6**, 15-50 (1996).
41. G. Kresse and J. Furthmuller, Phys. Rev. B **54** (16), 11169-11186 (1996).
42. J. P. Perdew, J. A. Chevary, S. H. Vosko, K. A. Jackson, M. R. Pederson, D. J. Singh and C. Fiolhais, Phys. Rev. B **46** (11), 6671-6687 (1992).
43. G. Kresse and D. Joubert, Phys. Rev. B **59** (3), 1758-1775 (1999).
44. H. J. Monkhorst and J. D. Pack, Phys. Rev. B **13** (12), 5188 LP - 5192 (1976).
45. J. F. Herbst, R. E. Watson and J. W. Wilkins, Phys. Rev. B **17** (8), 3089 LP - 3098 (1978).
46. V. I. Anisimov and O. Gunnarsson, Phys. Rev. B **43** (10), 7570 LP - 7574 (1991).
47. S. Fabris, S. d. Gironcoli, S. Baroni, G. Vicario and G. Balducci, Phys. Rev. B **71**, 041102 (2005).

48. S. Fabris, S. d. Gironcoli, S. Baroni, G. Vicario and G. Balducci, Phys. Rev. B **72**, 237102 (2005).
49. J. L. F. Da Silva, M. V. Ganduglia-Pirovano, J. Sauer, V. Bayer and G. Kresse, Phys. Rev. B **75** (4), 045121-045110 (2007).
50. M. Nolan, S. Grigoleit, D. C. Sayle, S. C. Parker and G. W. Watson, Surf. Sci. **576**, 217-229 (2005).
51. M. Nolan, S. C. Parker and G. W. Watson, Surf. Sci. **595**, 223-232 (2005).
52. Z. Yang, G. Luo, Z. Lu and K. Hermansson, J. Chem. Phys. **127** (7), 074704-074705 (2007).
53. K. Reuter and M. Scheffler, Phys. Rev. B **65** (3), 035406 (2001).
54. D. Knapp and T. Ziegler, J. Phys. Chem. C **112** (44), 17311-17318 (2008).
55. G. Henkelman, B. P. Uberuaga and H. Jonsson, J. Chem. Phys. **113** (22), 9901-9904 (2000).
56. G. Henkelman and H. Jonsson, J. Chem. Phys. **113** (22), 9978-9985 (2000).
57. R. F. W. Bader, Acc. Chem. Res. **18**, 9-15 (1985).
58. G. Henkelman, A. Arnaldsson and H. Jonsson, Comput. Mater. Sci. **36** (3), 354-360 (2006).
59. H. Zhang, J. Gromek, G. Fernando, H. Marcus and S. Boorse, Journal of Phase Equilibria **23** (3), 246-248 (2002).
60. S. Grimme, J. Comput. Chem. **27** (15), 1787-1799 (2006).
61. J. Rogal, K. Reuter and M. Scheffler, Phys. Rev. B **69** (7), 075421 (2004).
62. L. A. Curtiss, K. Raghavachari, P. C. Redfern and J. A. Pople, J. Chem. Phys. **106** (3), 1063-1079 (1997).
63. B. Hammer, L. B. Hansen and J. K. Nørskov, Phys. Rev. B **59** (11), 7413-7421 (1999).
64. D. R. Lide, (CRC Press, New York, 2004).

Chapter 7
Multi-scale Investigation of Active Sites at the Cluster-Support Interface

Abstract

We combine *ab initio* and ReaxFF simulation methods to assess stability and activity of unique sites at the Pd/ceria interface. ReaxFF-based Grand Canonical Monte Carlo (GC-MC) is employed to model oxygen uptake in Pd clusters, providing insight into the structure of the Pd/ceria interface at varying temperatures and oxygen pressures. PdO_x/ceria surface models (derived with GC-MC) serve as the basis for reactive molecular dynamics (RMD) simulations assessing methane activation kinetics. During RMD, Pd-Ce mixing at the interface increases catalytic activity, as methane light-off occurs more rapidly over embedded PdO_x clusters compared to supported clusters. These results motivate DFT investigations utilizing embedded-cluster models, which corroborate ReaxFF findings by demonstrating that Pd^{4+} states are stabilized in PdO_x clusters that are partially embedded in the ceria lattice. Activation barriers over embedded cluster sites yield combustion rates similar to those calculated for $Pd_3Ce_{33}O_{69}$(111) single-crystal models, demonstrating that high activity can be achieved at cluster/support interfaces in addition to doped $Pd_xCe_{1-x}O_\delta$ surfaces.

7.1. Introduction

Doped-oxides can provide emergent behavior leading to surface morphologies with unique catalytic properties.[1] A synergistic interaction between the ceria support and Pd cluster leads to the formation of transient mixed-metal oxide phases displaying high activity.[2, 3] Modeling the effect of phase transformations induced by exposure to a reactant gas phase is essential for identifying active sites created by cluster-support interactions. This, in turn, can inform design strategies during catalyst synthesis, pre-treatment, and operation. Density functional theory (DFT),[4, 5] when coupled with the formalism of *ab initio* thermodynamics,[6] is capable of modeling the stability of possible surface phases as a function of temperature and pressure. The computational expense of DFT, however, limits accessible system sizes and time scales, thus restricting studies to highly idealized surface models. Here, we employ the empirical ReaxFF[7] reactive force-field method in tandem with DFT to assess phase formation, and the corresponding creation of active sites, at the cluster-support interface of Pd/ceria catalysts. Our results demonstrate that interaction with the ceria support stabilizes transient Pd^{4+} states at conditions typical of low temperature combustion, leading to active methane dissociation sites at the cluster/support interface.

Recent studies point to a synergistic interaction at the Pd/ceria interface leading to rapid catalytic turn-over. Colussi *et al.*[8-10] demonstrated that the incorporation of Pd atoms in the ceria lattice *via* solution combustion synthesis (SCS) yields increased methane oxidation rates compared to traditional Pd/ceria catalysts prepared by incipient wetness impregnation (IWI). Similarly, Cargnello *et al.*[11] prepared core-shell $Pd@CeO_2$ catalysts

displaying exceptional methane combustion rates relative to typical IWI analogs. Again, the high performance of the Pd@CeO_2 catalysts can be attributed to Pd-ceria interactions at the metal/oxide interface, as the exposed area of this region is maximized by the core-shell construction. They further demonstrated the importance of this interaction in a subsequent CO oxidation study, reporting that conversion rates over Pd/ceria scale proportionally with the number of sites on the contact-line between the Pd cluster and the ceria support.[12] In our group, Mayernick *et al.*[2, 13, 14] utilized DFT calculations to show that Pd atoms can be thermodynamically stable when incorporated in fluorite ceria lattice, and that Pd^{4+} incorporated states can offer effective methane activation sites.

Recently, we demonstrated that there is a trade-off between stability and activity during methane activation over Pd^{4+} surface states, in which the incorporation of Pd in the ceria lattice yields meta-stable Pd^{4+} states on the catalyst surface.[3] This corroborates experimental characterizations by Boronin *et al.*[15] and Zhu *et al.*[16] reporting $Pd^{\delta+}$ states in Pd/ceria catalysts that may be oxidized beyond the thermodynamically preferred 2+ state. Similarly, Farrauto *et al.*[17] reported thermal gravimetric analysis (TGA) investigations and Nilsson *et al.*[18] reported X-ray absorption spectroscopy (XANES) and mass spectrometry (MS) results demonstrating that PdO formation occurs more readily on ceria compared to other supports, such as alumina and zirconia. Together, these results suggest that ceria promotes the oxidation of Pd, which serves as the active phase for catalytic oxidation. However, structural details of oxide formation at the Pd/ceria interface are still not well understood at the atomic level, motivating the use of multi-scale computational methods employing DFT and ReaxFF to investigate morphology and activity at the Pd/ceria interface.

ReaxFF is ideally suited to bridge the size gap separating quantum and classical simulation scales, which is instrumental to modeling heterogeneous catalysis over oxide-supported metal catalysts. The ReaxFF potential features a transferable description between atoms in gas phase molecules and in solid solution phases. This, coupled with a reactive bond dissociation description that eliminates the need for pre-defined reaction paths, allows ReaxFF to model phase formation induced by molecular adsorption, dissociation, and diffusion between gas, surface, and bulk phases. Chenoweth *et al.*[19, 20] demonstrated the use of reactive molecular dynamics (RMD) and Monte Carlo (MC) methods with the ReaxFF potential to assess hydrocarbon oxidation over vanadia catalysts. Similarly, Mueller *at al.*[21] and Neyts *el al.*[22] have employed ReaxFF to model carbon nanotube (CNT) growth over Ni-based catalysts. These studies demonstrate the ability of ReaxFF for modeling processes involving atom diffusion across solid-gas boundaries.

7.2. ReaxFF-Monte Carlo: Oxide formation at the Pd/ceria interface

To model oxide formation in ceria-supported Pd clusters, we employ the recently developed grand canonical Monte Carlo/molecular dynamics (GC-MC/MD)[23] approach with available Pd/O[23] and Ce/O[24] parameter sets. Here, Pd/Ce/O cross-terms in the parameter set are optimized to reproduce DFT oxygen vacancy formation energies in the Pd-incorporated surface models reported in our previous study.[3] The Ce/O interaction parameters are modified to better reproduce oxygen adsorption and vacancy formation energies on the CeO_2(111) surface. RMD simulations of methane activation on the Pd/ceria surface employ previously developed C/H[25] and Pd/C/H[26, 27] interaction parameters.

Additional data regarding parameter fitting are provided in the supplemental information, along with the full parameter set input file for ReaxFF implementation.

We utilize Monte Carlo in the grand canonical ensemble to simulate oxygen uptake at varying pressures, where MC moves include the insertion, deletion, and translation of O atoms in the system on an off-lattice basis (*i.e.* there are no pre-defined insertion sites). This simulation method incorporates a conjugant-gradient (CG) relaxation of forces after every trial MC move prior to applying the usual Metropolis acceptance criteria.[28] This allows the Pd/ceria lattice to restructure during oxygen uptake as the oxide phase is formed. The Metropolis criteria for oxygen insertion and deletion steps are calculated relative to the chemical potential of an oxygen reservoir, $\frac{1}{2}\mu_{O2}(T,P)$. The oxygen reservoir in this case is represented by gas phase O_2 under reaction conditions. Further details concerning the hybrid GC-MC/MD methodology and the calculation of $\frac{1}{2}\mu_{O2}(T,P)$ are available in our previous work.[23]

To assess the impact of the ceria support during oxide formation in Pd clusters, we utilize both supported and partially embedded Pd cluster models. The cluster model, motivated by the HRTEM characterization of Pd/ceria reported by Cargnello *et al.*[12], consists of a ~15 Å icosahedron cluster that is halved at the center, yielding a (100) surface termination along the basal plane of the cluster. The basal plane is placed on a CeO_2(111) surface consisting of three O-Ce-O tri-layers in a periodic 39.8 Å× 33.9 Å× 75.0 Å unit cell. This totals to 90 Pd atoms, 324 Ce atoms, and 648 O atoms. Pd demonstrates a propensity to mix into the ceria lattice, and as such we conduct simulations over partially embedded cluster models. To approximate an embedded cluster, the first O-Ce-O tri-layer

directly beneath the Pd cluster is removed and the cluster is lowered into the resulting void space, where a total of 26 Ce atoms and 52 O atoms were removed. The MC algorithm includes a CG optimization step at each iteration, allowing the supported and embedded surface models to structurally relax as the MC run equilibrates. This is seen in Figure 7-1, depicting supported and embedded oxide structures after GC-MC equilibration at T = 500 K and $P(O_2)$ = 1 atm. The inset of Figure 7-1(b) reveals distinct Pd mixing into the ceria lattice at the cluster edge in the embedded cluster model, where Pd atoms migrate toward open lattice positions created by ceria defects. This behavior is not evident over the pristine ceria surface, as seen in the inset of Figure 7-1(a).

Additional simulations were conducted at oxygen pressures ranging from 10^{-15} atm to 1 atm at 500 K, which encompasses conditions for low temperature combustion. Oxygen uptake is summarized in Figure 7-2, which plots the overall O:Pd ratio in the Pd cluster at each MC trial step. As seen in the figure, higher O:Pd ratios are achieved in embedded cluster models compared to supported models. This corroborates our recent DFT study,[3] which found that oxidized $Pd^{\delta+}$ states are stabilized by Pd incorporation in the ceria lattice, as well as supports the experimental findings of Farrauto *et al.*[17] and Nilsson *et al.*[18] demonstrating that ceria enhances PdO_x formation. The inset of Figure 1(b) shows that Pd atoms at the cluster/support interface migrate away from the Pd cluster to assume higher oxygen coordination offered by defects in the ceria lattice. This further indicates that incorporation will occur readily as Pd atoms and small clusters diffuse across the ceria surface and encounter step, vacancy, or grain boundary defects. The equilibrated GC-MC/MD structures obtained here serve as surface models for subsequent RMD simulations

of methane activation, as they approximate the thermodynamically stable surface morphology under reaction conditions.

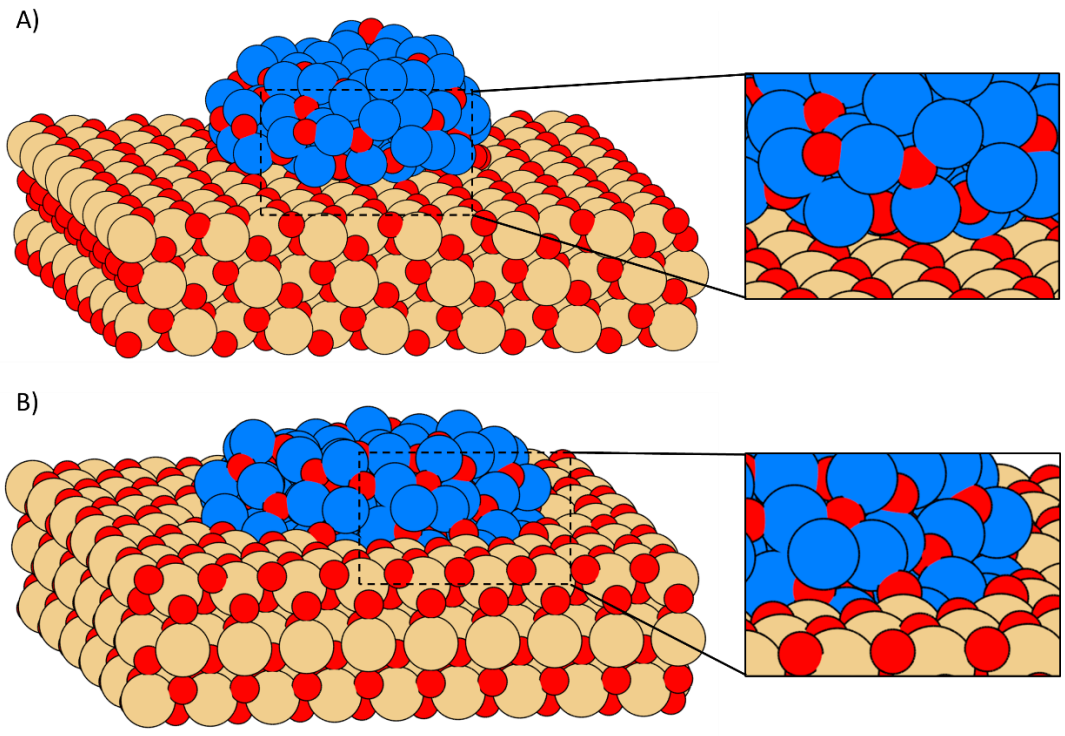

Figure 7-1. Final structure of (a) supported and (b) embedded Pd clusters after GC-MC simulation of oxygen uptake at T = 500 K and $P(O_2)$ = 1 atm.

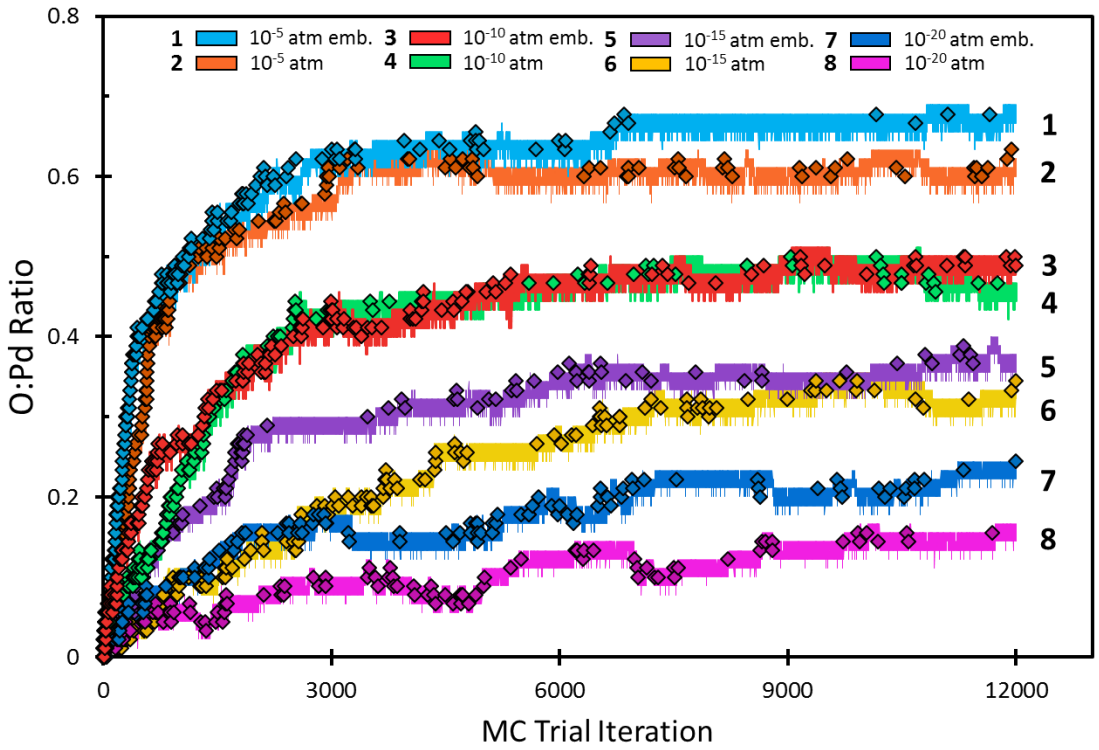

Figure 7-2. GC-MC simulations of oxygen uptake in supported and embedded Pd clusters on the CeO2(111) surface. Lines correspond to MC attempts and data points correspond to accepted MC moves. Additional oxygen uptake is observed over embedded cluster models

7.3. ReaxFF-Molecular Dynamics: Methane activation at the Pd/ceria interface

We employ RMD simulations of methane activation to assess relative activation rates over varying cluster/support interfacial morphologies. RMD simulations, conducted with the Verlet velocity algorithm,[29] were initiated with 30 CH_4 molecules placed randomly in the vacuum space above the surface, as shown in Figure 7-3(a), where the cell dimensions are unchanged from those employed in the GCMC simulations. A temperature programmed RMD scheme is used to simulate methane light-off, where temperature control is achieved with a Berendsen thermostat[30] employing a 100 fs damping constant.

To simulate light-off behavior, the target system temperature is ramped from 750 K to 1750 K over the course of the 50 ps simulation. High simulation temperatures (up to ~1750 K) are necessary to obtain methane dissociation within the accessible simulation time-frame (~50 ps). To prevent artificial surface restructuring at high temperatures, the surrounding ceria support is maintained at 500 K *via* dual-regime temperature control. Although high temperatures may enable spurious high-energy activation paths, comparing light-off temperatures between surface models will provide a reasonable assessment of relative activity, as demonstrated by Mueller *et al.*[21] when modeling Ni-catalyzed CNT growth.

To monitor methane activation, populations of molecular species in the system were recorded at 25 fs intervals throughout each simulation, with a bond-order cutoff of 0.30 employed to assess connectivity between all C/O/H atoms (connectivity involving Pd in the surface is ignored, allowing intermediate surface species to be identified). This is demonstrated in Figure 7-4(a), which plots species population against temperature during simulated methane light-off over the GC-MC (500 K, 1 atm) derived model of an embedded PdO_x cluster. As seen in the figure, methane activation at ~1440 K is marked by a sharp decrease in the number of gas phase CH_4 molecules accompanied by an increase in adsorbed H atoms, indicating dissociative methane adsorption. Additionally, partial combustion products (such as CHO, CH_2O, and CO) appear on the surface as intermediate species, along with total combustion products (H_2O and CO_2) in the gas phase. This demonstrates the feasibility of this method for assessing the onset of catalytic combustion.

Figure 7-4(b) compares methane light-off over Pd and PdO_x clusters that are both supported on and embedded in the ceria surface. Control simulations over pristine CeO_2(111), which result in no CH_4 activation events, were also conducted to ensure that

no activation sites reside on the ceria surface. As seen in the figure, the embedded PdO_x cluster achieves faster activation compared to the analogous supported cluster; this trend is reversed when comparing supported and embedded Pd metal clusters. This reversal is attributed to activation occurring over edge Pd atoms at the cluster/support interface, where such sites are less accessible to CH_4 in the embedded model compared to the supported model. Since the number of exposed sites decreases when the cluster is embedded, enhanced activation over the embedded PdO_x cluster must reflect lower barriers caused by PdO_x/CeO_x mixing at the interface. Additionally, analysis of the simulation trajectory shows that methane activation readily occurs at the cluster-support interface of the embedded cluster. This is demonstrated in Figure 7-3(b) depicting methane activation at 35 ps, and by Figure 7-3(c) showing a high concentration of hydrogen atoms adsorbed at the cluster/support interface.

Together, the GC-MC and RMD analyses help elucidate the role oxide formation at the Pd/ceria interface plays during methane oxidation. GC-MC reveals that Pd readily embeds in the ceria lattice under oxidizing conditions, leading to increased oxygen uptake. RMD demonstrates that CH_4 dissociation is facilitated by increased oxygen concentrations at the cluster/support interface. These results underscore that active participation of the ceria support enhances PdO_x formation, motivating the following DFT analysis of PdO_x stability and activity in partially embedded Pd clusters.

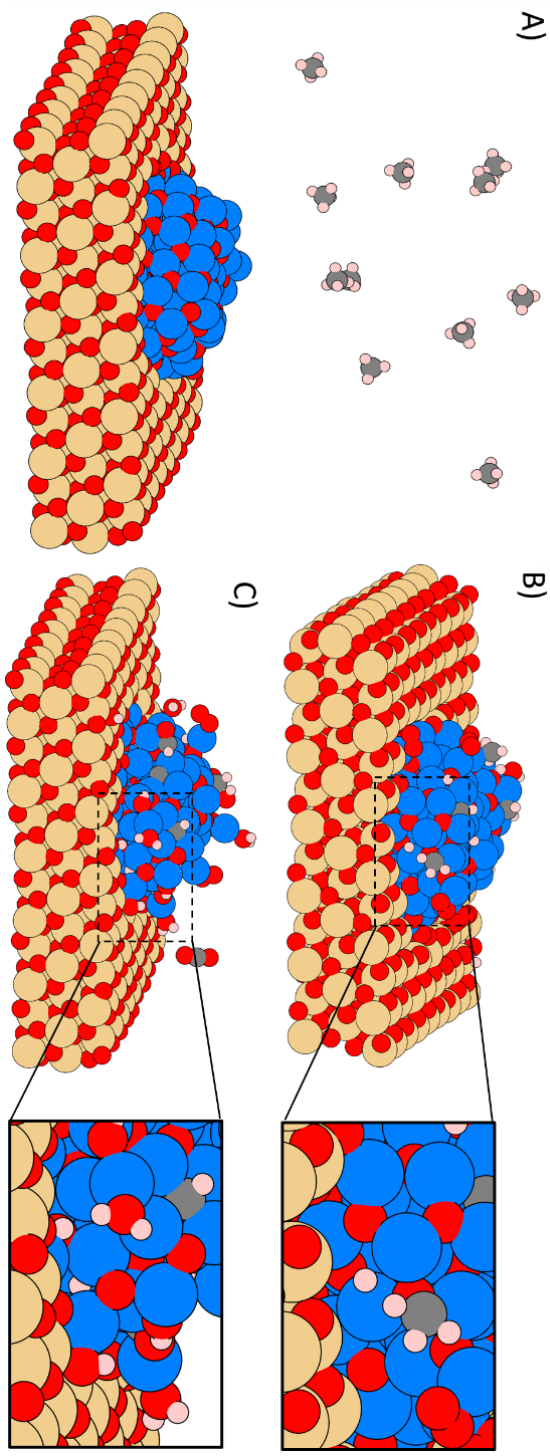

Figure 7-3. System structure in RMD simulation of methane activation over the GC-MC (T = 500 K, $P(O_2)$ = 1 atm) derived model of an embedded PdO_x cluster on the $CeO_2(111)$ surface at (a) 0 ps, (b) 35 ps, and (c) 50 ps. Gas phase CH_4 molecules far above the surface in (a) are omitted, and are omitted entirely in (b) and (c) for clarity.

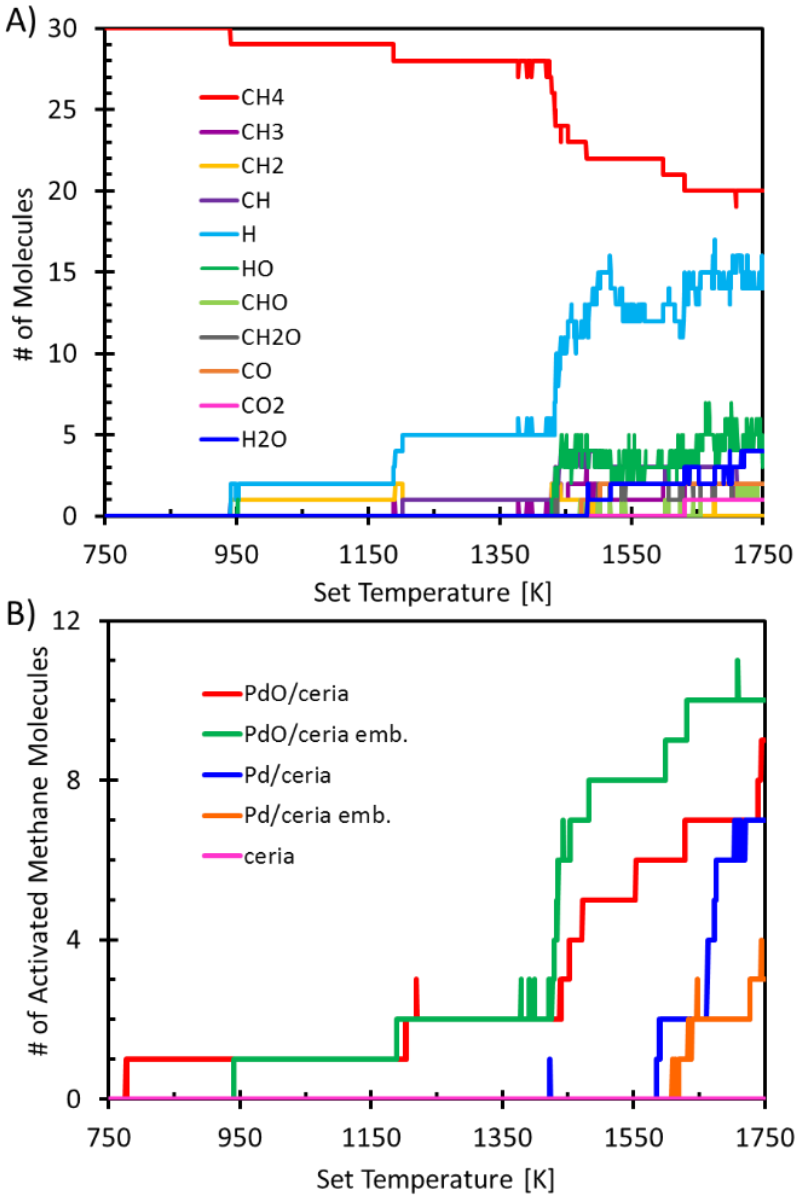

Figure 7-4. (a) RMD simulation of methane light-off curve over the GC-MC (T = 500 K, $P(O_2)$ = 1 atm) derived model of an embedded PdO_x cluster on the $CeO_2(111)$ surface. (b) Simulated methane light-off curves comparing supported and embedded PdO_x cluster models derived from GC-MC simulations.

7.4. DFT: PdO_x Stability and activity at the ceria interface

To complement the above ReaxFF results, we perform DFT calculations, in conjunction with *ab initio* thermodynamics, to assess the stability and activity of PdO_x formations at the metal/oxide interface of partially embedded clusters. Here, DFT total energies are calculated using the VASP simulation package with the PW91 exchange-correlation functional.[31] Following the methodology of our previous study, a U = 5 eV Hubbard correction is added to treat spurious electron delocalization in Ce 4f states.[13, 32] Plane-wave basis sets were truncated at 450 eV, and core electronic regions were represented by the projector augmented wave pseudo potential approximation[33] (PAW), with electronic valence configurations of $5s^2 5p^6 6s^2 4f^1 5d^1$ for Ce atoms, $4d^{10}$ for Pd atoms, $2s^2 2p^4$ for O atoms, $2s^2 2p^2$ for C atoms, and $1s^1$ for H atoms. Monkhorst-Pack[34] (MP) Brillouin zone sampling was used with a *2×2×1* MP k-point spacing, and all calculations were spin polarized.

Our previous *ab initio* thermodynamics investigation of $Pd_xCe_{1-x}O_\delta$ surfaces demonstrated that Pd^{2+} incorporated states are thermodynamically favored at ambient conditions, where an oxygen vacancy always accompanies Pd incorporation in the stoichiometric CeO_2 surface.[3] The study, however, also indicated that transient Pd^{4+} states may exist under catalytic operation, and that such states can offer low methane activation barriers. Here we extend the previously employed $Pd_3Ce_{33}O_{69}(111)$ surface model, featuring three incorporated Pd^{2+} atoms with square-planar oxygen coordination, to approximate oxide formation in a partially embedded cluster. This is accomplished by adsorbing a Pd_4O_4 cluster in the void space created by the three oxygen vacancies of the

$Pd_3Ce_{33}O_{69}$(111) surface, which yields an embedded Pd_4O_4 cluster with a formal oxidation state of 2+ for all Pd atoms. Models with Pd^{4+} states are derived by successively adding O atoms to the optimized $Pd_4O_4/Pd_3Ce_{33}O_{69}$(111) structure, as summarized in Figure 7-5. The Pd_4O_5 model (the surface designation is omitted from here on, as all Pd_4O_x clusters are adsorbed on the $Pd_3Ce_{33}O_{69}$(111) surface) shown in Figure 7-5(b) was obtained by adding the O2-labeled oxygen to the Pd_4O_4 model; the Pd_4O_6 model was obtained by adding oxygen O1 to the Pd_4O_5 model; and the Pd_4O_7 model is obtained by adsorbing an additional oxygen above the exposed cus-Pd on top of the cluster (not shown). The optimized PdO_x structures shown in the figure demonstrate a clear tendency for Pd to form square-planar units reminiscent of PdO bulk. The formation of the square-planar units is facilitated by Pd incorporation in the ceria lattice, as shown in cross-section view of the surface. This suggests that embedding Pd in ceria may aid the formation of stable Pd_4O_x clusters, as the fluorite lattice of ceria provides square-planar coordination sites for the incorporated Pd atoms. This notion is further quantified using *ab initio* thermodynamics to assess the relative stability of supported Pd_4O_x clusters as a function of temperature and oxygen pressure.

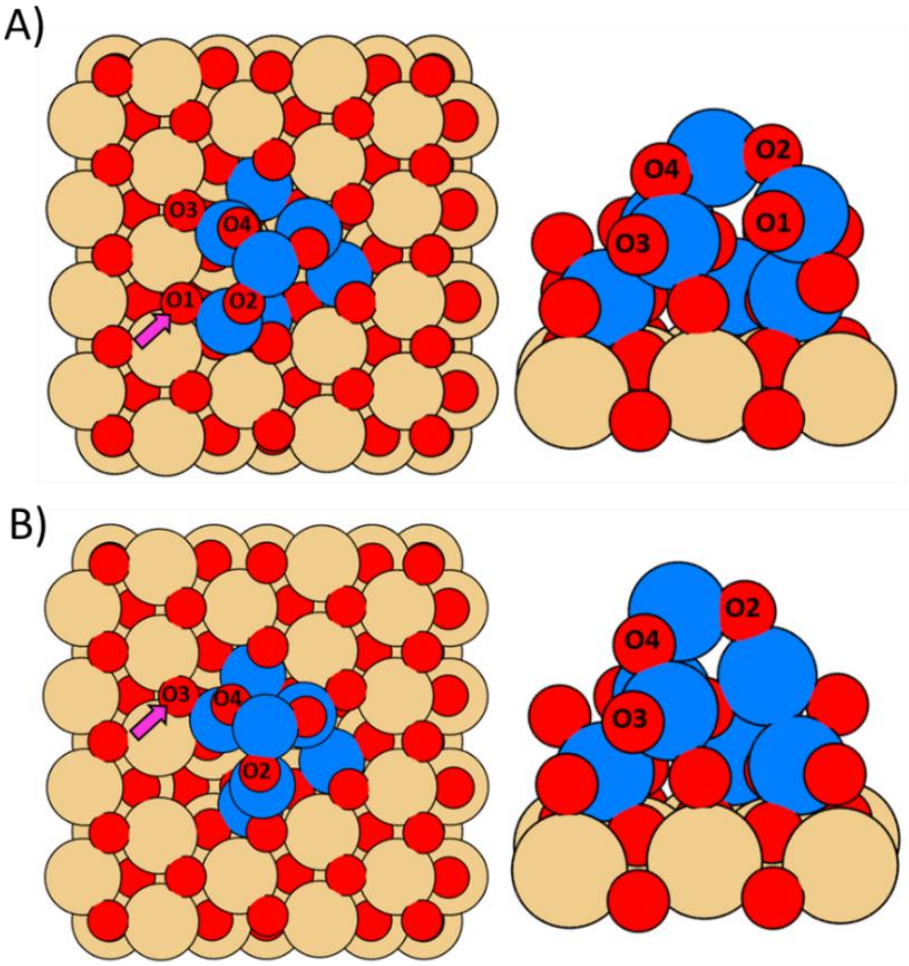

Figure 7-5. DFT optimized structure of the embedded (a) $Pd_4O_6/Pd_3Ce_{33}O_{69}$ cluster model and the (b) $Pd_4O_5/ Pd_3Ce_{33}O_{69}$ cluster model. A cross-section view of each model is shown in the right, with the first the CeO_2 layer omitted for clarity. Hydrogen abstraction sites during methane activation are indicated by magenta arrows.

As shown previously,[3, 14] the relative stability of surface models with varying amounts of oxygen is determined by comparing free energies of formation calculated with the formula:

$$G_{form} = E_{[Pd_4O_x/Pd_3Ce_{33}O_{69}]} + \left(E_{[Pd_3Ce_{33}O_{69}]} + 4E_{[PdO]} + \frac{4-x}{2}\mu_{O_2}(T,P)\right) \quad (1)$$

where $E_{[Pd_4O_x/Pd_3Ce_{33}O_{69}]}$ is the total energy of the surface with an adsorbed Pd_4O_x cluster, $E_{[Pd_3Ce_{33}O_{69}]}$ is the energy of the clean $Pd_3Ce_{33}O_{69}$ surface (with three incorporated Pd atoms and three oxygen vacancies relative to stoichiometric CeO_2), $E_{[PdO]}$ is the energy of bulk PdO, and $\mu_{O_2}(T,P)$ is the chemical potential of gas phase O_2. The oxygen chemical potential is calculated as a function of temperature and pressure using standard statistical mechanical formulas. Hence, to determine the thermodynamically stable O:Pd ratio in the embedded cluster, we compare the free energy of surfaces with varying amounts of oxygen, as shown in Figure 6. In Figure 7-6(a), the free energy of each cluster model is plotted against oxygen pressure at 500 K. At each pressure, the thermodynamically stable state is determined by identifying the surface with the lowest free energy. Phase boundaries are located at intersection points where two surface states have equal free energies, indicated by dotted lines in the figure.

The resulting *ab initio* phase diagram, shown in Figure 7-6(b), demonstrates that partially embedded Pd_4O_x clusters with $x > 4$ are stable under catalytic combustion conditions (*i.e.* clusters with Pd^{4+} states). Indeed at 500 K, Pd_4O_x clusters with $x > 4$ are thermodynamically stable at all oxygen pressures above 10^{-15} atm. For comparison, using the same calculation method we find that bulk PdO_2 (Pd^{4+}) is not more stable than bulk PdO (Pd^{2+}) below oxygen pressures of ~10^{10} atm at 500 K. This demonstrates that ceria

enhances oxide formation in embedded palladium clusters, in agreement with Farrauto *et al.*[17] and Nilsson *et al.*[18], which likely affects the Pd oxidation state under operating conditions.

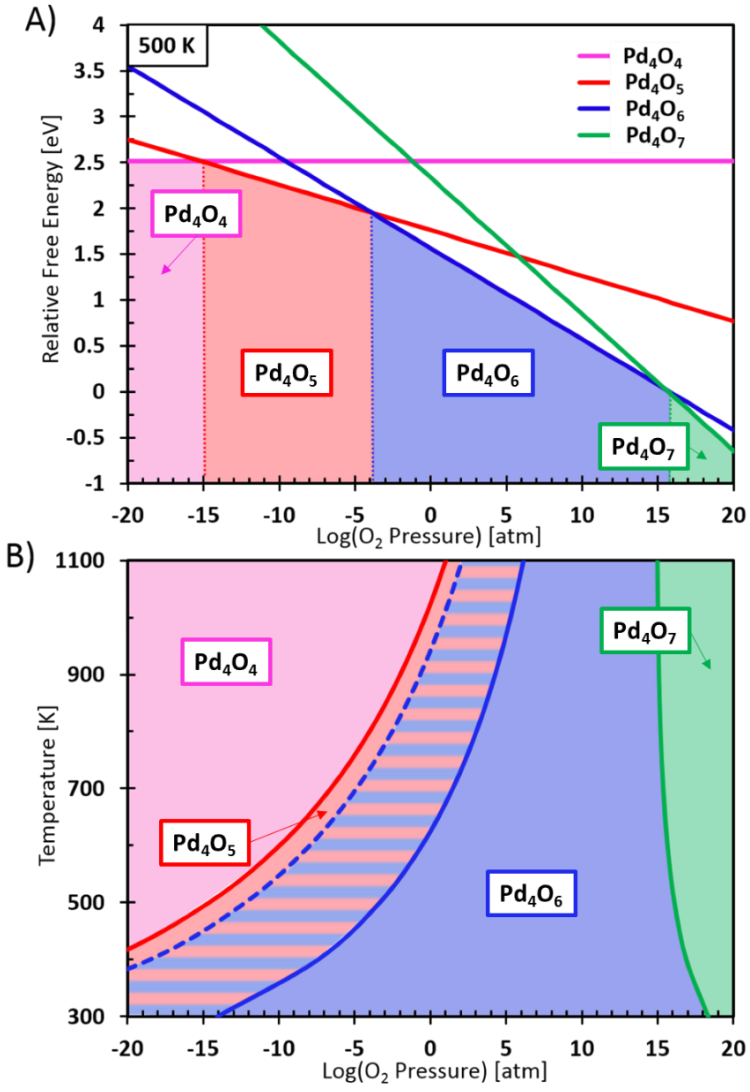

Figure 7-6. (a) Relative free energy of $Pd_4O_x/Pd_3Ce_{33}O_{69}(111)$ surfaces with varying Pd oxidation states at 500 K. The vertical dashed lines indicate the pressure regions in which each surface oxidation state is stable. (b) Phase diagram describing Pd oxidation states in the $Pd_4O_x/Pd_3Ce_{33}O_\delta(111)$ models. The solid shaded regions separated by solid colored lines indicate thermodynamically stable regions in (*T*,*P*) space. The striped region and dashed line indicate the region where the supported Pd_4O_5 cluster is thermodynamically stable, yet methane activation is kinetically preferred over the Pd_4O_6 cluster.

To assess the activity of sites at the $Pd_4O_x/Pd_3Ce_{33}O_{69}$ interface, we use a previously validated[2, 3, 35] pseudo-barrier approach to calculate the free energy of activation *via* hydrogen abstraction from gas-phase CH_4. In this approximation, the transition state is represented by an adsorbed hydrogen atom and a $\cdot CH_3$ radical separated from the surface:

$$\Delta G_{act} = E_{[surf-H]} + \mu_{\cdot CH_3} - \left(E_{[surf-clean]} + \mu_{CH_4}\right) \quad (2)$$

where $\mu_{\cdot CH_3}$ and μ_{CH_4} are calculated using standard statistical mechanical expressions, with translational and rotational contributions for $\cdot CH_3$ set to zero (*i.e.* the $\cdot CH_3$ radical has no translational or rotational degrees of freedom in the activated complex). The favored hydrogen adsorption site over the Pd_4O_5 and Pd_4O_6 surface models, indicated in Figure 5 by magenta arrows, occur over oxygen atoms in Ce-O-Pd units at the cluster/support interface. Additionally, the stability of each cluster model affects the apparent methane activation barrier, and is accounted for in the total apparent barrier expression by including in the barrier expression the state's formation energy relative to the most stable state:

$$\Delta G_{app} = \Delta G_{act} + \Delta G_{form} \quad (12)$$

Applied to the $Pd_4O_x/Pd_3Ce_{33}O_{69}(111)$ surface models at 500 K and $P(O_2)$ = 0.01 atm, we find that the Pd_4O_6 surface is less stable than the Pd_4O_5 surface. As such, the total barrier over the Pd_4O_6 surface at these conditions consists of the pseudo-barrier, ΔG_{act}, summed with the free energy difference between the Pd_4O_6 and Pd_4O_5 models, ΔG_{form}. This results in an apparent barrier over the Pd_4O_6 surface that is lower than the corresponding barrier over Pd_4O_5 surface, despite the additional free energy 'penalty' required to form the Pd_4O_6 state from the more stable Pd_4O_5 state. This defines a kinetic region in the *ab initio* phase diagram, where the Pd_4O_5 state is thermodynamically stable

yet the total apparent barrier is lowest over the Pd_4O_6 state, indicated in Figure 7-6(b) by the striped region separating the Pd_4O_5 and Pd_4O_6 states. The region begins at the stability boundary separating the states and extends to the boundary where the states yield an equal apparent barrier. The kinetic region in the figure demonstrates a trade-off between stability and activity, where a meta-stable Pd^{4+} state offers a lower activation path compared to direct activation on the more stable Pd^{2+} state. This analysis is extended to calculate apparent barriers for all $PdO_x/Pd_3Ce_{33}O_{69}(111)$ models, as summarized in Table 7-1. These data show that the apparent barrier and relative rate over the Pd_4O_6 surface is commensurate with that of the previously investigated[3] $Pd_3Ce_{33}O_{69}(111)$ and PdO(101) surfaces.[36] This demonstrates that sites at the embedded PdO_x/ceria interface display activation chemistry similar to the highly reactive $Pd_xCe_{1-x}O_\delta$ surfaces identified previously.

Table 7-1. Methane activation barriers (eV) and relative rates calculated at 500 K, $P(O_2)$ = 0.01 atm and $P(CH_4)$ = 0.01 atm.

Surface Model	ΔG_{act} (0 K)	ΔG_{act} (550 K)[a]	ΔG_{form} (550 K)[a]	ΔG_{total} (550 K)[a]	Relative Rate
$CeO_2(111)$[2]	1.65	2.84	-	2.84	1
$Pd(111)$[2]	0.86	2.05	-	2.05	1.7×10^{7}
$PdO(100)$[37]	1.22	2.41	-	2.41	8.7×10^{3}
$PdO(101)$[37]	0.50	1.69	-	1.69	3.4×10^{10}
$Pd_3Ce_{33}O_{72}(111)$[3]	0.42	1.61	2.52	4.13	1.4×10^{-12}
$Pd_3Ce_{33}O_{71}(111)$[3]	0.38	1.57	0.99	2.57	3.1×10^{2}
$Pd_3Ce_{33}O_{70}(111)$[3]	0.29	1.48	0.31	1.79	4.3×10^{9}
$Pd_3Ce_{33}O_{69}(111)$[3]	0.68	1.87	-	1.87	7.7×10^{8}
$Pd_4O_4/Pd_3Ce_{33}O_{69}(111)$	1.04	2.23	0.55	2.78	3.6×10^{0}
$Pd_4O_5/Pd_3Ce_{33}O_{69}(111)$	1.08	2.27	-	2.27	1.6×10^{5}
$Pd_4O_6/Pd_3Ce_{33}O_{69}(111)$	0.64	1.83	0.01	1.84	1.3×10^{9}
$Pd_4O_7/Pd_3Ce_{33}O_{69}(111)$	0.75	1.94	0.98	2.92	1.8×10^{-1}

7.5. Conclusion

DFT, ReaxFF/GC-MC, and ReaxFF/RMD methods were used to assess thermodynamic and kinetic driving forces affecting phase formation and activity at the Pd/ceria interface. GC-MC simulations with the ReaxFF potential demonstrate that additional oxygen uptake is achieved in embedded clusters due to Pd incorporation at the ceria interface. GC-MC equilibrated PdO_x/ceria surface models were then used in RMD simulations to assess methane activation. Again, RMD simulations suggest that the Pd/Ce mixing at the interface increases catalytic activity, as methane light-off occurs more readily over the oxidized embedded cluster compared to the supported cluster. These results motivated more detailed DFT investigations over embedded-cluster models, which corroborate ReaxFF findings by demonstrating that Pd_4O_x clusters adsorbed on the $Pd_3Ce_{33}O_{69}(111)$ surface are stable with Pd^{4+} states (*i.e.* $x > 4$) under typical operating conditions. This suggests that active Pd^{4+} states are stabilized by cluster-support interactions between Pd and ceria. The activity of the Pd^{4+} state in the $Pd_4O_x/Pd_3Ce_{33}O_{69}(111)$ model is similar to that of the more ideal $Pd_3Ce_{33}O_{69}(111)$ single-crystal surface. This demonstrates that high activity can be achieved at the cluster/support interface, and is not limited to sites occurring over pristine $Pd_xCe_{1-x}O_\delta$ surfaces. Together, these results demonstrate the emergent behavior of the Pd/ceria system leading to enhanced catalytic performance, in which the ceria lattice stabilizes active Pd^{4+} sites at the metal-oxide interface.

7.6. Supplemental Information

Details regarding the DFT training set employed for the optimization of ReaxFF Ce/O/Pd interaction parameters are provided below. Emphasis was placed obtaining a ReaxFF potential that correctly describes oxygen uptake in Pd-incorporated ceria surfaces. As such, we populated the training-set with geometries from our previous DFT study investigating $Pd_xCe_{1-x}O_\delta$ surfaces. Including these geometries in the training set allows ReaxFF to reproduce proper $Pd^{\delta+}$ oxidation state transitions as a function of temperature and pressure. This is demonstrated in the phase diagram in Figure S7-1, which compares DFT and ReaxFF phase boundaries separating adsorbed Pd^0 metal, Pd^{2+} incorporated, and Pd^{4+} incorporated states on the ceria(111) surface:

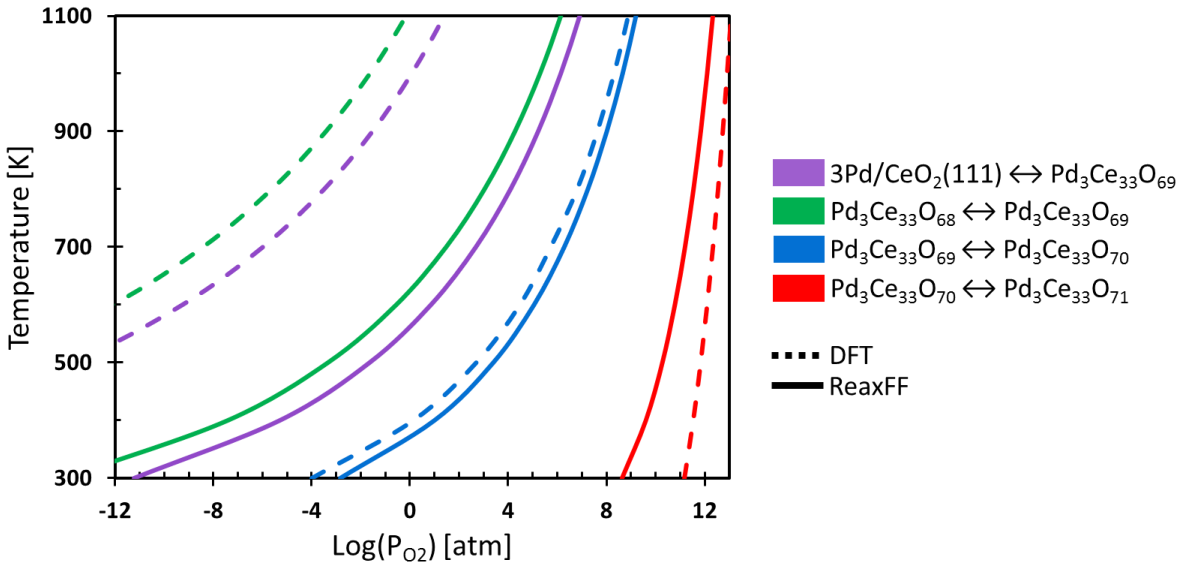

Figure S7-1. ReaxFF and DFT derived phase diagram describing Pd oxidation state transitions in $Pd_3Ce_{33}O_\delta(111)$ surface models. The solid data lines represent boundaries derived with ReaxFF, and dashed data lines indicate boundaries derived with DFT.

As seen in the figure, ReaxFF properly predicts the phase boundary separating the $Pd_3Ce_{33}O_{69}$ and $Pd_3Ce_{33}O_{70}$ surfaces. This boundary reflects the $Pd^{2+} \leftrightarrow Pd^{4+}$ transition responsible for the high activity of the $Pd_xCe_{1-x}O_\delta$ surface, and is therefore the most important boundary for ReaxFF to reproduce. ReaxFF adequately predicts that the $Pd_3Ce_{33}O_{71}$ surface, in which two Pd^{2+} states are present, will not become stable until oxygen pressures well above typical operating conditions are reached. Finally, ReaxFF yields a $Pd_3Ce_{33}O_{68} \leftrightarrow Pd_3Ce_{33}O_{69}$ boundary lying above the $3Pd/CeO_2(111) \leftrightarrow Pd_3Ce_{33}O_{69}$ boundary, indicating that ReaxFF correctly predicts that Pd will egress from the surface to form Pd^0 metal clusters under reducing conditions (*i.e.* the Pd^0 adsorbed state always has a lower free energy than the Pd^0 incorporated state). ReaxFF, however, significantly under predicts the temperature at which the $3Pd/CeO_2(111) \leftrightarrow Pd_3Ce_{33}O_{69}$ transformation occurs, indicating that ReaxFF will more readily form reduced Pd^0 states compared to DFT. Nevertheless, ReaxFF reproduces the qualitative trends governing $Pd^{\delta+}$ oxidation state transitions, especially regarding the $Pd^{2+} \leftrightarrow Pd^{4+}$ transitions that are the focus of this study.

Various other formation energies and adsorption energies regarding $Pd/CeO_2(111)$ surfaces were included in the training set. Formation and adsorption energies were calculated with the following formulas:

$$E_{Surf}^{Pd-Inc} = E_{[N_{Pd}-surf]} + N_{Pd}E_{[CeO_2]} + N_{[O-vac]}\frac{1}{2}E_{O_2} - \left(E_{[CeO_2-surf]} + N_{Pd}E_{[PdO_2]}\right) \quad (1)$$

$$E_{Surf}^{Pd-Ads} = E_{[N_{Pd}-surf]} + N_{Pd}E_{O_2} - \left(E_{[CeO_2-surf]} + N_{Pd}E_{[PdO_2]}\right) \quad (2)$$

where N_{Pd} is the number of Pd atoms in the unit cell, $N_{[O-vac]}$is the number of surface oxygen vacancies relative to the stoichiometric CeO_2 surface, $E_{[N_{Pd}-surf]}$ is the DFT

energy of the Pd-incorporated or Pd-adsorbed surface, $E_{[CeO_2]}$ and $E_{[PdO_2]}$ are the energies of the CeO_2 and PdO_2 bulk references (calculated per stoichiometric formula unit), and $E_{[CeO_2-surf]}$ is the energy of the clean CeO_2 surface. The parameterization results are summarized below in Table S7-1.

Table S7-1. DFT and ReaxFF energies for Pd adsorption and incorporation in ceria surfaces with varying amounts of oxygen. (All energies are in kcal mol^{-1})

Pd Incorporation	**ReaxFF**	**DFT**
$Pd_1Ce_{35}O_{72}$(111)	41.98	35.69
$Pd_1Ce_{35}O_{71}$(111)	47.47	39.51
$Pd_2Ce_{34}O_{72}$(111)	31.25	35.33
$Pd_2Ce_{34}O_{71}$(111)	31.67	32.49
$Pd_2Ce_{34}O_{70}$(111)	35.17	28.48
$Pd_3Ce_{33}O_{72}$(111)	30.18	34.33
$Pd_3Ce_{33}O_{71}$(111)	30.53	27.96
$Pd_3Ce_{33}O_{70}$(111)	30.53	28.07
$Pd_3Ce_{33}O_{69}$(111)	33.62	31.07
Pd Adsorption		
1Pd/CeO_2(111)	55.21	67.15
1Pd/CeO_2(111)-Ovac	142.91	137.74
2Pd/CeO_2(111)	54.37	63.16
2Pd/CeO_2(111)-Ovac	95.07	92.61
2Pd/CeO_2(110)	50.22	58.49
2Pd/CeO_2(110-Ovac	79.58	77.53
PdO_x Adsorption		
PdO/CeO_2(111)	59.82	58.23
PdO_2/CeO_2(111)	63.77	46.01
Oxygen Ads(des)orption		
CeO_2 + ½O_2 → O/CeO_2	22.31	9.64
CeO_2 → CeO_2(111)-Ovac + ½O_2	47.32	56.61
$Pd_1Ce_{35}O_{72}$(111) → $Pd_1Ce_{35}O_{71}$(111) + ½O_2	-5.49	-4.82
$Pd_3Ce_{33}O_{70}$(111) → $Pd_3Ce_{33}O_{69}$(111) + ½O_2	-9.27	-9.98

7.7. References

1. E. W. McFarland and H. Metiu, Chem. Rev. **113** (6), 4391-4427 (2013).
2. A. D. Mayernick and M. J. Janik, J. Catal. **278** (1), 16-25 (2011).
3. T. P. Senftle, A. C. T. van Duin and M. J. Janik, ACS Catalysis (2015).
4. P. Hohenberg and W. Kohn, Physical Review **136** (3B), B864-B871 (1964).
5. W. Kohn and L. J. Sham, Physical Review **140** (4A), A1133-A1138 (1965).
6. K. Reuter and M. Scheffler, Phys. Rev. B **65** (3), 035406 (2001).
7. A. C. T. van Duin, S. Dasgupta, F. Lorant and W. A. Goddard III, J. Phys. Chem. A **105** (41), 9396-9409 (2001).
8. S. Colussi, A. Gayen, M. F. Camellone, M. Boaro, J. Llorca, S. Fabris and A. Trovarelli, Angew. Chem. Int. Ed. **48** (45), 8481-8484 (2009).
9. S. Colussi, A. Gayen, J. Llorca, C. de Leitenburg, G. Dolcetti and A. Trovarelli, Ind. Eng. Chem. Res. **51** (22), 7510-7517 (2012).
10. S. Colussi, A. Trovarelli, C. Cristiani, L. Lietti and G. Groppi, Catal. Today **180** (1), 124-130 (2012).
11. M. Cargnello, J. J. D. Jaén, J. C. H. Garrido, K. Bakhmutsky, T. Montini, J. J. C. Gámez, R. J. Gorte and P. Fornasiero, Science **337** (6095), 713-717 (2012).
12. M. Cargnello, V. V. T. Doan-Nguyen, T. R. Gordon, R. E. Diaz, E. A. Stach, R. J. Gorte, P. Fornasiero and C. B. Murray, Science **341** (6147), 771-773 (2013).
13. A. D. Mayernick and M. J. Janik, J. Phys. Chem. C **112** (38), 14955-14964 (2008).
14. A. D. Mayernick and M. J. Janik, J. Chem. Phys. **131** (8), 084701-084712 (2009).
15. R. V. Gulyaev, T. Y. Kardash, S. E. Malykhin, O. A. Stonkus, A. S. Ivanova and A. I. Boronin, Phys. Chem. Chem. Phys. **16** (26), 13523-13539 (2014).
16. Y. Zhu, S. Zhang, J.-j. Shan, L. Nguyen, S. Zhan, X. Gu and F. Tao, ACS Catalysis **3** (11), 2627-2639 (2013).
17. R. J. Farrauto, J. K. Lampert, M. C. Hobson and E. M. Waterman, Applied Catalysis B: Environmental **6** (3), 263-270 (1995).
18. J. Nilsson, P.-A. Carlsson, S. Fouladvand, N. M. Martin, J. Gustafson, M. A. Newton, E. Lundgren, H. Grönbeck and M. Skoglundh, ACS Catalysis **5** (4), 2481-2489 (2015).
19. K. Chenoweth, A. C. T. v. Duin, P. Persson, M.-J. Cheng, J. Oxgaard and I. I. I. W. A. Goddard, J. Phys. Chem. C **112** (37), 14645-14654 (2008).
20. K. Chenoweth, A. C. T. van Duin and W. A. Goddard III, Angewandte Chemie International **48** (41), 7630-7634 (2009).
21. J. E. Mueller, A. C. T. van Duin and W. A. Goddard, J. Phys. Chem. C **114** (12), 5675-5685 (2010).
22. E. C. Neyts, K. Ostrikov, Z. J. Han, S. Kumar, A. C. T. van Duin and A. Bogaerts, Phys. Rev. Lett. **110** (6), 065501 (2013).
23. T. P. Senftle, R. J. Meyer, M. J. Janik and A. C. T. van Duin, J. Chem. Phys. **139** (4), 044109-044115 (2013).
24. P. Broqvist, J. P. Kullgren, M. J. Wolf, A. C. T. van Duin and K. Hermansson, J. Phys. Chem. C (2015).

25. K. Chenoweth, A. C. T. van Duin and W. A. Goddard, J. Phys. Chem. A **112** (5), 1040-1053 (2008).
26. T. P. Senftle, M. J. Janik and A. C. T. van Duin, J. Phys. Chem. C **118** (9), 4967-4981 (2014).
27. T. P. Senftle, A. C. T. van Duin and M. J. Janik, Catal. Commun. **52** (0), 72-77 (2014).
28. N. Metropolis, A. W. Rosenbluth, M. N. Rosenbluth, A. H. Teller and E. Teller, J. Chem. Phys. **21** (6), 1087-1092 (1953).
29. L. Verlet, Physical Review **159** (1), 98-103 (1967).
30. H. J. C. Berendsen, J. P. M. Postma, W. F. v. Gunsteren, A. DiNola and J. R. Haak, J. Chem. Phys. **81** (8), 3684-3690 (1984).
31. J. P. Perdew, J. A. Chevary, S. H. Vosko, K. A. Jackson, M. R. Pederson, D. J. Singh and C. Fiolhais, Phys. Rev. B **46** (11), 6671-6687 (1992).
32. J. L. F. Da Silva, M. V. Ganduglia-Pirovano, J. Sauer, V. Bayer and G. Kresse, Phys. Rev. B **75** (4), 045121-045110 (2007).
33. G. Kresse and D. Joubert, Phys. Rev. B **59** (3), 1758-1775 (1999).
34. H. J. Monkhorst and J. D. Pack, Phys. Rev. B **13** (12), 5188 LP - 5192 (1976).
35. M. D. Krcha, A. D. Mayernick and M. J. Janik, J. Catal. **293** (0), 103-115 (2012).
36. J. F. Weaver, C. Hakanoglu, A. Antony and A. Asthagiri, Chem. Soc. Rev. **43** (22), 7536-7547 (2014).
37. A. Hellman, A. Resta, N. M. Martin, J. Gustafson, A. Trinchero, P. A. Carlsson, O. Balmes, R. Felici, R. van Rijn, J. W. M. Frenken, J. N. Andersen, E. Lundgren and H. Grönbeck, J. Phys. Chem. Lett. **3** (6), 678-682 (2012).

Chapter 8
Summary, Conclusions, and Recommendations for Future Investigations

The objectives of this dissertation included the development, validation, and application of ReaxFF simulation techniques to investigate, in tandem with DFT, phase formation affecting the performance of Pd/ceria catalysts. Section 8.1 summarizes the completion of Objectives 1-4 outlined in Chapter 1, consisting of ReaxFF method development and initial implementation. Section 8.2 summarizes the application of these techniques to model the stability and activity of unique phases created at the cluster/support interface of Pd/CeO_2 catalysts (Objective 5). Answers to research questions and evaluations of hypotheses are provided in Section 8.3, and recommendations for future investigations are provided in Section 8.4.

8.1. Summary of ReaxFF method development and application to Pd/O/C/H

The initial development of ReaxFF interaction parameters for Pd/O/C/H systems was completed in Chapters 2-3. Additionally the grand canonical Monte Carlo method was developed for ReaxFF, enabling simulations to assess phase transitions occurring on the catalyst surface induced by varying operating conditions. In Chapter 2, the ReaxFF interaction potential was parameterized to describe metallic Pd and PdO_δ oxides. This chapter also presented the development of the ReaxFF-based grand canonical Monte Carlo/molecular dynamics (GC-MC/MD) approach, which was utilized to derive a theoretical phase diagram describing the oxidation of ~3 nm Pd clusters at temperatures ranging from 300 K to 1300 K, and at oxygen pressures ranging from 10^{-14} atm to 1 atm.

Separate MD simulations were conducted to investigate the initial stages of oxide formation on Pd surfaces, in which gas phase O_2 molecules dissociate on the surface and diffuse into the bulk. These results demonstrated that oxide formation in Pd bulk is kinetically limited by slow oxygen diffusion through the initial surface oxide. This is in agreement with experimental oxidation behavior, demonstrating the capability of the ReaxFF-based GC-MC and MD methods for assessing both kinetic and thermodynamic influences affecting phase formation.

The methodology developed in Chapter 2 is extended to Pd/H in Chapter 3, and to Pd/C/H in Chapter 4. Pd/H interaction parameters were derived in Chapter 3, and were employed in ReaxFF simulations assessing the Pd cluster size-dependence of hydride formation. GC-MC established that bulk phase transitions occur in Pd clusters as small as ~1 nm in diameter, and that the surface of Pd clusters becomes saturated with adsorbed hydrogen at low pressures (~10^{-13} atm). Hence, hydrogen uptake and release near ambient conditions reflects the alternation between high and low concentration phases in the cluster bulk, as the surface region remains passivated with hydrogen. Competition between hydride and carbide formation was assessed in Chapter 4, as this competition may occur under catalytic conditions upon exposure to a gas phase populated with hydrocarbon reactants. GC-MC indicates that low H_2 pressures are required to form a subsurface carbide phase, which is preferable because the carbide phase yields selective hydrogenation. Conversely, high hydrogen pressure results in the formation of a subsurface hydride phase leading to rapid, but unselective, hydrogenation. Overall, Chapters 2-4 illustrated the capability of ReaxFF for modeling phase formation in unsupported Pd clusters, demonstrating the completion of Objectives 1-3.

Chapter 5 reported the application of ReaxFF to investigate Pd interaction with a TiO_2 support, which was conducted in collaboration with the experimental lab of Prof. M. Batzill. STM experiments, DFT calculations, kinetic Monte Carlo (kMC) simulations, and ReaxFF GC-MC simulations were used to investigate Pd sintering and hydride formation on clean and hydroxylated TiO_2 surfaces. Experimental work, conducted by our collaborators, suggested that small (< 1 nm) Pd clusters are stable at room temperature on hydroxylated surfaces, whereas larger Pd clusters are formed under the same conditions on hydroxyl-free surfaces. Accounting for this behavior, DFT calculations demonstrated stronger Pd binding adjacent to surface hydroxyl groups. This results in high Pd diffusion barriers, preventing sintering on the hyroxylated surface. The DFT barriers were used in kinetic Monte Carlo simulations of the sintering process, yielding a cluster size distribution in agreement with STM. Also, GC-MC with the ReaxFF potential indicated that large Pd clusters can form PdH_x phases by absorbing hydrogen from surface hydroxyl groups. This agrees with STM evidence showing the disappearance of hydroxyl groups after a critical Pd concentration is reached on the surface. This chapter represents the completion of Objective 4, as the developed ReaxFF methods were used in conjunction with DFT to treat supported Pd systems.

8.2. Summary of Hydrocarbon Activation on Pd/ceria

The methods developed in Chapters 2-4 were applied in a multi-scale investigation of hydrocarbon activation over Pd/ceria catalysts in Chapters 6 and 7, representing the completion of dissertation Objective 5. In Chapter 6, DFT-based *ab initio* thermodynamics

established the role of site stability during methane activation on $Pd_xCe_{1-x}O_\delta$ surfaces. Rapid C-H activation is attributed to the emergent behavior of the doped oxide, enabling $Pd^{4+} \leftrightarrow Pd^{2+}$ transitions that cannot occur over unsupported PdO_x phases. We found that hydrogen abstraction over Pd^{4+} surface states, as opposed to σ-complex activation over PdO_x surfaces, is the favored activation mechanism under low temperature oxidation conditions (~400 K, 10^{-2} atm P_{O2}). This determination was accomplished by combining kinetic and thermodynamic stability arguments to derive the apparent methane activation barrier. The derived barrier expression accounts for oxygen pressure and temperature variations, ultimately demonstrating that active Pd^{4+} sites are metastable during catalytic turnover. The otherwise unstable Pd^{4+} state is stabilized by incorporation in the fluorite CeO_2 lattice, providing unique methane activation chemistry from the $Pd_xCe_{x-1}O_\delta$ mixture.

The conclusions of Chapter 6 motivate the multi-scale investigation presented in Chapter 7, which assesses Pd-ceria interactions in larger systems. DFT, ReaxFF/GC-MC, and ReaxFF/RMD methods were used to investigate both thermodynamic and kinetic driving forces affecting phase stability and activity at the interface. GC-MC simulations demonstrated that oxygen uptake is increased if Pd incorporation at the ceria interface is maximized. Cluster models derived from GC-MC simulations were then employed in RMD simulations to assess methane activation. These results demonstrated that additional oxygen present at the Pd/ceria interface leads to increased catalytic activity, as methane light-off occurs more readily over an embedded cluster compared to a supported cluster. DFT investigations over embedded-cluster models corroborate these findings, demonstrating that embedded Pd_4O_x clusters on a $Pd_3Ce_{33}O_{69}$(111) surface are stable with Pd^{4+} states (*i.e.* $x > 4$) under typical operating conditions. This is attributed to the formation

of square-planar oxygen coordination sites in the fluorite lattice of ceria that are accessible to Pd atoms at the cluster edge (*i.e.* Pd^{4+} states form at the cluster/support interface). The resulting combustion rates, calculated with the DFT expression derived in Chapter 6, over $Pd_4O_x/Pd_3Ce_{33}O_{69}(111)$ models are similar to those calculated for the $Pd_3Ce_{33}O_{70}(111)$ single-crystal surface. This demonstrates that the synergy between Pd and ceria is not limited to the idealized single-crystal $Pd_xCe_{1-x}O_\delta$ surface models investigated previously.

The multi-scale investigation reported in Chapters 6 and 7 demonstrates the emergent behavior of the Pd/ceria system, thus offering atomistic scale insight into the high activity of Pd/CeO_2 catalysts during low temperature methane oxidation. Chapter 6 demonstrates that Pd incorporation in ceria yields meta-stable Pd^{4+} states. Incorporation in ceria facilitates $Pd^{4+} \leftrightarrow Pd^{2+}$ transitions, leading to rapid methane activation as the fluorite lattice allows Pd atoms to shift between octahedral and square-planar oxygen coordination environments during catalytic turnover. Chapter 7 demonstrates that this behavior is not limited to Pd-doped single-crystal ceria surfaces, and may also occur at the metal/oxide-support interface of larger Pd clusters. In both instances, Pd^{4+} states serve as a reduction center allowing rapid methane activation and oxygen vacancy formation. This behavior is unique to Pd and CeO_2, and exemplifies a chemical interaction between a metal dopant and host oxide that may be exploited to optimize catalyst design.

8.3. Conclusions and Evaluation of Hypotheses:

1) Under what operating conditions (*i.e.* temperature and oxygen partial pressure) does the surface morphology transition from a supported Pd cluster to a mixed Pd/Ce surface oxide? Does this transition occur during the catalytic cycle? *Hypothesis: Under reaction conditions (T ~ 400 K, P_{O2} ~ 10^{-2} atm), dynamic Pd oxidation state transitions allow for facile oxygen exchange upon hydrocarbon activation. The feasibility of these transitions is controlled by operating conditions.*

Conclusion: In Chapter 6, we derived an expression for apparent methane activation that combines formation energies (assessing stability) with activation energies (assessing activity). This provides a clear measure for determining the regions in *(T,P)* space where each Pd/Ce mixed oxide phase is stable and/or active. Under reaction conditions, (T ~ 400 K, P_{O2} ~ 10^{-2} atm), Pd^{4+} incorporated states are not stable relative to Pd^{2+} states (however, both incorporated states are stable relative to supported Pd^{0} at these conditions). Yet, the activation barrier over the Pd^{4+} state is significantly lower than that of the Pd^{2+} state, leading to a well-defined region of the phase diagram where activation occurs over meta-stable Pd^{4+} surface states. $Pd^{4+} \leftrightarrow Pd^{2+}$ alternations occur during the catalytic cycle, where methane activation *via* $Pd^{4+} \rightarrow Pd^{2+}$ reduction occurs more readily under oxidizing conditions, as there is a lower formation energy contribution in the apparent barrier expression for activation over the Pd^{4+} state. Likewise, GC-MC simulations show that additional oxygen uptake is achieved in Pd clusters embedded in the ceria lattice at oxygen pressures ranging from 10^{-15} atm to 1 atm at 500 K. Subsequent DFT

calculations show that Pd^{4+} states in embedded PdO_x clusters are stable relative to Pd^{2+} states at T ~ 500 K, $P_{O2} \sim 10^{-2}$ atm. This supports the hypothesis that Pd^{4+} states are present on the catalyst surface under reaction conditions, and offer unique catalytic activity arising from the Pd/Ceria interaction.

2) What are the kinetic and thermodynamic driving forces that lead to Pd incorporation at the cluster-support interface? How does this affect catalysis? *Hypothesis: Restructuring of the metal-support interface occurs during the catalytic cycle, and is induced by highly oxidizing conditions. This forms unique mixed-metal oxide phases affecting the performance of Pd/CeO_2 catalysts.*

Conclusion: The $Pd_xCe_{1-x}O_\delta$ mixed-oxide phase features stable Pd^{2+} states under ambient conditions, where incorporation in the stoichiometric CeO_2 surface is accompanied by an oxygen vacancy (demonstrated in Chapter 6). Although this state is thermodynamically favored, kinetic limitations may prevent the formation of the mixed oxide phase when starting from a supported Pd^0 cluster. This is plainly evident, as Pd/ceria catalysts synthesized with traditional methods (such as IWI) contain supported Pd clusters, while those synthesized with SCS contain Pd-incorporated surface states. ReaxFF simulations demonstrate that interaction with a defective ceria surface facilitates Pd-incorporation (shown in Chapter 7 by GC-MC over embedded-cluster models). This interaction leads to increased oxygen uptake, which in turn creates more effective sites for catalytic oxidation. DFT and ReaxFF results demonstrate that, once Pd-incorporation is achieved, increased activity is attributed to the formation of meta-stable Pd^{4+} states at the Pd/ceria interface.

3) How does phase formation in Pd/ceria catalysts under reaction conditions affect overall stability and activity? *Hypothesis: The incorporation of Pd atoms in the ceria lattice yields meta-stable Pd^{4+} states that, although thermodynamically less stable than Pd^{2+} states, are catalytically active. Pd^{4+}states exist on the surface under reaction conditions, and their meta-stable nature yields highly reactive sites for surface reduction processes (i.e. hydrocarbon activation).*

Conclusion: *Ab initio* thermodynamics suggests that Pd-Ce mixed oxide phases can be thermodynamically stable under reaction conditions. Apparent activation barriers, calculated with DFT, demonstrate that Pd^{4+} states occurring in such mixed oxides can offer faster relative combustions rates compared to other possible active sites. As calculated in Chapter 6, the apparent rate over the (111)-1Pd^{4+}/2Pd^{2+} site at T = 400 K and P_{O2} = 0.01 atm is ~10^{16} times faster than the rate over clean CeO_2(111), ~10^7 times faster than Pd(111), and ~10^2 times faster than PdO(101). In Chapter 7, GC-MC and RMD simulations with the ReaxFF potential demonstrate that mixed-oxide phases form at the cluster/support interface, provided that defects in the CeO_2(111) surface allow for Pd incorporation near the cluster edge. DFT calculations on embedded-cluster models, designed to maximize Pd-incorporation, demonstrate that palladium oxide clusters with PdO_2 stoichiometry are stable under ambient conditions, thus providing active Pd^{4+} sites with combustion rates similar to the single-crystal $Pd_3Ce_{33}O_\delta$ surfaces investigated in Chapter 6. Hence, interaction with ceria facilitates PdO_x formation, leading to active Pd^{4+} states at the cluster/support interface.

8.4. Recommendations for Future Investigations

ReaxFF GC-MC/MD Methodology and Applications. The multi-scale investigation completed in this dissertation required the development of a GC-MC/MD simulation method for ReaxFF. This simulation methodology proved to be a useful for predicting phase formation without *a priori* knowledge of the phase structure. In essence, the GC-MC/MD method searches for the most stable structure, often revealing unexpected behavior in the system. This is of particular use during force-field optimization, as the GC-MC method can identify spuriously stable phases that were not included in the DFT training set. For example, during the initial stages of Pd/H parameterization, no PdH_2 bulk phases were included in the DFT training set. Chemical intuition from experimental evidence dictates that PdH_x phases with $x > 1$ are not stable, and where therefore not included in the ReaxFF training process. ReaxFF, however, has no chemical intuition. Initial testing utilizing GC-MC to simulate hydrogen uptake revealed that Pd/H interaction parameters allowed the formation of a PdH_2 phase under ambient conditions, exposing a weakness in the parameter fitting. As such, the structures derived with GC-MC were used to expand the DFT training set, allowing the updated Pd/H parameters to properly treat bulk PdH_x phases. Thus, the GC-MC method can be an effective tool for diagnosing problems with ReaxFF parameter sets, as it can identify unexpected behavior leading to incorrect phase formation. Alternatively, it can identify unexpected phases that are indeed stable, providing a useful screening tool to identify structures for more detailed DFT investigation.

Currently, the algorithm for the GC-MC method is only capable of running on a

single CPU. This leads to difficulties reaching equilibrium near phase boundaries, as critical-slowdown effects become limiting. Near the phase boundary, acceptance rates for MC trial steps diminish because the free energy of each phase is similar. Modifying the GC-MC algorithm to enable parallel processing is the ideal solution to this problem, as many MC trial steps can be executed at the same time. With more processors searching for the next acceptable MC move, less wall-time will be required to reach equilibrium. Additionally, parallel processing will enable simulations on larger systems, since ReaxFF total-energy calculations and structure optimizations can be split over multiple-processors. Initial steps toward parallelization have been taken, as the ReaxFF/GC-MC method is now available in both the ADF and Lammps simulation packages.

To aid the search for catalytically activity sites, the GC-MC methodology can be paired with automated nudged elastic band (NEB) calculations. The GC-MC method yields an ensemble of surface structures under the specified reaction conditions. This can be instrumental when searching for active sites that rarely arise on the surface. This is exemplified in Appendix B, which contains an investigation of Pd/Ar interactions. The GC-MC method was used to generate an ensemble of Pd cluster geometries, which is representative of the cluster distribution after experimental synthesis. To identify Pd/Ar interaction sites, the geometries derived from GC-MC were periodically exposed to Ar gas through separate MD simulations. This revealed that under-coordinated Pd atoms at corner sites, which are not present in every cluster model, interact with Ar leading to surface reconstruction. Instead of MD simulations, it would also be possible to conduct NEB simulations in search of active sites. This is feasible because ReaxFF is computationally inexpensive, allowing for numerous NEB calculations to be conducted over short

timeframes. This can help identify highly active sites that are relatively rare, or that only occur under very narrow operating conditions. Overall, the GC-MC method can be used to derive models that better represent the surface structure, complete with intermediate species and transient surface phases, present *under reaction conditions*. These models can then be used in both DFT and MD simulations to understand reaction kinetics at the atomistic scale.

Catalysis by Doped-Oxides. The conclusions to the investigation of activity at the Pd/ceria interface demonstrate that high activity is achieved due to the synergy between Pd and Ce in the mixed-metal-oxide phase. Cerium oxide is thermodynamically stable with a 1:2 Ce to O ratio, while palladium oxide prefers a 1:1 stoichiometry. However, under reducing conditions a Ce_2O_3 phase of cerium oxide is stable, and under extremely oxidizing conditions a PdO_2 phase of palladium oxide can be obtained. One may increase the reducibility of CeO_2 by including Pd dopants, and *vice versa* as Pd is more readily oxidized when interacting with cerium. The high activity of Pd/ceria arises from over-oxidized Pd states, as well as under-oxidized Ce states, that are created under reaction conditions by the Pd-Ce mixture. A good catalyst requires a trade-off between stability and activity, which is achieved in Pd-Ce mixed oxides because Pd prefers a 2+ oxidation state, yet can form a 4+ state when incorporated in the fluorite lattice structure of CeO_2. Hence, the Pd-Ce mixture will readily cycle between 4+ and 2+ oxidation states, offering a catalytically active site for oxidation and reduction.

This synergy can be exploited in other systems by identifying dopant-oxide pairs that are likely to exhibit a similar ‘trade-off’ in oxidation state. For example, to achieve selective oxidation, one might choose a catalyst with a mixed $Pt_xCe_{1-x}O_\delta$ phase. Such a

catalyst is likely to have a high activation barrier, as it is difficult to stabilize a Pt^{4+} state. This may not be desirable for total oxidation applications, but may offer better selectivity because activation will occur only at the most unstable sites of the reactant molecule. A similar effect may also be achieved by selecting less reducible oxide supports, such as MgO or SiO_2, that will less readily cycle between oxidation states. Sites created by metal-oxide pairs can be screened using the *ab initio* thermodynamics methodology presented in Chapter 6, which enables both stability and activity to be assessed over a range of operating conditions.

Appendix A
Application of Computational Methods to Supported Metal-Oxide Catalysis

This chapter is published as: T. P. Senftle, A. C. T. van Duin and M. J. Janik, in *Computational Catalysis*, The Royal Society of Chemistry, pg. 157-191. (2014)

Abstract

Advances in computational chemistry over the last few decades have greatly impacted design strategies for obtaining active, selective, and stable catalysts. This chapter outlines computational approaches for modeling metal-oxide catalytic systems at the atomic level, and reviews pertinent studies that exemplify these methods. Examples are chosen to emphasize both quantum-based methods (utilizing density functional theory (DFT) and *ab initio* thermodynamics) and classical force-field methods (utilizing the ReaxFF empirical potential). We discuss studies that use DFT to evaluate the relative energies of metal-oxide surface structures, studies that extend the formalism of DFT to non-zero temperature and pressure via *ab initio* thermodynamics, and finally studies that use the ReaxFF empirical force-field in MD and MC simulations to investigate system dynamics and structure at large scales. Reviewing the application of these methods will provide the reader with a general understanding of how computational methods can be applied to atomistic studies of supported metal-oxide catalysts.

A.1. Introduction

This chapter will highlight examples from the literature that apply DFT, *ab initio* thermodynamics, and empirical force-field methods to assess catalytic behavior of supported metal-oxide catalysts. Examples of supported metal-oxide catalysis include: catalytic combustion,[1-12] hydrocarbon steam-reforming,[13-24] CO removal from *syngas* via the water-gas-shift (WGS) reaction,[25-34] CO and NO oxidation,[35-41] automotive three-way catalysis,[42-46] solid oxide fuel cell (SOFC) electrodes,[47-53] and selective hydrogenation.[54-59] The activity and selectivity of supported metal-oxide catalysts can be tuned for these applications by altering the metal-support surface morphology.[60-93] Section A.2.1 considers studies that apply DFT to the design of water-gas-shift catalysts, evaluating the relative energies of metal-oxide surface structures and map reaction mechanisms. Section A.2.2 discusses studies that extend the formalism of DFT to non-zero temperature and pressure via *ab initio* thermodynamics, thus assessing the impact of surface stability on catalytic behavior. Section A.3 focuses on studies that use ReaxFF empirical force-fields in MD and MC simulations to investigate system dynamics at larger time and length scales.

Advances in computational chemistry over the last few decades have greatly impacted design strategies for obtaining active, selective, and stable catalysts.[94] In particular, density functional theory[95-98] (DFT) has shown tremendous success for modeling catalytic systems, thus enabling *a priori* approaches to designing metal-oxide catalysts. DFT is capable of determining the electronic ground state energy of a system as a function of atomic positions. Thus, one can determine the optimized structure of the catalyst surface during every step of a reaction - allowing one to determine stable

intermediates and activation barriers on the potential energy surface (PES) of a reaction coordinate. The computational expense of DFT, however, limits system sizes to around ~100 atoms. For this reason, it is often limited to periodic models of single crystal surfaces, which are used to represent the varying surface facets of large particles. Furthermore, characterizing the interactions between a metal cluster and an oxide support requires highly idealized models, featuring perfectly dispersed metal atoms and clusters that can only approximate the behavior of actual catalytic systems. Despite this limitation, DFT has proved instrumental for mapping reaction mechanisms and evaluating particle-support interactions at the electronic level.

The following sections highlight studies employing the computational methods discussed in the previous section to characterize supported metal-oxide systems. It is not intended to be an exhaustive review of the subject, but rather serves to illustrate the strengths and limitations of these methods when applied to supported heterogeneous catalysis. The studies discussed in this chapter are chosen to illustrate the capabilities and limitations of computational methods applied to supported metal-oxide catalysis. This chapter is not intended as a comprehensive review of the subject, and as such, numerous notable studies are not discussed in detail. Nevertheless, a brief summary is provided of especially notable studies before moving to more detailed discussions.

CO oxidation is an important industrial process, and has been the subject of many computational studies. Notable contributions have been made by Landman and co-workers, who applied DFT in conjunction with isotopic labeling experiments to determine the oxidation state of Pd clusters supported on MgO during CO oxidation.[104] This allowed them to determine that partially oxidized Pd clusters are active toward CO oxidation, along

with the temperature range in which the clusters will remain oxidized. In another study, these authors used QM calculations in tandem with infrared spectroscopy to demonstrate that charging effects lead to enhanced CO oxidation activity over Au/MgO catalysts. They show that this charging effect is prominent when Au clusters are adsorbed on oxygen-vacancy defects and is absent in clusters adsorbed on the pristine oxide.[105] Hammer, Molina, and co-workers demonstrate that oxide supports can play an active role in reaction mechanisms in their DFT work analyzing CO oxidation over Au/MgO.[106] They demonstrate the importance of interfacial sites and charge transfer between the oxide support and the metal cluster, which leads to enhanced CO oxidation activity over Au/TiO_2.[107] The interaction between supported metal clusters and adsorbed hydrogen plays a prominent role in many catalytic processes, such as selective hydrogenation, dehydrogenation, and water-gas-shift. Vayssilov, Rösch, and co-workers use DFT to explore hydrogen saturation on supported Ir, Rh, and Pt clusters.[108, 109] They found that the extent of hydrogen uptake is dependent on metal type, and is enhanced in metals that are easily oxidized by the support. Sautet and co-workers conducted multiple studies that investigate structural changes to Pt and Pd clusters adsorbed on γ-alumina caused by hydroxyl groups and H_2.[110, 111] Using *ab initio* thermodynamics, they found that in a hydrogen-free atmosphere Pt clusters prefer to adsorb on the oxide in a planar configuration. They subsequently show that the Pt cluster undergoes reconstruction to a cuboctahedral structure after exposure to hydrogen, induced by the formation of a metal-hydride. This restructuring occurs above a critical hydrogen pressure, and greatly affects the catalytic properties of the system. These studies underscore the need to consider interactions between metal clusters and oxide surfaces when assessing catalytic behavior.

This type of analysis is exemplified in the work of Ferrando, Fortunelli, Barcaro, and co-workers who use QM-global optimization methods to model the metal adsorption on oxides.[112-114]

Reaction conditions, dictated by the temperature and partial pressure of gaseous species, affect the stability and reactivity of the catalyst surface. Understanding this effect is necessary to identify surface phases that are stable and active under *reaction conditions*. As a quantum theory, DFT does not inherently account for the effects of temperature and pressure. DFT can be extended to treat systems at realistic temperatures and pressures through the formalism of *ab initio* thermodynamics.[79, 82, 98-102] *Ab initio* thermodynamics uses statistical mechanics to incorporate the effect of entropy in systems where solid catalyst surfaces are in equilibrium with a molecular gas phase. This method can calculate the *free energy* of a system, therefore allowing one to determine the relative *stability* of possible surface terminations and structures. With this information, one can construct phase diagrams predicting morphologies that will dominate the catalyst surface as a function of temperature and pressure.

Sufficient models of metal-support structures and dynamics are often beyond the length and time scales that are computationally tractable with DFT. This has provided the impetus to employ classical force-fields, such as the ReaxFF[103], that are empirically derived from quantum and experimental data. The classical basis for empirical potentials allows for the computational treatment of systems reaching the order of ~10^4 atoms for nanosecond timescales, which is sufficient to capture system *dynamics* through molecular dynamic (MD) and Monte Carlo (MC) simulations. The application of reactive force-field methods to heterogeneous catalysis is an emerging research area. Herein we highlight the

applications of ReaxFF to heterogeneous catalysis over metal and oxide surfaces. The success of these studies has led to on-going attempts to apply this method to supported metal-oxide systems.

A.2. Application of DFT to the WGS Reaction

DFT is a powerful method for determining reaction mechanisms over metal-oxide systems. We have chosen to review studies that focus on developing catalysts for the water-gas-shift reaction since this is a particularly active research area with numerous examples of DFT application to supported metal-oxide catalysis. The studies first considered herein assess the activity of unsupported gold and copper metal clusters, which can then be directly compared to studies over the analogous oxide-supported systems. The importance of considering particle-support interactions is emphasized, as the oxide support can often play an active role in catalytic mechanisms.

There is a growing interest in the production of pure H_2 for use in proton exchange membrane (PEM) fuel cell applications.[34] Typical H_2 production methods implement steam-reforming techniques that convert hydrocarbon feedstocks to a synthesis gas mixture of CO, H_2O, CO_2 and H_2. However, CO is detrimental to the efficiency of PEM fuel cells because it poisons the anode catalyst. For this reason, it is essential to remove CO in a downstream process between the steam-reforming and PEM stages. The water-gas-shift (WGS) reaction removes CO and recovers its energy content in a single process by converting CO and H_2O to CO_2 and usable H_2:

$$CO_{(g)} + H_2O_{(g)} \rightarrow CO_{2(g)} + H_{2(g)} \quad (1)$$

Recent DFT studies have characterized the nature of active sites on metal-oxide catalysts for WGS, which emphasize the unique aspects of particle-support interactions in Cu/ceria,[115] Au/ceria systems,[116] and Pt/ceria[117]. The primary intent of this section is to exhibit the utility and limitations of DFT for investigating the many aspects of metal-oxide catalysis, rather than to serve as an exhaustive review of computational work on WGS catalysis in the literature. For a more detailed discussion of the subject, we refer the reader to the recent review of computational work on Au/ceria can be found in a recent perspective article by Zhang, Michaelides, and Jenkins.[118]

A.2.1. Activity of Au and Cu Nanoparticles.

P. Liu, J.A. Rodriguez, and co-workers[115, 116, 119] applied DFT methods together with experimental studies to investigate how particle-support interactions affect the WGS activity of Au and Cu nanoparticles supported on reducible oxides, such as ceria and titania. With DFT, the authors calculated reaction energies and activation barriers over unsupported Au and Cu particles.[120] They then compared the activity of Au and Cu particles supported on CeO_2 and ZnO substrates.[115] Their experimental evidence suggests that Au supported on CeO_2 is highly active despite the low activity of both metallic and ZnO supported Au clusters. This contrast suggests that particle-support interactions in CeO_2 supported catalysts play a critical role activating metal clusters for WGS. Computational methods have elucidated the unique behavior of Au/CeO_2 not present on Au/ZnO or unsupported Au-clusters. To accomplish this, the authors utilized DFT methods to evaluate candidate reaction mechanisms by locating optimized intermediate and

transition structures on the potential energy surface.

To better understand the effect of the oxide support, the authors first study the activity of unsupported particles in the gas phase. The authors constructed model Au and Cu particles consisting of 29 atoms in a pyramidal geometry, whose shape and size are consistent with those observed by scanning tunneling microscopy[121] and x-ray diffraction.[122] Once the reaction energetics over unsupported particles are understood, they can be directly compared to energetics over the same particles supported on an oxide substrate. The catalytic performance of clean Au(100) and Cu(100) surfaces were also evaluated for comparison against the performance of the nanoparticles. This provides a basis for assessing the importance of edge and corner sites in the reaction mechanism. The authors investigated two reaction mechanisms. The first is a redox mechanism, shown in Figure A-1, which features the oxidation of the metal surface by the adsorption of CO and H_2O, followed by a subsequent surface reduction as adsorbed O atoms combine with CO before desorbing as CO_2. The second is an associative mechanism that proceeds through either formate or carboxyl surface intermediates. The optimized structures and corresponding reaction energy diagrams for these mechanisms are shown in Figures 1 and 2.

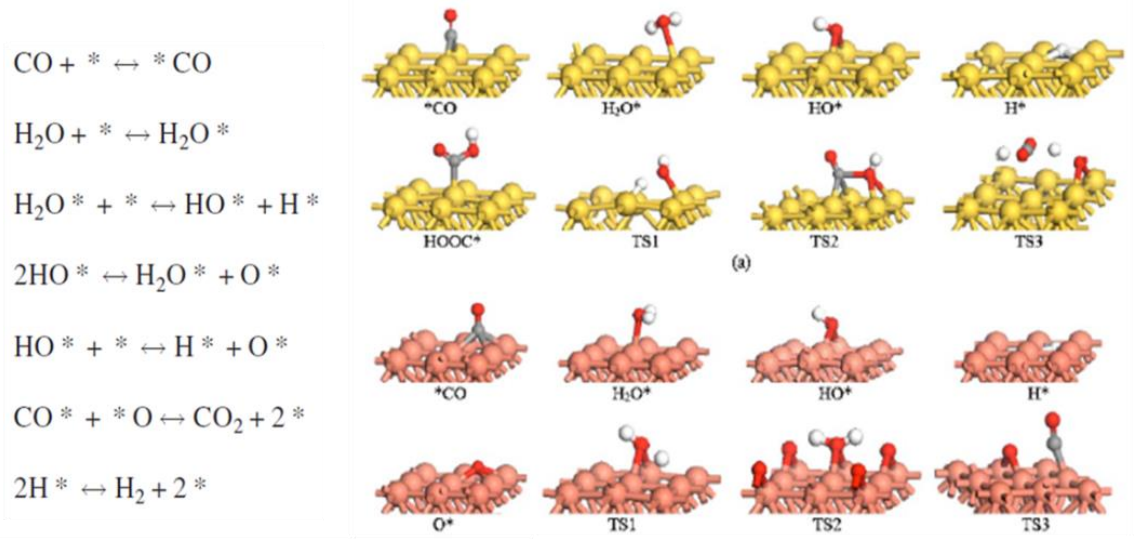

Figure A-1. WGS redox reaction mechanism (left) and structures (right). (Adapted with permission from ref. 120. Copyright 2007 American Institute of Physics)

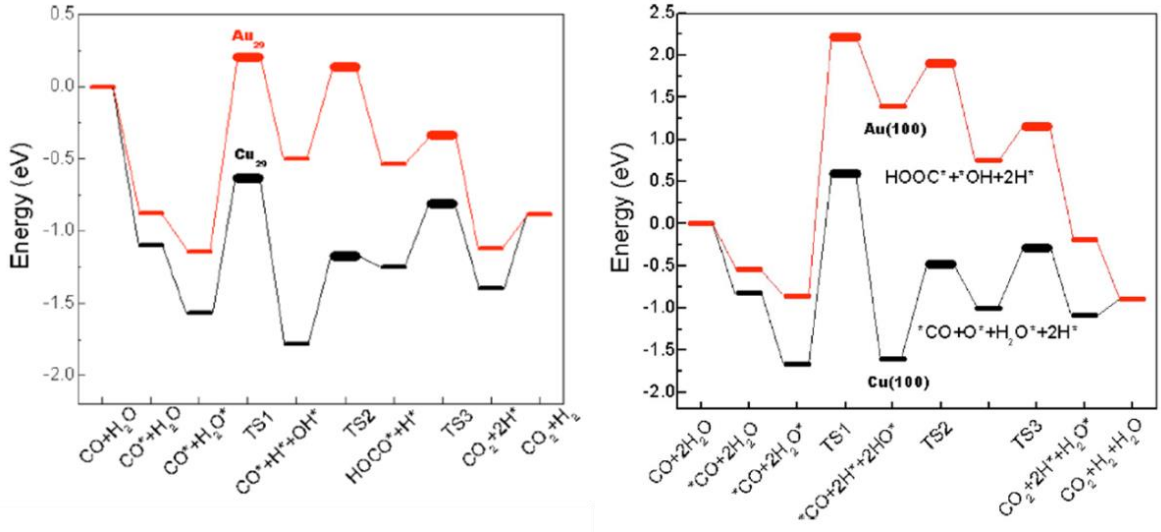

Figure A-2. DFT energies for WGS reaction path over Au and Cu nanoparticles (left) and surfaces (right), demonstrating that lower energy paths are available over Cu catalysts compared to Au in the absence of support effects. (Adapted with permission from ref. 120. Copyright 2007 American Institute of Physics)

DFT allows the authors to compare the energetic favorability of the possible mechanisms, thus identifying the likely reaction path over different catalytic surfaces. Cu(100) favors the redox mechanism, while the Au(100) surface (as well as the unsupported Au_{29} and Cu_{29} clusters) favor the associative mechanism. The reaction energy diagrams shown in Figure A-2 further suggest that the rate limiting step for the WGS reaction is the dissociation of adsorbed water for both mechanisms over Au and Cu. Determining the magnitude of the reaction barrier for the rate limiting step allows the authors to estimate the relative reaction rates over the varying catalytic surfaces. These results show that Cu is consistently more active than Au, and that step and edge sites lead to a further increase in the reaction rate.

If support effects do not influence activity, the above results suggest that supported Cu particles should yield activities higher than supported Au. The authors, however, cite numerous experimental results demonstrating that Au supported on ceria achieves higher conversions and faster reaction rates than the analogous Cu/ceria catalysts. The authors' experimental reaction rates and computed activation barriers demonstrate the low activity of Au compared to Cu, and suggest that high activity of Au/ceria must be the result of support interactions that activate the otherwise inactive Au clusters. Conversely, DFT results predicting low activity over unsupported Au are in qualitative agreement with the experimentally determined activity of Au supported on ZnO, which suggests that ZnO does not activate the particle or participate in the reaction mechanism. Liu, Rodriguez, and co-workers[115] also computed the activity of charged Cu and Au particles to determine if charge transfer between the cluster and the support could alone alter the activity of the metal clusters. DFT computed activation barriers over such ionic clusters show that neither

cationic nor anionic Au particles are as active as Cu particles, demonstrating that the activity of Au/ceria is not solely the result of active sites on ceria-stabilized ionic Au species. Since the metal sites alone cannot activate the gas phase reactants, the reaction may proceed through interfacial sites involving both the metal cluster and oxide support. The support not only activates the metal clusters, but likely plays a role in the reaction mechanism. The authors contrast this observation with the behavior of ZnO supported catalysts, in which the oxide may merely act as an inert substrate supporting the Au cluster for this reaction. These results demonstrate the utility of DFT (applied together with experimental studies) for differentiating between *active* and *spectator* supports.

A.2.2. Characteristics of Au Supported on CeO_2.

DFT methods can model both the structural and the electronic properties of a metal-oxide system. Since the computational expense of DFT scales heavily with system size, it is often necessary to analyze small model systems that, hopefully, capture the fundamental behavior at play in larger systems. This strategy was employed by P. Liu and co-workers, who conducted systematic DFT calculations investigating the binding trends and electronic properties of a *single* Au atom adsorbed on stoichiometric CeO_2(111), on CeO_2(111) with O-vacancies, and on reduced Ce_2O_3(0001) surfaces.[71] Many properties observed for the single Au atom can be extended to make predictions regarding the properties of larger clusters. Au atoms bind most strongly to O-vacant sites on the partially reduced CeO_2 surface (ΔE_{bind} = -1.86 eV), and they bind least strongly to the fully reduced Ce_2O_3 surface (ΔE_{bind} = -0.86 eV). Binding affinity on the stoichiometric CeO_2 is also considerable in

magnitude, with ΔE_{bind} = -1.26 eV. Using a Bader charge analysis,[123] the authors demonstrated that Au adsorbed in an oxygen vacancy on reduced CeO_2 has a negative partial charge (-0.58 e), while Au adsorbed on stoichiometric CeO_2 has a positive partial charge (+0.35 e). The negative partial charge on Au adsorbed in an O-vacancy suggests that Au acts as a reduction center, accepting a portion of the two electrons left in the surface after the formation of an O-vacancy. This demonstrates that oxygen vacancies serve as anchor sites that accommodate negative $Au^{\delta-}$ species adsorbed on the ceria surface.

The authors note that CO binding energy calculations, however, demonstrate that positive Au species, rather than negative species, are capable of adsorbing CO; and that these sites may play a key role in the WGS reaction mechanism. A density of state (DOS) analysis can determine how ceria stabilizes an active $Au^{\delta+}$ species within $Au_{n>1}$ clusters. The authors posit that the empty band of cerium *f* orbitals near the Fermi level accepts a Au $6s^1$ electron that would otherwise enter an anti-bonding Au(*6s*)-O(*2p*) orbital. A single Au atom can serve as a reduction center, stabilizing an O-vacancy in the ceria lattice. In turn, cerium atoms can subsequently oxidize adsorbed Au atoms by accepting a Au-$6s^1$ electron in the *f*-band. This explains the WGS activity of Au supported on *reduced* CeO_2: the O-vacancy serves as an anchor site for a Au atom, which then serves as a nucleation base for subsequent Au atoms that are oxidized by the surrounding Ce neighbors. This creates $Au^{\delta+}$ sites that favorably adsorb gas phase reactants, which can then interact with neighboring sites on both the cluster and the oxide. This result offers guidance for determining the behavior of larger Au clusters on the ceria surface, and how these structures may create active sites for the WGS mechanism.

A.2.3. WGS Mechanism over Au Supported on CeO_2.

Next we consider studies that use DFT to explicitly evaluate the energetics of candidate reaction mechanisms over various Au/ceria surface configurations. Chen et al.[124,26] used DFT+U to probe possible reaction mechanisms that proceed over the Au/ceria interface. In one study they examine redox and formate mechanisms over Au_3 and Au_{10} clusters on $CeO_2(111)$.[124] Both mechanisms feature rate limiting water O-H bond dissociation steps occurring over CeO_2 O-vacancies. The redox mechanism requires H_2O to dissociate after filling an oxygen vacancy on the ceria surface, leaving H_2 on the metal cluster after oxidizing the support. The CO reactant, which is adsorbed on the metal cluster, then reduces the oxide by removing an O atom from the ceria lattice, thus recreating an O-vacancy.

Similarly, the formate mechanism requires an O-H bond breaking step after H_2O adsorbs in an O-vacancy. CO adsorbed on the metal cluster then removes a H atom from the OH group adsorbed in an oxygen vacancy, creating a CHO group on the cluster. The resultant CHO group then removes an oxygen from the oxide surface and desorbs as CO_2, with an H atom left behind on the metal cluster. This recreates the O-vacancy in the surface, and leaves a H atom that can react with H_2O in the next cycle, thus desorbing H_2 and leaving OH adsorbed in the O-vacancy. The authors consider that breaking OH bonds to refill O-vacancies is rate limiting in both cases. DFT is used to determine the activation barriers for possible elementary steps that accomplish the necessary O-vacancy filling step. The authors conclude that both mechanisms must overcome a reaction barrier greater than 1 eV, which is prohibitive at low temperatures. This suggests that neither mechanism can

explain the experimentally observed activity of Au/ceria toward WGS at low temperatures, and for this reason they propose a different mechanism, the carboxyl mechanism, that is unique to the supported system and not subject to this limitation.

In a second study,[26] Chen et al. propose a carboxyl mechanism for WGS over Au/ceria in which the rate limiting H_2O dissociation step occurs at the Au/ceria interface. The mechanism, summarized in the reaction energy diagram shown in Figure A-3, requires H_2O from the gas phase to fill an oxygen vacancy near a Au cluster. Once in the vacancy, the H_2O molecule dissociates, as shown in Figure A-4, by allowing H to adsorb on the metal cluster while leaving OH behind on the oxide. The OH group then reacts across the Au/ceria interface with CO adsorbed on the metal cluster, thus forming a carboxyl group and regenerating the oxygen vacancy in the ceria lattice. To further support the carboxyl mechanism, the authors use a microkinetic model to compare the performance of the carboxyl mechanism to the formate and redox mechanisms discussed earlier. The result shows that the carboxyl mechanism yields a higher rate than the formate and redox mechanisms, and therefore better explains the high activity of Au/ceria catalysts. The carboxyl mechanism requires sites at the Au-ceria boundary, thus demonstrating the importance of considering metal-support interactions when postulating reaction mechanisms on supported metal-oxide catalysts.

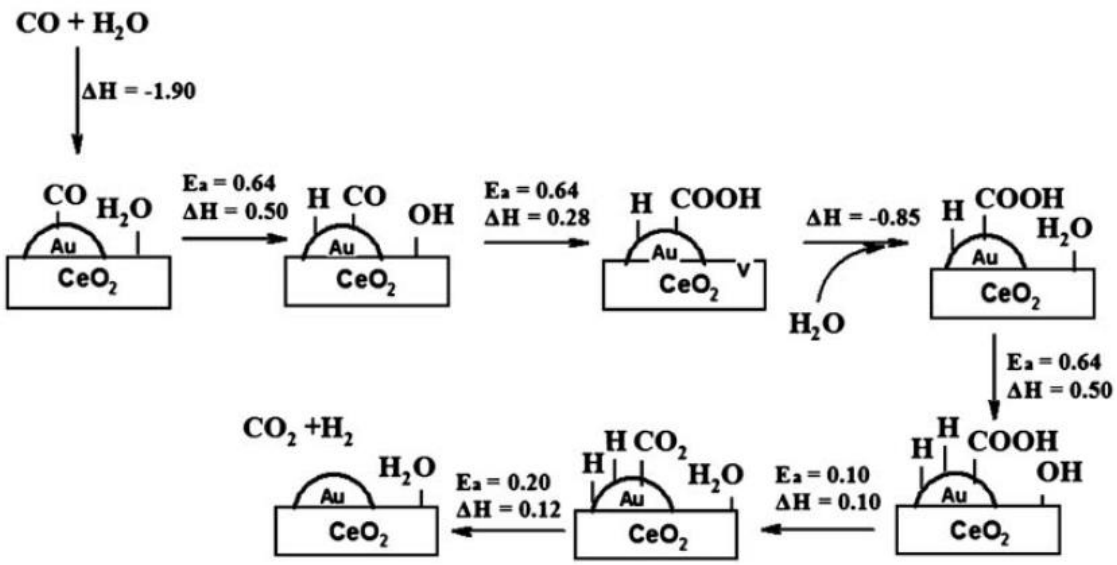

Figure A-3. Water -gas-shift reaction mechanism proceeding through a carboxyl surface intermediate as proposed by Chen et al. (Reprinted with permission from ref. 26. Copyright 2011 Royal Society of Chemistry)

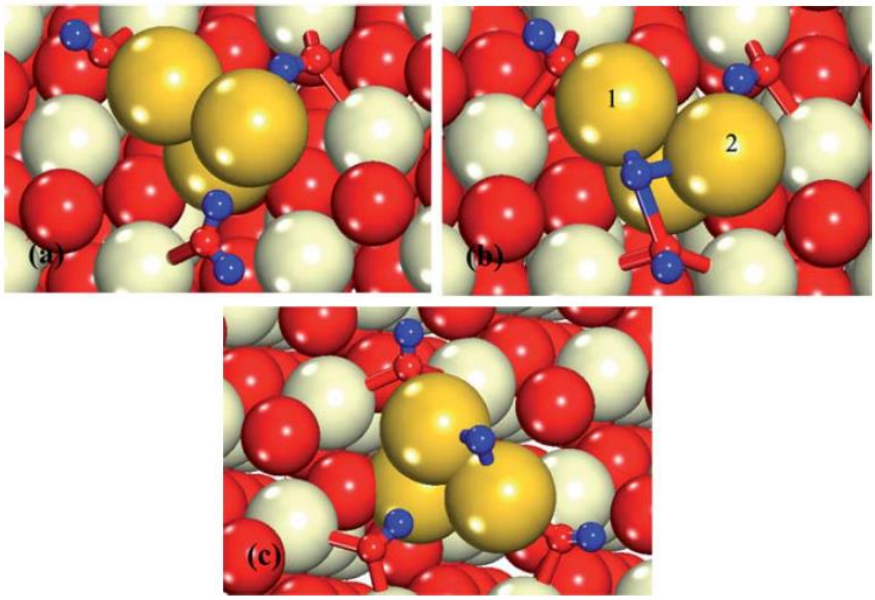

Figure A-4. (a) Initial, (b) transition, and (c) final structures for the dissociation of H_2O across the Au/CeO_2 interface, where H = blue, Au = yellow, O = red, Ce = white. (Reprinted with permission from ref. 26. Copyright 2011 Royal Society of Chemistry)

The studies discussed in the previous sections did not explicitly consider the effects of a gas phase environment at operating temperatures and pressures. Although providing useful insight, the methods employed could not model thermodynamic stabilities, adsorbate coverage effects, or *free energy* differences. This section will review studies that apply *ab initio* thermodynamics to accomplish such assessments. We first review the work of Reuter and Scheffler on RuO_2 systems, which was one of the first applications of *ab initio* thermodynamics to catalysis. This study assessed the catalytic behavior of an oxide, which is readily extended to studies of supported metal-oxide catalysts since the oxide support often plays an active role in the catalytic mechanism. We then will consider examples that apply *ab initio* thermodynamics to supported metal-oxide catalysts. In particular, we highlight systems in which particle-support interactions play an important role in overall catalytic activity.

A.3. *Ab initio* Thermodynamics

When conducting DFT to assess catalytic mechanisms over a surface, it is essential to choose an appropriate model. Namely, one must choose a model surface that is thermodynamically or kinetically stable under the reaction conditions of interest. Reuter and Scheffler applied the formalism of *ab initio* thermodynamics in a series of studies that assess the structure, stability, and reactivity of the RuO_2 (110) surface in equilibrium with a mixed O_2 and CO atmosphere.[100,102] This series of publications was one of the earliest applications of *ab initio* thermodynamics, and effectively demonstrates the methodology for bridging the gap between DFT calculations (at zero T and P) and experimental results

under catalytic reaction conditions. They applied *ab initio* thermodynamics to determine the relative stability of RuO_2(110) surface terminations in different oxidation states as a function of T and P_{O2} as function T, P_{O2}, and $P_{CO.}$ Although these studies were explicitly applied to the catalytic properties of RuO_2 toward CO oxidation, the formalism presented therein can be readily extended to studies investigating the stability and activity of oxide surfaces in supported metal-oxide systems. This methodology can be used to determine plausible surface models for detailed analyses of the reaction mechanism energetics.

A.3.1 Investigating Metal Clusters on Oxide Supports

Reuter and Scheffler first outline the theory and methodology of *ab initio* thermodynamics in a study applied to RuO_2 in equilibrium with an O_2 atmosphere.[100] The authors consider three possible surface terminations of RuO_2(110. The RuO_2(110)-O_{bridge} surface is predicted to be the most stable since it has the least number of uncoordinated O atoms and has no net dipole. The second surface considered is RuO_2(110)-O_{cus}, which features coordinately unsaturated (cus) oxygen atoms placed directly above the surface row of Ru atoms, creating a 6-fold coordination on all surface Ru atoms. The final structure, RuO_2(110)-Ru, has rows of 5-fold coordinated cus-Ru atoms and 4-fold coordinated bridge-Ru atoms on the oxide surface. The authors investigate the stability of the three RuO_2(110) surface terminations by calculating the surface free energy of each termination as a function T and $P_{O2.}$ These calculations show that at typical operating temperatures for CO oxidation (T = 600 K), the O-bridge surface termination is most stable at lower P_{O2} and that the over oxidized O-cus surface is favored at high P_{O2}. The Ru terminated surface is

never favored in the P_{O2} ranges of interest. The results reveal that the RuO_2-O_{bridge} surface termination is not always the most stable, and that a different surface phase is likely to form at high P_{O2}. The authors argue that the emergence of the RuO_2-O_{cus} phase at high O_2 chemical potentials, which was previously unknown, must be considered when interpreting experimental data collected under such conditions. This result highlights the importance of investigating the stability of a system for the entire temperature and pressure ranges of interest before drawing conclusions regarding the nature of active surface sites.

In subsequent studies, the authors incorporated the effect of both P_{O2} and P_{CO} on surface site occupation.[101] Using the resultant surface phase diagram they predict the regions in *T,P* space that are likely to display the highest catalytic activity. They conclude that the boundary between the O_{br}/CO_{cus} phase and the O_{br}/O_{cus} phase will balance CO_2 desorption creating O-vacancies at O_{cus} sites with the subsequent filling of O_{cus} vacancies by gas phase oxygen. Deep in the O_{br}/O_{cus} phase region, catalytic activity will be hampered by the high O_{cus} vacancy formation energy; whereas in the CO_{br}/O_{cus} phase, CO_{br} will consume O_{cus} faster than the resultant vacancies can be refilled by the gas phase. These results demonstrate the important role phase coexistence plays in catalytic mechanisms, and they exemplify the utility of *ab initio* thermodynamics for identifying favored reaction paths in *T,P* regions, bridging the gap between quantum calculations and experimental conditions.

A.3.2 Investigating Oxide-Supported Metal Clusters

The formalism presented in the previous section for predicting the stability of oxide surfaces in equilibrium with a muti-component gas phase is readily extended to systems that contain catalytic metal particles supported on oxide surfaces. Identifying stable particle-support constructions is indispensable for predicting the catalytic activity of the particle-support interface. This section will outline studies on reducible oxides (TiO_2 and CeO_2) that display unique particle-support interactions where the oxide support plays an active role in the catalytic mechanism. These examples demonstrate the ability of *ab initio* thermodynamics for determining the stability of metal clusters on oxide supports under realistic catalytic conditions. Such calculations can be used in concert with DFT reactivity studies to assess the activity of stable metal-oxide surfaces. Together, these methods offer a powerful means for predicting and characterizing the catalytic activity of a wide range of metal-oxide systems.

Au/TiO_2. In a study by Laursen and Linic,[68] the authors analyzed the behavior of Au on titanium oxide. They considered two model Au formations on the oxide surface: a nanorod and a 2 mono-layer sheet. They assessed the stability of these formations as a function of oxygen pressure over reduced, stoichiometric, and oxidized surfaces. The results shown in Figure A-5(c) demonstrate that both the nanorod and sheet constructions are most stable over the oxidized support. Formations over the reduced support can be stabilized at high temperatures in a highly reducing atmosphere at low oxygen chemical potential.

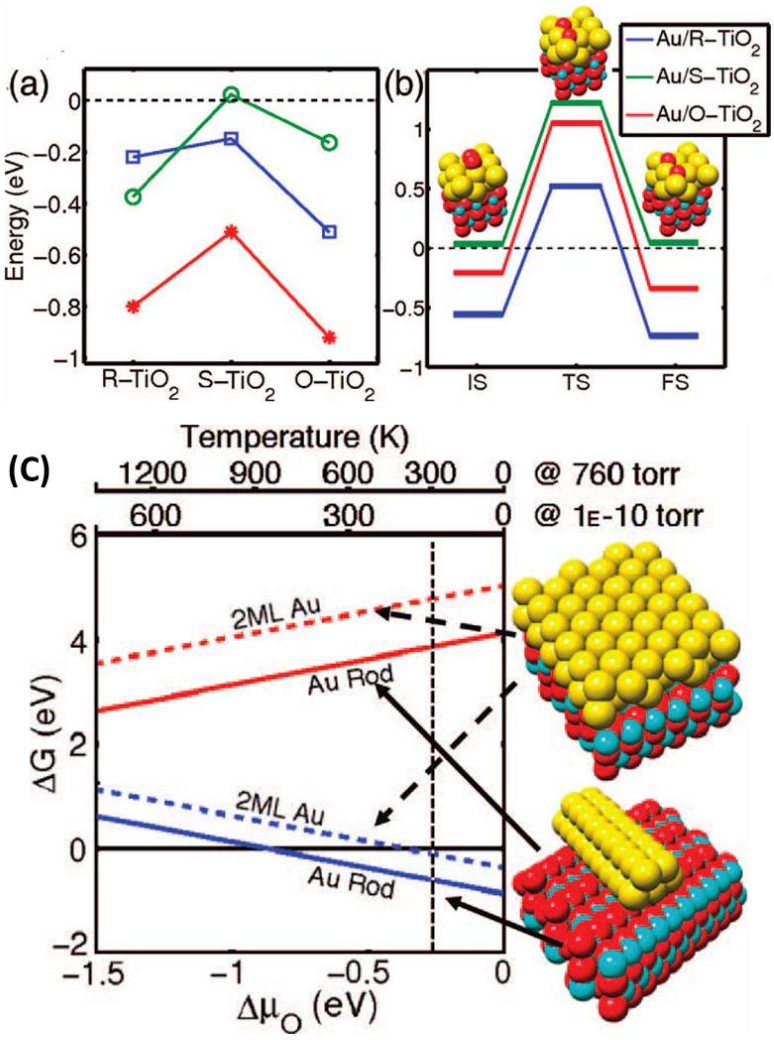

Figure A-5. (a) Adsorption energy of molecular oxygen and CO with respect to gas phase species on reduced, stoichiometric, and oxidized Au/TiO_2 surfaces for oxygen on a Au sheet (green, o), oxygen on a Au nanorod (blue, □), and CO on a Au sheet (red, *). (b) Activation barrier for O_2 dissociation over a Au bilayer sheet on reduced, stoichiometric, and oxidized TiO_2. (c) Free energy calculated as a function of oxygen chemical potential for Au rod and bilayer sheet structures on reduced (red, positive slope) and oxidized (blue, negative slope) TiO_2. (Reprinted with permission from ref. 68. Copyright 2009 American Chemical Society)

After determining the stability of these model systems, the authors calculated the adsorption and dissociation energies of O_2, along with the adsorption energy of CO, to probe the activity of possible sites on the supported Au clusters. The results of these calculations, shown in Figure A-5(a), show that the adsorption energy for both O_2 and CO

is significantly more exothermic over both the reduced and oxidized catalysts compared to equivalent sites on Au formations supported by a stoichiometric titania surface. The same trend holds for the dissociation barrier of O_2 over all three catalyst models shown in Figure A-5(b). The authors note that the most favorable adsorption sites involve Au atoms that are adjacent to Au atoms bound to point defects on the reduced and oxidized surfaces (the defects consist of an O-vacancy or an added O-atom, respectively). They explain this trend in terms of bond conservation theory, in which the strengthening of a Au/defect bond will weaken the neighboring Au/Au bond to the next adjacent Au atom, thus creating a chemically active site on the adjacent Au atom for bonding with a gas phase molecule.

The authors support this theory with charge density and local density of states (LDOS) calculations, which show that charge transfer between the surface and the particle (either from Au to the surface for oxidized-TiO_2 or vice versa for reduced-TiO_2) results in a strong polar-covalent bond between the Au atom and the point defect. This in turn weakens the bond to the next adjacent Au atom, making adsorption on that atom more favorable. The strong covalent bonds present in both the reduced and oxidized systems are largely absent in the stoichiometric system. Both unsupported Au nanorods and nanorods supported on the stoichiometric surface display low activity because neither system is activated by the covalent-type Au-oxide bonds present in the defected systems. The authors conclude that point defects on the oxide surface not only serve as anchor points for the metal clusters, but that they are also largely responsible for activating the particle through charge transfer. This contrasts with the findings of Corma and co-workers, who found that *neutral* Au particles display higher activity toward the dissociation of H_2, demonstrating the need to assess the relative activity of both charged and neutral clusters.[56, 57] These

studies exemplify the importance of particle-support interactions for predicting the catalytic activity of a system, and demonstrates how *ab initio* thermodynamics - in conjunction with standard DFT energy calculations - can explain the stability and activity of oxide-supported metal clusters.

Pt/TiO_2. In a similar study, Ammal and Heyden[125, 126] investigated the effects of particle-support interactions between Pt/TiO_2 under water-gas shift *T,P* conditions. They first determined the effect of Pt clusters on the reducibility of titania by systematically assessing the stability of small Pt_n (n = 1-8) clusters adsorbed on a partially reduced TiO_2(110) surface. Using *ab initio* thermodynamics, the authors calculated the free energy change for forming a single oxygen vacancy in the TiO_2 surface under oxidizing (O_2-rich) and reducing (CO-rich or H_2-rich) atmospheres. Not surprisingly, the authors found that vacancy formation is never favorable under oxidizing conditions. However, they found that Pt clusters greatly increase the favorability of oxygen vacancy formation under CO and H_2 rich atmospheres. This is demonstrated by the results reproduced in Figure A-6(a) showing vacancy formation free energy as a function of P_{H2} and *T*. Vacancy formation energy is significantly lower for surfaces with Pt_n clusters compared to the clean TiO_2 surface, which never favors oxygen vacancy formation in the *T,P* regions of interest. These results are similar to those by Laursen and Linic discussed above, in which the metal particle is anchored to the reduced TiO_2 surface through a covalent-type interaction that is largely absent over the stoichiometric surface. The subsequent charge transfer from the reduced TiO_2 surface to the Pt particle alters the adsorption behavior of gas phase molecules on the Pt cluster. This further demonstrates the unique effects of particle-surface interactions.

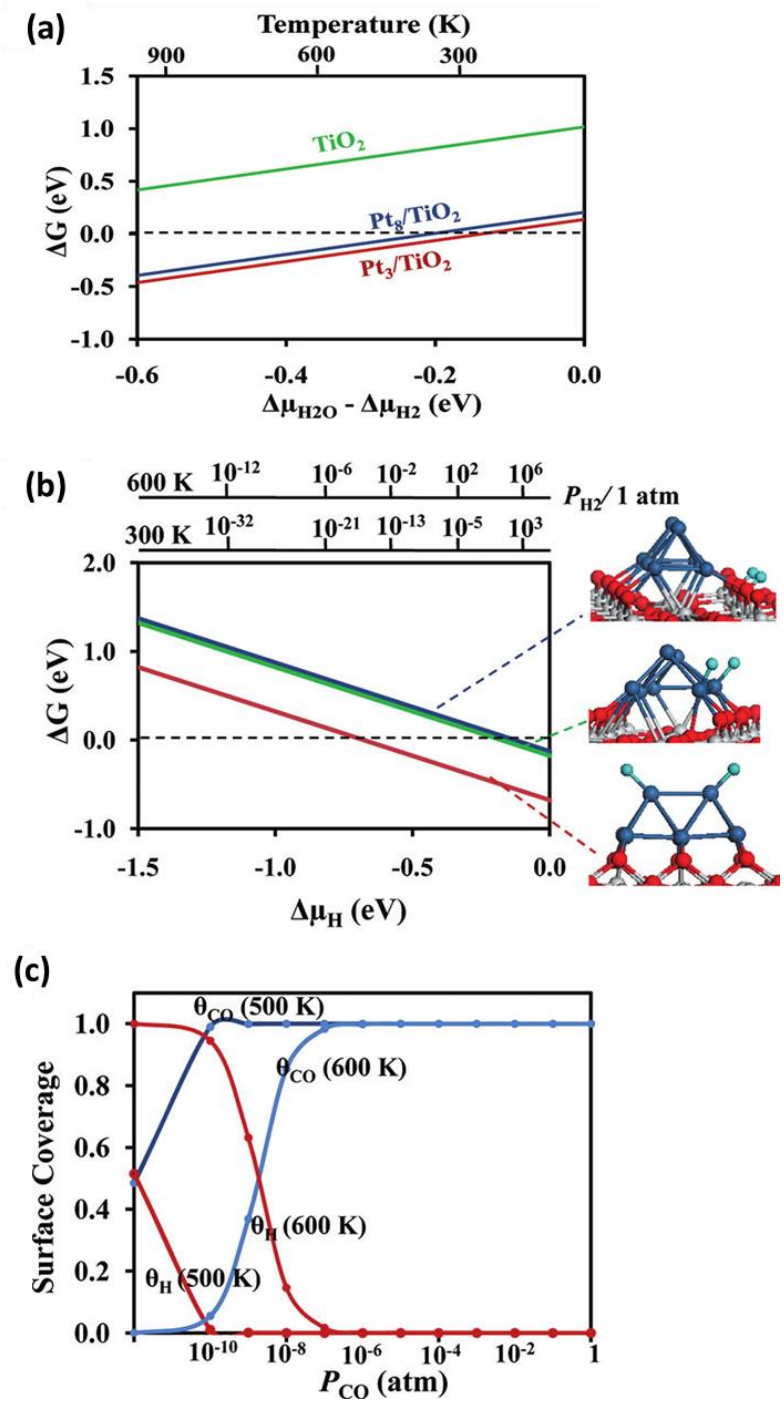

Figure A-6. (a) Free energy difference for oxygen vacancy formation on the clean TiO_2 surface (green, top), on TiO_2 in the presence of Pt_8 (blue, middle), and in the presence Pt_3 (red, bottom). (b) Free energy of H_2 adsorption on the oxide (blue, top), the metal-oxide interface (green, middle), and on the metal cluster (red, bottom). (c) Computed equilibrium surface coverage of CO and hydrogen at constant P_{H2} = 1 atm. (Reprinted with permission from refs. 126, 127. Copyright 2011 American Chemical Society)

The authors next assessed the stability of H_2 and CO gas phase adsorbates on the Pt_8 cluster, at the Pt/TiO_2 interface, and on the TiO_2 surface adjacent to the Pt cluster. They computed the free energy of adsorption for gas phase molecules at these sites, as well as calculated the equilibrium surface coverage as a function of partial pressure and temperature. It is possible that the WGS reaction mechanism involves hydrogen spillover from the metal particle to the TiO_2 surface. For this reason, the authors investigated H_2 adsorption in the vicinity of a Pt cluster, which is summarized in Figure A-6(b). The presence of H atoms at the Pt/TiO_2 interface can have adverse effects on the catalytic performance of the surface if H atoms bind too strongly to the interfacial sites under WGS conditions. The results shown in Figures 8(b-c) show that H atoms bind more strongly to Pt cluster sites than to interfacial Pt and O sites, suggesting that interfacial sites will not hinder hydrogen spillover between the Pt cluster and the oxide surface. By calculating the surface coverage of CO and H at various temperatures, the authors also show that CO adsorption on Pt cluster sites will dominate over H adsorption, indicating that Pt cluster sites will be filled by adsorbed CO under WGS conditions. These results demonstrate that interfacial sites will remain open under WGS conditions, and that they may be responsible for the high WGS activity of the catalyst.

The authors note that this result corroborates experimental findings,[127, 128] in which the WGS reaction rate scales positively with the interfacial boundary length. Using *ab initio* thermodynamics, the authors were able to assess the stability of candidate model systems for the Pt/TiO_2 surface under WGS conditions. Having identified a plausible model system, the authors mention their plans to use DFT to investigate the WGS mechanism over the Pt/TiO_2 interfacial model they identified in this study. We note that the authors

also conducted a similar study on an analogous Pt/CeO_2(111) system,[129] which applies similar methods to characterize the effect of Pt-ceria interactions.

Cu/CeO_2. The previous studies have shown that metal clusters typically enhance the reducibility of metal-oxide surfaces, thus altering the electronic properties of both the metal cluster and the oxide surface. Fabris and co-workers[73] demonstrate that this trend does not hold for all metal-oxide supported systems. They conducted a systematic computational study of Cu/CeO_2 systems that feature Cu atoms adsorbed on a stoichiometric surface, on a surface containing oxygen vacancies, and on a surface containing cerium vacancies. In particular, they use *ab initio* thermodynamics to assess the stability of Cu adsorption on the various CeO_2 surfaces in equilibrium with an oxygen atmosphere. *Ab initio* thermodynamics predicts that Cu typically prefers to adsorb on the stoichiometric CeO_2 surface, rather than on surfaces containing oxygen vacancies or cerium vacancies. These results are shown in Figure A-7, where the free energy of adsorption is plotted against oxygen chemical potential. Under oxidizing conditions, the formation of surface solution phases featuring a Cu atom substituted for a Ce atom is thermodynamically favored over Cu adsorption on the stoichiometric surface.

These observations lead to interesting conclusions regarding the redox behavior of Cu/CeO_2. The authors note that substituted Cu ions form stabilized CuO_4 units that permit the reversible release of oxygen under catalytically relevant thermodynamic conditions. This is reflected by the stability of the O^{vac}/Cu@Ce^{vac} phase that neighbors the Cu@Ce^{vac} phase seen in Figure A-7. This demonstrates that the surface can act as an oxygen buffer during reactions conducted under oxidizing conditions. Furthermore, it shows that redox processes over Cu/CeO_2 surfaces do not involve the reduction of cerium atoms (from Ce^{4+}

to Ce^{3+}) neighboring oxygen vacancies, which is typically characteristic of reaction paths involving a CeO_2 redox process. Other metal/ceria systems (e.g. Au/ceria discussed in previous sections) typically feature a redox mechanism in which metal clusters adsorbed on the surface stabilize the formation of oxygen vacancies. In the case of copper, however, oxygen vacancies are stabilized by substitution defects where Cu atoms fill Ce vacancies. Together with electronic structure calculations, the authors demonstrate that the redox behavior of Cu/CeO_2 does not follow the typical redox mechanism of other metal/ceria surfaces.

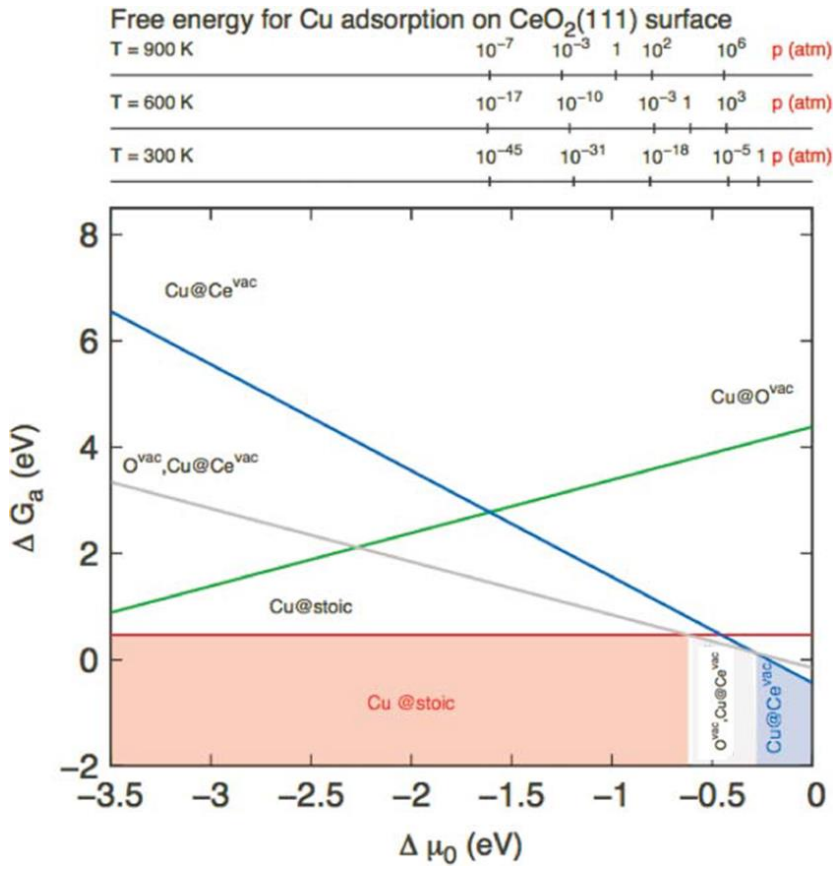

Figure A-7. (a) Free energy for the adsorption of Cu adatoms on stoichiometric ceria (red), on ceria with an oxygen vacancy (green), on ceria with a cerium vacancy (blue), and on ceria with both an oxygen and a cerium vacancy (grey). (Reprinted with permission from ref. 73. Copyright 2010 American Institute of Physics)

A.4. Classical Atomistic Modeling

The computational expense of quantum (QM) methods limits these methods to highly idealized system models, such as the single crystal surfaces and small ($\sim M_{n<8}$) clusters considered in the studies above. However, many catalytically interesting properties of supported metal-oxide systems arise from structural irregularities and possibly from the dynamic effect of surface reconstruction during reaction. Although it is difficult to characterize such effects using QM, it becomes possible with the use of empirical force-fields that have a relatively low computational expense. Reactive force-fields are designed to model bond dissociation and formation, and can therefore be implemented in *reactive* molecular dynamics (RMD) simulations that are capable of describing the dynamic nature of a catalyst at longer length and time scales (up to $\sim 10^4$ atoms and ~1 ns). This section will review research examples implementing the ReaxFF potential to model dynamic catalyst behavior under reactive conditions.

ReaxFF uses bond-length/bond-order relationships to model bond formation and dissociation in covalent systems, making it readily applicable to catalytic systems. This section will summarize two studies that demonstrate the ability of ReaxFF to accurately describe supported metal-oxide catalysts. The first study focuses on the catalytic properties of nickel surfaces and particles interacting with hydrocarbon reactants. The second study demonstrates the use of ReaxFF to describe complicated multi-metal-oxide (Mo/V/O) catalysts under reactive hydrocarbon environments. Together these studies show how ReaxFF extends the reach of computational methods to length and time scales required for characterizing the dynamic behavior of supported metal-oxide catalysts.

A.4.1. Hydrocarbon Catalysis on Metals.

The ReaxFF force-field can model catalytic properties of metal clusters toward C-H and C-C bond activation. This is exemplified by the work of Mueller, van Duin, and Goddard, in which the authors developed a Ni/C/H potential by parameterizing the ReaxFF force-field to reproduce a training set populated with DFT results for hydrocarbon-nickel adsorption energies, activation barriers, and bulk formation energies.[130] The authors note that surface defects may play an important role in reaction paths that lead to the high activity of the nickel surface, and that surface science experiments of hydrocarbon chemisorption and decomposition often seek to limit the number defects on the surface in order to characterize the reactivity of ordered low-index nickel surfaces. Similarly, DFT is computationally unable to reach the necessary system sizes for analyzing the effect of defects on irregular surfaces. For these reasons, the authors applied the Ni/C/H force-field in reactive molecular dynamics (RMD) simulations to assess the reactivity of various hydrocarbons over Ni catalyst particles that expose multiple irregular surface terminations, yielding insight into the role defect sites play in Ni catalyzed hydrocarbon reaction mechanisms.[131]

The study consisted of a series of RMD simulations with a spherical Ni particle consisting of 468 atoms surrounded by a single-species hydrocarbon gas phase in an 80x80x80 $\dot{A}^3$ periodic box. Simulations where conducted with six representative hydrocarbon species (methane, ethyne, ethene, benzene, cyclohexane, and propene) that were chosen to cover a variety of hydrocarbon behaviors arising from varying degrees of saturation. In each simulation, the temperature was ramped from 500 K to 2500 K at a rate

of 20 K/ps over the course of the 100 ps simulation. The authors extracted species population data at each time step, thus identifying reaction intermediates and their corresponding formation and decomposition rates. This data was then used to construct reaction networks from which elementary reaction paths can be identified. The results and analysis of the simulation for propene are reproduced in Figure A-8. The figure depicts the initial and final structures of the system, as well as the molecular population analysis as the simulation progresses. As seen in the figure, the authors can determine the temperatures at which key reactive events occur. This includes the temperature at which gas phase propene begins to chemisorb on the surface (T_A), at which dehydrogenation commences (T_H), and at which carbon-carbon bonds are broken (T_C). These temperatures yield insight into the kinetic barriers for hydrocarbon dissociation over nickel particles.

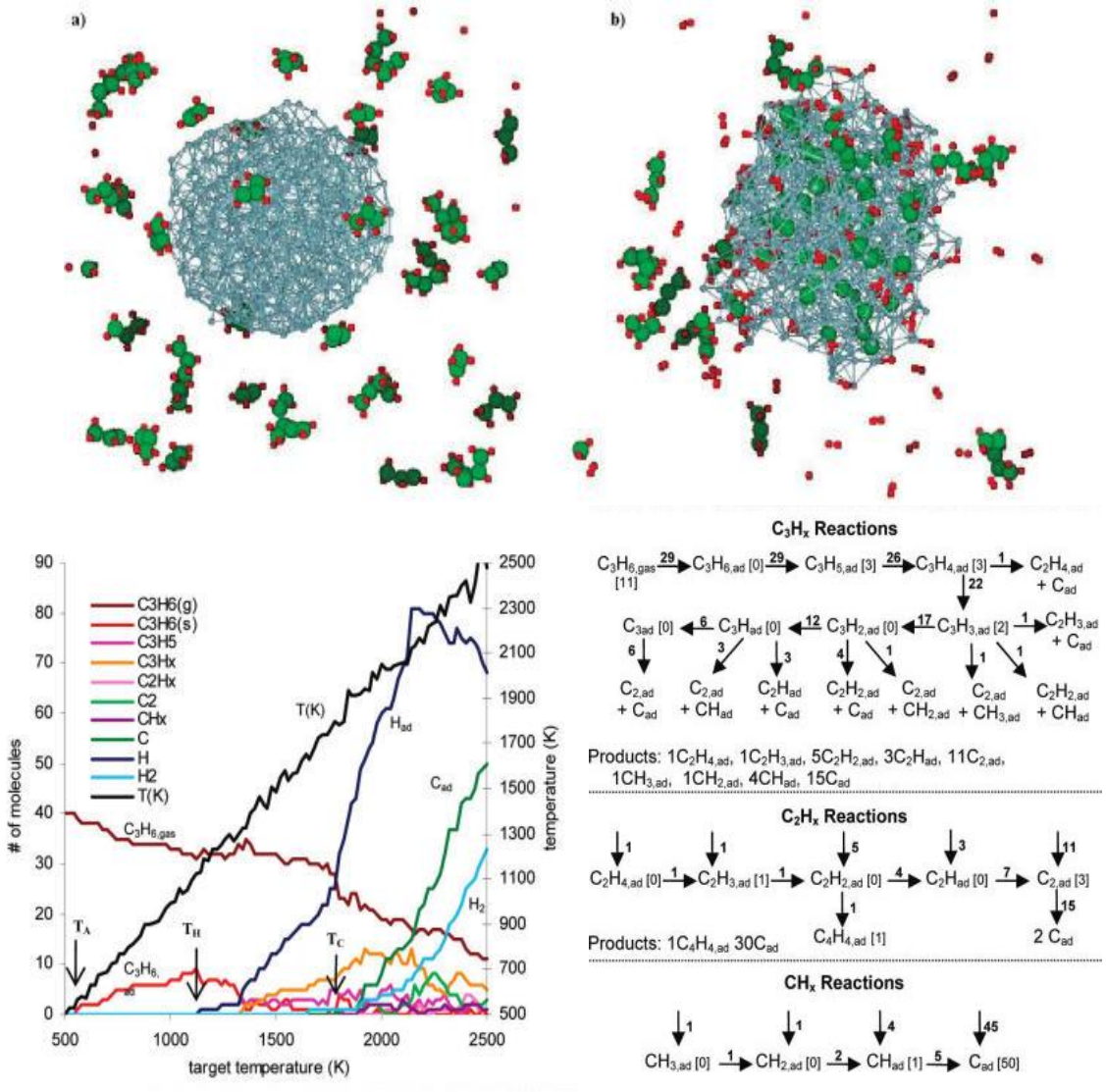

Figure A-8. (top) Initial and final structures of a RMD simulation demonstrating propene adsorption and decomposition on a nickel nanoparticle. (bottom) Molecular populations plotted against simulation temperature, and the corresponding reaction networks. Numbers in brackets indicate the number of species present at the end of the simulation and numbers over arrows indicate the corresponding number of reactive events. (Adapted with permission from ref. 132. Copyright 2010 American Chemical Society)

Analysis of the simulation trajectory yields reaction networks that reveal the preferred reaction mechanism over the Ni catalyst. For propene, molecules begin to chemisorb rapidly since C-C π bonds can be readily broken to form C-Ni σ bonds. Correspondingly, chemisorption of saturated hydrocarbons does not occur until higher temperatures where C-H bonds are broken by dehydrogenation. Analyses of the simulation trajectories show that C-H bond breaking is catalyzed by the insertion of a Ni atom between the C-H bond. The simulations also reveal that dehydrogenation typically precedes C-C bond scission, which is reflected in the figure by a low T_H compared to T_C. In contrast with DFT approaches, reaction paths are identified by MD analysis as opposed to explicitly hypothesized and evaluated, which allows the method to find reaction paths that are not immediately apparent. These results have many implications for designing Ni catalysts for hydrocarbon treatment. This work exemplifies the ability of empirical force fields to characterize reactions involving covalent hydrocarbon species interacting with irregular metal surfaces, which is necessary for modeling supported metal-oxide heterogeneous catalysts at large scales.

A.4.2. Multi-Metal-Oxide Catalysis.

The ReaxFF potential has also been utilized to study the catalytic properties of complex metal oxides. Chenoweth et al. developed and implemented a V/O/C/H force-field that, when combined with the existing hydrocarbon force-field, can model the interaction between gas phase hydrocarbons and the vanadium oxide surface.[132, 133] For motivation, the authors cite numerous examples in which V_2O_5 is used to catalyze industrial

processes that selectively oxidize both saturated and unsaturated hydrocarbon species, such as the conversion of methanol to formaldehyde. They stress that although V_2O_5 can be used for the oxidative dehydrogenation of methanol, it lacks selectivity when applied to the partial oxidation of larger hydrocarbons. The selectivity of vanadium oxide can be improved with the addition of appropriate supports and metal dopants (such as V, Te, Ta, and Nb) that alter the surface geometry and electronic structure. The addition of supports and dopants to form multi-metal-oxide catalysts often introduces a confluence of structural and electronic effects that are too complex for experimental efforts to untangle. For this reason, the authors propose that theoretical methodologies, such as RMD simulations via ReaxFF, are essential for establishing the necessary atomistic understanding of reaction processes over the complex oxide surface for designing more selective catalysts.

To demonstrate the validity of the ReaxFF potential for modeling catalytic V/O/C/H interactions, the authors simulated the oxidative dehydrogenation of methanol over the V_2O_5(001) surface.[132] They conducted a 250 ps NVT-MD simulation of a three layer oxide slab surrounded by 30 gas phase methanol molecules in a 20x20x20 $\dot{A}^3$ periodic box. A dual temperature constraint was applied in which the oxide slab was held at 650 K and the gas phase molecules were held at 2000 K. The final MD structure, along with the species population analysis, is shown in Figure A-9. Methanol species adsorb on the oxide surface and, after rearrangement, desorb as formaldehyde. Analysis of molecular populations and the MD trajectory shows that the reaction mechanism proceeds through the abstraction of hydrogen from the methyl group. The authors note that this result seems to contradict experimental evidence (from DRIFTS spectroscopy) that suggests an O-H bond dissociation mechanism. The authors demonstrate, however, that the C-H abstraction

path is preferred on the fully oxidized V_2O_5(001) surface and that the O-H abstraction path is preferred over a defect site where an oxo group has been removed from the surface. This result demonstrates the viability of the ReaxFF method for oxide-based catalysis, as well as exhibits the power of atomistic modeling for complementing experimental efforts to discern structural factors that influence the reaction path.

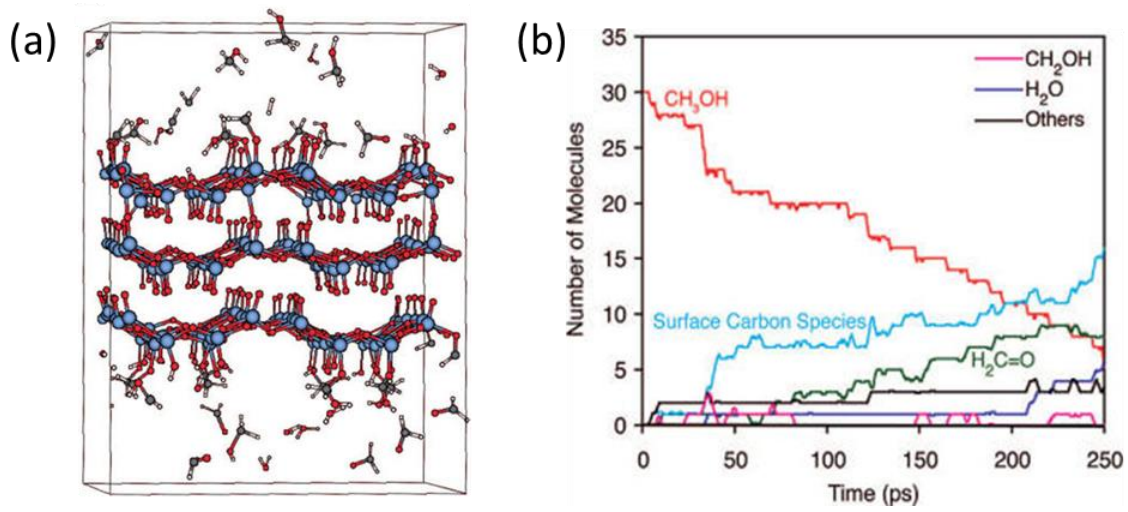

Figure A-9. (a) Final structure of a NVT-MD simulation of methanol interacting with a V_2O_5 slab and (b) the corresponding species population plot. (Reprinted from ref. 133, Copyright 2008 American Chemical Society)

The ReaxFF method can also be used to determine the structure and nature of active sites on complex oxide surfaces. This is demonstrated by the same authors in a subsequent publication,[133] in which they applied ReaxFF to predict the structure of a highly disordered multi-metal Mo_3VO_x catalyst. As mentioned earlier, the selectivity of vanadium oxide catalysts toward the partial oxidation of hydrocarbons can be altered by the addition of metal dopants to form multi-metal-oxides (MMO). MMO catalysts typically feature partial or mixed occupations of crystallographic sites, making it difficult to characterize the structure and nature of active sites by experimental methods. The authors apply the ReaxFF

potential to conduct a combined Monte Carlo/Reactive Dynamics (MC/RD) procedure to determine the Mo_3VO_x structure. The catalyst surface has metal sites that can be occupied by either Mo or V atoms. The MC/RD scheme identifies the preferred occupation of each site by systematically interchanging two atoms that occupy the same crystallographic site and determining the resultant energy change after re-optimizing the structure through RD. The new structure is either accepted or rejected according the MC-Metropolis criterion,[134] and the process is repeated until the energy converges at an optimal configuration for the chemical environment of the system.

The authors used the optimized structure to conduct RMD simulations in which hydrocarbons interact with the catalyst. The optimized catalyst displays several channels in the oxide through which hydrocarbons can diffuse to reach active sites. This particular simulation reveals that propane can diffuse through the $C7_2$-labeled channel in the oxide, but not through the $C7_1$-labeled channel. Such observations can reveal structural factors that influence catalyst selectivity, since differing hydrocarbon species will tend to diffuse through different channels. This property can be exploited to design highly selective MMO catalysts. This result demonstrates the applicability of the ReaxFF method for characterizing complex metal-oxide catalysts, which can be readily extended to supported metal-cluster/metal-oxide catalysis.

A.5. Summary

DFT methods can calculate the ground state electronic structure and energy of a system as a function of nuclear coordinates, allowing one to determine the preferred reaction path by identifying optimal structures on the DFT calculated potential energy surface (PES). Thus, the utility of DFT lies in its ability to accurately describe the energetics of reactive bond breaking/forming events, which reveals important aspects of the underlying electronic structure, such as oxidation states in atoms, orbital occupancies in molecules, and electronic band structures in solids. *Ab initio* thermodynamics uses statistical mechanics to extend DFT to high temperature and pressure descriptions, which allows one to calculate free energies to assess the stability the catalyst surface as a function of chemical environment. Such knowledge is a powerful tool for determining preferred reaction paths over catalytic surfaces, and for building a fundamental understanding of the electronic driving forces behind catalytic mechanisms.

The computational expense of QM limits these DFT and *ab initio* thermodynamics to highly idealized models, such as the single crystal surfaces and small clusters considered in the studies above, that only approximate the complex geometry of actual systems. These methods are also limited in their ability to consider dynamic structural transitions at a metal-oxide interface. Although it is difficult to characterize long range and dynamic effects using QM, it becomes possible with the use of empirical force-fields that are based on classical principles and therefore have a relatively low computational expense. The ReaxFF potential is designed to model bond dissociation and formation, and can therefore be implemented in *reactive* molecular dynamics and Monte Carlo simulations that are

capable of describing the dynamic nature of a catalyst at longer length and time scales (up to ~10^4 atoms and ~1 ns). Studies utilizing these methods can systematically probe catalytically interesting properties of supported metal-oxide systems that arise from structural irregularities and dynamic effects of surface reconstruction at interfaces.

Together, the computational methods discussed herein allow for a detailed determination of many phenomena influencing the behavior of supported metal-oxide catalysts. The studies considered in this review demonstrate the power of computational methods for assessing the stability and activity of supported metal-oxide catalysts.

A.6. References

1. E. Aneggi, C. de Leitenburg, G. Dolcetti and A. Trovarelli, Catalysis Today Catalytic Control of Diesel Exhaust Emissions, 2006, **114**, 40-47.
2. R. Burch, P. K. Loader and F. J. Urbano, Catalysis Today, 1996, **27**, 243-248.
3. L.-h. Xiao, K.-p. Sun, X.-l. Xu and X.-n. Li, Catalysis Communications, 2005, **6**, 796-801.
4. S. Colussi, A. Gayen, J. Llorca, C. de Leitenburg, G. Dolcetti and A. Trovarelli, Industrial & Engineering Chemistry Research, 2012, **51**, 7510-7517.
5. S. Specchia, E. Finocchio, G. Busca, P. Palmisano and V. Specchia, Journal of Catalysis, 2009, **263**, 134-145.
6. L. Shi, W. Chu, F. Qu and S. Luo, Catalysis Letters, 2007, **113**, 59-64.
7. T. Kuznetsova, V. Sadykov, L. Batuev, E. Moroz, E. Burgina, V. Rogov, V. Kriventsov and D. Kochubey, Journal of Natural Gas Chemistry, 2006, **15**, 149-163.
8. C. Bozo, N. Guilhaume, E. Garbowski and M. Primet, Catalysis Today, 2000, **59**, 33-45.
9. C. Bozo, N. Guilhaume and J.-M. Herrmann, Journal of Catalysis, 2001, **203**, 393-406.
10. M. A. Malecka, L. Kepinski and W. Mista, Applied Catalysis B: Environmental, 2007, **74**, 290-298.
11. G. Picasso, M. Gutierrez, M. P. Pina and J. Herguido, Chemical Engineering Journal, 2007, **126**, 119-130.

12. M. Cargnello, J. J. D. Jaén, J. C. H. Garrido, K. Bakhmutsky, T. Montini, J. J. C. Gámez, R. J. Gorte and P. Fornasiero, Science, 2012, **337**, 713-717.
13. G. Jacobs, R. A. Keogh and B. H. Davis, Journal of Catalysis, 2007, **245**, 326-337.
14. X. Wang and R. J. Gorte, Applied Catalysis A: General, 2002, **224**, 209-218.
15. Q. Zhuang, Y. Qin* and L. Chang, Applied Catalysis, 1991, **70**, 1-8.
16. E. Nikolla, J. Schwank and S. Linic, Journal of Catalysis, 2007, **250**, 85-93.
17. H.-L. Chen, S.-H. Liu and J.-J. Ho, Journal of Physical Chemistry B, 2006, **110**, 14816-14823.
18. Y. Matsumura, W.-J. Shen, Y. Ichihashi and H. Ando, Catalysis Letters, 2000, **68**, 181-183.
19. W.-J. S. Y. Matsumura, Physical Chemistry Chemical Physics, 2000, **2**, 1519-1522.
20. A. Yee, S. J. Morrison and H. Idriss, Journal of Catalysis, 1999, **186**, 279-295.
21. J. Lahiri, A. Mayernick, S. L. Morrow, B. E. Koel, A. C. T. van Duin, M. J. Janik and M. Batzill, The Journal of Physical Chemistry C, 2010, **114**, 5990-5996.
22. H. Idriss, Platinum Metals Review, 2004, **48**, 105-115.
23. D. Mei, N. A. Deskins, M. Dupuis and Q. Ge, Journal of Physical Chemistry C, 2008, **112**, 4257-4266.
24. D. Mei, N. Aaron Deskins and M. Dupuis, Surface Science, 2007, **601**, 4993-5001.
25. R. Burch, A. Goguet and F. C. Meunier, Applied Catalysis a-General, 2011, **409**, 3-12.
26. Y. Chen, H. Wang, R. Burch, C. Hardacre and P. Hu, Faraday Discussions, 2011, **152**, 121-133.
27. A. Goguet, F. C. Meunier, D. Tibiletti, J. P. Breen and R. Burch, The Journal of Physical Chemistry B, 2004, **108**, 20240-20246.
28. C. M. Y. Yeung, F. Meunier, R. Burch, D. Thompsett and S. C. Tsang, The Journal of Physical Chemistry B, 2006, **110**, 8540-8543.
29. G. Jacobs and B. H. Davis, Applied Catalysis A: General, 2005, **284**, 31-38.
30. D. Pierre, W. Deng and M. Flytzani-Stephanopoulos, Topics in Catalysis, 2007, **46**, 363-373.
31. X. G. Wang, R.J.; Wagner, J.P., Journal of Catalysis, 2002, **212**, 225-230.
32. X. Wang, J. A. Rodriguez, J. C. Hanson, D. Gamarra, A. Martinez-Arias and M. Fernandez-Garcia, Journal of Physical Chemistry B, 2006, **110**, 428-434.
33. C.-H. Lin, C.-L. Chen and J.-H. Wang, The Journal of Physical Chemistry C, 2011, **115**, 18582-18588.
34. R. Burch, Physical Chemistry Chemical Physics, 2006, **8**, 5483-5500.
35. T. Bunlesin, E. S. Putna and R. J. Gorte, Catalysis Letters, 1996, **41**, 1-5.
36. M. Boaro, C. de Leitenburg, G. Dolcetti and A. Trovarelli, Journal of Catalysis, 2000, **193**, 338-347.
37. D. Teschner, A. Wootsch, O. Pozdnyakova-Tellinger, J. Krohnert, E. M. Vass, M. Havecker, S. Zafeiratos, P. Schnorch, P. C. Jentoft, A. Knop-Gericke and R. Schlogl, Journal of Catalysis, 2007, **249**, 318-327.
38. V. Shapovalov and H. Metiu, Journal of Catalysis, 2007, **245**, 205-214.
39. S. H. Oh and G. B. Hoflund, Journal of Physical Chemistry A, 2006, **110**, 7609-7613.
40. H. Wang and W. F. Schneider, Catalysis Today, 2011, **165**, 49-55.

41. R. B. Getman and W. F. Schneider, ChemCatChem, 2010, **2**, 1450-1460.
42. W.-J. Zhu, J. Zhang, X.-Q. Gong and G. Lu, Catalysis Today, 2011, **165**, 19-24.
43. H. W. Jen, G. W. Graham, W. Chun, R. W. McCabe, J. P. Cuif, S. E. Deutsch and O. Touret, Catalysis Today, 1999, **50**, 309-328.
44. G. W. Graham, H. W. Jen, R. W. McCabe, A. M. Straccia and L. P. Haack, Catalysis letters, 2000, **67**, 99-105.
45. E. Aneggi, M. Boaro, C. d. Leitenburg, G. Dolcetti and A. Trovarelli, Journal of Alloys and Compounds, 2006, **408-412**, 1096-1102.
46. A. Trovarelli, C. d. Leitenburg, M. Boaro and G. Dolvetti, Catalysis Today, 1999, **50**, 353-367.
47. M. K. Debe, Nature, 2012, **486**, 43-51.
48. S. McIntosh, J. M. Vohs and R. J. Gorte, Electrochemical and Solid-State Letters, 2003, **6**, A240-A243.
49. S. McIntosh and R. J. Gorte, Chemical Reviews, 2004, **104**, 4845-4865.
50. R. J. Gorte, J. M. Vohs and S. McIntosh, Solid State Ionics, 2004, **175**, 1-6.
51. S. An, C. Lu, W. L. Worrell, R. J. Gorte and J. M. Vohs, Solid State Ionics, 2004, **175**, 135-138.
52. M. Gong, X. Liu, J. Trembly and C. Johnson, Journal of Power Sources, 2007, **168**, 289-298.
53. J.-H. Wang, M. Liu and M. C. Lin, Solid State Ionics, 2006, **177**, 939-947.
54. A. Borodziński and G. C. Bond, Catalysis Reviews, 2008, **50**, 379-469.
55. A. Borodziński and G. C. Bond, Catalysis Reviews, 2006, **48**, 91-144.
56. M. Boronat, F. Illas and A. Corma, The Journal of Physical Chemistry A, 2009, **113**, 3750-3757.
57. P. Concepción, S. Carrettin and A. Corma, Applied Catalysis A: General, 2006, **307**, 42-45.
58. N. Khan, S. Shaikhutdinov and H. Freund, Catalysis Letters, 2006, **108**, 159-164.
59. W. Ludwig, A. Savara, K.-H. Dostert and S. Schauermann, Journal of Catalysis, 2011, **284**, 148-156.
60. M. W. Tew, M. Janousch, T. Huthwelker and J. A. van Bokhoven, Journal of Catalysis, 2011, **283**, 45-54.
61. Z.-P. Liu and P. Hu, J. Am. Chem. Soc., 2003, **125**, 1958-1967.
62. G. Jacobs, S. Ricote, U. M. Graham, P. M. Patterson and B. H. Davis, Catalysis Today, 2005, **106**, 259-264.
63. J. H. Holles, R. J. Davis, T. M. Murray and J. M. Howe, Journal of Catalysis, 2000, **195**, 193-206.
64. J. A. Farmer and C. T. Campbell, Science, 2010, **329**, 933-936.
65. G. B. Hoflund, H. A. E. Hagelin, J. F. Weaver and G. N. Salaita, Applied Surface Science, 2003, **205**, 102-112.
66. W.-J. Shen and Y. Matsumura, Journal of Molecular Catalysis A: Chemical, 2000, **153**, 165-168.
67. H. Gabasch, K. Hayek, B. Klötzer, W. Unterberger, E. Kleimenov, D. Teschner, S. Zafeiratos, M. Hävecker, A. Knop-Gericke, R. Schlögl, B. Aszalos-Kiss and D. Zemlyanov, The Journal of Physical Chemistry C, 2007, **111**, 7957-7962.
68. S. Laursen and S. Linic, Journal of Physical Chemistry C, 2009, **113**, 6689-6693.

69. A. D. Mayernick and M. J. Janik, The Journal of Physical Chemistry C, 2008, **112**, 14955-14964.
70. H. Borchert, Y. Borchert, V. V. Kaichev, I. P. Prosvirin, G. M. Alikina, A. I. Lukashevich, V. I. Zaikovskii, E. M. Moroz, E. A. Paukshtis, V. I. Bukhtiyarov and V. A. Sadykov, Journal of Physical Chemistry B, 2005, **109**, 20077-20086.
71. Z.-P. Liu, S. J. Jenkins and D. A. King, Physical Review Letters, 2005, **94**, 196102.
72. Z. Yang, G. Luo, Z. Lu, T. K. Woo and K. Hermansson, Journal of Physics: Condensed Matter, 2008, **20**, 035210.
73. L. Szabova, M. F. Camellone, M. Huang, V. Matolin and S. Fabris, The Journal of Chemical Physics, 2010, **133**, 234705-234711.
74. M. Nolan, S. Grigoleit, D. C. Sayle, S. C. Parker and G. W. Watson, Surface Science, 2005, **576**, 217-229.
75. M. Nolan, S. C. Parker and G. W. Watson, Surface Science, 2005, **595**, 223-232.
76. S. Bernal, J. J. Calvino, M. A. Cauqui, J. M. Gatica, C. Larese, J. A. Perez Omil and J. M. Pintado, Catalysis Today, 1999, **50**, 175-206.
77. B. Wang, D. Weng, X. Wu and J. Fan, Catalysis Today, 2010, **153**, 111-117.
78. A. D. Mayernick and M. J. Janik, The Journal of Chemical Physics, 2009, **131**, 084701-084712.
79. K. Reuter, D. Frenkel and M. Scheffler, Physical Review Letters, 2004, **93**, 116105.
80. J. F. Weaver, J. A. Hinojosa Jr, C. Hakanoglu, A. Antony, J. M. Hawkins and A. Asthagiri, Catalysis Today, 2011, **160**, 213-227.
81. H. Zhang, J. Gromek, G. Fernando, H. Marcus and S. Boorse, Journal of Phase Equilibria and Diffusion, 2002, **23**, 246-248.
82. J. Rogal, K. Reuter and M. Scheffler, Physical Review B, 2004, **69**, 075421.
83. J. Klikovits, E. Napetschnig, M. Schmid, N. Seriani, O. Dubay, G. Kresse and P. Varga, Physical Review B, 2007, **76**, 045405.
84. J. A. Rodriguez, X. Wang, J. C. Hanson, G. Liu, A. Iglesias-Juez and M. Fernandez-Garcia, J. Chem. Phys., 2003, **119**, 5659-5669.
85. X. Wang, J. A. Rodriguez, J. C. Hanson, D. Gamarra, A. Martinez-Arias and M. Fernandez-Garcia, Journal of Physical Chemistry B, 2005, **109**, 19595-19603.
86. G. Zhou, P. R. Shah, T. Kim, P. Fornasiero and R. J. Gorte, Catalysis Today, 2007, **123**, 86-93.
87. S. Colussi, A. Gayen, M. F. Camellone, M. Boaro, J. Llorca, S. Fabris and A. Trovarelli, Angewandte Chemie International, 2009, **48**, 8481-8484.
88. L. M. Misch, J. A. Kurzman, A. R. Derk, Y.-I. Kim, R. Seshadri, H. Metiu, E. W. McFarland and G. D. Stucky, Chemistry of Materials, 2011, **23**, 5432-5439.
89. A. D. Mayernick and M. J. Janik, Journal of Catalysis, 2011, **278**, 16-25.
90. M. L. Drummond, B. G. Sumpter, W. A. Shelton and J. Z. Larese, J. Phys. Chem. C, 2007, **111**, 966-976.
91. R. B. Getman, Y. Xu and W. F. Schneider, The Journal of Physical Chemistry C, 2008, **112**, 9559-9572.
92. H. Wang and W. F. Schneider, J. Chem. Phys., 2007, **127**, 064706.
93. D. R. Mullins and S. H. Overbury, Surface Science, 2002, **511**, L293-L297.
94. J. K. Norskov, T. Bligaard, J. Rossmeisl and C. H. Christensen, Nat Chem, 2009, **1**, 37-46.

95. P. Hohenberg and W. Kohn, Physical Review, 1964, **136**, B864-B871.
96. W. Kohn and L. J. Sham, Physical Review, 1965, **140**, A1133-A1138.
97. W. Kohn, A. D. Becke and R. G. Parr, The Journal of Physical Chemistry, 1996, **100**, 12974-12980.
98. D. S. Sholl and J. A. Steckel, Density Functional Theory: A Practical Introduction, Wiley, 2009.
99. C. Stampfl, Catalysis Today, 2005, **105**, 17-35.
100. K. Reuter and M. Scheffler, Physical Review B, 2001, **65**, 035406.
101. K. Reuter and M. Scheffler, Physical Review B, 2003, **68**, 045407.
102. K. Reuter and M. Scheffler, Physical Review Letters, 2003, **90**, 046103.
103. A. C. T. van Duin, S. Dasgupta, F. Lorant and W. A. Goddard, Journal of Physical Chemistry A, 2001, **105**, 9396-9409.
104. M. Moseler, M. Walter, B. Yoon, U. Landman, V. Habibpour, C. Harding, S. Kunz and U. Heiz, J. Am. Chem. Soc., 2012, **134**, 7690-7699.
105. B. Yoon, H. Häkkinen, U. Landman, A. S. Wörz, J.-M. Antonietti, S. Abbet, K. Judai and U. Heiz, Science, 2005, **307**, 403-407.
106. L. M. Molina and B. Hammer, Physical Review Letters, 2003, **90**, 206102.
107. L. M. Molina, M. D. Rasmussen and B. Hammer, The Journal of Chemical Physics, 2004, **120**, 7673-7680.
108. G. P. Petrova, G. N. Vayssilov and N. Rösch, The Journal of Physical Chemistry C, 2007, **111**, 14484-14492.
109. P. S. Petkov, G. P. Petrova, G. N. Vayssilov and N. Rösch, The Journal of Physical Chemistry C, 2010, **114**, 8500-8506.
110. C. H. Hu, C. Chizallet, C. Mager-Maury, M. Corral-Valero, P. Sautet, H. Toulhoat and P. Raybaud, Journal of Catalysis, 2010, **274**, 99-110.
111. C. Mager-Maury, G. Bonnard, C. Chizallet, P. Sautet and P. Raybaud, ChemCatChem, 2011, **3**, 200-207.
112. R. Ferrando, G. Rossi, F. Nita, G. Barcaro and A. Fortunelli, ACS Nano, 2008, **2**, 1849-1856.
113. G. Barcaro and A. Fortunelli, The Journal of Physical Chemistry C, 2007, **111**, 11384-11389.
114. G. Barcaro, A. Fortunelli, G. Granozzi and F. Sedona, The Journal of Physical Chemistry C, 2009, **113**, 1143-1146.
115. J. A. Rodriguez, P. Liu, J. Hrbek, J. Evans and M. Pérez, Angewandte Chemie International Edition, 2007, **46**, 1329-1332.
116. J. A. Rodriguez, S. Ma, P. Liu, J. Hrbek, J. Evans and M. Pérez, Science, 2007, **318**, 1757-1760.
117. A. Bruix, J. A. Rodriguez, P. J. Ramírez, S. D. Senanayake, J. Evans, J. B. Park, D. Stacchiola, P. Liu, J. Hrbek and F. Illas, J. Am. Chem. Soc., 2012, **134**, 8968-8974.
118. C. Zhang, A. Michaelides and S. J. Jenkins, Physical Chemistry Chemical Physics, 2011, **13**, 22-33.
119. P. Liu and J. A. Rodriguez, The Journal of Chemical Physics, 2007, **126**, 164705-164708.
120. P. Liu and J. A. Rodriguez, J. Chem. Phys., 2007, **126**.

121. J. A. Rodriguez and F. Illas, Physical Chemistry Chemical Physics, 2012, **14**, 427-438.
122. X. Wang, J. A. Rodriguez, J. C. Hanson, M. Perez and J. Evans, The Journal of Chemical Physics, 2005, **123**, 221101-221105.
123. R. F. W. Bader, Accounts of Chemical Research, 1985, **18**, 9-15.
124. Y. Chen, J. Cheng, P. Hu and H. Wang, Surface Science, 2008, **602**, 2828-2834.
125. S. C. Ammal and A. Heyden, The Journal of Physical Chemistry C, 2011, **115**, 19246-19259.
126. S. C. Ammal and A. Heyden, The Journal of Physical Chemistry C, 2011, **116**, 1624-1624.
127. T. Ishida, N. Kinoshita, H. Okatsu, T. Akita, T. Takei and M. Haruta, Angewandte Chemie International Edition, 2008, **47**, 9265-9268.
128. Z. Zhou, S. Kooi, M. Flytzani-Stephanopoulos and H. Saltsburg, Advanced Functional Materials, 2008, **18**, 2801-2807.
129. S. Aranifard, S. C. Ammal and A. Heyden, The Journal of Physical Chemistry C, 2012, **116**, 9029-9042.
130. W. A. Goddard, J. E. Mueller and A. C. T. van Duin, Journal of Physical Chemistry C, 2010, **114**, 4939-4949.
131. J. E. Mueller, A. C. T. van Duin and W. A. Goddard, The Journal of Physical Chemistry C, 2010, **114**, 5675-5685.
132. K. Chenoweth, A. C. T. v. Duin, P. Persson, M.-J. Cheng, J. Oxgaard and I. I. I. W. A. Goddard, The Journal of Physical Chemistry C, 2008, **112**, 14645-14654.
133. K. Chenoweth, A. C. T. van Duin and W. A. Goddard III, Angewandte Chemie International, 2009, **48**, 7630-7634.
134. N. Metropolis, A. W. Rosenbluth, M. N. Rosenbluth, A. H. Teller and E. Teller, The Journal of Chemical Physics, 1953, **21**, 1087-1092.
135. P. A. Deshpande, M. S. Hegde and G. Madras, AIChE Journal, 2010, **56**, 1315-1324.

Appendix B

Illuminating Surface Atoms in Nanoclusters by Differential X-ray Absorption Spectroscopy

This chapter is published as:
C. S. Spanjers, T. P. Senftle, A. C. T. van Duin, M. J. Janik, A. I. Frenkel and R. M. Rioux,
Physical Chemistry Chemical Physics **16** (48), 26528-26538 (2014).
Author contributions are specified at the beginning of each section.

Abstract

We use differential extended x-ray absorption fine structure (Δ-EXAFS) to monitor the Ar-induced surface restructuring of Pd nanoclusters (1 nm diameter, silica-supported) at 77 K. Δ-EXAFS analysis shows 9 ± 2 nearest-neighbor Pd-Pd bonds expand by 0.104 ± 0.005 Å as a result of Ar adsorption. Atomistic molecular dynamics simulations provide evidence for a model in which Ar drives restructuring of under-coordinated Pd atoms, leading to an increased Pd-Pd bond length of surface Pd atoms with no change in overall nearest-neighbor Pd-Pd coordination number. Based on observations of the atomistic simulations, it is likely that under-coordinated atoms are trapped in metastable states at 77 K and Ar provides the kinetic energy needed to overcome the barrier for surface restructuring. Together, experiment and theory highlight the ability of Δ-EXAFS to probe surface atoms of Pd nanoclusters.

B.1. Introduction

(**Note: Text written by C.S.S. and edited by T.P.S.)**

Nanoscience relies on the ability of researchers to detect ultra-small changes on the atomic scale that arise from the non-bulk-like properties of nanostructures. Applications of such materials are far reaching — extending from drug delivery[1] to catalysis,[2] photonics,[3] magnetic storage,[4] and spintronics.[5] In catalysis, surface atoms of metal nanoparticles (under-coordinated surface atoms in particular) often control catalytic properties.[6-10] Detecting the number and coordination environment of surface metal atoms, as well as their response to stimulation (*i.e.* molecules), is of utmost importance in understanding catalytic behavior. X-ray absorption spectroscopy (XAS) is particularly well-suited for this task due to its sensitivity to local structure (within a few coordination shells around an x-ray absorbing atom) and its ability to be used *in situ*, but the inherent ensemble-averaging nature of XAS measurements that probe both interior and surface types of atoms makes surface characterization difficult. External stimulation, such as the chemisorption of molecules, can be used to enhance the detectability of the surface atoms by XAS. For example, XAS can be used to determine the surface compositions of Pd and Pt in bimetallic nanoparticles by detecting changes in the x-ray absorption near edge structure (XANES) after CO adsorption.[11] The use of differential extended x-ray absorption fine structure (EXAFS) allows for more sensitive detection of local structure compared to traditional EXAFS. Applied to catalysis, this can isolate the active surface atoms from spectator bulk atoms.[12-17] Application of this technique to magnetostriction makes detection of femtometer atomic displacements possible.[18]

Despite the number of methods developed in the last decade, improving the selectivity of structural probes to surface metal atoms in nm-scale nanoclusters remains one of the main objectives of catalysis science. In this work we will show the application of a differential EXAFS (Δ-EXAFS) method that we developed for probing surface atoms of SiO_2-suppoted Pd nanoclusters. The Δ-EXAFS data were obtained by measuring the EXAFS signals before and after Ar adsorption, and subsequently modeled by taking into account only the unsubtracted, surface Pd contributions. In addition to the EXAFS data analysis and modeling, we have also employed atomistic molecular dynamics (MD) simulations to differentiate between models compared in the EXAFS data analysis process, thus determining the most plausible restructuring mechanism. Further application of the technique is not limited to a particular set of materials; instead, it can be applied to any system in which modulation causes small changes in local structure.

B.2. Experimental and Computational Methods

(**Note: Text covering experimental methods written by C.S.S. and text covering computational methods written by T.P.S.)**

B.2.1. Synthesis of Pd/SiO_2

3% Pd/SiO_2 was synthesized using the strong electrostatic adsorption (SEA) method, according to a previously reported procedure.[19] Briefly, $Pd(NH_3)_4(NO_3)_2$ was added to a slurry of silica (Davisil A60) at pH = 11. The sample was filtered, washed, and dried at 398 K prior to reduction at 438 K under flowing 4% H_2/He for 1 h.

B.2.2. X-ray Absorption Spectroscopy (XAS)

XAS measurements were performed at beamline 10-BM of the Advanced Photon Source (APS) at Argonne National Lab (ANL). The 3% Pd/SiO_2 catalyst (~50 mg) was pressed into a 4 mm ID cylindrical steel holder to obtain an edge step of ~0.4 at the Pd K-edge. The sample was loaded into a specially designed *in situ* reactor cell capable of heating the sample to 523 K for reduction and cooling the sample to 77 K during XAS measurements. Ultra-high purity (UHP, 99.999%) 3% H_2/He was used for pretreatment without further purification. UHP He and UHP Ar were passed through triple gas purifiers to remove oxygen, moisture, and hydrocarbons (Restek Super Clean gas purifier) prior to admission onto the catalyst sample. The sample was purged at room temperature under flowing 3% H_2/He at a rate of 30 mL/min for 15 min before heating to 523 K and holding for 1 h. The system was purged with He at a rate of 30 mL/min for 20 min prior to cooling to remove absorbed and adsorbed hydrogen from the Pd nanoclusters (NCs). The sample was then immediately cooled to 77 K by sliding the sample holder into the liquid nitrogen Dewar with a magnet.

The temperature of the catalyst was measured in a separate experiment to be 79 K. However, it is unclear if the thermocouple was inducing a heat loss and was the cause of the increased temperature. Therefore, the temperature of the EXAFS measurements will be referred to as 77 K. All EXAFS scans were acquired in transmission geometry with an energy range from 200 eV before to 1227 eV after the Pd K-edge (24350 eV). A reference Pd foil was placed between the transmission and reference ionization chambers for energy calibration and alignment. The EXAFS scans referred to as “Clean Pd NCs” were acquired

under flowing He at a rate of 30 mL/min at 77 K. The EXAFS scans referred to as "After Ar adsorption" were acquired under a mixture of Ar (5 mL/min) and He (30 mL/min) at 77 K. At this partial pressure of Ar (~100 Torr), we expect the silica and Pd surfaces to be covered by approximately one statistical monolayer of Ar based on BET surface area measurements. The IFEFFIT package was used for XAS data processing, and analysis.[20, 21] Energy calibration was performed by aligning all scans with the reference Pd foil prior to further processing.

B.2.3. Scanning Transmission Electron Microscopy (STEM)

STEM images were acquired at the University of Chicago Research Resources Center facility using a JEOL-ARM 200CF aberration corrected microscope (70 pm spatial resolution and 300 meV energy resolution). STEM imaging for this sample was previously reported.[19] Samples were prepared for analysis by dispersing in isopropyl alcohol, sonicating for 20 min, dropping onto a holey-carbon copper grid, and drying under a heat lamp for 20 min. Images were taken using the High Angle Annular Dark Field (HAADF) mode and the Particle2 program was used for counting particle sizes. 90 particles were counted to get an accurate representation of the particle size distribution.

B.2.4. Computational Methods

ReaxFF[22] is a classical interatomic interaction force-field that consists of both bonding and non-bonding interactions, which enables the potential to describe both

metallic bonding and van der Waal interactions that occur in a system consisting of Pd clusters exposed to a noble gas. To treat simulations involving metal/metal and metal/noble gas interactions, we combined a recently developed ReaxFF Pd/Pd[23] interaction potential with Ar and He parameter sets.[24] Model 1 nm Pd_{43} clusters were generated using a hybrid Monte Carlo-molecular dynamics scheme (MC/MD),[23] in which MC steps randomly displace Pd atoms in the cluster according to the usual Metropolis criteria.[25] After every 500 MC trial steps, a 100 ps MD run was conducted to diversify the configuration space explored by the cluster. The temperature of the MC/MD simulation was set to 500 K, which corresponds to the temperature of the experimental system prior to being quenched to 77 K. Hence, the MC/MD simulation yields a set of model clusters in reasonable approximation to those contained in the poly-disperse experimental sample upon exposure to Ar gas.

To assess the impact of an Ar gas phase on Pd cluster reconstruction, we conducted molecular dynamics simulations in the NVT ensemble *via* the velocity Verlet method[26] with a 0.25 fs time step. A Berendsen thermostat[27] with a damping constant of 100 fs was used to maintain a temperature of 77 K through the duration of the 1 ns simulations. The model clusters were equilibrated for 1 ns in vacuum before being exposed to 50 gas phase Ar atoms in a 50×50×50 Å periodic simulation cell (yielding an effective pressure of ~0.5 MPa, estimated from the ideal gas law) for an additional 1 ns. Average Pd-Pd bond distances were determined for each atom from atomic coordinates that were archived at 125 fs intervals throughout the simulation. Additional control simulations were conducted under He to ensure that observed Pd cluster reconstructions can be attributed to the effect of the Ar gas phase.

Nearest-neighbor (NN) coordination numbers were calculated using a cutoff radius of 3.5 Å around each atom. The Ar-induced bond length expansion was calculated by taking the difference between the average NN bond length of each atom before and after being exposed to Ar. The data were averaged over the last 125 ps (1000 frames) of each simulation to obtain representative NN bond lengths and coordination numbers.

B.3. Results

(Note: Text covering experimental results written by C.S.S. and text covering computational results written by T.P.S.)

B.3.1. Adsorption of Ar on Pd/SiO_2 at 77 K

The Pd K-edge EXAFS data for the Pd nanoclusters (NCs) at 77 K under a He atmosphere (30 mL/min) are shown in Figure B-1 (referred to as "Clean Pd NCs"). After reducing at a temperature of 523 K with 3% H_2/He, the sample was purged with pure He prior to cooling to prevent palladium hydride (PdH_x) formation. Based on the Pd-Pd first shell bonding distance, it is clear PdH_x is not present in the sample. The data show only Pd-Pd bonding and there is no indication of low-Z scatterers (e.g. C, O, or N). The first shell was modeled with a single Pd-Pd scattering path and the fit is shown along with the data in Figure B-1. The results of the fit are shown in Table B-1. The clean Pd NCs have a Pd-Pd coordination number and bond length of 7.0 ± 0.2 and 2.700 ± 0.005 Å, respectively. The bond length is contracted with respect to Pd foil, indicating the presence of small Pd NCs, which is in agreement with STEM data. The Pd-Pd coordination number is consistent

with Pd nanoclusters of about 40 atoms (~1 nm diameter).[28] Attempts to fit the EXAFS data past the first coordination shell following established methods[29, 30] failed due to the high disorder of the ultra-small Pd NCs. A STEM image for the sample is shown in Figure B-2. The average particle size determined from STEM is 1.0 ± 0.2 nm, which is consistent with the EXAFS results.

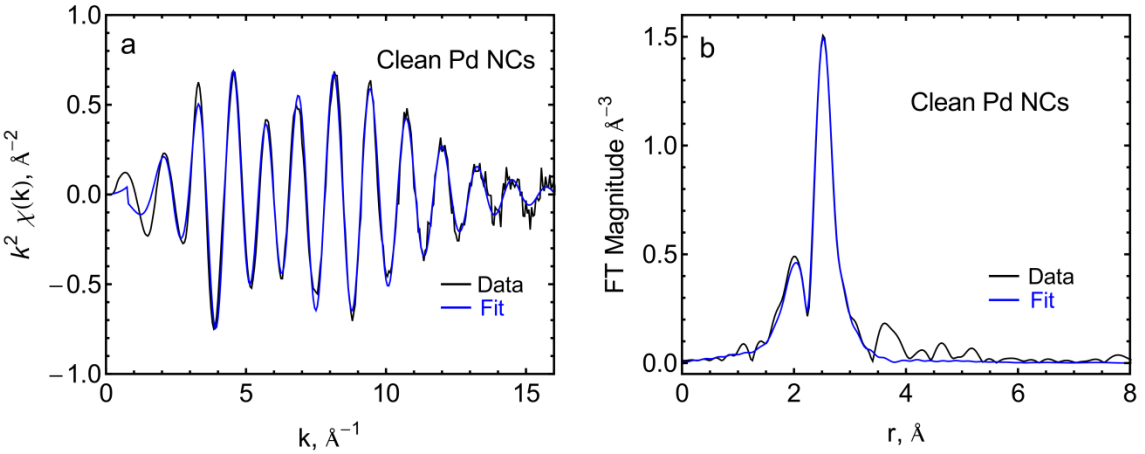

Figure B-1. (a) Edge-step normalized and background-subtracted k^2-weighted $\chi(k)$ EXAFS data and (b) Fourier transform magnitude of k^2-weighted $\chi(k)$ for the clean Pd NCs in He atmosphere at 77 K at the Pd K-edge. The first-shell fit of the data is shown in blue.

Table B-1. Pd K-edge EXAFS first shell fits.

Sample	**N[a]**	**r (Å)**	**σ^2 [b] (Å^2)**
Pd Foil	12	2.731 ± 0.002	0.0058 ± 0.0002
Clean Pd NCs	7.0 ± 0.2	2.700 ± 0.005	0.0088 ± 0.0002
After Ar Exposure	7.2 ± 0.4	2.707 ± 0.008	0.0094 ± 0.0004

[a]Calculation of N was performed using the amplitude reduction factor obtained from the Pd foil (0.86).
[b]EXAFS Debye-Waller factor.

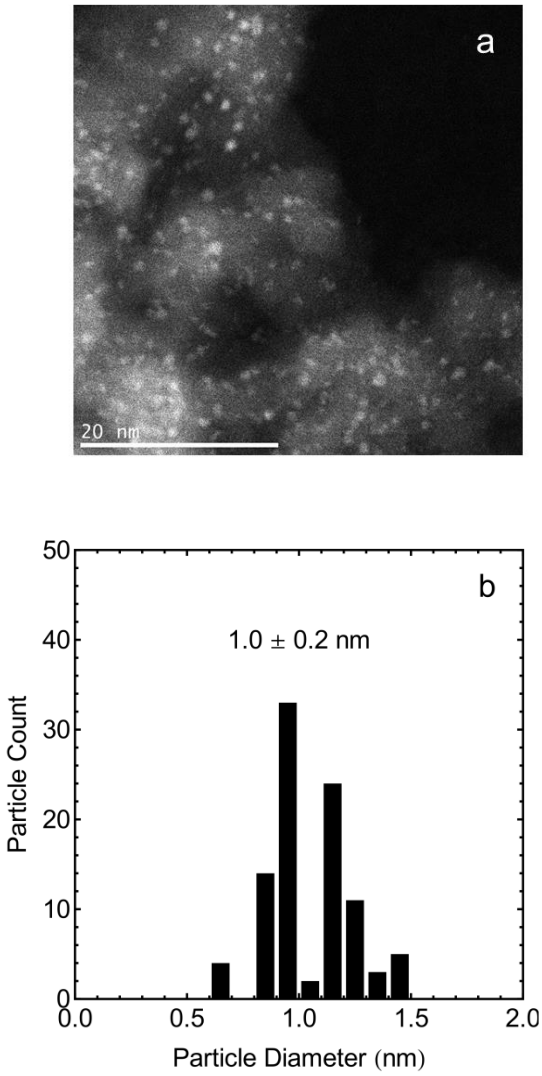

Figure B-2. a) STEM image of Pd/SiO_2 nanoclusters and (b) particle size distribution of Pd/SiO_2 catalyst. The calculated number average particle diameter is 1.0 ± 0.2 nm.

After Ar adsorption (5 mL/min Ar in 30 mL/min He), the EXAFS data highly resemble the data for the clean Pd NCs. The first shell fit of the data after Ar adsorption provides identical results (within error) to the clean Pd NCs. This analysis strategy, however, is not adequate for detection of changes that may have occurred in Ar atmosphere because only a few surface atoms of Pd particles would have been affected by Ar while XAS signal probes all atoms in the nanocluster. Differential EXAFS (Δ-EXAFS) spectrum

obtained after subtracting the two spectra (the one measured in Ar from the other, measured in He) should have much greater sensitivity to the atoms directly affected by Ar because the contributions to the Δ-EXAFS from unaffected ("spectator") atoms will cancel. The Δ-EXAFS signal is shown in Figure B-3. The mostr striking characteristic of this spectrum is a shift of the phase of the oscillations by ca. $\pi/2$, clearly visible in Figure B-3. We will show analytically below that the $\pi/2$ phase shift in the Δ-EXAFS compared to the total spectrum is consistent with the small change of the Pd-Pd bond length provided that the total coordination number of Pd atoms remains approximately the same. After the adsorption of Ar, the sample was heated to room temperature and purged with flowing He (30 mL/min) and subsequently cooled to 77 K. Taking the difference of the clean Pd NCs EXAFS spectrum and a spectrum after heating to room temperature, shows only noise: therefore, the observed change in the Pd bond length is reversible.

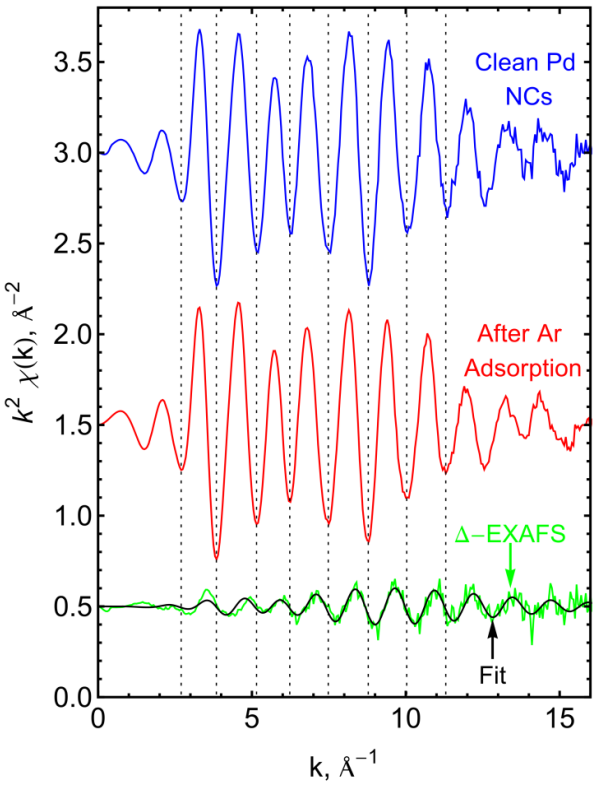

Figure B-3. k^2-weighted $\chi(k)$ EXAFS data for the clean Pd NCs, after Ar adsorption, and the Δ-EXAFS spectrum obtained by subtracting the spectrum after Ar adsorption from the clean Pd NCs spectrum. The fit of the Δ-EXAFS data is shown in black.

Below, we describe a general method useful for the analysis of differential EXAFS data of small metal nanoclusters and provide a quantitative assessment of the restructuring of the Pd NCs. The EXAFS signal $\chi(k)$ for modeling the first shell scattering of nanocluster sample, with two types of bonds, core (*i*) and surface (*i*') , is shown in below (prime refers to surface bonds):

$$\chi(k) = \frac{S_0^2 N_i f(k) e^{-\frac{2r_i}{\lambda(k)}} e^{-2k^2\sigma_i^2}}{kr_i{}^2} \sin\left(2kr_i + \delta(k)\right) + \frac{S_0^2 N_{i'} f(k) e^{-\frac{2r_{i'}}{\lambda(k)}} e^{-2k^2\sigma_{i'}^2}}{kr_{i'}{}^2} \sin\left(2kr_{i'} + \delta(k)\right) \quad (1)$$

where *k* is the photoelectron wave number, S_0^2 is the passive electron reduction factor, $f(k)$ and $\delta(k)$ are the photoelectron scattering-path amplitude and phase, respectively, N is the

coordination number, r is the interatomic distance, σ^2 is the mean-square deviation in r, and $\lambda(k)$ is the photoelectron mean free path. Correspondingly, the EXAFS equation for the "Clean Pd NCs" sample, χ_{Clean}, is:

$$\chi_{Clean}(k) =$$

$$\frac{S_0^2 N_1 f(k) e^{-\frac{2r_1}{\lambda(k)}} e^{-2k^2\sigma_1^2}}{kr_1{}^2} \sin\left(2kr_1 + \delta(k)\right) + \frac{S_0^2 N_1{}' f(k) e^{-\frac{2r_1{}'}{\lambda(k)}} e^{-2k^2\sigma_1^2{}'}}{kr_1{}'^2} \sin\left(2kr_1{}' + \delta(k)\right) \quad (2)$$

The EXAFS equation for the "After Ar adsorption" sample, χ_{After}, is:

$$\chi_{After}(k) =$$

$$\frac{S_0^2 N_2 f(k) e^{-\frac{2r_2}{\lambda(k)}} e^{-2k^2\sigma_2^2}}{kr_2{}^2} \sin\left(2kr_2 + \delta(k)\right) + \frac{S_0^2 N_2{}' f(k) e^{-\frac{2r_2{}'}{\lambda(k)}} e^{-2k^2\sigma_2^2{}'}}{kr_2{}'^2} \sin\left(2kr_2{}' + \delta(k)\right) \quad (3)$$

Since the interior atoms are unchanged during the Ar adsorption, $N_1 = N_2$, $r_1 = r_2$, and $\sigma_1^2 = \sigma_2^2$. In addition, S_0^2 , $f(k)$, and $\lambda(k)$ will be identical in all terms since they all refer to a Pd-Pd single scattering path. The number of surface atoms, $N_1{}'$ or $N_2{}'$ will also remain unchanged and this will be referred to as N_s. If Eq. (3) is subtracted from Eq. (2), the following expression is derived for Δ-EXAFS ($\chi_{Clean} - \chi_{After}$):

$$\Delta\text{-EXAFS} =$$

$$\frac{S_0^2 N_s f(k) e^{-\frac{2r_1{}'}{\lambda(k)}} e^{-2k^2\sigma_1^2{}'}}{kr_1{}'^2} \sin\left(2kr_1{}' + \delta(k)\right) - \frac{S_0^2 N_s f(k) e^{-\frac{2(r_1{}' + \Delta r)}{\lambda(k)}} e^{-2k^2\sigma_2^2{}'}}{k(r_1{}' + \Delta r)^2} \sin\left(2k(r_1{}' + \Delta r) + \delta(k)\right) \quad (4)$$

where $r_{2'}$ is expressed as $r_{1'} + \Delta r$. We note that Eq. (4), in the approximation that the bond length disorder did not change between the two states, and that $\Delta r \ll r$, reduces to a simple ansatz:

$$\Delta\text{-EXAFS} \approx \frac{S_0^2 N_s f(k) e^{-\frac{2r_{1'}}{\lambda(k)}} e^{-2k^2\sigma_{1'}^2}}{k r_{1'}^2} (2k\Delta r) \sin\left(2kr_{1'} + \delta(k) + \frac{\pi}{2}\right) \quad (5)$$

Eq. (5) features a π/2 phase shift compared to the equation for χ_{Clean}, validating our conclusions based on visual examination of the Δ-EXAFS (Figure B-3) which also shows the π/2 phase shift compared to the spectrum measured in He or Ar atmospheres. We note that Eq. (5) is equivalent to that used for analysis of differential signal in magnetostriction experiment by modulation excitation method.[18]

The differential spectrum can be modeled by implementing Eq. (4) into a suitable data analysis program. In this work it was accomplished by using FEFF models for each spectrum and fitting the difference between the two modeled signals to the experimental data. The total number of Pd-Pd bonds affected by Ar adsorption, $n_{Pd-Pd,aff}$, can be estimated directly from the measured N_s, the coordination number of Pd-Pd atoms in the differential spectrum, and the total number of atoms in a representative particle (n) as follows:

$$N_s = \frac{2n_{Pd-Pd,aff}}{n} \quad (6)$$

We note that the denominator is the total number of atoms per particle, not the total number of affected atoms, which would make it analogous to a conventional expression for coordination number[31] because the differential signal was obtained by subtracting the edge-step normalized EXAFS spectrum. Edge step normalization is the procedure that

relates the total EXAFS signal from all absorbing atoms in the sample to that corresponding to an "an equivalent absorber", hence, the total number of atoms is used in the denominator of Eq. (6).

The terms $r_{1'}$ and $\sigma^2_{1'}$ were obtained from the fit of the "Clean Pd NCs" (Figure B-1 and Table B-1) under the approximation the surface atoms have a bond length and EXAFS Debye-Waller factor equivalent to the bulk value of the Pd NCs (*i.e.* $r_1 = r_{1'}$ and $\sigma^2_1 = \sigma^2_{1'}$) However, in other cases, higher data quality may allow for the determination of $r_{1'}$ and $\sigma^2_{1'}$ directly from the differential data.

The results of fitting the Δ-EXAFS with Eq. 4 are presented in Table B-2 and the Fourier transform magnitude EXAFS for the data and the fit are presented in Figure B-4. The number of Pd-Pd bonds that changed during the Ar-induced restructuring is 9 ± 2. These bonds expanded by Δr = 0.104 ± 0.005 Å. In addition, the disorder of these bonds decreased since the EXAFS Debye-Waller factor decreased from 0.0088 ± 0.0002 to 0.0045 ± 0.0009. Thus, the EXAFS analysis shows that 9 ± 2 NN Pd-Pd bonds expand as a result of introducing Ar at 77 K. This is compared to the total number of NN Pd-Pd bonds in a 40-atom Pd cluster of 140.

Table B-2. Fit parameters obtained from the differential data using Eq. (4).

Parameter	**Value**	**Allowed to Vary?**
N_s	0.46 ± 0.07	Yes
$r_{1'}$	2.700 ± 0.005 Å	No[a]
$\sigma^2_{1'}$	0.0088 ± 0.0002	No[a]
Δr	0.104 ± 0.005 Å	Yes
$\sigma^2_{2'}$	0.0045 ± 0.0009	Yes
$n_{Pd-Pd,aff}$	9 ± 2	No[b]

[a]Obtianed from fit of Clean Pd NCs.
[b]Determined after the fit using Eq. (6).

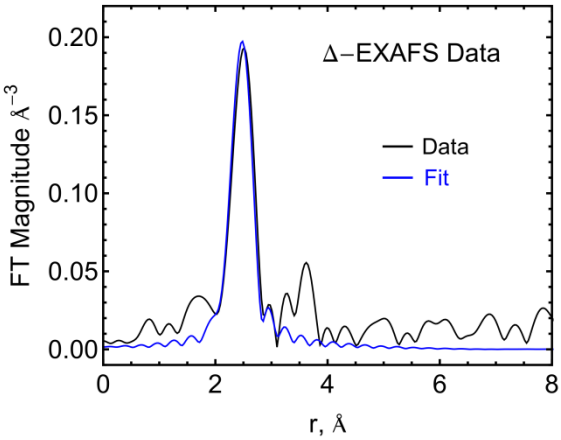

Figure B-4. Fourier transform magnitude of k^2-weighted $\chi(k)$ for the Δ-EXAFS spectrum (black) and the fit of the data (blue) using the model in Eq. (4).

EXAFS analysis by fitting method often depends on the model used, and comparing several models is necessary to avoid possible misinterpretation of the data. We have compared two additional models that are described below. The first model was a Pd-Ar single-scattering model that assumes that the differential signal could arise from Pd-Ar scattering only. Attempts to fit the Δ-EXAFS signal with the Pd-Ar scattering model results in an unrealistic fit parameter for the energy shift and a poor-quality fit to the data. Therefore, we dismiss the possibility that the differential signal arises from Pd-Ar contributions. The second model was a direct fit of the differential data with Pd-Pd scattering. This model would only be appropriate if the number Pd-Pd bonds changed, such that the amplitude of the differential data represents additional Pd-Pd bonds that arose during the adsorption of Ar (or Pd-Pd bonds that were removed during the adsorption). Fitting the differential data with this model results in a good fit to the data, and the Pd-Pd bond length expansion was comparable to what was found in the present differential model EXAFS model. However, this model is under the presumption that the overall Pd-Pd

coordination number changed during Ar adsorption. On the other hand, the differential EXAFS model described in Eq. (4) shows that the differential EXAFS signal arises from a change in bond length only, with no change in the overall Pd-Pd coordination number. Thus, using EXAFS alone, it is impossible to differentiate between the two aforementioned models. We will show through the atomistic modeling described below that we are able to use theory to break the degeneracy of the two competing EXAFS models.

B.3.2. Atomistic modeling of Ar-induced restructuring

To support our experimental observation of Ar-induced surface restructuring of Pd atoms and to differentiate between the proposed EXAFS models, we conducted a series of ReaxFF-MD simulations in which model Pd clusters were exposed to both vacuum and an Ar gas phase (*i.e.* 50 Ar atoms in the periodic cell) at 77 K. In each simulation, the average Pd-Pd bond distance was assessed from the atomic coordinates of the system, thus allowing changes in average Pd-Pd bond distance after the introduction of Ar atoms to be determined. Figure 5-5 depicts the initial and final system geometries in an MD simulation where a 1 nm Pd cluster was exposed to Ar. As seen in the figure, Ar interacts weakly with the cluster, forming a physisorbed layer of Ar atoms on the surface of the cluster. The calculated adsorption energy for an isolated Ar atom on Pd is 1 - 2 kcal mol^{-1}, which is dependent on the adsorption configuration.

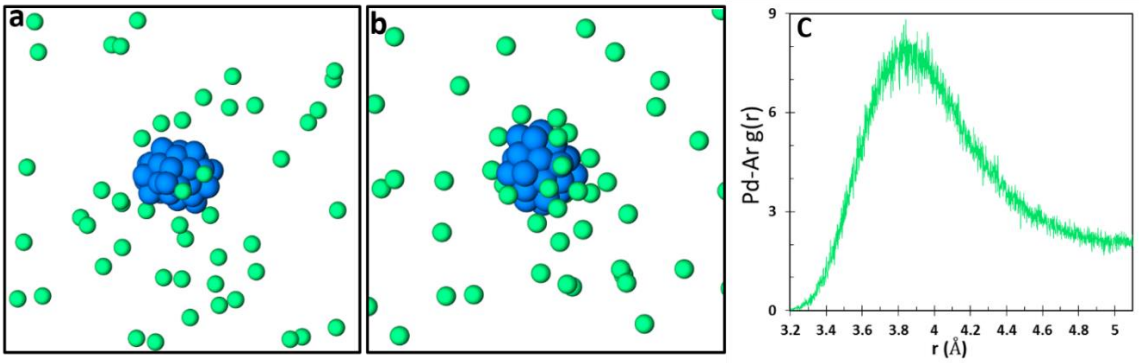

Figure B-5. (a) Initial and (b) final system geometry in a 1 ns MD-NVT simulation at 77 K. (c) Pd-Ar radial pair distribution function, *g(r)*, demonstrating an Ar physisorption well centered near *r* = ~3.9 Å from the cluster surface.

To assure modeling results were not biased by the initial selection of cluster geometry, we employed a hybrid MC/MD simulation method to generate a set of model Pd clusters. The MC/MD simulation was conducted at 500 K, which corresponds to the experimental annealing temperature the Pd clusters were exposed to before being quenched to 77 K. This results in an ensemble of cluster geometries that are representative of those present in the experimental sample, where the energy differences between clusters arise due to thermal fluctuations in the system, as shown in Figure B-6. The model clusters do not include the SiO_2 support used experimentally, and therefore we neglect any effect the support could have on initial Pd nanocluster structure or the restructuring process. The relative impact of this simplification is further addressed in the discussion section.

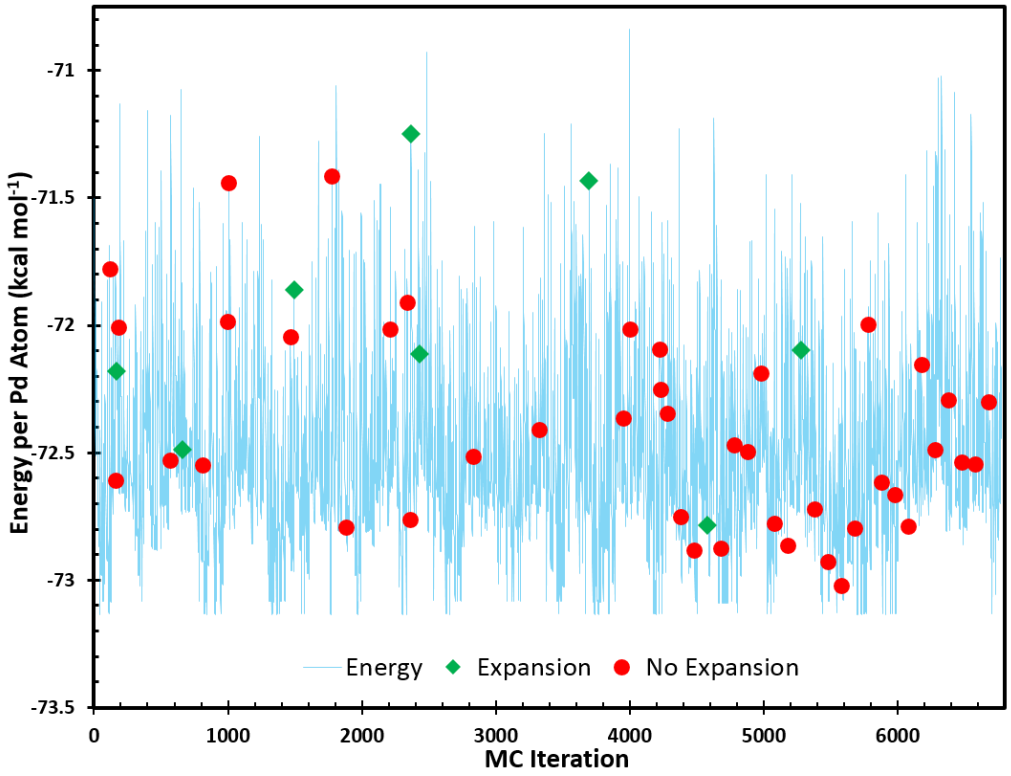

Figure B-6. Energy of clusters generated from a hybrid MC/MD simulation at 500 K. The green and red data points indicate clusters that were selected for separate MD simulations to assess Pd-Pd expansion upon exposure to Ar. Green diamonds indicate that an average Pd-Pd expansion > 0.001 Å was observed and red dots indicate that there was no change > 0.001 Å.

We selected 50 clusters (using a random number generator) from the 500 K MC/MD sample set to serve as starting geometries for MD simulations at 77 K. The selected clusters correspond to the green and red data points in Figure B-6. During each 77 K MD simulation, average Pd-Pd bond distances were determined by calculating the Pd-Pd radial pair distribution, *g(r)*, over the last 250 ps of the 1 ns MD simulations. As shown in Figure B-7 for a single cluster geometry, each simulation initially allows the Pd cluster to equilibrate at 77 K for 1 ns in vacuum before exposure to Ar (or He/vacuum in the case of control simulations). As seen in the figure, the simulation yields no change in Pd-Pd bond distance after exposure to vacuum or He, whereas cluster restructuring with a 0.003

Å Pd-Pd expansion occurs under Ar. The radial distribution function in Figure B-7(d), in comparison to those for control simulations in Figure B-7(a-c), demonstrates a clear restructuring of the cluster, where the shoulder appearing at r = ~2.60 Å in the control simulations shifts to r = ~2.75 Å (indicated by black arrows in the figure). This suggests the average Pd-Pd bond expansion can be attributed to a large increase in a few Pd-Pd bonds involving one or two atoms, as opposed to a small increase in all Pd-Pd bonds throughout the cluster. This is further depicted in Figure 5-8, which shows snapshots from the 15 ps MD-trajectory window in which the surface restructuring occurs. The restructuring occurs immediately after the Pd cluster interacts with an incoming Ar atom, suggesting that the momentum transfer from the Ar atom to the cluster induces the surface reconstruction. This reconstruction does not occur in the absence of the Ar gas phase. An animated video of this 15 ps trajectory demonstrating surface reconstruction is provided in the ESI, along with a 250 ps video of the cluster in vacuum showing no reconstruction.

A similar analysis was conducted for all 50 model clusters, where 8 clusters demonstrated an average Pd-Pd bond length expansion greater than 0.001 Å upon exposure to Ar and the remaining 42 exhibited no change greater than 0.001 Å, indicated by green diamonds and red dots, respectively, in Figure B-6. The expansion of Pd-Pd bond lengths was further quantified by assessing the average Pd-Pd bond length change for a single Pd atom as a function of its average coordination number under vacuum conditions. This is shown in Figure B-9, where we have plotted average bond length expansion against coordination number in vacuum averaged over all 50 clusters investigated. Figure B-9(a) contains data from clusters that exhibited an expansion, while Figure B-9(b) contains data from clusters that did not exhibit expansion. This analysis reveals that only under-

coordinated Pd atoms with low nearest-neighbor coordination numbers (*i.e.* 3-5) are affected by the Ar adsorption, with a typical bond length expansion of ca. 0.05 to 0.1 Å. Figure B-9(b) demonstrates some under-coordinated atoms are not affected by the Ar gas phase, indicating that some under-coordinated atoms are more stable than others. Observed coordination numbers greater than 12 reflect that these clusters have a disordered, non-crystalline lattice structure, which is expected for platinum-group-metals in this size range.[32]

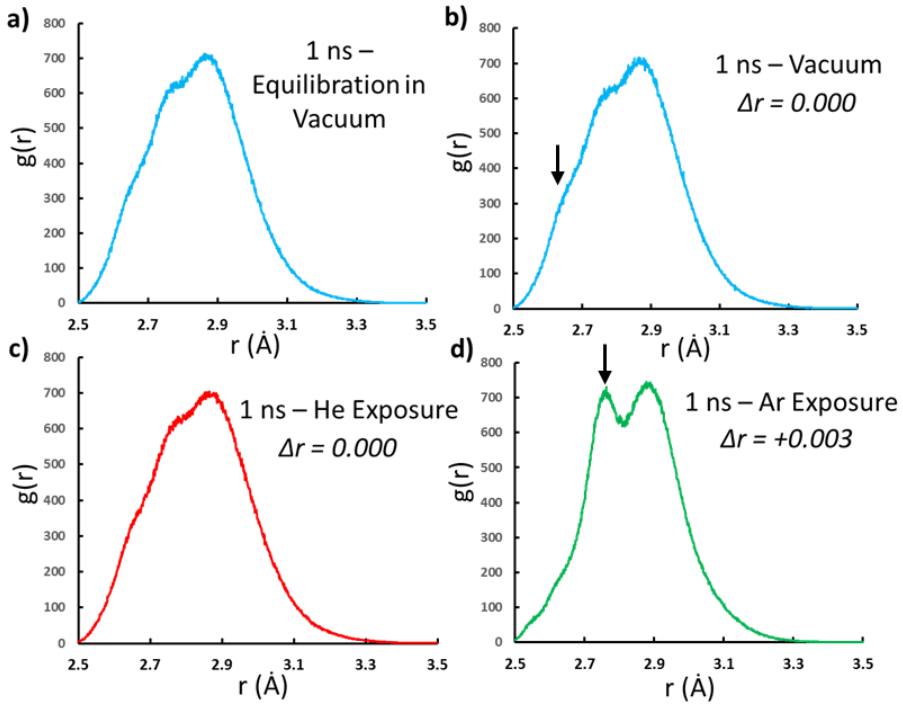

Figure B-7. Pd-Pd radial distribution function, *g(r)*, reflecting the average NN Pd-Pd bond distances during a 1 ns MD simulations at 77 K. (a) The Pd cluster was first allowed to equilibrate in vacuum for 1 ns, and was then exposed to (b) vacuum, (c) He gas, or (d) Ar gas for an additional 1 ns. Arrows indicate the peak shift attributed to the average Pd-Pd bond expansion of an under-coordinated surface atom.

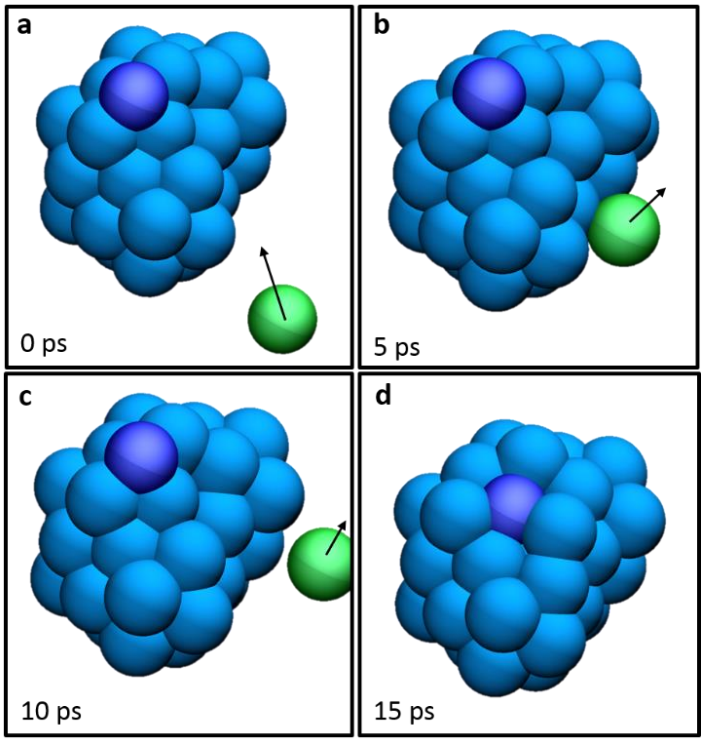

Figure B-8. 15 ps MD trajectory window demonstrating an Ar (green) collision with a Pd cluster (blue) inducing the restructuring of an under-coordinated Pd surface atom (purple). Only the Ar atom interacting with the Pd cluster is shown, all others are omitted for clarity.

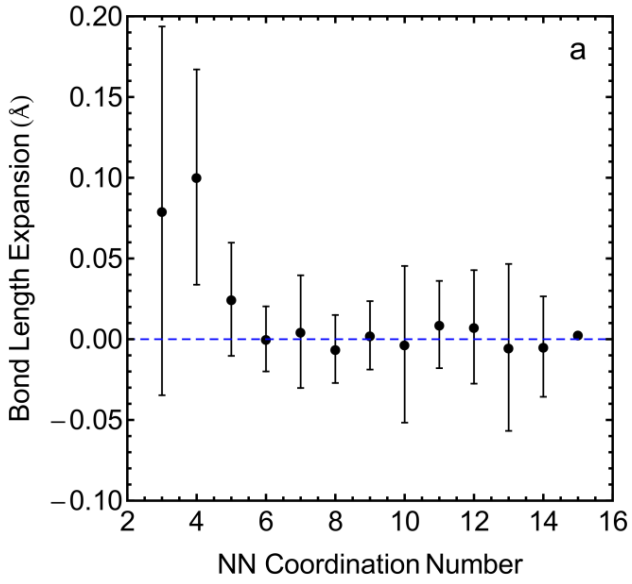

Figure B-9. Bond length expansion (relative to the clusters in vacuum) plotted versus first shell coordination number for all of the atoms in each of the Pd clusters that exhibited expansion after exposure to Ar at 77 K. Error bars indicate the standard deviation in bond length of the ensemble of atoms from each of the clusters.

Since Ar induces restructuring of under-coordinated surface atoms, it is likely that these atoms are kinetically trapped in metastable positions during the quench to 77 K, and that a transfer of kinetic energy from an Ar gas phase atom provides the additional energy required to allow relaxation of the metastable Pd atom to a more favorable site with higher average coordination and longer average Pd-Pd bonds. Not all under-coordinated sites are affected by Ar which could be the result of short simulation timescales, where a sufficient Pd-Ar interaction simply never occurred in the simulation timeframe. Also, some under-coordinated sites may be more stable than others, indicating that Ar can only induce the restructuring of sufficiently unstable Pd atoms. A ReaxFF nudged-elastic-band (NEB) barrier calculation, shown in Figure B-10, yielded a barrier of 11.4 kcal mol^{-1} for the reconstruction shown in Figure B-8, which is sufficiently high to suggest that this structure would be kinetically stable at 77 K under vacuum. Together, these simulations demonstrate that Ar may drive surface reconstructions of under-coordinated atoms, thus leading to an increased Pd-Pd bond length of surface Pd atoms.

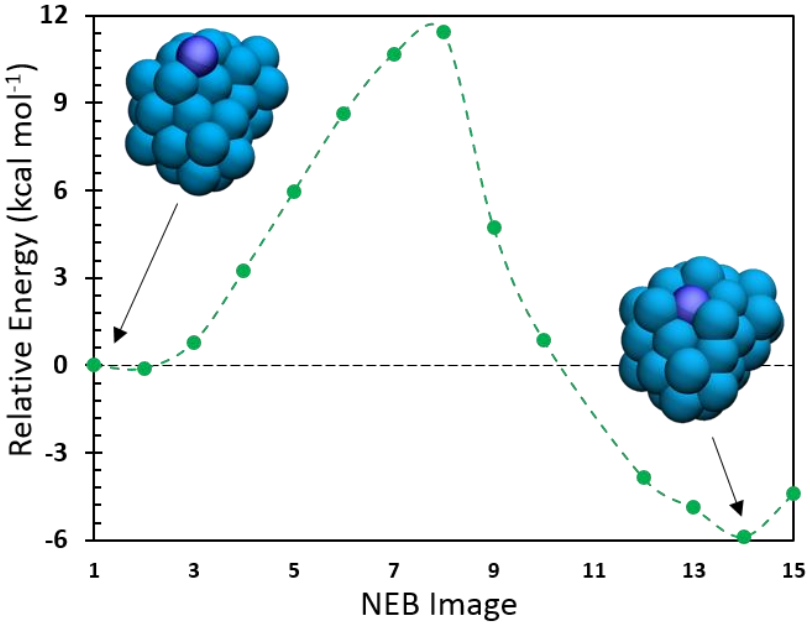

Figure B-10. ReaxFF-NEB barrier for surface reconstruction. Insets depict the initial and final cluster structures, where the NEB images were obtained by linear interpolation of the atomic coordinates.

B.4. Discussion

(Note: Discussion section written by C.S.S. and edited by T.P.S.)

Analysis of the differential EXAFS data using the model in Eq. (4) shows that Ar adsorption on Pd/SiO_2 at 77 K induces small changes in the Pd-Pd coordination environment, which can be attributed to the expansion in the bond length of surface Pd atoms. However, this model was created under the presumption that the overall Pd-Pd coordination number remained unchanged during Ar adsorption, and the correctness of such an approximation can be verified by examining simulated clusters before and after Ar adsorption. We calculated the average Pd-Pd coordination number of the clusters shown in Figure B-9(a) before and after Ar adsorption. The results are presented in Table B-3. In

each of the 8 simulations in which Ar caused restructuring, under-coordinated Pd atoms formed new Pd-Pd bonds, which is concomitant with expansion in their bond length. The number of Pd-Pd bonds formed varied, as this is dependent on the starting structure. Meanwhile, a similar number of Pd-Pd bonds were broken such that the average change in Pd-Pd coordination number was ~0. Therefore, the atomistic simulations are in agreement with the proposed differential EXAFS model in Eq. (4) and the experimental results shown in Table B-2.

Table B-3. Coordination environment changes of Pd clusters as a result of Ar adsorption.

Simulation[a]	**# of Pd-Pd bonds formed[b]**	**# of Pd-Pd bonds broken[c]**	**Δ avg NN CN[d]**
1	7.2	-9.6	-0.06
2	9.0	-9.8	-0.02
3	3.2	-1.3	0.04
4	5.1	-3.0	0.05
5	5.7	-1.0	0.11
6	4.5	-1.1	0.08
7	3.0	-5.0	-0.05
8	2.7	-7.1	-0.10
Averages	**5.1**	**-4.7**	**0.01**

[a]Simulations in which Ar caused restructuring.
[b]Number of Pd-Pd bonds formed during Ar adsorption.
[c]Number of Pd-Pd bonds that were broken during Ar adsorption.
[d]Average nearest-neighbor coordination number after Ar adsorption minus the average nearest-neighbor coordination number under vacuum.

It is intuitive to suggest that restructuring without an overall coordination number change requires strongly disordered nanoclusters because restructuring of a faceted particle will always lead to either an increase or decrease in coordination number if the total number of atoms in the particle remains the same. McKenna and Shluger showed that faceted Au nanoparticles restructure under CO adsorption, leading to an increase in coordination number.[33] Thus, for our theoretical models to be compatible with those real clusters used in our experiments, it is advantageous to model strongly disordered Pd/SiO_2 NCs rather

than faceted, crystalline, structures. Experimentally it has been demonstrated that alumina- and carbon- supported Pt clusters are predominantly non-crystalline in the size range less than 1-1.5 nm.[32]

The high effective pressure of Ar and omission of SiO_2-supported Pd NCs from the theoretical portion of this study are limitations in obtaining quantitative results of the restructuring. We expect that introduction of the SiO_2 support might result in a different distribution in Pd particle shapes and the time scale for energy transfer from Ar to Pd could be impacted by dissipation into the support. However, the overall mechanism for restructuring is likely independent of support, since the exposed Pd atoms in low coordination environments present on the Pd particle exterior, which participate in the observed restructuring, would likely not be adjacent to the support. Furthermore, the large difference in masses between Pd and SiO_2 atoms suggest a low amount of vibrational coupling, and therefore we could expect that dissipation of kinetic energy passed from Ar to Pd may remain in Pd related modes on the time scale observed in simulation. Thus, atomistic modeling qualitatively supports the hypothesis that under-coordinated surface atoms are those affected and helps us gain an atomistic level understanding of the process.

Other examples of Ar-induced restructuring include the work of Pellenq et al. who measured the neutron diffraction of ^{40}Ar adsorption in silicate-1 zeolite and showed that a step in the Ar isotherm coincides with a change in the neutron diffraction pattern.[34] Using grand canonical Monte Carlo simulations (GCMC), the authors concluded the change in diffraction pattern can be attributed to a rearrangement of the adsorbed phase. This conclusion has been further substantiated by García-Pérez et al., who showed through GCMC simulations that a flexible host structure is likely responsible for the stepped Ar

isotherm at 77 K of MFI zeolite.[35] More recently, Mallon et al. surmised that the hysteresis of the Ar 87 K adsorption isotherm of silicate-1 is a result of an orthorhombic-monoclinic symmetry shift.[36] On the other hand, Ar ion bombardment at low energy (c.a. 15 eV) has been shown to heal defects of carbon nanotubes.[37]

The EXAFS differential data analysis method we show in this paper is applicable to other systems where only a small fraction of surface species (active species) respond to the external stimulation (e.g. gas, pH, electric potential, temperature, etc.) while the majority of the atoms (spectators) are unaffected. In this study, we are able to measure a change in coordination environment of only 7% of the total number of Pd atoms, which highlights the sensitivity of the combined measurement and analysis scheme.

B.5. Conclusions

(Note: Conclusions written by C.S.S. and edited by T.P.S.)

Differential extended x-ray absorption fine structure (Δ-EXAFS) and atomistic molecular dynamic simulations have been used to detect under-coordinated surface Pd atoms of SiO_2-supported nanoclusters. The increased sensitivity of Δ-EXAFS allows for detection of small changes in the coordination environment of surface Pd atoms that would otherwise go undetected with conventional XAS techniques. Differentiating between possible models, a common problem associated EXAFS analysis, was accomplished through analysis of the simulation results. Further theoretical modeling of supported clusters might provide quantitative comparison between experiment and theory.

Using an inert gas such as Ar to probe surface atoms may be advantageous over conventional surface probe molecules such as CO, NO, and H_2 because it physically adsorbs without specificity, different from the highly selective binding associated with chemical adsorption. In this regard, inert gas adsorption might prove to be a general method for determining surface composition of multimetallic catalysts. We also note the possibility of using Δ-EXAFS at the Ar K-edge or Kr K-edge to probe metal surfaces from the perspective of the inert gas.

B.6. Acknowledgements

Use of the Advanced Photon Source was supported by the U.S. Department of Energy, Office of Science, Office of Basic Energy Sciences, under Contract No. DE-AC02-06CH11357. MRCAT operations are supported by the Department of Energy and the MRCAT member institutions. C. S. S. acknowledges the National Science Foundation under Grant No. DGE1255832. T. P. S, A. C. T. v. D., and M. J. J. acknowledge funding from the National Science Foundation under Grant No. CBET-1032979. Any opinions, findings, and conclusions or recommendations expressed in this material are those of the author(s) and do not necessarily reflect the views of the National Science Foundation. C. S. S., R. M. R., and A. I. F. acknowledge funding from the Department of Energy, Office of Basic Energy Sciences, Chemical Sciences, Geosciences, and Biosciences Division, Catalysis Sciences Program under grant numbers DE-FG02-12ER16364 (to R. M. R.) and DE-FG02-03ER15476 (to A. I. F.). The authors thank Randall J. Meyer, David Childers, and Jeffrey T. Miller for providing the Pd/SiO_2 sample and STEM images.

B.7. References

1. J. Rao, ACS Nano **2** (10), 1984-1986 (2008).
2. S. I. Sanchez, L. D. Menard, A. Bram, J. H. Kang, M. W. Small, R. G. Nuzzo and A. I. Frenkel, J. Am. Chem. Soc. **131** (20), 7040-7054 (2009).
3. D. Pacifici, H. J. Lezec and H. A. Atwater, Nat Photon **1** (7), 402-406 (2007).
4. D. Alloyeau, C. Ricolleau, C. Mottet, T. Oikawa, C. Langlois, Y. Le Bouar, N. Braidy and A. Loiseau, Nat. Mater. **8** (12), 940-946 (2009).
5. A. Sundaresan, R. Bhargavi, N. Rangarajan, U. Siddesh and C. N. R. Rao, Phys. Rev. B **74** (16), 161306 (2006).
6. J. K. Norskov, T. Bligaard, J. Rossmeisl and C. H. Christensen, Nat Chem **1** (1), 37-46 (2009).
7. M. S. Chen and D. W. Goodman, Science **306** (5694), 252-255 (2004).
8. P. L. Hansen, J. B. Wagner, S. Helveg, J. R. Rostrup-Nielsen, B. S. Clausen and H. Topsøe, Science **295** (5562), 2053-2055 (2002).
9. H. J. Freund, Chem. – Eur. J. **16** (31), 9384-9397 (2010).
10. A. R. Tao, S. Habas and P. Yang, Small **4** (3), 310-325 (2008).
11. T. Wu, D. J. Childers, C. Gomez, A. M. Karim, N. M. Schweitzer, A. J. Kropf, H. Wang, T. B. Bolin, Y. Hu, L. Kovarik, R. J. Meyer and J. T. Miller, ACS Catal. **2** (11), 2433-2443 (2012).
12. A. Eyssler, E. Kleymenov, A. Kupferschmid, M. Nachtegaal, M. S. Kumar, P. Hug, A. Weidenkaff and D. Ferri, J. Phys. Chem. C **115** (4), 1231-1239 (2010).
13. D. Ferri, M. S. Kumar, R. Wirz, A. Eyssler, O. Korsak, P. Hug, A. Weidenkaff and M. A. Newton, Phys. Chem. Chem. Phys. **12** (21), 5634-5646 (2010).
14. D. Ferri, M. Newton and M. Nachtegaal, Top. Catal. **54** (16-18), 1070-1078 (2011).
15. D. Ferri, M. A. Newton, M. Di Michiel, S. Yoon, G. L. Chiarello, V. Marchionni, S. K. Matam, M. H. Aguirre, A. Weidenkaff, F. Wen and J. Gieshoff, Phys. Chem. Chem. Phys. **15** (22), 8629-8639 (2013).
16. C. F. J. König, T. J. Schildhauer and M. Nachtegaal, J. Catal. **305** (0), 92-100 (2013).
17. C. F. J. König, J. A. van Bokhoven, T. J. Schildhauer and M. Nachtegaal, J. Phys. Chem. C **116** (37), 19857-19866 (2012).
18. R. F. Pettifer, O. Mathon, S. Pascarelli, M. D. Cooke and M. R. J. Gibbs, Nature **435** (7038), 78-81 (2005).
19. D. Childers, A. Saha, N. Schweitzer, R. M. Rioux, J. T. Miller and R. J. Meyer, ACS Catal. **3** (11), 2487-2496 (2013).
20. B. Ravel and M. Newville, J. Synchrotron Radiat. **12** (4), 537-541 (2005).
21. M. Newville, J. Synchrotron Radiat. **8** (2), 322-324 (2001).
22. A. C. T. van Duin, S. Dasgupta, F. Lorant and W. A. Goddard III, J. Phys. Chem. A **105** (41), 9396-9409 (2001).
23. T. P. Senftle, R. J. Meyer, M. J. Janik and A. C. T. van Duin, J. Chem. Phys. **139** (4), 044109-044115 (2013).
24. A. M. Kamat, A. C. T. van Duin and A. Yakovlev, J. Phys. Chem. A **114** (48), 12561-12572 (2010).

25. N. Metropolis, A. W. Rosenbluth, M. N. Rosenbluth, A. H. Teller and E. Teller, J. Chem. Phys. **21** (6), 1087-1092 (1953).
26. L. Verlet, Physical Review **159** (1), 98-103 (1967).
27. H. J. C. Berendsen, J. P. M. Postma, W. F. v. Gunsteren, A. DiNola and J. R. Haak, J. Chem. Phys. **81** (8), 3684-3690 (1984).
28. A. M. Beale and B. M. Weckhuysen, Phys. Chem. Chem. Phys. **12** (21), 5562-5574 (2010).
29. A. I. Frenkel, C. W. Hills and R. G. Nuzzo, J. Phys. Chem. B **105** (51), 12689-12703 (2001).
30. A. Frenkel, J. Synchrotron Radiat. **6** (3), 293-295 (1999).
31. A. I. Frenkel, Chem. Soc. Rev. **41** (24), 8163-8178 (2012).
32. L. Li, L.-L. Wang, D. D. Johnson, Z. Zhang, S. I. Sanchez, J. H. Kang, R. G. Nuzzo, Q. Wang, A. I. Frenkel, J. Li, J. Ciston, E. A. Stach and J. C. Yang, J. Am. Chem. Soc. **135** (35), 13062-13072 (2013).
33. K. P. McKenna and A. L. Shluger, J. Phys. Chem. C **111** (51), 18848-18852 (2007).
34. R. J. M. Pellenq and D. Nicholson, Langmuir **11** (5), 1626-1635 (1995).
35. E. García-Pérez, J. B. Parra, C. O. Ania, D. Dubbeldam, T. J. H. Vlugt, J. M. Castillo, P. J. Merkling and S. Calero, J. Phys. Chem. C **112** (27), 9976-9979 (2008).
36. E. E. Mallon, M. Y. Jeon, M. Navarro, A. Bhan and M. Tsapatsis, Langmuir **29** (22), 6546-6555 (2013).
37. E. C. Neyts, K. Ostrikov, Z. J. Han, S. Kumar, A. C. T. van Duin and A. Bogaerts, Phys. Rev. Lett. **110** (6), 065501 (2013).

VITA
Thomas Patrick Senftle

Education

The Pennsylvania State University, University Park, PA
Doctor of Philosophy – Chemical Engineering
University of Notre Dame, South Bend, IN
Bachelor of Science – Chemical Engineering (Major), Philosophy (Supplemental Major)

Publications

1. **Senftle, T. P.**; Janik, M. J.; van Duin, A. C. T., "The role of site stability during methane activation on $Pd_xCe_{1-x}O_\delta$." Submitted to *ACS Catalysis*.
2. Strayer, M. E.; **Senftle, T. P.**; Winterstein, J. P.; Vargas-Barbosa, N. M.; Sharma, R.; Rioux, R.; Janik, M. J.; Mallouk, T. E., "Strong adsorption of late transition metal nanoparticles correlates with sintering resistance on niobium oxides." Submitted for publication.
3. Tavazza, F.; **Senftle, T. P.**; Zou, C.; Becker, C. A.; van Duin, A. C. T., "Molecular dynamics investigation of the effects of tip-substrate interactions during nanoindentation." Accepted to *Journal of Physical Chemistry C*.
4. **Senftle, T. P.**; Janik, M. J.; van Duin, A. C. T., "A ReaxFF Investigation of hydride formation in Pd nanoclusters *via* Monte Carlo and molecular dynamics simulations." *Journal of Physical Chemistry* C 2014, 118, 4967.
5. Addou, R.*; **Senftle, T. P.***; O'Connor, N.; Janik, M. J.; van Duin, A. C. T.; Batzill, M., "Influence of hydroxyls on Pd atom mobility and clustering on rutile TiO2(011)-(2×1)." *ACS Nano* 2014, 8(6), 6321-6333. *Equal author contribution.
6. Spanjers, C. S.; **Senftle, T. P.**; van Duin, A. C. T.; Janik, M. J.; Frenkel, A. I.; Rioux, R. M., "Illuminating surface atoms in nanoclusters by differential X-ray absorption spectroscopy." *Physical Chemistry Chemical Physics* 2014, 16 (48), 26528-26538.
7. **Senftle, T. P.**; van Duin, A. C. T.; Janik, M. J., "Application of computational methods to supported metal-oxide catalysis." *Computational Catalysis (Book Chapter)*, Royal Society of Chemistry, 2014, 157-191.
8. **Senftle, T. P.**; Meyer, R. J.; Janik, M. J.; van Duin, A. C. T., "Development of a ReaxFF potential for Pd/O and application to palladium oxide formation." *Journal of Chemical Physics* 2013**,** 139 (4), 044109-15.
9. **Senftle, T. P.**; van Duin, A. C. T.; Janik, M. J., "Determining *in situ* phases of a nanoparticle catalyst *via* grand canonical Monte Carlo simulations with the ReaxFF potential." *Catalysis Communications* 2013, 52(0), 72-77.
10. Wu, C.; **Senftle, T. P.**; Schneider, W. F., "First-principles-guided design of ionic liquids for CO_2 capture." *Physical Chemistry Chemical Physics* 2012, 14 (38), 13163-13170.
11. Hudgens, J. W.; Pettibone, J. M.; **Senftle, T. P.**; Bratton, R. N., "Reaction mechanism governing formation of 1,3-Bis(diphenylphosphino)propane-protected gold nanoclusters." *Inorganic Chemistry* 2011, 50 (20), 10178-10189.
12. Gurkan, B.; Goodrich, B. F.; Mindrup, E. M.; Ficke, L. E.; Massel, M.; Seo, S.; **Senftle, T. P.**; Wu, H.; Glaser, M. F.; Shah, J. K.; Maginn, E. J.; Brennecke, J. F.; Schneider, W. F., "Molecular design of high capacity, low viscosity, chemically tunable ionic liquids for CO_2 capture." *Journal of Physical Chemistry Letters* 2010, 1 (24), 3494